A new class of Two-Dimensional Optoelectronic Materials in Accommodating Intraocular Lens Design

Emma Jade Ward

A Thesis submitted in partial fulfilment of the requirements of the University of Brighton for the degree of Doctor of Philosophy.

Abstract

Intraocular lenses (IOL), used to treat cataracts, successfully replace the cloudy crystalline lens of the eye to restore vision. However, no clinically available lens can effectively mimic the accommodative ability of the natural lens, responding to reflexive ciliary muscle movements to allow changes in optical focus. An optoelectronic approach could be used, incorporating smart sensor biomaterials which respond to optical stimulus by lens accommodation. However, materials with a suitable combination of optoelectronic and biological properties are limited. The two-dimensional transition metal carbides and/or nitrides, MXenes, are a family of nanomaterials with physical properties including high electronic conductivity, optical transparency, flexibility, biocompatibility, and hydrophilicity suggesting their suitability for use within an accommodating lens design. The aim of this work was therefore to investigate the suitability of $Ti_3C_2T_x$ (MXene) for use as a transparent conductive electrode within an accommodating lens design.

$Ti_3C_2T_x$ was synthesised through liquid exfoliation of the MAX phase precursor with lithium fluoride and hydrochloric acid. X-ray powder diffraction (XRD), X-ray photoelectron spectroscopy (XPS), UV-Vis spectroscopy and dynamic light scattering (DLS) size analysis was performed on the synthesised $Ti_3C_2T_x$ colloidal solution. The solution was spin-coated onto hydrophobic acrylate IOLs, and optical measurements of lens power and modulation transfer function were made. Optoelectronic performance was evaluated through spectral transmittance and conductivity using UV-Vis spectroscopy and a four-point probe technique. Biocompatibility was assessed using a human lens epithelial B-3 cell line with the CellTiter 96® AQueous One Solution Cell Proliferation Assay (MTS) and the CytoTox96 non-radioactive cytotoxicity assay (LDH). A monocytic THP-1 cell line was used to evaluate oxidative stress using the dichloro-dihydro-fluorescein diacetate (DCFH-DA) assay and stimulation of inflammation by enzyme-linked immunosorbent assay (ELISA) for inflammatory markers interleukin (IL)-6, IL-8, and TNF-α. A nematic liquid crystal (LC), 4'-Pentyl-4-cyanobiphenyl, 5CB, was used in the fabrication of a $Ti_3C_2T_x$ test cell to explore an electronically stimulated adjustable focus proof-of-concept design. The electric field-induced refractive index modulation of the LC was measured using

a purpose-built refractometer. $Ti_3C_2T_x$/LC lens design was explored in a glass-based model and optical methods were used to evaluate focusing performance and spatial frequency. In the development of an accommodative IOL prototype, a polymer-based $Ti_3C_2T_x$/LC design was investigated, as a more appropriate IOL base material.

$Ti_3C_2T_x$ physical characterisation studies produced an optimised synthesis route for spin-coating onto hydrophobic acrylate IOLs. The coatings optoelectronic evaluation found sheet resistance to range from 0.2 – 1.0 kΩ sq^{-1} with transmittance in the visible region ranging from 50 – 80 %. *In vitro* biological studies investigating the interaction of $Ti_3C_2T_x$ coated IOLs with human lens epithelial cells indicated that the $Ti_3C_2T_x$ coatings were non-cytotoxic with cell numbers of $3.5x10^4 \pm 5.1x10^3$ for the cell only and $3.8x10^4 \pm 5.4x10^3$ and $4.1x10^4 \pm 5.4x10^3$ for the $Ti_3C_2T_x$ coated IOLs and uncoated IOL. A monocytic cell was used to evaluate inflammatory pathways, that demonstrated no significant upregulation of pro-inflammatory markers exposed to the coating ($p < 0.05$). The proof-of-concept adjustable focus test cell was constructed with a layer of LC sandwiched between $Ti_3C_2T_x$ coatings on glass substrates. The LC layer experienced molecular reorientation with an applied electric field that resulted in optical changes to the point of focus. The fabrication of a $Ti_3C_2T_x$/LC lens was optimised in a glass model which demonstrated adjustable focus through electrical stimulation.

In conclusion, the synthesis, physical, and biological characterisation of the $Ti_3C_2T_x$ nanomaterial, spin-coated onto hydrophobic IOLs for use within an ophthalmic IOL has been demonstrated for the first time. Moreover, the proof-of-concept test cell and adjustable focus lens indicated the feasible use of $Ti_3C_2T_x$ as a transparent conductive electrode within a smart lens device capable of inducing changes in optical power on the application of an external force.

Table of Contents

Acknowledgements

I would like to begin by expressing my gratitude to my supervisory team, Dr Susan Sandeman, Dr Marcus Dymond, Prof. Cyril Crua, Dr Joseph Lacey and Prof. Yury Gogotsi. Thank you for your guidance and support throughout this work. I would also like to thank the University of Brighton, Drexel University, Rayner Intraocular Lenses, and the Medical Research Council.

Nic, thank you for everything you have done to allow me to get me to this point. Thank you for your encouragement, positivity and for motivating me to write with take-aways. The past four years have been the most difficult I have ever experienced, and it was your ongoing support that got me here, so thank you with all my heart. Thank you for your assistance in developing the MATLAB scripts, for teaching me how to use Illustrator and for always being patient with me.

Thank you to my family, in particular my mum who has always supported me and made me the person I am today. Thank you to my siblings, Laura, Owen, and Aidan, and to their children, specially Thyan who will probably follow in my footsteps. Thank you to Charlie, Gunn, Laura, Tim, Valley, and Albi. Thank you to the peanuts, Kayleigh, Ian, Henley, and Harlow, you bring so much happiness to my life, especially at times when the PhD has been stressful.

A special thanks to my friends and colleagues. Thank you to Charis, we started our PhDs together, it's been tough, but we did it and had so many laughs along the way. I wouldn't be here without your constant reassurance that it's all going to be okay. Thank you, Hannah, for listening to me whining and for always encouraging me to

work hard. To Grace and Alex, thank you for everything, you'll never know how much you really helped me.

Thank you for your advice, support, and entertainment over the years to Fernando, Flavia, Filippo, Marcela, Blair, Neda, Natalia, Nadia, Media, Ryan, Francois, and Rico. I would also like to thank the colleagues I met at Drexel University that have become great friends. Sam, Kanit and Asia, thank you for the great memories we shared in Philly and your continuous support that get me here.

This work is dedicated to my dad, Clifford Ralph Ward, who sadly passed away on December 9th, 2020.

I know he would be very proud of me, and I miss him so much.

Declaration

I declare that the thesis has been composed by myself and that the work has not been submitted for any other degree or professional qualification. I confirm that the work submitted is my own, except where stated otherwise by reference or acknowledgement.

Emma J Ward  Date: 3rd July 2022

List of figures

List of tables

Abbreviations

3T3	Mouse embryo fibroblast cell line
5CB	4’-Pentyl-4-cyanobiphenyl
AAc	Acrylic acid
AFM	Atomic force microscope
AIOL	Accommodative intraocular lens
CVD	Chemical vapour deposition
DLS	Dynamic light scattering
EDS	Energy dispersive spectroscopy
ELISA	Enzyme-linked immunosorbent assay
EM	Electromagnetic
ETO	DC Resistivity/electrical transport option
FoM	Figure of merit
HLEs	Human lens epithelial cells
IFU	Instructions for use
IL-6	Interleukin-6
IL-8	Interleukin-8
IOL	Intraocular lens

ISO	International Organisation for Standardisation
ITO	Indium tin oxide
LC	Liquid crystal
LCD	Liquid crystal display
LDH	Lactate dehydrogenase
LPS	Lipopolysaccharide
MAX	$M_{n+1}AX_n$
MILD	Minimally intensive layer delamination
MTF	Modulation transfer function
MTS	3-(4,5-Dimethylthiazol-2-yl)-5-(3-carboxymethoxyphenyl)-2-(4-sulfophenyl)-2H-tetrazolium, inner salt
Nd:YAG	Neodymium-doped yttrium aluminium garnet
NIR	Near-infrared
PCO	Posterior capsule opacification
PMMA	Poly(methylmethacrylate)
PTT	Photothermal therapy
PVA	Poly(vinyl alcohol)
ROS	Reactive oxygen species
SEM	Scanning electron microscopy

TCE	Transparent conductive electrode
THP-1	Human peripheral blood monocyte cell line
TN	Twisted nematic
TNF-α	Tumour necrosis factor-alpha
UV	Ultra-violet
UV-Vis	Ultraviolet-visible spectroscopy
XAS	X-ray absorption spectroscopy
XPS	X-ray photoelectron spectroscopy
XRD	X-ray diffraction

Chapter 1

1 Introduction

1.1 Overview

Globally, cataracts are the leading cause of preventable blindness, contributing to a healthcare burden of approximately 2.2 billion cases of vision impairment worldwide, of which 94 million are cataract related[1]. As an age-related disorder, cataracts, and cataract surgery, place a growing strain on healthcare services with an increasing and ageing population. The prevalence of the disorder will continue to rise as people live longer contributing to a demand for improved lens technology.

The current effective yet invasive treatment for cataracts is the extraction of the crystalline lens from the capsular bag and the implantation of an intraocular lens (IOL)[2]. The implanted IOL restores visual acuity for distant vision, but glasses are required for near vision due to the unavoidable loss of the natural accommodative function of the lens. Accommodation, or pseudophakia, is the eye's ability to vary its optical power to observe objects at all distances[3]. Some IOLs have been marketed as accommodative intraocular lenses (AIOLs). However, a lens that adequately mimics the eye’s sensitive, adaptive change in optical power, for near, intermediate, and distance vision has yet to be developed.

One approach toward the development of lens technology that may lend itself to AIOL design is the use of an emerging class of nanomaterials. MXenes are two-dimensional transition metal carbides and/or nitrides that have gained interest owing to their combination of high electrical conductivity, mechanical strength, optical transparency, hydroxide/oxide-like surface chemistry, and hydrophilicity[4]. Since their discovery in

2011, they have demonstrated promise in various interdisciplinary applications such as energy storage and water purification[5–7]. Additionally, MXenes have demonstrated capabilities for biomedical applications, including photothermal therapy and biosensing, displaying favourable biocompatibility properties[8–11].

This chapter provides background physiology of the human eye, with reference to the ageing process and the mechanism of formation of senile cataracts. Outcomes of current cataract treatments, by which accommodation is lost, are discussed. Existing IOLs, manufacturing materials, design considerations, and recent advancements in the field are presented. Current AIOL designs are presented, and their functionality, performance, limitations, and remaining challenges/ knowledge gaps are discussed. MXenes are presented as an appropriate nanomaterial for AIOL design. Highlighting current biomedical applications of MXenes, which suggest further applications in implantable lens technologies.

1.2 The crystalline lens of the human eye

The eye's crystalline lens is an avascular, biconvex, and transparent structure that enables precise light refraction as part of the human visual system. The lens, located behind the iris, is suspended by zonules that connect to the ciliary body, as demonstrated in ***Figure 1-1***. The fine-tune adjustments of the lens combined with the refractive power of the cornea result in single-point focus on the retina.

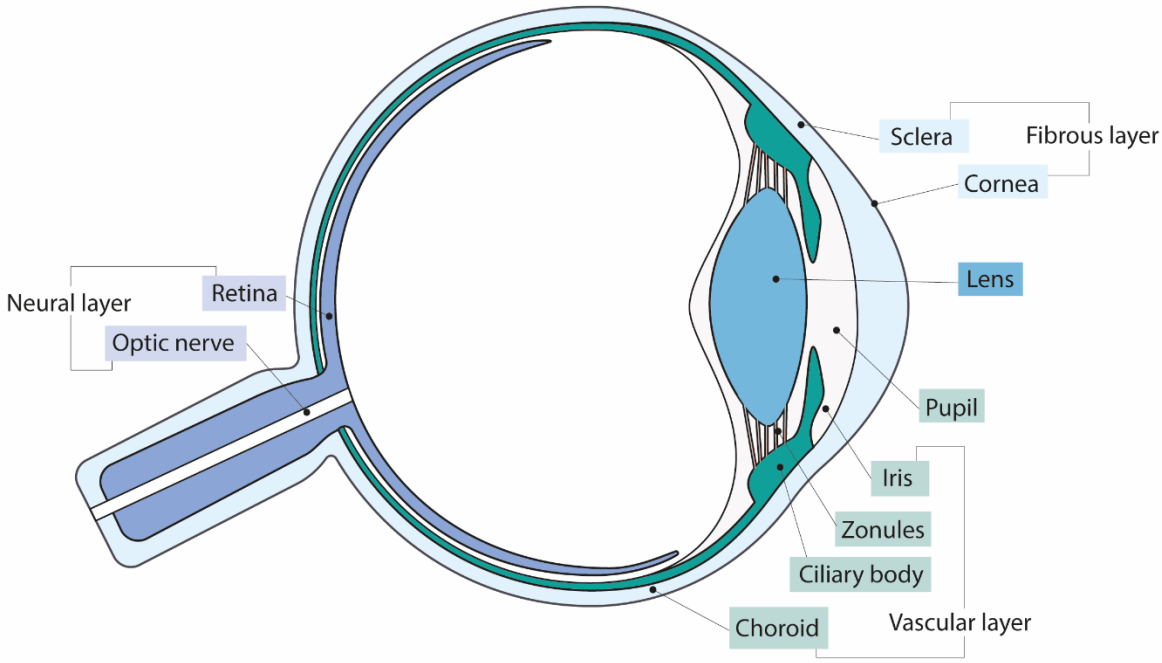

Figure 1-1 – A schematic of the cross-section of the human eye detailing the key features of the outermost, fibrous, vascular, and innermost neural layers.

The lens adjusts its radius of curvature through a mechanism called accommodation, which allows objects at all distances to be observed, providing an image that is continuously in focus. When observing a nearby object, the ciliary muscles of the ciliary body contract, the zonule ligaments relax and the sphericity of the anterior and

posterior surfaces of the lens increase. The increase in lens curvature leads to increased optical power, referred to as near sight[12]. Conversely, the ciliary muscles relax when observing a distant object, and tension is restored in the zonules. The lens flattens, which decreases optical power, as explained by the Helmholtz model[13]. Optical power, also described as dioptric power, is the level of convergence or divergence of an optical system. Optical power is calculated as the reciprocal of the optical system's focal length, measured in metres^{-1} or dioptres (D). A long focal length corresponds to low optical power and vice versa. The accommodation process provides fine-tune refraction to efficiently converge light to a single point on the retina as the lens undergoes continuous shape changes[14]. A series of photoreceptor cells, rods and cones, translate the eye's optical response to an electrical neural impulse sent to the optic nerve and visual pathways.

The crystalline lens is composed of an elastic lens capsule, lens epithelium and lens fibre cells shown in ***Figure 1-2***. The extracellular matrix of the lens capsule surrounds the lens. It contributes to the overall structure and elasticity of the lens with its lamellar arrangement of collagen fibres. The anterior lens epithelium is a monolayer of cells responsible for the continuous growth and development of the lens. The region of the epithelium slightly anteriorly to the equator of the lens is the germinal zone where mitosis occurs. Epithelial cells begin to differentiate through partial apoptosis, losing cellular organelles, leaving only their cytoskeleton. The removal of organelles results in transparent cells, which elongate into lens fibres and move towards the cortex[15]. The lens fibres form a densely packed hexagonal array as newly differentiated fibres surround pre-existing fibres. This process is continuous throughout life, with older fibres found in the nucleus and new fibres located at the periphery of the cortex. High

concentrations of lens proteins called crystallins are found in lens fibre cytoplasm. Crystallins maintain the elongated shape of lens fibres and, the overall structure of the lens itself. They account for approximately 90 % of all water-soluble lens proteins, while the remaining 10 % are water-insoluble proteins such as membrane and cytoskeleton proteins[16]. The three significant crystallin proteins are α-crystallin, β-crystallin, and γ-crystallin (α, β, and γ), they are categorised based on their molecular weight, detailed in ***Table 1-1***, with their subunits and relative abundances[17]. The concentration of these proteins varies across the lens, affecting the refraction of light, with higher concentrations in the nucleus and lower in the cortex. Therefore, a refractive index gradient is observed, high to lower, from the centre out towards the periphery[18].

Table 1-1 – Crystallin α, β, and γ, their subunits, molecular weights, and relative abundances within the crystalline lens[17].

	Subunits	Molecular Weight (daltons)	Relative abundance
α-Crystallin	αA, αB	750 000	35 %
β-Crystallin	βL, βH	(β_L) 50 000, (β_H) 160 000	55 %
γ-Crystallin	γA, γB, γC, γD, γE, γF	20 000	10 %

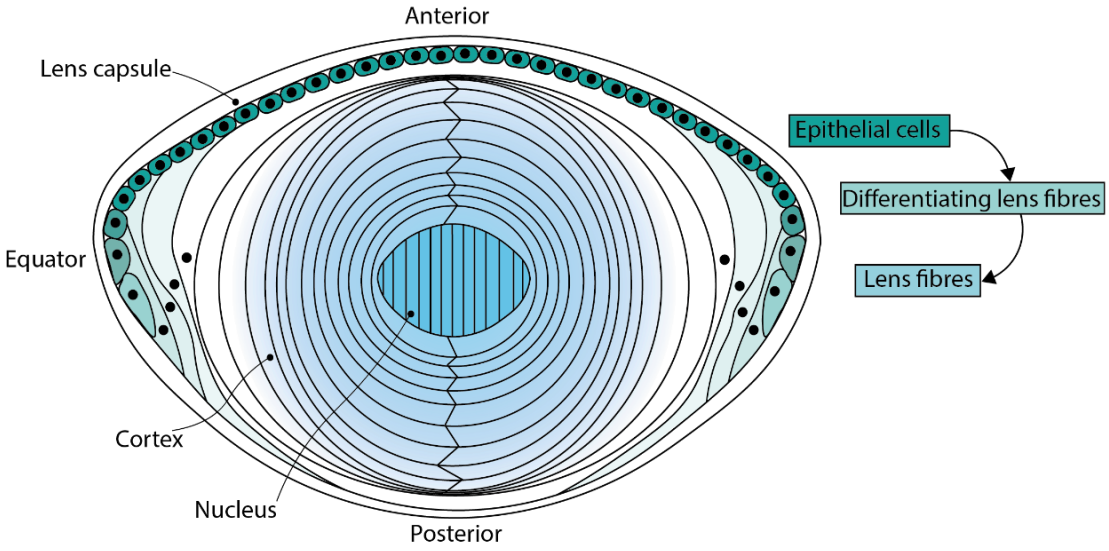

Figure 1-2 – Schematic of the crystalline lens of the eye.

Numerous age-correlated changes occur within the crystalline lens, which impacts visual acuity. For example, presbyopia is the progressive and inevitable deterioration of the eye's accommodative ability to focus on near objects[19]. The reduction in the amplitude of accommodation is measured as the difference between the refractive power at relaxation and maximum accommodation. At 10 years old accommodation is around 14 D, whereas at the age of 40 it is reduced to 6 D and at 60 it is about 1 D[20]. The reduction in accommodative amplitude occurs because new lens fibres lay down onto pre-existing fibres and this cumulative growth increases the overall thickness of the lens. The resultant thickening influences the elasticity and sclerosis of the lens tissue[21]. The denser and less malleable lens has significant adverse effects on the quality of vision and, consequently, quality of life[22].

Transparency of the lens is also a key component concerning the ageing process and visual acuity. Throughout an individual's lifetime, lens transparency is maintained through precise alignment of the lens fibres, high concentrations of crystallin proteins,

tight inter-fibre spaces and the correct functioning of transport mechanisms that supply the lens with metabolic substances and antioxidants from the aqueous humour[15]. Nevertheless, the efficiency of these systems can diminish over time. For instance, crystallins undergo transformations such as phosphorylation, disulphide bond formations, deamidation and peptide bond disruption that leads to agglomerations, hence irregularities in their structural arrangement[23]. As crystallins are not metabolically regenerated in lens fibres, their transformations are significant and impact the lens's overall opacity, causing light to be scattered, which is exacerbated through exposure to environmental stresses like heat and sunlight[15,24]. The gradual reduction in acuity, the clouding of the lens, observed over time, is described as a senile or age-related cataract.

1.3 Cataracts

The term cataract refers to any degree of opacity or clouding of the crystalline lens causing blurred vision, lowered contrast sensitivity, halos, double vision and increased sensitivity to glare[25,26]. Age-related cataracts are the most common type that occurs through the natural ageing processes of the crystalline lens. These ageing changes can be exacerbated by smoking, excessive alcohol consumption, over-exposure to direct sunlight, obesity, and high blood pressure[27]. Cataracts can also develop following trauma to the eye, from congenital conditions or secondary to other health issues such as glaucoma or diabetes[22,28]. It was estimated that by 2020 in the United Kingdom alone, there would be approximately 695 000 people living with the disorder[29,30]. The ageing population will continue to put increased pressure on healthcare services for

cataract treatment, including the need for technological improvement to artificial implantable lens performance.

1.3.1 Cataract treatment

Cataract treatment is the most common procedure performed in the developed world, with 400 000 routine outpatient surgeries carried out in England each year[31]. Prior to the development of modern-day phacoemulsification, a range of methods were explored. In 1747, the first document of an extracapsular extraction was reported where the cataract was removed through an inferior corneal incision[32]. By 1753, an intracapsular extraction technique was used and remained the predominant procedure until the late 19th century, with some developing countries still using this method. Phacoemulsification was introduced in the late 1960s. Phacoemulsification is a technique used to fragment and remove the natural crystalline lens from the capsular bag where an IOL is implanted in its place. The method uses a handheld ultrasonic probe which breaks up the cataract. A small incision of 2 – 3 mm is made in the cornea and capsular bag. The ultrasonic probe is inserted into the capsular bag, and the opaque lens is mechanically disrupted. The fragments are aspirated from the eye whilst viscoelastic gel fills the anterior chamber, maintaining ocular pressure throughout the procedure. An IOL is implanted in the capsular bag in place of the natural lens, restoring the patient's visual acuity. The technique has since undergone several modifications, with ophthalmic viscosurgical devices (OVDs), which are gel-like substances introduced to maintain space in the eye during surgery[33]. IOL technology has also undergone many modifications, both to manufacturing material and design functionality, with the most recent developments being AIOLs.

1.3.2 The intraocular lens

In 1949, the world's first IOL was implanted. The inventor and pioneer of the lens, Sir Harold Ridley, first considered an IOL for cataract treatment when he observed that poly(methylmethacrylate) (PMMA) fragments lodged in pilots' eyes did not cause inflammation[34]. Since the discovery, IOLs have undergone significant development to optimise fundamental aspects such as biocompatibility for the ocular environment and the reduction of optical phenomena.

One of the most impactful advances in IOL technology was introducing foldable materials. In the 1980s, foldable materials emerged, introducing the opportunity for smaller incisions during implantation[26]. At the time, the average PMMA lens required a 12.0 mm incision, while foldable materials reduced the wound to an average size of 2.5 mm[35]. Silicone, phenylethyl methacrylate, and hydroxyethyl methacrylate are examples of foldable materials that allowed reduced incision sizes and presented the convenience of preloaded injectors. This pivotal change significantly improved patient outcomes and surgeon experiences by reducing surgical complications, shortened recovery time, and minimised post-surgery adverse events, including endophthalmitis, posterior capsule rupture, and posterior capsule opacification (PCO)[25,34,36]. ***Table 1-2*** summarises the strengths and weaknesses of these materials.

Table 1-2 – A generalised comparison of current IOL materials used in IOL manufacture, their structures, properties and respective advantages and disadvantages *posterior capsule opacification (PCO).

Material	Properties	Benefits	Limitations
Hydrophobic Acrylate [20,37–41]	Non-foldable poly(methyl methacrylate) (PMMA), first IOL, sharp edge optic, rigid, ~1% water content	Low PCO* rate, rigidity means resistance to tilt	Larger wound size, damage to the corneal endothelium, non-foldable
Hydrophobic Acrylate [20,37–41]	Foldable, phenyl ethyl methacrylate, most commonly used, ~1%water content, high refractive index, high material memory, capsular biocompatibility	Good biocompatibility and unfolds in a controlled style	Optical glistening internal reflections due to high refractive index causes edge glare
Silicone [20,37–41]	High thermal stability, first foldable IOL, low refractive index	PCO* blocking ability	It cannot be used in monobloc open-loop design, which is required for preloaded injectors, inflammation, calcification
Hydrophilic Acrylate [20,37–41]	Hydroxyethyl methacrylate, foldable, ~26% water content (considered high), manufactured in a dehydrated state	Produce a lower level of inflammatory response	Calcification and higher PCO rate

Additional features incorporated into IOL material formulations include ultra-violet (UV) filters to block harmful light that could damage the retina[40]. Whilst modifications to the chemical composition influence properties like biocompatibility, mechanical strength, and flexibility, IOL coatings and surface functionalities have also

been explored to investigate cellular adhesion toward the prevention of PCO formation[42]. Depending on the manufacturer, IOLs can be made as a single- or multipiece design, with the options of plate haptics, open-loop, or a combination of a plate loop shown in ***Figure 1-3***. A single-piece material with an open-loop haptic allows the IOL to be rolled into a smaller diameter injector, minimising the risk of damaging the optic or haptics during implantation[40].

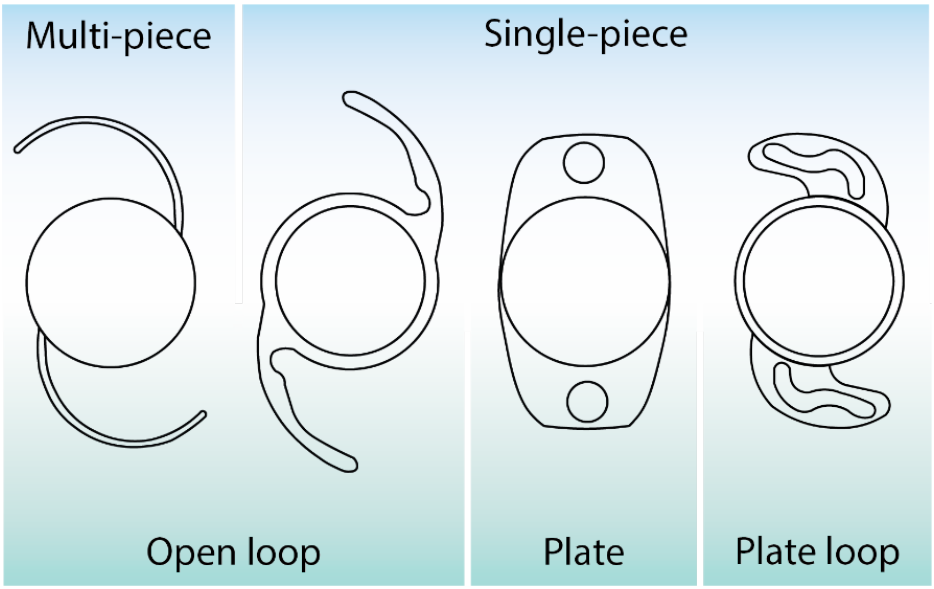

Figure 1-3 – Schematic of IOL designs including multipiece, single-piece, open loop, plate, and plate loop.

The examples in the figure (1-3) are standard IOLs that are used to treat cataracts, called monofocal IOLs that provide distance vision. Patients are required to use glasses for near and intermediate vision[20]. Multi- and trifocal lenses are alternative IOL models providing more than one focal point, with the potential to offer near, middle, and far focus. Concentric circles on the optic create different focal lengths[43].

Extended-depth-of-focus (EDOF) IOL technology, used to treat presbyopia, offers an improved depth of focus compared to multi-focal lenses but is limited by reduced retinal image quality due to aberrations[44]. Nevertheless, these lenses have not been the solution to restoring accommodation following cataract surgery. Furthermore, they are associated with undesirable optical phenomena such as contrast sensitivity, halos, and glare[20].

1.4 Accommodative intraocular lens

IOL research into accommodative intraocular lenses (AIOLs) is ongoing. Truly AIOLs aim to provide a rapid and dynamic shift in optical power, that permits continuous focus for near, intermediate, and distance vision under the activation of the ciliary body, where 2.5 to 3.0 D of divergence is required for near vision [20,45]. Hence, an ideal AIOL would be one that provides visual acuity and restoration of accommodation. Approaches that have been explored are changing the axial position of the lens relative to the capsular bag and shape or curvature alterations in the lens.

1.4.1 Axial displacement accommodative intraocular lenses

Axial displacement AIOLs cause a change in optical power through the position of the lens in combination with the cornea. Therefore, the eye experiences a global change in power rather than a change in power of the IOL itself. This is referred to as apparent accommodation or psuedoaccommodation rather than true accommodation. These types of AIOLs are typically plate lens designs, that when implanted in the capsular bag, rest on the vitreous face. During ciliary contraction, vitreous cavity pressure

increases, displacing the lens in a forward movement along the eye's axis and in conjunction with the cornea. Theoretically, displacement by 1 mm corresponds to a change of 2 D[20]. ***Table 1-3*** summarises several examples of AIOLs that function through axial movement.

Table 1-3 – Examples of axial displacement AIOLs with descriptions of their materials, design, mechanism of accommodation, and reported accommodation.

Lens	Material and design	Mechanism	Commercially available	Reported accommodation
Crystalens (Bausch & Lomb, USA) 2005	Single-optic, silicone, multipiece, flexible T-shaped plate haptics	Displacement along the eye's axis	Yes	< 0.4 D [46–48] 1 D [49,50] 2.5 – 4 D [51]
TetraflexHD (Lenstec, Inc., USA) 2007	Single-optic, one-piece, hydroxyethyl methacrylate (HEMA) lens, closed-loop haptics	Displacement along the eye's axis	Yes	2 D [52] 1.5 D [53]
Synchrony AIOL (Visiogen, Abbott Medical Optics, USA) 2010	Dual-optic, silicone, single-piece, plate haptic design, two optics attached with spring function	Displacement through spring-activated haptics	Yes	1 – 2.5 D [54]
The Lumina (AkkoLens, The Netherlands) 2016	Dual-optic, hydrophilic acrylic, two lenses attached at haptics	Displacement perpendicular to the optical axis	Yes	1 D [55]

The Crystalens is a single-optic axial displacement AIOL that hinges forward during ciliary contraction to increase the eye's overall optical power. It was approved by the Food and Drug Administration (FDA) in 2003, stating the lens "provides approximately 1 D of monocular accommodation"[49]. Since that time, studies have further investigated its performance as an AIOL, presenting contradictory data. In one example, the Crystalens improved intermediate and near vision compared to monofocal IOLs[51]. Several other investigations report poor results, stating no significant difference was observed between the AIOL and monofocal IOLs[47,48,56,57].

The TetraflexHD is another single-optic lens that functions similarly to the Crystalens, with ribbon-like haptics that allows flex along the eye's axis during ciliary accommodative contraction. Some reports showed temporary improvements in near and intermediate vision at six months post-operative evaluations, although these results were significantly reduced when reviewed at twelve months[52,58,59]. Clinical studies have, however, shown the Tetraflex lens to outperform the Crystalens in providing patients with improved near vision[60,61]. While limited accommodative amplitude is the main disadvantage of single-optic AIOLs, PCO incidence has been higher when compared to standard monofocal lenses with an enhanced sharp edge[62,63].

The Synchrony AIOL is a dual-optic lens with its anterior and posterior lenses connected by spring-like haptics[64]. The posterior lens is fixed in place during ciliary contraction while the anterior lens translates forward on the eyes axis, increasing the inter-optic separation, thus optical power for near vision[65]. Minimal accommodative amplitude was demonstrated in clinical trials[66]. When compared to monofocal visual

acuity, the Synchrony has shown superior near and intermediate vision, although most patients still require glasses for distant vision[67].

The Lumina is another dual-optic lens design. This lens is implanted in the ciliary sulcus, which is the space between the posterior of the iris and the anterior of the ciliary body. The two hydrophilic acrylate lenses overlap and move across one another in a centripetal motion. Ciliary contraction forces the lenses in opposite directions, perpendicular to the eye's optical axis, to increase the eye's overall optical power changes[68]. An improvement has been reported in distant and near vision for the Lumina AIOL compared with a monofocal IOL, though studies are relatively sparse for this lens[56].

Investigations into single- and dual-optic designs demonstrate that similar limitations to standard IOLs remain with regard to near vision and postoperative complications. Although theory suggests that 1 mm of anterior displacement of the lens results in 2 D of accommodation, investigations demonstrated a 0.4 D shift[69]. Capsular bag fibrosis will further restrict axial movement as the bag stiffens over time, decreasing the accommodative amplitude[70]. Dual-optics AIOLs have shown greater contrast sensitivity and optical quality than single-optic accommodative lenses. A higher rate of PCO development was observed with single-optic AIOLs[67]. Lens material and design are major contributors to light issues and PCO development. Although the reports suggest that some degree of pseudoaccommodation is restored with axial displacing AIOLs, the demand to develop a truly AIOL remains.

1.4.2 Shape- and curvature-changing accommodative intraocular lenses

The natural crystalline lens accommodates through adjustments in lens curvature, producing dynamic changes in optical power. AIOLs aim to respond to ciliary stimuli in a similar way. The active mechanism of shape- and curvature-changing lenses take advantage of the forces exerted onto the equator of the lens, altering the lens shape. Several investigations have demonstrated different designs aiming to achieve controlled and reversible changes in optical power based upon changes in optic curvature, presented in ***Table 1-4***.

Table 1-4 – Examples of shape- and curvature-changing AIOLs with descriptions of their materials, design, mechanism of accommodation, and reported accommodation.

Lens	Material and design	Mechanism of accommodation	Commercially available	Reported accommodation
Wichterle Intraocular Lens-Continuous Focus (WIOL-CF) (Medicem, Czech Republic) 2010	Methacrylic copolymer hydrogel resembles the crystalline lens, with no haptics, optic on one side	Shape changes during ciliary contraction, and lens thickness in the centre increases	Yes	1 D [71]
Fluid vision AIOL (PowerVision, USA) 2015	One-piece, fluid-filled haptic reservoirs	Shape/curvature changing, fluid moves from the haptics during contraction of the ciliary muscles to the optic in the centre of the lens, changing the anterior radius and shifting the lens forward	Developmental stages	Not specified[72]
NuLens Dynacurve AIOL (NuLens, Ltd., Herzliya Pituah, Israel) 2015	Multipiece lens, PMMA haptics and optic, chamber of silicone gel	Shape-changing, when the ciliary contracts, the gel bulges to increase the optical power.	Clinical trial	Not specified[20]

The Wichterle Intraocular Lens-Continuous Focus (WIOL-CF) is a full optic, haptic-free design. This lens was developed to mimic the function of a youthful crystalline

lens. Due to its anterior surface and polyfocal posterior surface, a refractive index gradient is produced with a higher power in the centre of the IOL. Reports state that this lens performs similarly to a multifocal lens, offering superiority over a standard monofocal lens[73,74]. One study found that half of their participants no longer required glasses for near vision following implantation, although the same amount had issues with light phenomena such as glare[75].

The FluidVision AIOL is another shape-changing design with oil-filled haptic reservoirs, where the oil fills up the optic upon contraction[72,76]. The back and forth flow of oil between the haptics and optic results in lens curvature changes. A pilot study described near, intermediate, and distance vision improvements[77]. Literature on this design is limited and poses possible refractive issues with capsular fibrosis if the oil is restricted of movement.

The NuLens has a deformable surface with a gel in the central chamber that bulges forward under ciliary contraction[20]. It is implanted in the ciliary sulcus, located between the iris and the ciliary body; therefore, the potential of capsular fibrosis will not influence its functionality. Although the magnitude of surface curvature, hence accommodative amplitude is directly correlated to ciliary forces. A clinical trial demonstrated good corrected near vision. However, 60 % of patients developed PCO, and two serious adverse events occurred. Posterior synechiae, where the iris adhered to the lens and capsulorhexis edge capture of the haptic, which stretched the capsule and put pressure on the lens[55]. Though the design has the possibility to address accommodation, patient safety must be investigated further.

Shape-changing lenses demonstrate clear advancements in IOL technology and AIOL development with mechanisms that behave more closely to the crystalline lens.

However, the available literature to support the accommodative outputs is limited. Issues regarding postoperative complications are prevalent; thus, safety and efficacy remain a significant challenge. Additionally, concerns related to capsular fibrosis and the weakening of ciliary muscles influence the resultant accommodative amplitude. The mechanism of accommodation would benefit from relying less on ciliary activation.

1.4.3 The current state-of-the-art accommodative intraocular lenses

Since the development of the first monofocal IOL, many modifications in material and design have improved patient visual and clinical outcomes. Multi- and trifocal lenses have aided the development of IOL technology, however, challenges associated with optical phenomena and providing unassisted near vision remain. The demand to produce an IOL with the refractive abilities of the crystalline lens is at an all-time high because of the ageing population[78].

The studies range from clinical evaluations to developmental proof-of-concept designs. The lack of literature presents significant issues when comparing the lenses. A common theme observed in many investigations was the inconsistency in measuring accommodation. Alio *et al*.[20] discuss the importance of addressing accommodation clearly through standardised protocols including subjective and objective testing. While some evaluations are based upon patient satisfaction and reading speeds, others performed measurements for near and distant visual acuities using ETDRS targets with standardised spacing[79]. Inconsistencies were also apparent regarding implantation as some cases provided bilateral implantations and others implanted in

just one eye[46,79]. The difference between bilaterally implanting and not can impact the responsiveness of the brain, thus influencing patient satisfaction. Sample size is another parameter that varied throughout the literature. Many investigations examined small groups of participants ranging from approximately 10 to 50[55,71]. Such small sample sizes are not appropriate for representing a population. In addition, the long-term impact of AIOLs is yet to be investigated. The majority of studies did not exceed twelve months[60]. Furthermore, it is unknown how postoperative complications such as PCO, calcification, and capsular fibrosis will be influenced by these lenses long-term. Studies have expressed the need for more data, as the evidence is insufficient to confirm any accommodative amplitude with short-term results[59].

Current advancements in IOL technology are demonstrated with AIOLs. For axial displacement lenses, minimal amplitude of accommodation has been shown[46–48]. Capsular fibrosis is a concern for these AIOLs as the bag stiffens over time, diminishing the little accommodation achieved, making results temporary. Postoperative complications need to be addressed, as with standard IOLs, the material and design influence complications. Incorporating the sharp edge into the AIOL designs would decrease PCO occurrence. In addition, axial displacement lenses do not produce true accommodation of the lens. They result in a combined change in optical power with the cornea, pseudoaccommodation. In contrast, shape- and curvature-changing lenses have the advantage of true accommodation, intending to operate similarly to the crystalline lens. Despite the similarity to the mechanism of the natural lens, these lenses have raised questions regarding safety and efficacy. The literature is somewhat limited, so it is challenging to make like-for-like comparisons of these AIOL approaches. However, the same challenges as with axial movement AIOLs

remain as side effects of cataract surgery, including ciliary force deterioration and capsular fibrosis, have the potential to influence the accommodative function of the lens. With this in mind, it is clear that an alternative mechanism to address the eyes' accommodative function following cataract treatment is required.

1.5 Nanomaterials for smart lens applications

Recently, there has been a rise in the use of nanomaterials for ocular smart devices and wearable electronics[80–83]. The International Organisation for Standardisation (ISO) define a nanomaterial as a "material with any external dimension in the nanoscale or having internal structure or surface structure in the nanoscale" where nanoscale is described as 1 – 100 nm[84]. The physical and chemical properties of nanomaterials differ from their bulk materials leading to unique mechanical, optical, and electronic characteristics. For instance, graphene's nanostructure has been utilised in smart contact lens applications because of its transparent, conductive, and flexible properties in its two-dimensional form, introducing possibilities in applications such as drug delivery systems and protection from corneal dehydration and damage through electromagnetic (EM) shielding[85,86]. Graphene has also been used in electronic contact lenses for applications including point-of-care monitoring of intraocular pressure for the management of glaucoma and diabetes[81,87]. Another application of smart contact lenses with an electronic component is electronically adjustable focus lenses. Kaur et al.[88] incorporated a graphene electrode into a liquid crystal (LC) contact lens to correct presbyopia. The lens was able to produce a 0.7 D change in optical power, utilising graphene's optical and electronic properties.

1.5.1 Smart liquid crystal lenses

LC lenses, with variable focus, operate similarly to liquid crystal displays (LCDs), where an electric field modulates the refractive index of an LC that is sandwiched between two transparent conductive electrodes (TCE)[89]. Indium tin oxide (ITO) is the standard TCE used in rigid LCD applications, however, the rise in wearable devices has introduced the need for flexible electrodes. Due to the brittle nature of ITO electrodes, they are not suitable for flexible devices. Two-dimensional materials, including graphene, offer flexibility along with transparency and conductivity towards the development of curved/flexible LC lenses for ocular applications.

As well as presbyopia, an electronically controlled variable focus LC mechanism could lend itself to AIOL design to address the loss of accommodation, the inevitable consequence of cataract treatment. As described in section 1.4.3, one of the key drawbacks of axial displacement and shape-changing AIOLs is the minimal accommodative amplitude they produce. An LC-based mechanism has the potential to provide significant accommodative amplitude with little contraction from the ciliary body, as the amplitude of accommodation would not be solely dependent on the magnification of contraction, a more sensitive mechanism could be developed.

The current treatment for cataracts involves the use of a foldable IOL-base material that is implanted through a 2 – 3 mm incision using an injector after the natural crystalline lens is removed. To comply with this current procedure, a flexible TCE must be used. Graphene has been proposed for several ocular applications and has displayed potential in the field, however, numerous reports express concerns regarding

its toxicity toward living organisms and stability within a physiological medium[90–92]. It is also limited by complex processing and high fabrication costs[93]. Moreover, recent investigations have found graphene to display substantially inferior optoelectronic properties when compared to the novel two-dimensional material, MXene[94,95].

1.6 Two-dimensional transition metal carbides, carbonitrides and/or nitrides, MXenes

The new class of two-dimensional transition metal carbides, carbonitrides, and/or nitrides, MXenes, were discovered in 2011 by Yury Gogotsi and Michel Barsoum at Drexel University, USA[96]. The family of materials were given the name, MXenes, to reference their precursor, MAX phase, and to acknowledge their similarity to graphene. These nanomaterials have a unique combination of properties from high optical transparency to high mechanical strength, conductivity, and hydrophilicity resulting from their surface terminations[97–100].

In the short time since MXenes were discovered, they have demonstrated potential across a wide range of research communities for a variety of interdisciplinary applications owing to their versatile composition and tunable properties. Such applications include transparent conductors[101,102], gas and pressure sensors[103,104], energy storage[105,106], EM shielding[107,108], water remediation[7,109], and plasmonics[110]. With more than 30 MXene variations experimentally synthesised and many more theorised, they are generating significant interest in cross-disciplinary applications[97,102,111–113].

1.6.1 MAX phase precursor

The MAX phase precursors are layered hexagonal ternary carbides and nitrides that have the general formula $M_{n+1}AX_n$, where M is an early transition metal (such as Ti, V, Nb, Cr, Mo, etc.), A is an element from group 13 or 14 of the periodic table, and X indicates carbon and/or nitrogen, as demonstrated in ***Figure 1-4***[97]. Their range of stoichiometries are also shown in ***Figure 1-4***, referred to as 211, 312, and 413 when n = 1, 2, and 3, respectively. The first number is the transition metal, the second number indicates the A element, and the third is carbon and/or nitrogen. MAX phases are typically formed through a pressureless sintering method. For example, 312 Ti_3AlC_2 MAX phase is produced when titanium carbide (TiC), titanium (Ti), and aluminium (Al) powders are mixed and purged with argon (Ar), and heated to 1360 °C. The sintered Ti_3AlC_2 product is milled to a powder and subsequently washed and sieved[114]. Other bulk synthesis methods can be used[115], but the above route is the most commonly used for MXene synthesis[116].

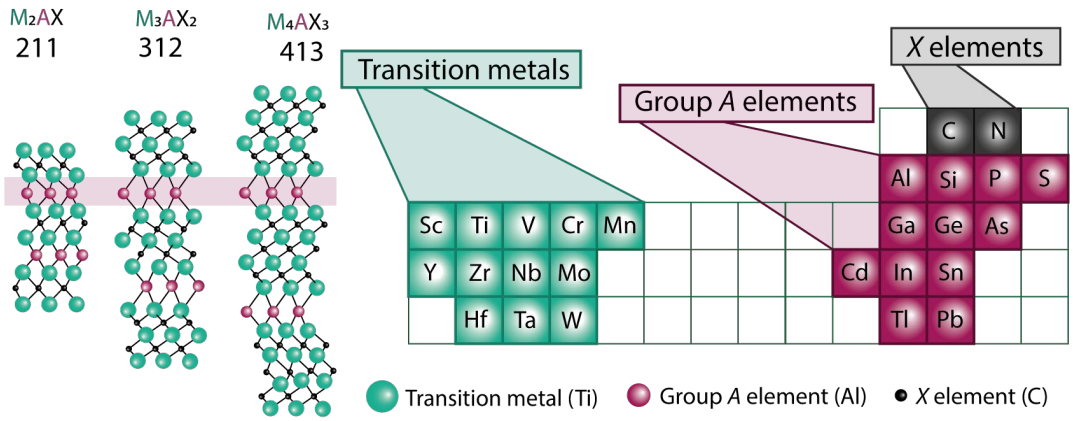

Figure 1-4 – MAX phase and MXene combinations, showing twelve transition metals and *A* elements and two *X* elements. MAX phase structures 211, 312, and 413 are shown.

1.6.2 MXene overview

MXenes have the general formula $M_{n+1}X_nT_x$, where *M* represents the early transition metal, *X* is carbon and/or nitrogen, and T_x indicates the surface terminations of fluoride (F), oxide (O) and/or hydroxide (OH)[117]. MXenes are synthesised through selective chemical etching with acidic solutions containing or forming hydrofluoric acid (HF) selectively etch away the *A* element from the MAX phase, which resides between the transition metal layers. At this stage of the synthesis, MXene is in its multi-layered form, two-dimensional flakes are obtained by delaminating the multi-layered product.

1.6.2.1 MXenes optical and electronic tunability

Studies have shown that MXene characteristics are composition, synthesis, and processing dependent. For instance, the most commonly researched of the MXene

family is the 312 titanium carbide ($Ti_3C_2T_x$). A recent study described a modified synthesis method with excess aluminium MAX phase, that improved the stoichiometry and crystallinity of the $Ti_3C_2T_x$ product. The modified method increased the material's bulk conductivity to more than 20 000 S cm^{-1}[114]. MXenes structure allows electrons to transfer from the transition metal core to the electronegative surface terminations[118]. Through x-ray absorption spectroscopy (XAS) and density functional theory (DFT) calculations, $Ti_3C_2T_x$ was compared to a double transition metal MXene, $Mo_2TiC_2T_x$, and identified electronic differences. The differences were attributed to the contribution between surface terminations and Ti atoms at the surface and sub-surface[118]. Thus, the addition of elements with more valence electrons provides higher carrier concentrations which result in greater conductivity, identifying a mode of electronic tuneability. Further to transition metal customisation for specific properties, the X element (in $M_{n+1}X_nT_x$) can also be changed. By substituting the carbon atom in $Ti_3C_2T_x$ to form Ti_3CNT_x, the absorption peak moved from 780 nm to 670 nm, demonstrating optical tunability[119]. Similarly, MXenes surface functionalities influence the electronic structure and also play a role in tuning optical properties[120]. For instance, greater fluorination results in smaller absorption coefficients compared to a higher degree of oxygen terminations[121].

1.6.2.2 MXenes optical and electronic applications

The many modes of optical and electronic tunability contribute to their potential possibilities for optoelectronic applications, wireless antennas for example. Sarycheva et al.[122] designed and investigated translucent radio frequency MXene antennas using a single-step coating method. $Ti_3C_2T_x$, Ti_2CT_x, and $Mo_2TiC_2T_x$ were each used to

fabricate the 100 nm thick low-frequency antennas. The thickness-dependent antennas displayed good performance with reflection coefficients of less than – 10 dB. Another optoelectronic MXene application that used a similar single-step coating method was an investigation fabricating organic light-emitting diodes (LEDs). The LEDs exhibited high power and current efficiency and good transparency, up to 85 %. This application demonstrates the optical and electronic properties of MXenes as well as provides guidelines to fabricate a simple, low-cost solution-processable electrode that could be used in other flexible TCE applications. MXenes have also displayed potential as photodetectors with the possibility of replacing gold in GaAs photodetectors. The spin-coated $Ti_3C_2T_x$ electrodes showed enhanced responsivity and quantum efficiency compared to current photodetectors[123].

MXenes optical and electronic capabilities suggest potential use in ocular applications with the possibility to incorporate LC lens technology in the development of an AIOL lens.

1.6.2.3 Solution processing methods for transparent conductive electrodes

MXenes combined properties render them useful transparent electrodes specifically with regard to their ease of processibility. The first $Ti_3C_2T_x$ transparent films were fabricated via sputter-coating. These MXene films were approximately 19 nm thick and roughly 90 % transparent[124]. Despite displaying good optical characteristics, this deposition technique requires temperatures as high as 780 °C, limiting production scalability. High-functioning MXene films can be fabricated through various solution processing techniques, including spray-, spin- and dip-coating onto solid or flexible substrates with adjustable thickness[102,125]. Dip-coating is a simple, cost-effective

technique, though spray-coating benefits large-scale film fabrication. One spray-coated $Ti_3C_2T_x$ example exhibited transmittance (T) of 40 % corresponding to a thickness of 70 nm and sheet resistance (R_s) of 500 Ω sq^{-1}, whereas a 5 nm thick film, improved transmittance (T ~ 90 %), yet proved detrimental to *Rs* (8 kΩ sq^{-1})[102]. Moreover, spin-coating has shown a higher degree of conductivity through highly substrate-aligned nanoflakes caused by the centrifugal force. A $Ti_3C_2T_x$ film of approximately 1.2 nm thickness achieved 6600 S cm^{-1} whilst retaining > 97 % transparency[126]. In another instance, a $Ti_3C_2T_x$ spin-coated film maintained 86 % transparency with *Rs* of 330 Ω sq^{-1}. Subsequently, the film thickness is tuned by controlling solution concentration and spin speed.

The TEC MXene literature includes simple, optimised solution processing methods for a range of applications, yet the utilisation of the approaches, thus MXenes optical and electronic properties for ocular applications has not been explored. And what's more, numerous biomedical applications have been investigated, however, no in-eye examples have been considered.

1.6.3 Biomedical MXene applications

Emerging MXene biomedical applications have gained increasing interest recently. Similarly to the optical and electronic applications previously described, the success of these applications relies on material composition, and physiochemical characteristics, as well as interactions and stability within biological environments. MXene's advantageous properties such as their two-dimensional geometry, mechanical strength, and reactive surface chemistry make them particularly interesting

for biomedical applications. Despite biomedical MXene research being in its infancy, ***Figure 1-5*** highlights the key application classes that MXenes have been proposed for, with the first application demonstrated in 2016[127]. Applications include diagnostic imaging[128,129], in theranostics[130–132], as antibacterial materials[133,134], and biosensing[11,103,135].

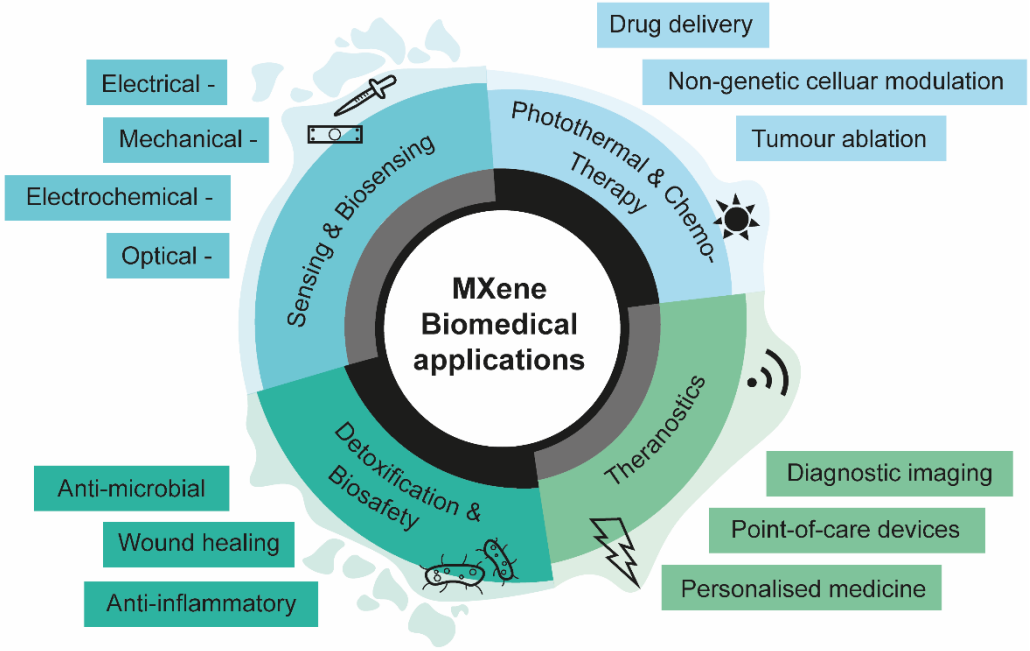

Figure 1-5 – A schematic of biomedical applications including photothermal therapy, diagnostic imaging, antimicrobial and biosensing.

1.6.3.1 MXenes for diagnostic imaging

The fluorescent properties of MXene quantum dots (QDs) have presented opportunities in bioimaging for diagnostics through tunable wavelengths, photostability, and high yields. $Ti_3C_2T_x$ QD has shown multicolour cellular imaging with the potential for bioimaging and optics in biomedicine. Their hydrophilic nature and monolayer structure permit strong photoluminescent behaviour. $Ti_3C_2T_x$ QD have

demonstrated use as multicolour cellular imaging probes by labelling the mouse RAW264.7 cell line[129]. The macrophages were exposed to 10 – 20 μg mL^{-1} of the MXene QD for 24 hours and remained viable. Another example developed a method of fabricating ultrasmall MXenes using a mild approach of intralayer cutting and interlayer delamination of $Ti_3C_2T_x$. The ultrasmall $Ti_3C_2T_x$ displayed strong absorption and excitation-dependent emission with the possibility of investigating niobium carbide (Nb_2C) and titanium carbide (Ti_2C) MXenes ultrasmall dots for cellular imaging[136]. Another investigation developed a sensitive $Ti_3C_2T_x$ QD-based fluorescent probe for the alkaline phosphatase activity assay with a low detection limit of 0.02 U L^{-1}[137].

1.6.3.2 MXenes in theranostics

Theranostics combines diagnostics and therapeutics to improve the efficiency of patient outcomes. A MXene-based manganese oxide ($MnO_x/Ti_3C_2T_x$) composite was fabricated as a pH-responsive contrast agent for magnetic resonance imaging (MRI). The composite showed acidic responsivity to the tumour sites in tumour-bearing animal models. The MnO_x on the $Ti_3C_2T_x$ surface experienced *in situ* growth when met with a tumour environment[138]. MXenes have also been investigated for photoacoustic imaging combined with photothermal therapy (PTT), demonstrating good photo-response in the near-infrared (NIR) window. PTT has advanced as an alternative to conventional cancer treatments with high ablation efficiency and minimal damage to healthy tissue. The treatment promotes cancerous cell necrosis and/ or apoptosis using light as an external stimulus. Photothermal agents accumulate within tumours and absorb the NIR radiation that is converted into heat. Soybean

phospholipid modified tantalum carbide (Ta_4C_3-SP) MXene, presented significant X-ray CT contrast and good light-to-heat conversion. Mouse 4T1-breast tumour cells were exposed to the modified MXene. Cell viability was not significantly impacted over the 0 – 400 μg mL^{-1} concentration range. 4T1 tumour-bearing mice were treated with Ta_4C_3-SP and 808 nm laser irradiation. The tumour site was exposed to the radiation for 10 minutes, which caused complete ablation of the cells as the temperature increased from 30 to 58 °C, confirming the effectiveness of the treatment[8]. Moreover, photothermal ablation was successful with complete cancer cell necrosis and suppression of proliferation[139]. MXenes photothermal conversion was demonstrated in another study with $Ti_3C_2T_x$, where the material was loaded with the chemotherapy drug doxorubicin and tumour targeting hyaluronic acid. The *in vitro* and *in vivo* experiments demonstrated the ability of the $Ti_3C_2T_x$ composite to target the tumour microenvironment for specific accumulation, drug release and irradiation[132].

1.6.3.3 MXenes for biosensing

Biosensing is used for various applications, from clinical diagnosis to medical research and environmental monitoring. MXenes's two-dimensional structure with high surface-to-volume ratio and light absorption abilities enable applications in biosensing. Lei *et al.*[140] fabricated a wearable and stretchable electrochemical biosensor for sweat analysis to detect glucose and lactose biomarkers. The sensor composite was composed of a $Ti_3C_2T_x$ and Prussian blue. It showed high sensitivity and accuracy, wirelessly transmitted to a mobile device in real-time, demonstrating MXenes potential for non-invasive monitoring[140]. Another MXene-based biosensor

was proposed for monitoring neurotransmitters[141]. This study was the first to micropattern $Ti_3C_2T_x$ to fabricate a field-effect transistor (FET). The FET was developed to monitor dopamine in hippocampal neurons. The micropatterned $Ti_3C_2T_x$ was deposited as an active surface for the small biological molecules to bind to, allowing monitoring in real-time. This investigation displayed the long-term compatibility of $Ti_3C_2T_x$ for neuronal cultures. Due to the extremely thin device, making it almost transparent, fluorescent images could be taken of the neurons over time. The device detected low dopamine concentrations significantly lower than previously published graphene-based biosensors[142]. Implantable microelectrodes were proposed by Driscoll *et al.*[143] in another investigation using a photolithographic patterning fabrication process. $Ti_3C_2T_x$ was micropatterned onto flexible polymer substrates forming multichannel neural electrodes. The study demonstrated a reduction in impedance compared to gold electrodes of similar geometry. The *in vivo* investigation demonstrated enhancements in signal quality, sensitivity and reduced noise. The compatibility of $Ti_3C_2T_x$ with neuronal cultures was identified as cell viability was not affected[143]. The rich surface chemistry of MXenes provides reactive sites for functionalisation, and hydrophilic surface soluble in aqueous solutions prevents the requirement for potentially toxic organic solvents. It allows efficient solution processing, high surface area, volumetric capacitance, and metallic conductivity desirable for low-noise biosensors.

Their versatile composition, adaptive surface reactivity, tunable optical and electronic properties, mechanical strength, and large surface-to-area ratio illustrate the multifaceted potential of MXenes for biomedical research. Surprisingly, a clear void in MXene research is for use in ocular applications. Furthermore, their combined

properties suggest suitability to explore optoelectronic LC lens technology and AIOL design.

1.7 Research questions and objectives

Cataracts remain the leading cause of blindness, with cataract patients rising year on year. Advances in IOLs have yet to yield a truly accommodative IOL. Current approaches are hindered by capsular bag fibrosis, post-operative complications due to materials and design and the stability/reliability of their ability to mimic the crystalline lens. The new generation of electroactive adaptive focus LC lenses could answer a number of the current AIOL restraints, such as a dynamic optical power range, reversible shifts in optical power, and unpredictable capsular fibrosis. LC-based lenses are an alternative approach that does not rely on mechanical movement or deformation and have demonstrated potential in glasses and contact lenses to correct presbyopia. Therefore, this provides significant possibilities for wearable and implantable optoelectronic devices. Two-dimensional nanomaterials such as graphene have been studied in ocular devices, including smart lenses. However, graphene and graphene variants are hindered by issues regarding ease of processing and fabrication limitations. Since the discovery of MXenes, characteristics of transparency, conductivity, and mechanical strength have proven superior to that of graphene due to their more complex and tunable surface chemistry[5,144]. Consequently, MXenes present greater suitability for optoelectronic implantable lenses. Therefore, the project will investigate the hypothesis that MXenes can be incorporated into an AIOL design to produce a transparent, flexible, biocompatible, highly electrically conductive coating coupled with an LC layer to develop an adaptive focus implantable lens.

1.7.1 Research questions

1. Can a thin and transparent coating of $Ti_3C_2T_x$ be deposited onto an IOL polymer and retain conductivity and how is the conductivity affected when the coated IOL is deformed over a set radius?
2. Do $Ti_3C_2T_x$ coatings on an IOL polymer affect cell viability and inflammation within the physiological environment of the eye?
3. Can transparent coatings of $Ti_3C_2T_x$ on solid substrates facilitate the refractive index modulation of a nematic LC?
4. Can $Ti_3C_2T_x$ coatings be incorporated into a lens to enable a change of focus through an external stimulus?

1.7.2 Objectives

- Synthesis of MXene, focusing on the optimisation properties required for the application and characterisation.
- Establish the deposition technique of $Ti_3C_2T_x$ thin, uniform coatings to balance optoelectronic performance.
- Critically evaluate the influence of the $Ti_3C_2T_x$ coatings to perform as an IOL through optical power and modulation transfer functions.
- To assess the flexibility of $Ti_3C_2T_x$ coated IOLs as a function of conductivity.

- To investigate the biocompatibility of $Ti_3C_2T_x$ coatings to address suitability for ophthalmic environments through cell viability, oxidative pathways, and immune response.
- To establish the performance of $Ti_3C_2T_x$ as a TCE, by facilitating molecular reorientation of a nematic LC with an electrical stimulus.
- To fabricate an adaptive focus lens using the electroactive $Ti_3C_2T_x$/LC mechanism.
- To evaluate lens performance of fabricated $Ti_3C_2T_x$/LC lens by demonstrating a change in focus and assessing image quality.

Chapter 2

2 MXene synthesis, solution processing, and physical characterisation

2.1 Introduction

2.1.1 MXene synthesis

MXenes can be synthesised through several methods, although top-down wet chemical etching approaches are the most widely used due to their simplicity and processability[6,117]. These methods selectively reduce macroscopic phase MXenes (MAX phases) to nano-particles[116]. Bottom-up approaches, such as chemical vapour deposition (CVD), are also used, producing high-quality large MXene flakes, yet limitations associated with high fabrication costs remain[145].

MXene synthesis has been widely researched since the first demonstration of *A* element removal from Ti_3AlC_2, MAX phase, in 2011, when MXenes emerged as a new class of two-dimensional material[96]. MXenes are a rapidly growing family of theoretical and synthesised nanomaterials with unique and multifaceted properties of significant research, along with their ease of production and low cost in relatively large quantities. As introduced in section 1.6.2, MXenes are formed through wet chemical approach that uses strong acids to exfoliate the *A* element from the MAX phase shown in ***Figure 2-1***[146]. The acid targets the weaker M-A metallic bond, and as the *A* element reacts with the fluoride ions of the hydrofluoric (HF) acid, the gaseous hydrogen exfoliates the MXene layers, as shown in equation (2.1)[113]. After etching away the *A* layers, surface terminations (F, O and/ OH) occur, bonding to the outer transition metal layers, shown in equations (2.2) and (2.3)[96,113,147].

$$M_{n+1}AlX_{n(s)} + 3HF_{(aq)} \rightarrow M_{n+1}X_{n(s)} + AlF_{3(s)} + 3/2H_{2(g)} \quad (2.1)$$

$$M_{n+1}X_{n(s)} + 2H_2O_{(l)} \rightarrow M_{n+1}X_n(OH)_{2(s)} + H_{2(g)} \quad (2.2)$$

$$M_{n+1}X_{n(s)} + 2HF_{(aq)} \rightarrow M_{n+1}X_nF_{2(s)} + H_{2(g)} \quad (2.3)$$

Reaction by-products are removed during washing cycles, where the MXene is centrifuged with deionised water to reach a neutral pH. The sediment collected from centrifugation is termed multi-layered MXene. The sheets making up the multi-layered MXene are bonded by hydrogen bonding and Van der Waals forces to form an accordion-like structure shown in the multi-layered SEM image in ***Figure 2-1***[117]. The two-dimensional properties of multi-layered MXenes were explored when large organic molecules were intercalated within the nanoflakes. The organic molecules increase the interlayer spacing and weaken the electrostatic interactions, which leads to the delamination of the layers into single MXene flakes, first demonstrated in 2013[148]. The surface terminations, the hydroxide/oxide-like surface chemistry and hydrophilicity allow stable colloidal solutions to form.

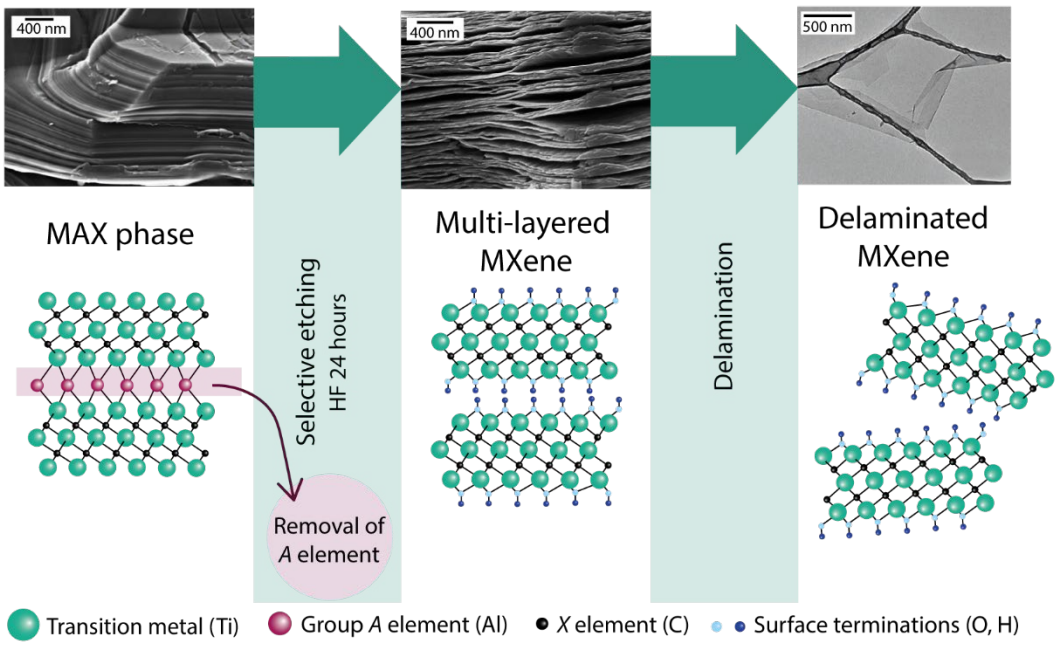

Figure 2-1 – MXene synthesis of a 312 MAX phase, SEM images show MAX phase, multi-layered MXene, and delaminated MXene, from left to right, respectively. SEM images for MAX phase, multi-layered MXene, and delaminated MXene re-worked into the schematic with permission, Copyright 2017, Springer Nature[97].

Alternative etchants such as HF-containing or -forming routes are available and have the advantage of being less hazardous than using pure HF. In 2014, an ammonium hydrogen bifluoride (NH_4HF_2) salt was used to synthesise $Ti_3C_2T_x$[149], followed shortly by another method which used a mixture of lithium fluoride (LiF) salt and hydrochloric acid (HCl) forming HF in situ to produce a $Ti_3C_2T_x$ clay[150]. This method simplified MXene synthesis as the solvated Li-ions intercalated within the layers were enough to delaminate into single MXene sheets or flakes through sonication. However, the mechanical disruption resulted in small defective flakes. With the need to increase flake yield, size and quality, a technique termed the minimally intensive layer delamination (MILD) method was developed. It was given this name to

distinguish between the original LiF/HCl $Ti_3C_2T_x$ clay procedure and this more optimised method. The MILD method is a less aggressive alternative to other MXene synthesis approaches and has the added benefit of not requiring additional intercalation agents to delaminate, nor does it require a sonication stage. Manual handshaking sufficiently isolates the multi-layered MXene into single flakes and have found to have greater lateral sizes than reported with the previous methods[151]. This approach significantly simplified synthesis further and improved MXene performance, specifically for electronic and optical studies where larger lateral sizes and high-quality flakes are necessary.

2.1.2 Solution processing of MXene

It is important to consider the final application of the MXene when choosing a solution processing method. This is because the different processing techniques contribute to the overall MXene properties, such as electrical conductivity. For example, printing and coating are processing techniques commonly used in MXene research. Inkjet printing of MXenes is suggested for use in flexible energy storage applications that requires specific rheological properties to permit solution flow and prevent clogging of the nozzle[152]. Direct coating onto the substrate is favourable for optically transparent applications, where thin films and uniformity are required.

Dip-coating is known for its simplicity as a coating technique, where a substrate is immersed into a MXene solution, and a thin layer is deposited on the surface. Excess material is drained by removing the substrate from the solution, evaporation allows the film to form and adhere to the substrate[152]. Dip-coating has been used to fabricate

MXene composites and coat fibres for applications such as wearable sensors, where high MXene flake loading and scalability are the main requirements[122,153–155]. This technique does not result in sufficient transparency for the optical applications concerned in this thesis. Spray-coating, however, allows the tunable thickness of coatings. MXene solutions are dispersed onto the substrate through a high-pressure spray gun. MXene antennas are one example of an application that utilised spray-coating, fabricating an 8 μm-thick antenna for wireless communications[113,122]. Although this technique offers tunable thickness and scalability for large surface areas, uniformity of the coverage is governed by numerous factors such as fluid velocity and the distance between the nozzle of the gun and the substrate. This makes it challenging to produce homogenous and consistent coatings[156].

Spin-coating is well-known for producing highly uniform, thin coatings. MXene solutions are deposited onto the substrate, the substrate reaches the desired rotation speed, a layer is formed on the surface, excess material spins off, and evaporation enables the coating to further adhere to the substrate[157,158]. The centrifugal force exerted on the solution forces the MXene flakes to align parallel to the substrate resulting in highly aligned coatings. Coating thickness is controlled by solution concentration and spin speed. For example, a more concentrated solution will form a thicker coating compared to a more dilute solution. Equally, a faster spin speed will produce a thinner coating than a slower speed. MXene coatings or thin films fabricated through spin-coating have shown promising performance for FETs, supercapacitors, and TCEs due to their highly ordered structures[101,141,159].

It is evident that over time, synthesis methods and solution processing techniques have been optimised to achieve the properties required for the application[117]. To this end, currently, the most suitable solution processing technique for TCEs is spin-coating.

2.1.3 Optoelectronic performance of spin-coated $Ti_3C_2T_x$

The electronic and optical properties of spin-coated $Ti_3C_2T_x$ films are significant, maintaining > 97 % transparency whilst reaching conductivity of 6600 S cm^{-1}. Linearity between thickness and conductivity was demonstrated with coatings as thin as 10 nm, indicating that the substrate-aligned coating retained a continuous overlapping network of nano-flakes[101]. After repeated bend cycles, transparent $Ti_3C_2T_x$ coatings demonstrated good flexibility and retained high conductivity with a 14 % increase in sheet resistance[102]. The ordered alignment of flakes improves the transport of charge carriers. However, the extreme thin thickness of the film could be slightly detrimental to retaining conductivity when mechanically deformed. The recovery of the substrate material following deformation would also contribute to the conductivity retention when compared to before and after deformation cycles.

Optoelectronic devices such as touch screens and LCDs are well integrated into everyday life. As TCEs are critical components of these devices, it is essential that they are fit for purpose, specifically with the development towards flexible electronics. Historically, indium tin oxide (ITO) has been the standard TCE used commercially, with low sheet resistance (10 – 100 Ω sq^{-1}) and high transparency T > 85 %[160]. Although, it does come with its limitations, including high indium costs and high temperatures required for fabrication, which makes ITO a relatively expensive

material[161]. Yet the main drawback is related to the intrinsic properties of the ceramic material. The brittle nature of ITO means it is fragile and susceptible to cracks, fractures, and is easily scratched. The disruptions in electrical flow diminish overall conductivity. Hence, limiting the development of flexible optoelectronic devices. Over the past decade, there has been increased interest in research towards flexible TCEs. Due to the requirement for transparency whilst maintaining the flow of electrons, an informative and reliable method of comparison of TCEs can be made by evaluating their electrical figure of merit (FoM). FoM is established through a ratio of electronic (σ_{DC}) and optical (σ_{OP}) conductivities that can be measured through transmittance (%) and sheet resistance of the TCE[162]. As an example, a TCE with sheet resistance < 100 Ω sq^{-1} and T > 90 %, corresponds to a FoM of 35, thus the greater the FoM the greater the optoelectronic performance of the electrode[94]. ***Table 2-1*** presents a comparison of the FoMs for various coated substrate examples produced through spin-coating. In most cases, glass was used as the substrate and the FoM for $Ti_3C_2T_x$ ranges from 0.5 – 5.0. A reduced graphene oxide example was also included to highlight its optoelectronic performance compared to that of $Ti_3C_2T_x$. Studies have identified that vacuum annealing and annealing in a nitrogen-rich environment leads to an increase in the FoM[163].

Table 2-1 – A comparison of the figure of merit (FoM) for spin-coated two-dimensional materials presenting the substrate they are coated on, the percentage transmission at 550 nm, the sheet resistance and their corresponding FoMs

Material	Substrate	Transmission at 550 nm (%)	Sheet resistance (Ω sq^{-1})	σ_{DC}/σ_{Op}	Ref
Reduced-Graphene oxide	Glass and quartz	80	1000	1.6	[164]
$Ti_3C_2T_x$	Sodalime glass	77	437	3.1	[165]
$Ti_3C_2T_x$	Polyetherimide	86	330	5.0	[101]
$Ti_3C_2T_x$	Glass	80	5250	5.0	[166]
$Ti_3C_2T_x$	Glass	82	7911	0.5	[102]

The optoelectronic properties of $Ti_3C_2T_x$ are essential characteristics for fabricating an effective TCE, as are the overall optical properties of the substrate for a lens application. The IOL restores visual acuity to cataract patients who have undergone cataract removal. Standard characterisation and quality tests are used in the industrial manufacture of IOLs to evaluate the lens' optical power and modulation transfer function (MTF) measurements. While optical power is measured in dioptres and is equal to the reciprocal of focal length, lens calculations based upon the patient's eye's axial length are performed to determine the optical power required. Whereas MTF is a universal metric based on a lens system's ability to transfer contrast and resolution information from the observed object to the image[167]. These measurements are essential in the design and development of IOLs to evaluate if additional features such as coatings significantly impact the lens's optical performance.

2.1.4 Aim

Whilst early research has shown that MXenes are highly suitable for optoelectronic applications, no research has been done to investigate the suitability of MXene in AIOL design. It has been demonstrated that $Ti_3C_2T_x$ combines properties of high electrical conductivity, hydrophilicity, optical transparency, and flexibility in contrast to other two-dimensional alternatives. However, the successful application of these properties within an implantable intraocular lens polymer has yet to be demonstrated. The work presented in this chapter aims to determine if $Ti_3C_2T_x$ can be synthesised, characterised, and coated onto a lens polymer to perform as a flexible TCE without disrupting the optical quality of the lens. It is hypothesised that $Ti_3C_2T_x$ is an appropriate TCE material for IOL technology. Therefore, the objectives of this chapter are:

1. To synthesise high-quality, single $Ti_3C_2T_x$ flakes with large lateral size via the MILD method.
2. To establish a method to produce a thin, uniform and continuous coating of $Ti_3C_2T_x$ on a lens polymer.
3. To evaluate the electronic, and optical properties and flexibility of the $Ti_3C_2T_x$ coated lens polymers.
4. To determine if the coating impacts the lens's optical power and modulation transfer function.

2.2 Materials and methods

2.2.1 Materials

- Lithium fluoride (powder 300 mesh), purity ≥ 98 % (Sigma-Aldrich, UK)
- Hydrochloric acid (HCl), 12 M diluted to 9 M for reaction, purity ≥ 37 % (Sigma-Aldrich, UK)
- Ti_3AlC_2 (MAX phase) (supplied by A.J. Drexel Nanomaterials Institute, Drexel University, USA)
- Lithium chloride (LiCl), purity ≥ 99.98 %, (Sigma-Aldrich, UK)
- Durapore PVDF 0.22 µm membrane (Fisher Scientific, UK)
- Whatman anodisk inorganic filter membrane (Sigma-Aldrich, UK)
- Polystyrene cuvettes, 1 cm, (Sigma-Aldrich, UK)
- RayOne hydrophobic, 800C intraocular lenses, (Rayner Intraocular Lenses Ltd, UK)
- Conductive paint (Electrolube) (RS components, UK)

2.2.2 Synthesis of $Ti_3C_2T_x$

$Ti_3C_2T_x$ was synthesised through the MILD method, where 1 g of Lithium fluoride (LiF) was dissolved in 20 mL of 9 M hydrochloric acid (HCl). Ti_3AlC_2 (MAX phase) was gradually added over 5 minutes and left to etch for 24 hours within a temperature range of 35 – 40 °C with continuous stirring. Reaction by-products were removed through repeated washing with deionised water (DI) and centrifuging. The wash cycles were performed in 50 mL (x4) centrifuge tubes, filled to their maximum capacity, and spun for 5 minutes at 3500 rpm using an ALC PK 120 centrifuge, T515 rotor. Once a neutral pH was achieved, over 3 – 5 wash cycles, the sediments were redispersed in

approximately 10 mL of DI water and collected to form one solution. Here, the $Ti_3C_2T_x$ product is in its multi-layered form. However, for the application presented in this thesis, delaminated $Ti_3C_2T_x$ was required. Therefore, 1 g of lithium chloride was added to the multi-layered $Ti_3C_2T_x$ and stirred for 30 minutes to increase delamination resulting in a higher yield. The wash cycles were repeated to achieve a neutral pH, and all dark supernatants were collected. The supernatants were centrifuged at 10 000 rpm for 10 minutes using a ALC PK 121R centrifuge, T523 rotor. The sediments were collected and redispersed in approximately 20 mL of DI water. The solution was further centrifuged at 500 rpm up to 3 times and any sediment (containing agglomerates) was wasted. The solution was stored for further processing. Herein, where $Ti_3C_2T_x$ is detailed in the following sections of this chapter and the later chapters, it is refereeing to delaminated $Ti_3C_2T_x$.

2.2.3 Physical characterisation of $Ti_3C_2T_x$

2.2.3.1 Vacuum filtration of $Ti_3C_2T_x$ solution

A known volume of the synthesised $Ti_3C_2T_x$ solution was vacuum filtered using an EMD Millipore™ 47 mm Glass Vacuum Filter (Fisher Scientific, UK), membrane, connected to a pump to remove as much water as possible. Once filtered, the now free-standing film was dried further in the oven for 24 hours at 80 °C. Through a gravimetric analysis, the concentration of the $Ti_3C_2T_x$ solution was established. The free-standing film's mass and the known volume filtered were used to determine the concentration of the colloidal suspension (mg mL^{-1}).

2.2.3.2 Scanning electron microscopy of $Ti_3C_2T_x$

High-resolution images of the as-synthesised $Ti_3C_2T_x$ were produced through scanning electron microscopy (SEM) (Zeiss Supra 50VP, Germany), with a 5 kV accelerating voltage. A scalpel was used to cut a free-standing film to image its cross-section. The scalpel created a defined cross-section of the film that was then mounted to the side of a hexagonal nut, perpendicularly aligned with the electron beam. A dilute $Ti_3C_2T_x$ solution was vacuum filtered onto a porous membrane to obtain images of the single flakes (Anodisk, inorganic filter membrane, Whatman). No sputter coating was required for any of the samples.

2.2.3.3 X-ray diffraction of $Ti_3C_2T_x$ free-standing film

Elemental analysis was performed on the $Ti_3C_2T_x$ free-standing film by X-ray diffraction (XRD) with a powder diffractometer (Rigaku SmartLab, USA) using CuKα radiation (λ = 1.54 Å) with $\theta - 2\theta$ continuous scan with 0.02° 2θ step size, 1 s step time, and 10 × 10 mm^2 window slit. The free-standing film was compared to Ti_3AlC_2 to demonstrate the differences in structural characterisation between the two.

2.2.3.4 X-ray photoelectron spectroscopy of $Ti_3C_2T_x$ free-standing film

Elemental composition and bonding environments of the free-standing film were performed on the free-standing film through X-ray photoelectron spectroscopy (XPS) (Physical Electronics VersaProbe 5000, USA) with a 100 μm Al Kα X-ray beam. Photoelectrons were detected at an angle of 45° between the sample and the energy analyser. Charge neutralisation was applied using a dual-beam charge neutraliser,

irradiating low-energy electrons and ion beams. The binding energy of survey scans was collected from 1000 to -4 eV with pass energy of 117.4 eV. CasaXPS Version 2.3.16 RP 1.6 was used to analyse the spectra. A Shirley function was used to address background contributions.

2.2.3.5 Ultraviolet-visible (UV-Vis) spectroscopy of $Ti_3C_2T_x$ solution

Ultraviolet-visible (UV-Vis) spectroscopy was carried out using an Evolution 201 UV−Vis spectrophotometer (Thermo Scientific, USA) in the wavelength range of 200 to 1100 nm and path length of 1 cm to characterise optical properties. DI water was used as the blank, and all measurements were performed in polystyrene cuvettes. The concentration of the solution was determined as described in section 2.2.3.1 and a series of dilutions were produced to form a calibration curve. The molar absorptivity coefficient was calculated following the Beer-Lambert law:

$$A = \varepsilon l C \tag{2.4}$$

Where A is the absorbance measured, l is optical path length, and C is the concentration of the $Ti_3C_2T_x$ solution (mg mL^{-1}).

2.2.3.6 Dynamic light scattering size analysis of $Ti_3C_2T_x$ solution

Particle size analysis was carried out on the $Ti_3C_2T_x$ solution using dynamic light scattering (DLS) (Zetasizer Nano ZS, UK). The MXene solution was prepared as stated in section 2.2.2. Polystyrene cuvettes were used for the analysis. The solution was diluted 1 in 100, the upper size detection limit was set 10 μm, at 25 °C, and the data was averaged over five measurements for each sample.

2.2.3.7 Bulk conductivity of $Ti_3C_2T_x$ free-standing film

A free-standing film of the $Ti_3C_2T_x$ solution was produced, as described in 2.2.3.1. A four-point probe stand SR-4, and Keithley SMU 2450 Source meter (Tektronix, USA) was used to determine the bulk conductivity of the free-standing film. The probe spacing was 1.0 mm. Current was sourced on the two outer probes, and voltage was measured on the two inner probes. The free-standing film thickness was measured using a digital micrometre (Mitutoyo, 293-130 ABSOLUTE Digimatic High Accuracy MDH Micrometer 0-25mm). The bulk conductivity was established through sheet resistance and resistivity calculations.

$$R_S = \frac{\pi}{\ln(2)} \frac{\Delta V}{I} \tag{2.5}$$

$$\rho = R_S \cdot t \tag{2.6}$$

$$\sigma = \frac{1}{\rho} \tag{2.7}$$

Where R_s is sheet resistance (Ω sq^{-1}), V is the voltage measured (V), I is the current sourced (A), ρ is resistivity (Ω m), t is the thickness of the free-standing film (cm), σ is conductivity (S cm^{-1}).

2.2.4 $Ti_3C_2T_x$ solution processing

2.2.4.1 Polymer pre-treatment

Surface pre-treatments were required to produce uniform coatings on hydrophobic intraocular lenses (Rayner Intraocular Lenses Ltd, UK), in the form of oxygen plasma using a Henniker plasma etcher (Henniker plasma, UK). The substrate was subject to

a 3-minute treatment of pure oxygen plasma at 100 W and 10 cm^3 min^{-1}. The treatment cleaned the surface and increased the hydrophilicity to allow the $Ti_3C_2T_x$ an adequate coating.

2.2.4.2 Spin coating $Ti_3C_2T_x$ on the lens

20 µL of a 5 mg mL^{-1} $Ti_3C_2T_x$ solution was deposited onto the lens. A two-step spin coating method was used with an Ossila spin coater (Ossila, UK), 5000 rpm for 2 minutes to evenly deposit the coating, followed by 6000 rpm for 1 minute to ensure drying of the coated layer. The substrates were transferred to the oven for 24 hours at 80 °C to allow annealing of the coating.

2.2.5 Physical characterisation of $Ti_3C_2T_x$ coated lens

2.2.5.1 X-ray photoelectron spectroscopy of coated lens

The surface of the polymer was characterised to identify the $Ti_3C_2T_x$ coating by XPS (Physical Electronics VersaProbe 5000, USA) with a 100 µm Al Kα X-ray beam. Photoelectrons were detected at an angle of 45° between the sample and the energy analyser. Charge neutralisation was applied using a dual-beam charge neutraliser, irradiating low-energy electrons and ion beams. High-resolution scans were obtained in the interested regions using pass energy of 23.5 eV. The software package CasaXPS was used to analyse the data, and the background intensities were subtracted using a Shirley function.

2.2.5.2 Atomic force microscopy of $Ti_3C_2T_x$ coated lens

A Bruker MultiMode 8-HR with standard tapping mode atomic force microscopy (AFM) was used to investigate the thickness of the $Ti_3C_2T_x$ coating on the IOL polymer. The coating was applied to the polymer as stated in section 2.2.4. A step was made in the coating using plastic forceps. The image was produced with the analysis software package Gwyddion.

2.2.5.3 Transmittance spectroscopy of $Ti_3C_2T_x$ coated lenses

The coated IOLs' spectral transmission was measured using a UV-Vis spectrometer in the wavelength range of 300 – 1100 nm (Shimadzu, UV-Vis Spectrophotometer, UV-2600, Japan) with an integrating sphere to collect any light scattered by the lens optic. The $Ti_3C_2T_x$ coating was applied to the lens polymer as stated in section 2.2.4. and sequential coatings applied incrementally (n = 3).

2.2.5.4 Sheet resistance measurements of $Ti_3C_2T_x$ coated lenses

The sheet resistance of the coated IOLs was measured using a DC Resistivity/electrical transport option (ETO) puck fit to a purpose-built stage, shown in ***Figure 2-2***, connected to a Keithley SMU 2450 Source meter (Tektronix, USA). Four silver wires were arranged on the $Ti_3C_2T_x$ coated lens in a four-point probe orientation with 1 mm spacing, and to ensure a good connection was made between the coated lens and the wires, silver conductive paint was applied. Current was sourced between the two outer probes, and voltage was measured through the inner probes. Three measurements were made per lens, and the average values were reported.

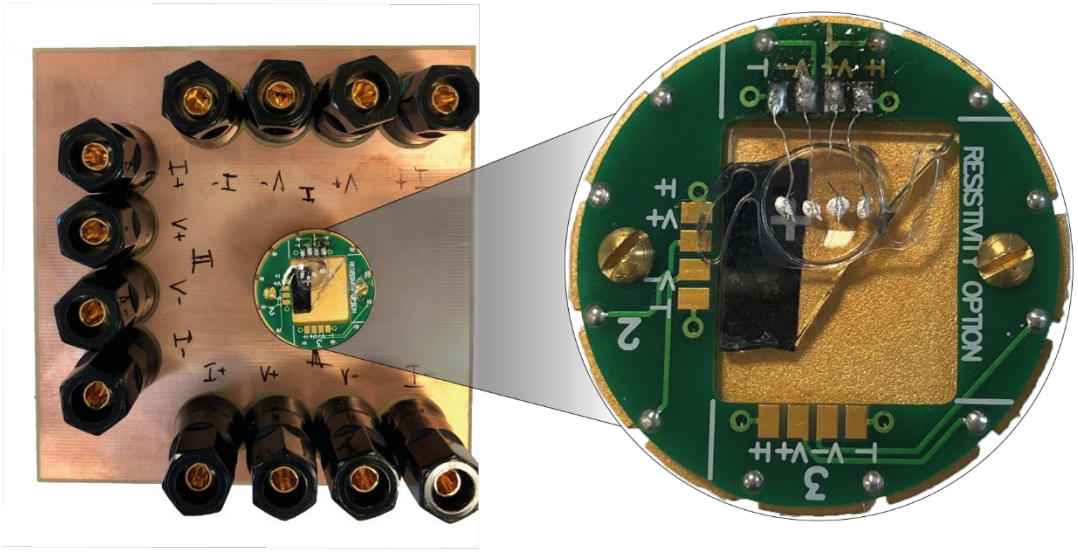

Figure 2-2 - Digital photograph of the ETO puck and stage used for electrical measurements. The sheet resistance was calculated using equation (2.5) and a geometric correction factor (equation (2.8)), based upon the diameter of the coating on the lens, was incorporated as the width of the coating is not infinitely large, where s is spacing of the probes and d is the diameter of the lens. Without the correction, an overestimation of the sheet resistance would be calculated[168].

$$c = \frac{ln\,(2)}{ln(2)+ln\,(d^2/s^2+3)-ln\,(d^2/s^2-3)} \tag{2.8}$$

2.2.5.5 Sheet mechanical resistance of $Ti_3C_2T_x$ coated lenses

The sheet resistance of coated IOLs was measured before and after manual deformation using a Rayner intraocular lenses standard injector. Sheet resistance was measured using the method described above. Next, the lens was inserted into the cartridge of the injector in the "z" position described by Rayners's instructions for use

(IFU). The cartridge was closed, rolling the IOL over the standard bend radius, and holding for 3 minutes, as per the IFU. The sheet resistance was measured following the manipulation demonstrating the flexibility of the conductive $Ti_3C_2T_x$ coating.

2.2.5.6 Optical power and modulation transfer function

Lens quality was assessed through optical measurements of lens optical power and MTF using a measurement system called a NIMO (NIMO TR0815, Lambda-X, Belgium). These measurements were performed before and after deposition of $Ti_3C_2T_x$ to ensure that the coating did not affect the lens optically or interfere with resolution or contrast.

2.2.5.7 Statistical analysis

The statistical software package GraphPad Prism 7.05 (GraphPad Software Inc., USA) was used for all statistical analyses. Optical power and MTF measurements were made, and the data was first analysed with the Shapiro-Wilk normality test followed by a paired t-test, $p < 0.05$.

2.3 Results

$Ti_3C_2T_x$ was investigated for use as a TCE in the development of an AIOL. Solutions were synthesised and coated onto IOL polymers to evaluate their performance. A series of physical characterisation techniques were carried out to optimise high-quality large flakes. Spin-coating was used to apply thin, conductive, transparent, and flexible $Ti_3C_2T_x$ coatings onto the polymers. Their optoelectronic performance and influence on optical quality was assessed toward the development of $Ti_3C_2T_x$ as a TCE for AIOL design.

2.3.1 Physical characterisation of the synthesised $Ti_3C_2T_x$

2.3.1.1 Scanning electron microscopy of $Ti_3C_2T_x$

Colloidal dispersions of delaminated $Ti_3C_2T_x$ were synthesised through chemical exfoliation of the precursor Ti_3AlC_2, then vacuum filtered to form free-standing, paper-like films. ***Figure 2-3*** demonstrates the single flake structure of $Ti_3C_2T_x$, first in the free-standing, paper-like, compact film (***Figure 2-3*** (a)). The force of the filtration compressed the flakes to a paper-like film. The second image shows an example of a dilute $Ti_3C_2T_x$ solution that was dried over a porous membrane to view the nanostructure of the flakes, where the dashed red line indicates a single flake layered on top of the other flakes (***Figure 2-3*** (b)).

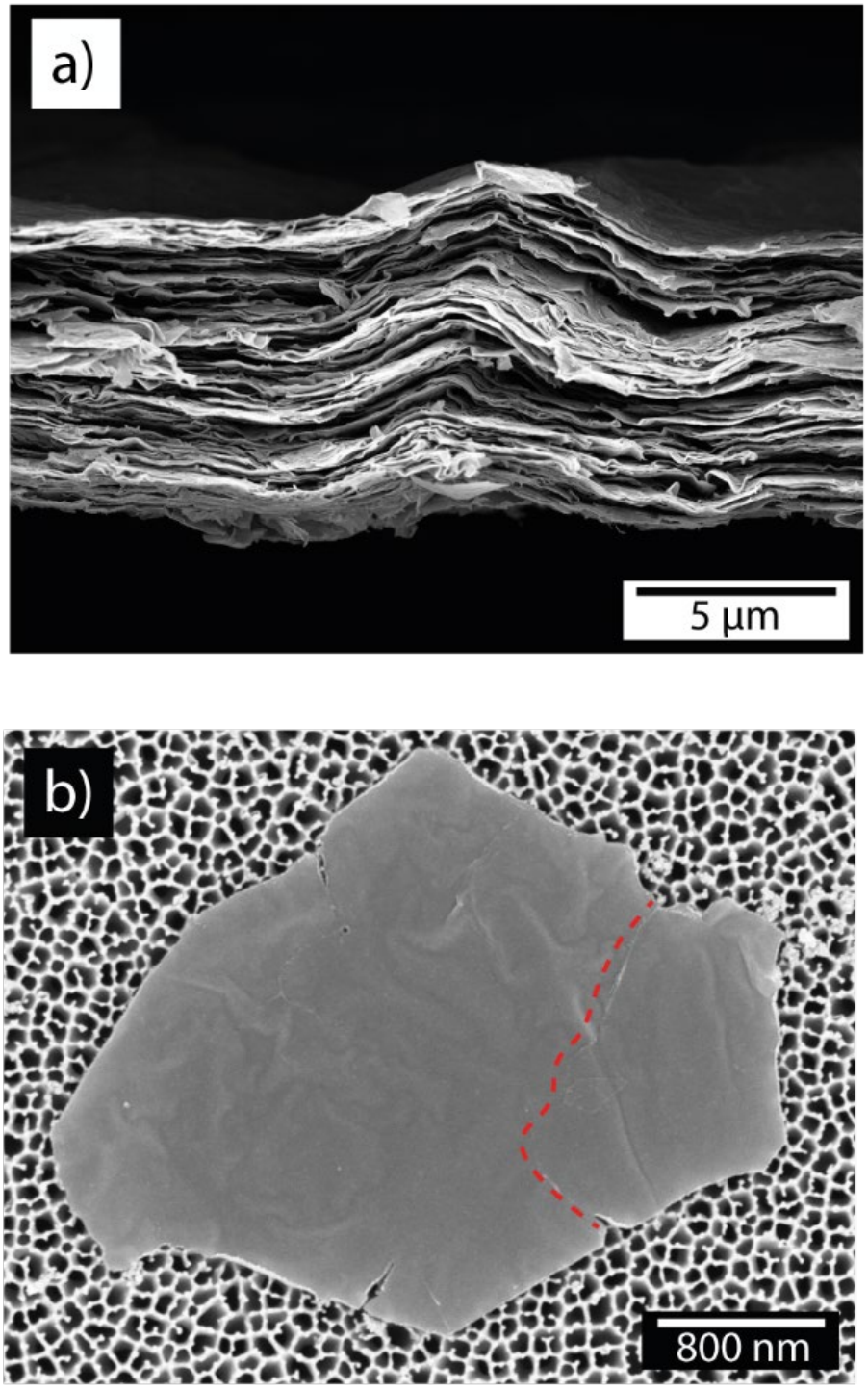

Figure 2-3 – Scanning electron microscopy (SEM) (Zeiss Supra 50VP, Germany). (a) Cross-section of a $Ti_3C_2T_x$ free-standing film produced through vacuum filtration. (b) A dilute $Ti_3C_2T_x$ solution was dried over a porous membrane and imaged with SEM, demonstrating a few $Ti_3C_2T_x$ flakes layered on the membrane, red dashed line to highlight a single flake.

2.3.1.2 *X-ray diffraction of $Ti_3C_2T_x$ free-standing film*

The XRD patterns were used to identify structural characteristics of the MAX phase compared to the MXene, Ti_3AlC_2 and $Ti_3C_2T_x$. The diffraction patterns in ***Figure 2-4*** show a shift in the 002 peak from 9.5° to ~ 7.1°. The apparent shift indicates the successful synthesis of the MAX phase to MXene, whereby the Al was selectively etched away, and surface functionalities bonded in its absence. The schematic was included to indicate the c-lattice parameter, d-spacing and interlayer spacing from one another.

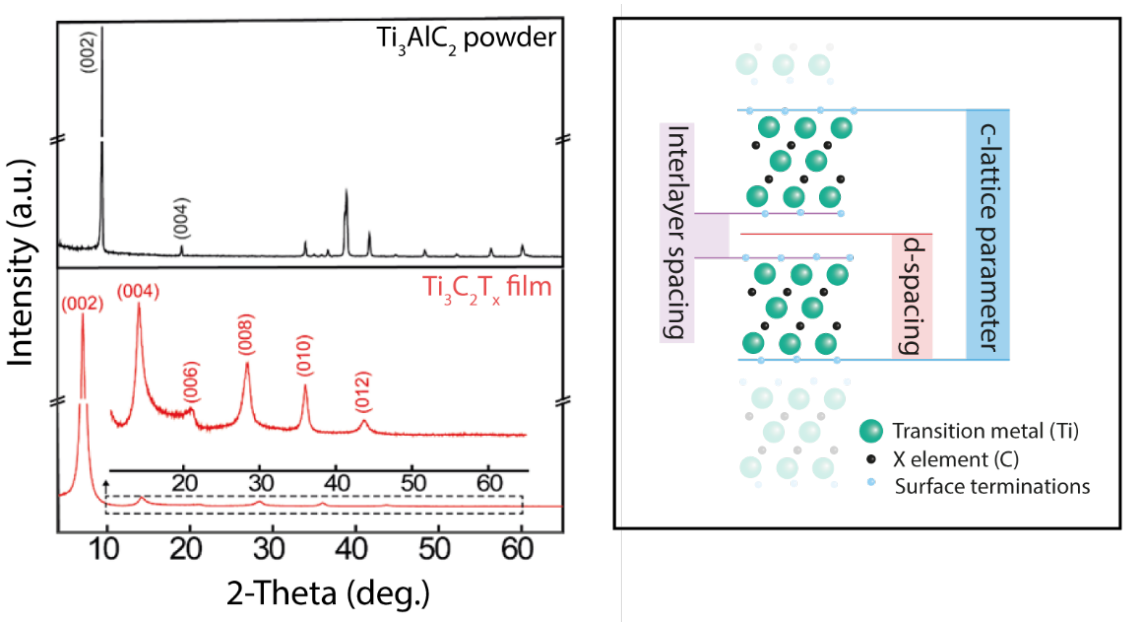

Figure 2-4 – (Left) X-ray diffraction (XRD) patterns of Ti_3AlC_2 MAX phase (black) and $Ti_3C_2T_x$ MXene (red) (Right) The schematic shows the c-lattice parameter, d-spacing and the interlayer spacing for a $Ti_3C_2T_x$. The c-lattice parameter is double the d-spacing, calculated using Braggs law, an increase from 18.6 Å to ~ 25 Å was observed.

2.3.1.3 X-ray photoelectron spectroscopy of $Ti_3C_2T_x$ free-standing film

The high-resolution XPS data shown in ***Figure 2-5*** provides elemental and binding environment details for $Ti_3C_2T_x$ free-standing film. The atomic spin-orbit splitting of the Ti 2p subshell produced $2p_{3/2}$ and $2p_{1/2}$ configurations for assigned peaks with the most abundance attributed to Ti – Tx. The C 1s spectra identified C – C and C – Ti binding energies, and the F 1s and O 1s identified F terminations and Ti – Ox binding energies. Further detail on binding energies and peak fitting in ***Table 2-2***.

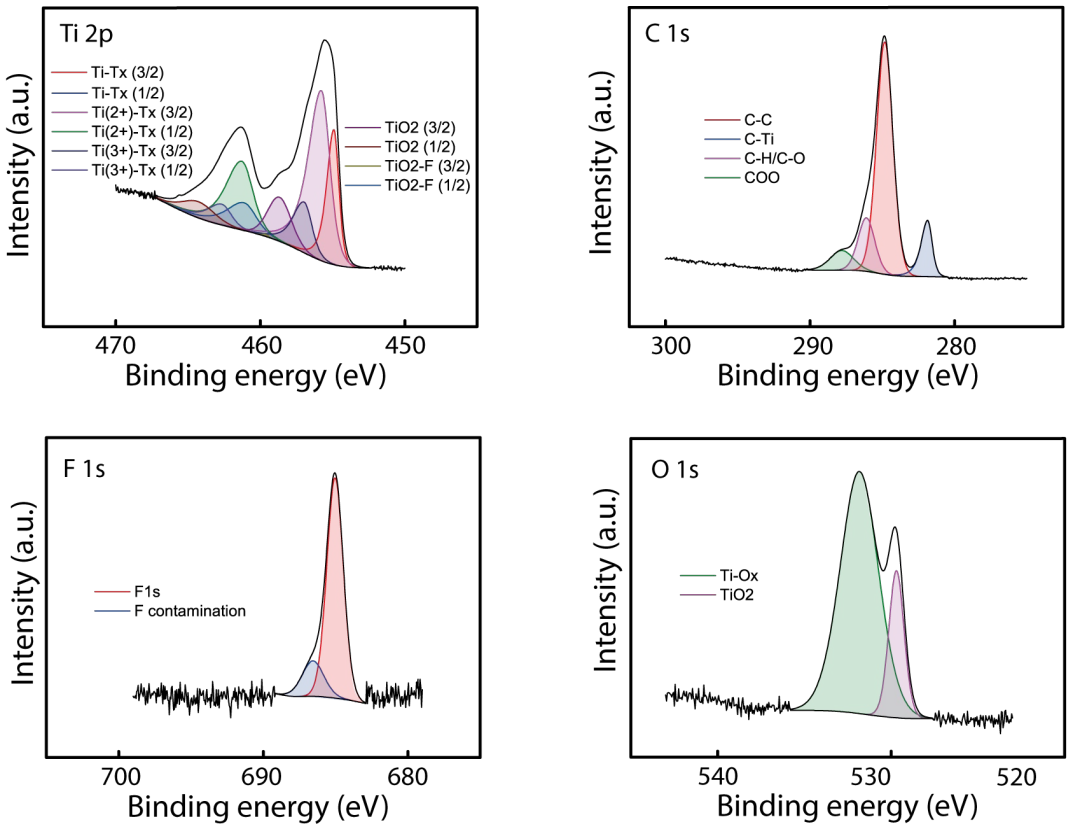

Figure 2-5 – Ti 2p, C 1s, F 1s and O 1s high-resolution X-ray photoelectron spectroscopy (XPS) spectra of the $Ti_3C_2T_x$ free-standing film.

Table 2-2 – High-resolution XPS (Physical Electronics VersaProbe 5000, USA) with a 100 µm Al Kα X-ray beam of the $Ti_3C_2T_x$ coating, showing the T1 2p, C 1s, F 1s, and O 1s data detailing the binding energy peaks and the corresponding assigned peaks[169].

Spectra	Binding energy (eV)	Assigned to
Ti 2p	454.90	Ti – Tx (3/2)
	461.25	Ti – Tx (1/2)
	455.80	Ti (2^+) – Tx (3/2)
	461.35	Ti (2^+) – Tx (1/2)
	457.05	Ti (3^+) – Tx (3/2)
	462.80	Ti (3^+) – Tx (1/2)
	458.75	TiO_2 (3/2)
	464.75	TiO_2 (1/2)
O 1s	531.85	Ti – Ox
	529.70	TiO_2
F 1s	685.05	F 1s
	686.55	F contamination
C 1s	284.85	C – C
	281.85	C – Ti
	286.10	C – H / C – O
	287.80	COO

2.3.1.4 Ultraviolet-visible (UV-Vis) absorbance spectroscopy of $Ti_3C_2T_x$ solution

The absorbance of dilute colloidal $Ti_3C_2T_x$ solutions were measured by UV-Vis spectroscopy, shown in ***Figure 2-6***. A broad 700 – 800 nm peak was observed. A calibration curve was plotted, and following Beer-lamberts law, the extinction coefficient was calculated as 31.34 L g^{-1} cm^{-1}, in agreement with the literature[170].

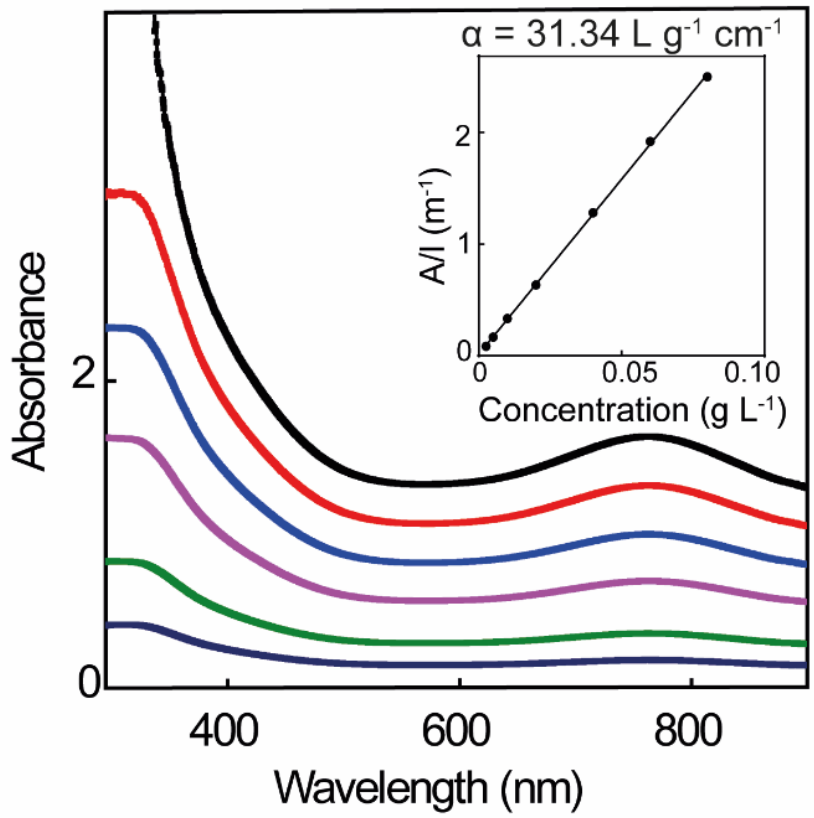

Figure 2-6 – UV-Vis absorbance spectra for $Ti_3C_2T_x$ at varying concentrations. Inset is the calibration curve produced from the $Ti_3C_2T_x$ UV-Vis spectra following Beer-Lamberts law, and the extinction coefficient was calculated as 31.34 L g^{-1} cm^{-1}.

2.3.1.5 Dynamic light scattering size analysis of $Ti_3C_2T_x$ solution

DLS was used to estimate the hydrodynamic size distribution of the dilute colloidal $Ti_3C_2T_x$ solution. Average size of 1250 nm was identified with a polydispersity index (PDI) of 0.5 shown in ***Figure 2-7***.

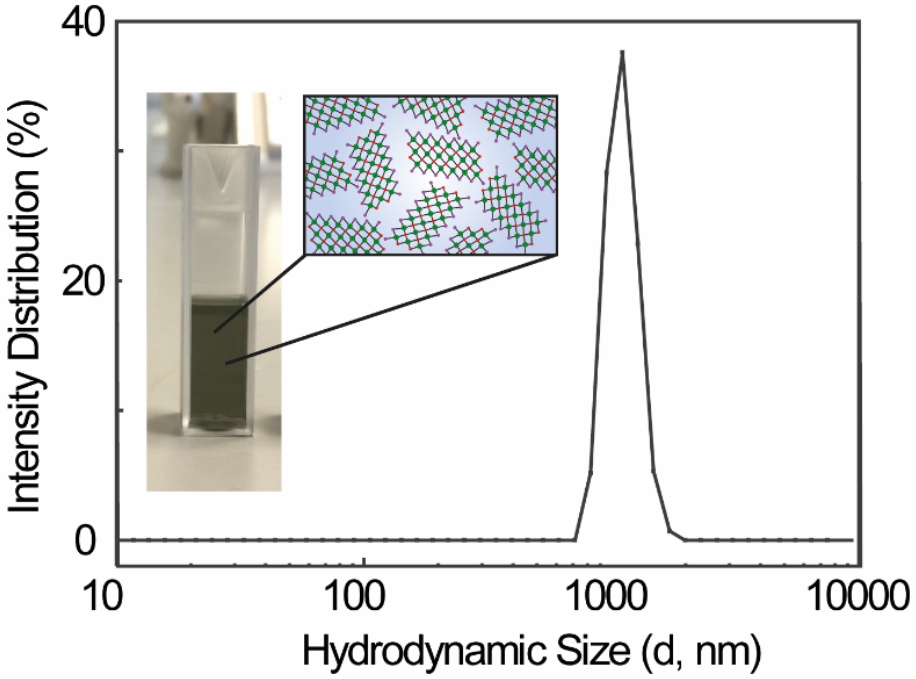

Figure 2-7 – Dynamic light scattering (DLS) intensity distribution for a colloidal solution of $Ti_3C_2T_x$, with an average size of 1250 nm and a polydispersity index (PDI) of 0.5. The plot inset shows a digital image of a colloidal solution of $Ti_3C_2T_x$ in a PMMA cuvette with a schematic of a $Ti_3C_2T_x$ solution.

2.3.1.6 Bulk conductivity of $Ti_3C_2T_x$ free-standing film

The bulk conductivity was established through sheet resistance measurements of the thin films. The lateral resistance measurement is independent of size therefore it is an efficient means of comparison between samples measured directly with a four-point

probe. The bulk conductivity of the $Ti_3C_2T_x$ free-standing film shown in ***Table 2-3*** was found to be $5.9x10^3 \pm 4.4\ x10^2$ S cm^{-1}.

Table 2-3 – Sheet resistance measurements of the $Ti_3C_2T_x$ free-standing film, measured using a four-point probe technique, calculations detailed in section 2.2.3.7.

	Voltage (V)	Current (A)	Sheet resistance (Ω sq^{-1})	Thickness (cm)	Resistivity (Ω)	Conductivity (S cm^{-1})
1	$1.0x10^{-3}$	$1.0x10^{-2}$	$4.5x10^{-1}$	$3.5x10^{-4}$	$1.6x10^{-4}$	$6.4x10^3$
2	$9.8x10^{-4}$	$1.0x10^{-2}$	$4.4x10^{-1}$	$4.1x10^{-4}$	$1.8x10^{-4}$	$5.5x10^3$
3	$9.3x10^{-4}$	$1.0x10^{-2}$	$4.2x10^{-1}$	$4.1x10^{-4}$	$1.7x10^{-4}$	$5.9x10^3$
					Average	$5.9x10^3$
					SD	$4.4\ x10^2$

2.3.2 Solution processing of $Ti_3C_2T_x$ and characterisation

2.3.2.1 X-ray photoelectron spectroscopy of $Ti_3C_2T_x$ coated lens polymer

The high-resolution XPS spectra, shown in ***Figure 2-8***, for the uncoated IOL and $Ti_3C_2T_x$ coated IOL was used to evidence the presence of the spin-coated $Ti_3C_2T_x$. The spectra for the uncoated IOL indicate typical peaks characteristic of a polymer. Though, the coated IOL attributed $Ti_3C_2T_x$ peaks consistent with the XPS data for the free-standing $Ti_3C_2T_x$ film characterised in section 2.3.1.3.

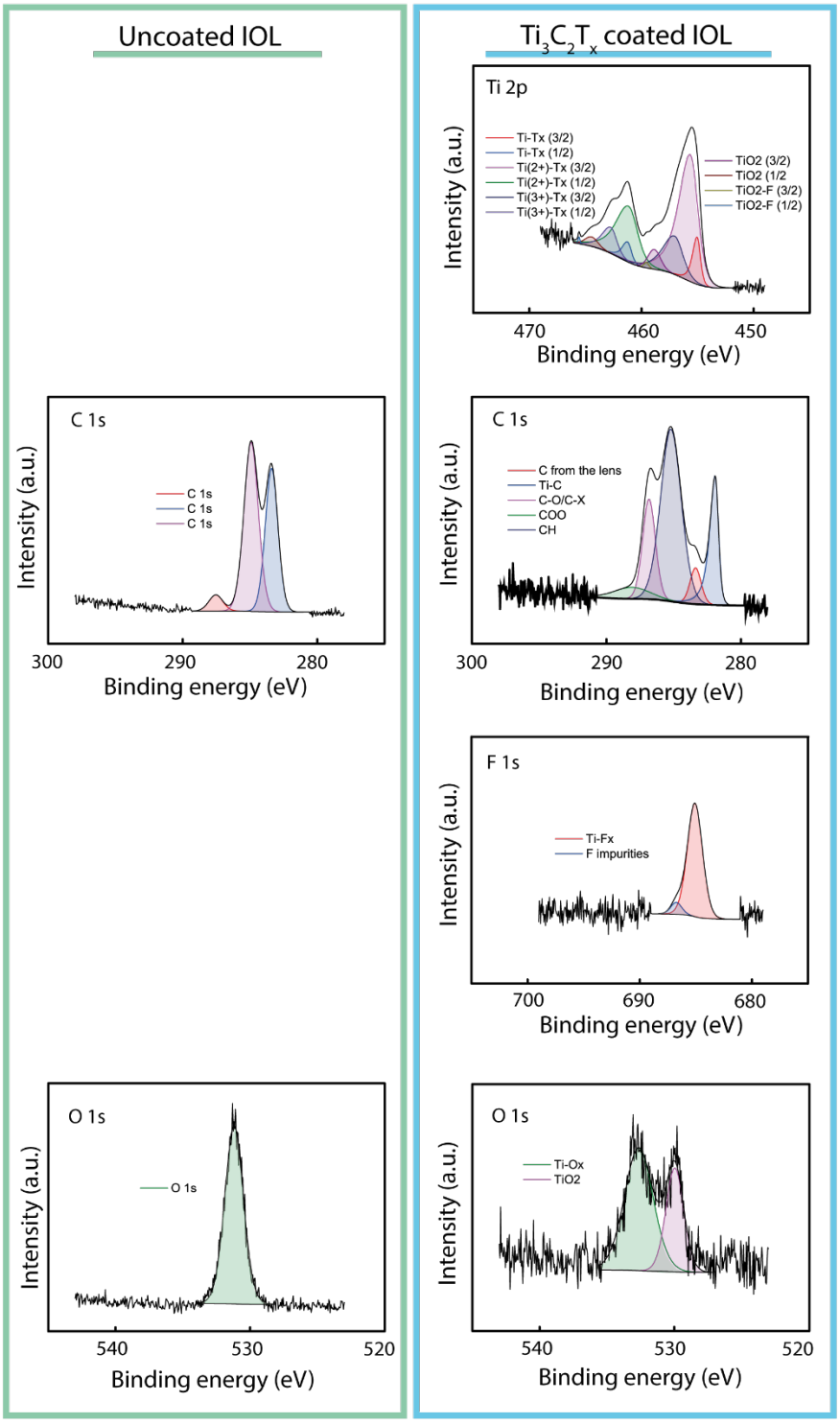

Figure 2-8 – Ti 2p, C 1s, F 1s and O 1s high-resolution X-ray photoelectron spectroscopy (XPS) spectra of the uncoated commercially available hydrophobic IOL (left) and the $Ti_3C_2T_x$ spin-coated IOL (right). The C 1s and O 1s spectra of the uncoated IOL show characteristic peaks of a polymer with no Ti nor F peaks identified.

The spectra for the coated IOL featured the distinctive $Ti_3C_2T_x$ peaks with relative binding energies observed in the previous XPS data for the free-standing film (***Figure 2-5***).

2.3.2.2 Atomic force microscopy of $Ti_3C_2T_x$ coated lens

AFM was used to characterise the thickness of the $Ti_3C_2T_x$ coating on the IOL following the spin-coating procedure. The step made in the coating was evaluated in tapping mode, shown in ***Figure 2-9***, however it was not distinguishable. The optical microscopy image demonstrates the step in the coating.

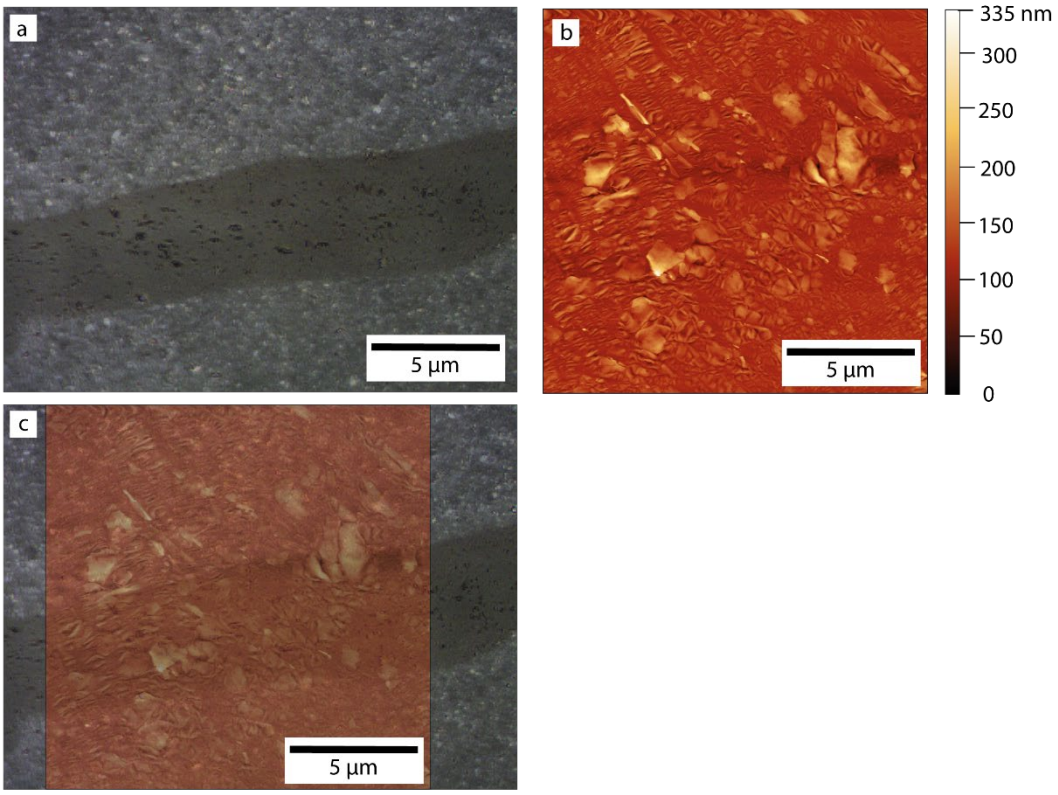

Figure 2-9 – Atomic force microscopy (AFM) image of $Ti_3C_2T_x$ coated hydrophobic IOL, (a) Optical microscope image to demonstrate the position of the step made in the coating. (b) Image produced with the AFM analysis software package Gwyddion of

the coated polymer to determine coating thickness. (c) Overlay of the optical microscope image of the step position in the $Ti_3C_2T_x$ coating with the image produced with the Gwyddion AFM analysis software to provide reference to the step location on the analysed image.

2.3.2.3 Transmittance spectroscopy of $Ti_3C_2T_x$ coated lenses and estimated the thickness

IOLs were spin-coated with a 5 mg mL^{-1} solution of $Ti_3C_2T_x$, and sequential coatings were added to observe the relationship between coating thickness and transmittance, demonstrated in ***Figure 2-10*** *(a)*. A $Ti_3C_2T_x$ characteristic peak was observed in the near-infrared region of the electromagnetic spectrum at 700 – 800 nm. A relationship between absorbance and thickness was established by Hantanasirisakul *et al.* shown in equation (2.9), where A is absorbance and t thickness in nm [102]. The transmittance data, shown in ***Figure 2-10*** *(a)*, was used to find the corresponding absorbance of the coated IOLs, and the estimated thicknesses of the $Ti_3C_2T_x$ coatings are plotted in ***Figure 2-10*** *(b)* ranged from approximately 15 – 70 nm.

$$A = 0.005t \tag{2.9}$$

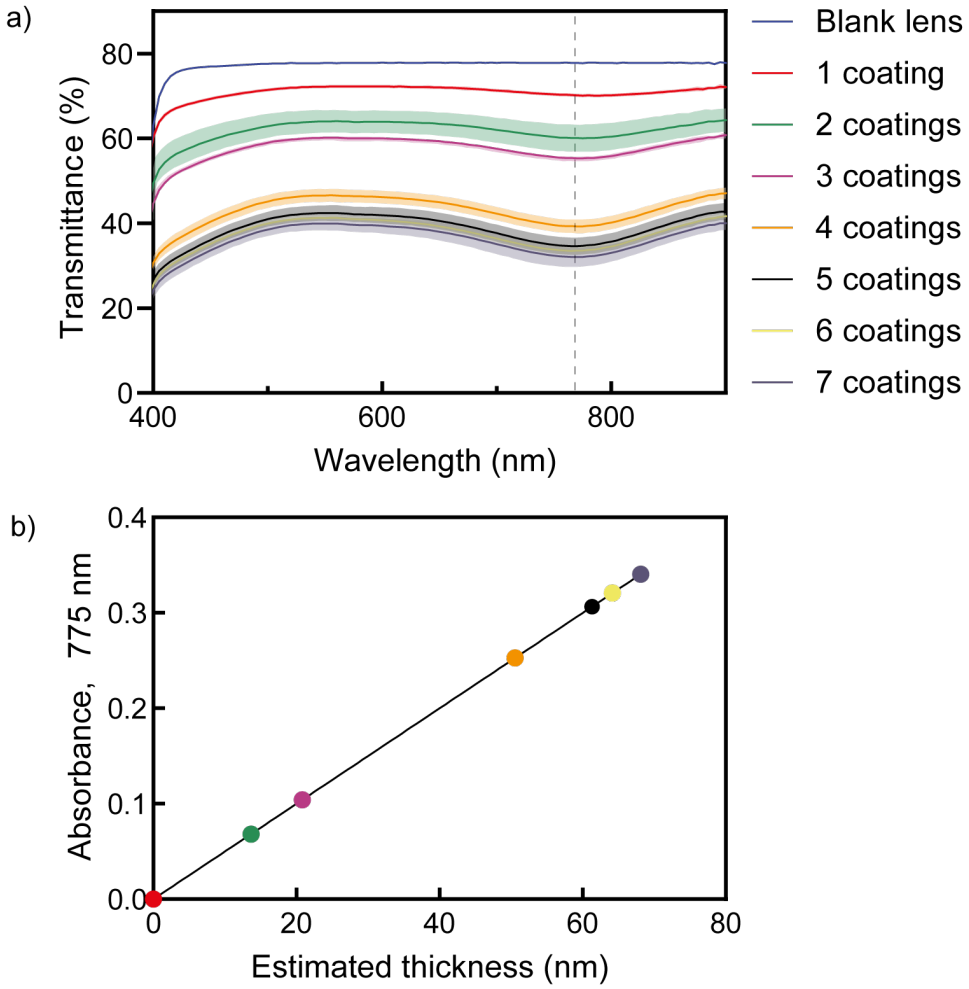

Figure 2-10 – Transmittance spectra of $Ti_3C_2T_x$ spin-coated IOLs and estimated thickness. (a) Transmittance spectra of the spin-coated IOLs, (mean ± SD, n = 3). Lenses were spin-coated with a 5 mg mL^{-1} solution, and sequential coatings were added to increase thickness whilst keeping concentration and spin speed constant. (b) Estimated thickness versus absorbance at 775 nm using equation (2.9), where A is absorbance and t thickness in nm[102].

2.3.2.4 Sheet resistance measurements of $Ti_3C_2T_x$ coated lenses

The optoelectronic performance of the coated IOLs was evaluated through transmittance and sheet resistance measurements. The sheet resistance of the $Ti_3C_2T_x$ coated IOLs was measured in a four-point probe orientation and plotted against transmittance in ***Figure 2-11***. The sheet resistance of the series of coatings was found to range from 0.2 to 1.0 kΩ sq^{-1} with the corresponding transmittance of 50 to 80 %.

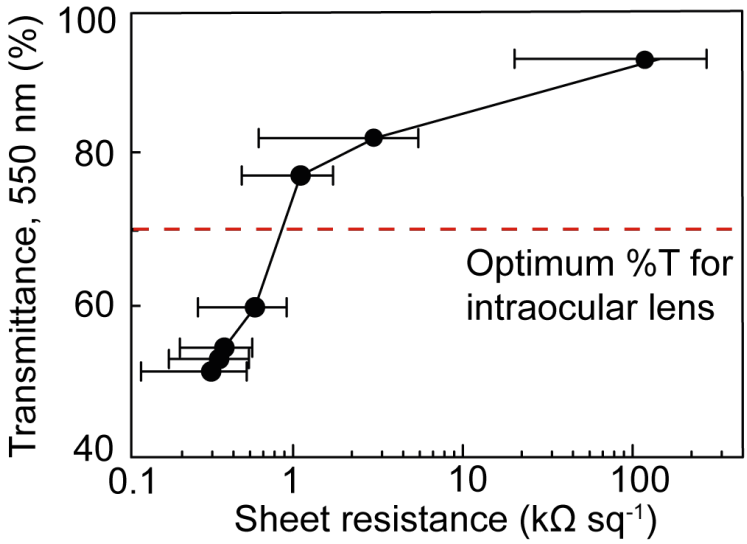

Figure 2-11 – Sheet resistance versus transmittance of the $Ti_3C_2T_x$ coated lenses at 550 nm (mean ± SEM, n = 3), error bars for transmittance too small to be visible on the plot.

2.3.2.5 The figure of merit for the $Ti_3C_2T_x$ coated on lens polymer

The FoM defined by the ratio of electronic and optical conductivities (σ_{DC}/σ_{OP}), is used to compare TCEs to one another. It is determined through transmittance and sheet resistance measurements using the following equation:

$$T = \left(1 + \frac{Z_0 \sigma_{opt}}{2R_s \sigma_{DC}}\right)^{-2} \tag{2.10}$$

Where Z_0 is the impedance of free space equal to 377 Ω, and the slope is equal to $(\sigma_{DC}/\sigma_{Op})^{-1}$. The FoM for the coated IOLs was calculated to be 1.8 shown in ***Figure 2-12***.

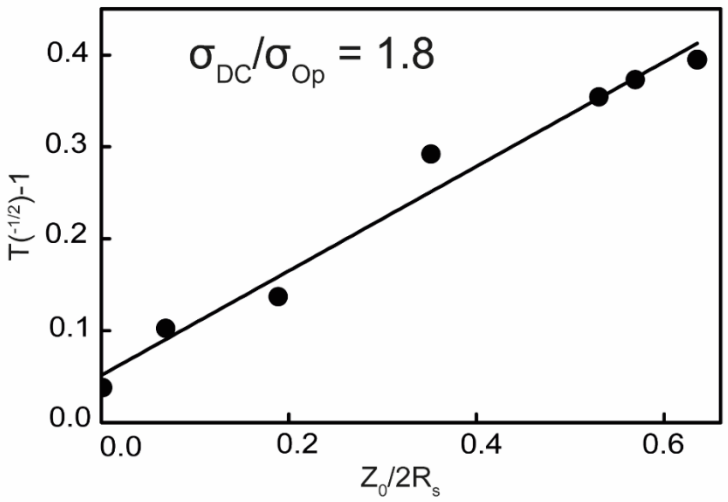

Figure 2-12 – Transmittance (T) and sheet resistance (R_s) of $Ti_3C_2T_x$ coated lenses were used to evaluate their transparent conductive electrode performance through the electrical figure of merit (FoM). Z_0 is the impedance of free space equal to 377 Ω.

2.3.2.6 Sheet mechanical resistance of $Ti_3C_2T_x$ coated lenses

The sheet resistance of the $Ti_3C_2T_x$ coated lenses was found to increase two-fold after manipulation of the coating using Rayner's injector demonstrated in ***Figure 2-13***. Before deformation, the sheet resistance was 92.9 ± 31.1 Ω sq^{-1} and increased to 197.9 ± 43.7 Ω sq^{-1}. A paired t-test was used to compare the sheet resistance of the coating before and after deformation. A statistical significance (p = 0.0011) was identified when $p < 0.05$.

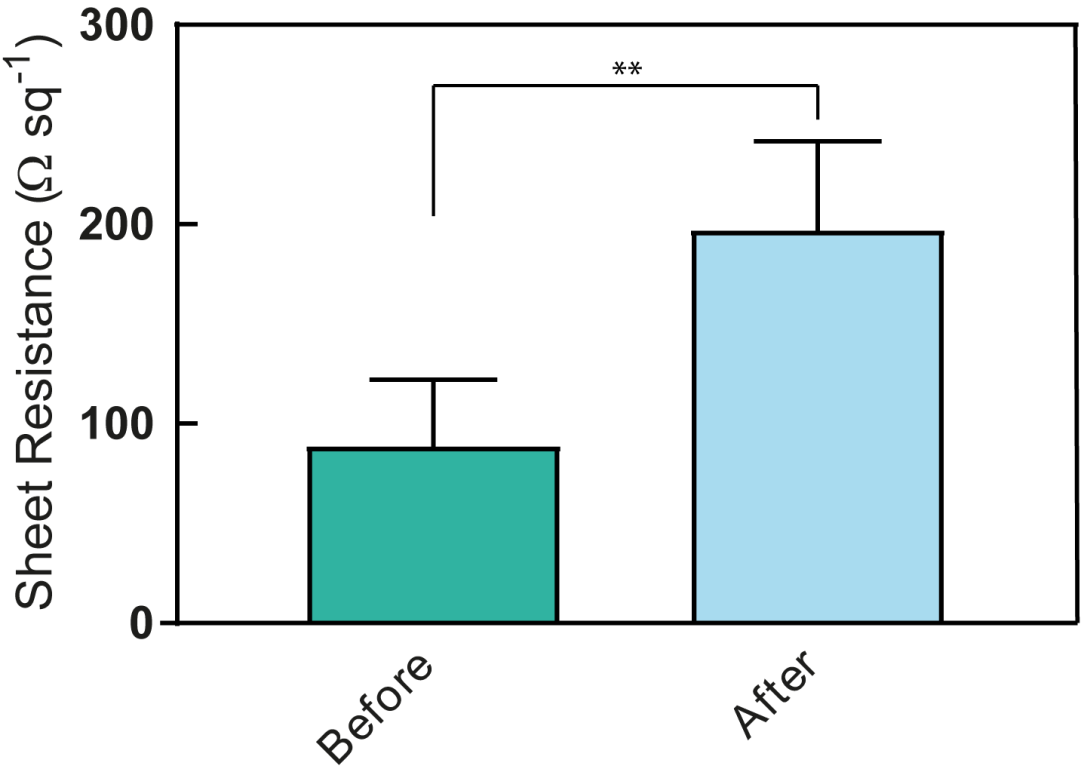

Figure 2-13 – Sheet resistance measurements of $Ti_3C_2T_x$ coated IOLs before and after manual deformation with Rayner's injector cartridge. Statistical analysis using a paired t-test, (mean ± SD, n = 6, $p < 0.05$).

2.3.2.7 Optical power and modulation transfer function

During the manufacture of the IOL, quality and performance are evaluated through optical power and MTF measurements. It is essential that the TCE coating does not negatively affect these properties of the lens. The measurements were made before and after coating, the presence of $Ti_3C_2T_x$ did not impact optical power, nor did it affect MTF, as shown in ***Figure 2-14***.

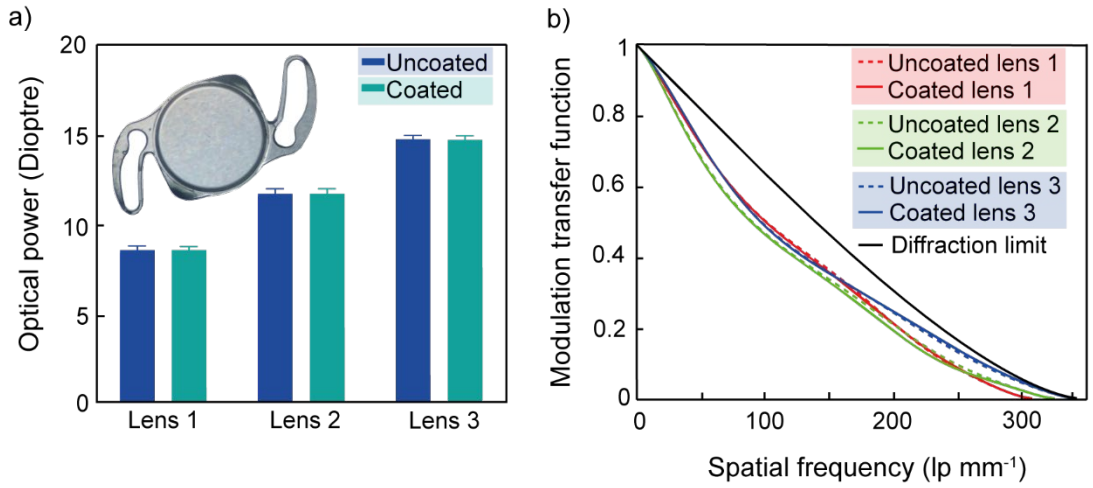

Figure 2-14 – Lens performance (a) Optical power measurement on three different lens powers before and after coating with $Ti_3C_2T_x$ (mean ± SD, n = 5, $p < 0.05$) analysed by one-way ANOVA. Inset (a) Digital image of a spin-coated IOL. (b) Modulation transfer function (MTF) measurement on three different lens powers before and after coating with $Ti_3C_2T_x$ for each type n = 5. Both measurements were made using a NIMO (NIMO TR0815, Lambda-X, Belgium).

2.4 Discussion

In this chapter, $Ti_3C_2T_x$ was synthesised, and a series of characterisation techniques, including SEM, XRD, XPS, UV-Vis spectroscopy, and DLS, were used to confirm the composition and structural characteristics of the MXene product that was etched from its precursor and optimised for the transparent electrode application. Colloidal solutions of $Ti_3C_2T_x$ were spin-coated onto the IOL, and XPS was used to confirm that the coating was successfully applied. The optoelectronic properties of the coated IOLs were characterised through percentage transmittance and sheet resistance measurements. These measurements were used to determine the optimal coating methodology balancing high conductivity with adequate light transmission for lens application. Flexibility was evaluated to determine the potential for retention of optoelectronic properties in an AIOL application following deformation. Optical power and MTF measurements were used to assess whether the coating negatively impacted lens performance.

2.4.1 Synthesis and physical characterisation

$Ti_3C_2T_x$ solutions were synthesised and a 1 mL aliquot vacuum filtered to form a free-standing, paper-like film shown in ***Figure 2-3***. The flake-like structure observed provides a good initial indication of the synthesis and delamination of $Ti_3C_2T_x$. Further corroborating this finding are the XRD patterns, shown in ***Figure 2-4***, of Ti_3AlC_2 powder compared to a $Ti_3C_2T_x$ free-standing film. A shift of the (002) peak was observed from 9.5° to ~ 7.1°, which corresponds to the d_{002}-spacing of 9.3 Å and ~12.5 Å. The relative increase observed occurs as a result of the removal of Al and the introduction of surface terminations. The magnitude of spacing is determined by the

intercalant, in this case by the Li^+ ions and water molecules. The findings are in good agreement with previously reported investigations[171–173]. XPS was used to identify the elemental composition and bonding environments of the free-standing $Ti_3C_2T_x$ film, shown in ***Figure 2-5***. Due to the atomic spin-orbit interaction, the Ti 2p spectra consists of $2p_{3/2}$ and $2p_{1/2}$ configurations. The 2p subshell produces a doublet photoemission in the ratio 2:1 ($2p_{3/2}$: $2p_{1/2}$) for the peak intensities[174]. The 545.90 eV and 461.25 eV peaks were assigned to Ti-T_x bonds in the $2p_{3/2}$ and $2p_{1/2}$ orbitals, respectively. ***Table 2-2*** demonstrates the binding energies from the spectra and the assigned peaks that further confirm the absence of Al and are consistent with similar investigations in the literature[175]. UV-Vis absorbance spectroscopy was used to investigate the optical properties of $Ti_3C_2T_x$ solutions (***Figure 2-6***). A broad peak was observed in the near-infrared region at 700 to 800 nm. This peak is characteristic of a transverse surface plasmon mode in $Ti_3C_2T_x$[176]. From the calibration curve, the extinction coefficient was determined to be 31.34 L g^{-1} cm^{-1}, which agrees with previous reports[170]. DLS was used to provide average flake size estimations. A single peak was identified in the distribution (***Figure 2-7***) with an average size of 1250 nm and a polydispersity index (PDI) of 0.5. Despite particle sphericity being an essential assumption of DLS hydrodynamic size measurements, K. Maleski *et al*.[177] presented a good approximation of the lateral size of $Ti_3C_2T_x$ flakes with the aspect ratio ~1.6 : 1 (length/width). The bulk conductivity of the $Ti_3C_2T_x$ free-standing film was measured with a four-point probe and found to be ~6000 S cm^{-1}, indicating the high quality of the two-dimensional flakes produced.

2.4.2 Solution processing and characterisation

Spin-coating was the solution processing technique used to apply thin and uniform $Ti_3C_2T_x$ coatings onto commercially available hydrophobic acrylate IOLs. Literature states that a relatively high concentration of $Ti_3C_2T_x$ solution is required for spin-coating to obtain considerably thick coatings, usually 5 mg mL^{-1} or more[113,166]. Therefore, a 5 mg mL^{-1} solution was cast onto the IOL surface at varying speeds to produce uniform and continuous coatings. The high-resolution C 1s and O 1s XPS spectra, shown in ***Figure 2-8*** left, detected C and O peaks typical of a polymer for the uncoated IOL. The spectra of the coated IOL (***Figure 2-8*** right) displayed additional peaks attributed to the $Ti_3C_2T_x$ coating with the same binding energies as seen in the $Ti_3C_2T_x$ free-standing film analysed in the previous section. Moreover, XPS data confirmed the presence of the coating for further evaluation. AFM was employed to characterise the coating thickness applied (***Figure 2-9*** (a)). A scratch was made using plastic forceps to create a step in the coating. The step region (***Figure 2-9*** (b)) was subjected to AFM tapping mode. However, the step could not be distinguished, which could be attributed to the surface roughness relative to the extremely thin coating.

The relationship between coating thickness and transmittance, identified in ***Figure 2-10*** *(a)*, indicated the inverse relationship between the two properties that were further characterised using the formula established by Hantanasirsakul *et al*.[102] that relates absorbance and thickness shown in equation (2.9). Despite concentration and spin speed being the usual modes of tuning coating thickness, the coating protocol had been optimised to give thin, uniform, and continuous coverage on the hydrophobic IOL with an estimated thickness of 15 – 70 nm[116]. Therefore, sequential layers were coated onto the IOL to permit a controlled increase in coating thickness. As with the

UV-Vis absorption spectra for the $Ti_3C_2T_x$ solution, the coated IOLs displayed the same NIR peak, typical of this member of the MXene family. ***Figure 2-10*** *(b)* demonstrated the estimated coating thickness to range from approximately 15 – 70 nm.

The sheet resistance of the coated lenses ranged from 0.2 – 1.0 kΩ $sq^{-1,}$ corresponding to 50 – 80 % transmittance demonstrated in ***Figure 2-11***. The electrical FoM, meaning the ratio of electronic and optical conductivities, was calculated as 1.8, demonstrated in ***Figure 2-12***. This value is comparable to previously reported FoMs for $Ti_3C_2T_x$ coatings, yet little is explained in the literature regarding the substrate being coated. Most reported examples are coated on glass, and surface roughness is not investigated, here it is speculated that the surface roughness of the polymer influences the resultant FoM. When coating with MXene, the flakes orient with the plane of the substrate. It is known that greater alignment of flakes results in improved transport of electrons through inter-flake junctions[156]. This suggests that a substrate with a less rough surface would improve the FoM. Although, studies have demonstrated improved FoMs through vacuum-annealing and drying coatings in a nitrogen environment[94]. The increase in sheet resistance of the coated lenses shown in ***Figure 2-13***, identified that conductivity was maintained post manipulation of the $Ti_3C_2T_x$ coating. This is essential for IOL design as the current cataract procedure implants the IOL through a 2.5 mm incision. Moreover, the device must retain its electronic properties to operate after implantation.

As the purpose of the IOL is to restore visual acuity for the patient following cataract removal, visual acuity must not be diminished with the addition of a coating to the lens. Therefore, the $Ti_3C_2T_x$ coated IOLs were assessed to determine the impact of the

coating on the lens' intrinsic optical performance in terms of optical power and spatial resolution. No significant difference in optical power nor MTF was observed on a series of lens powers when measured before and after coating (***Figure 2-14***). Moreover, the $Ti_3C_2T_x$ coatings did not negatively affect the optical performance or quality. The work demonstrated in this chapter addresses the aim by showing that $Ti_3C_2T_x$ can be synthesised, characterised, and coated onto a lens polymer and perform as a flexible TCE without disrupting the optical quality of the lens.

2.5 Conclusion

The suitability of $Ti_3C_2T_x$ was evaluated for use in an AIOL design by assessing its optoelectronic performance when coated on an IOL substrate. The literature suggested the potential of the nanomaterial as a flexible TCE, allowing the passage of light and permitting the flow of electrons, yet no investigation for an ocular application has been explored. The as-synthesised MXene was spin-coated onto the IOLs, and shear forces resulted in highly substrate-aligned, thin, uniform, and continuous coatings. The sheet resistance (0.2 – 1.0 kΩ sq^{-1}) and transmittance (50 – 80 %) were found to agree with previously reported studies. Sufficient sheet resistance was retained following mechanical manipulation, displaying the truly flexible TCE characteristics of the coating. The coating did not negatively influence lens performance. The findings in this chapter show for the first time the use of MXenes for AIOL design to support the hypothesis of the suitability of $Ti_3C_2T_x$ for lens applications as a flexible TCE.

Chapter 3

3 *The Biocompatibility of MXene coated intraocular lens*

3.1 Introduction

3.1.1 Biocompatibility of IOLs

Postoperative ocular inflammation is an inevitable side effect of cataract treatment caused by surgical trauma. The incision into the lens capsule, termed capsulorhexis, followed by phacoemulsification and implantation of an IOL, stimulates a wound healing response. An important consideration in IOL design is material choice since this can influence the biocompatibility of the lens. Biocompatibility describes if a material meets appropriate biological requirements, is specific to the site of use and is part of the safety evaluation of a new biomaterial considering the host immune response and purpose of the material within a medical device. In terms of uveal compatibility, concerning the middle layer of the eye, an inflammatory foreign-body reaction to the implant can occur due to the physical break in the blood-aqueous barrier from cataract surgery, causing inflammatory mediator releases into the aqueous humour. Additionally, the IOL directly interacts with surrounding tissue and triggers inflammation[178]. Capsular biocompatibility includes the interaction between the lens and the lens epithelial cells (LECs). Following cataract surgery, remnant LECs in the capsule can adhere to the IOL surface, proliferate, differentiate into fibroblast-like cells, and migrate over the visual axis, causing a secondary cataract[179]. Inflammatory mediators released by residual LECs and migrating macrophages and monocytes include inflammatory cytokines that can drive the upregulation of pathways

contributing to the opacification of the IOL[180]. This upregulation of hyper-inflammatory pathways leading to myofibroblast transdifferentiation and migration of LECs to form a secondary cataract behind the polymer lens describe the primary complication of cataract surgery known as posterior capsular opacification (PCO), which affects approximately 20 – 50 % of patients[181].

IOL optic and haptic designs aim to satisfy uveal and capsular biocompatibility. Nevertheless, design properties can influence PCO occurrence and other complications. It is widely accepted that a sharp edge around the optic of the IOL reduces PCO rates and requirements for further treatment, as the sharp edge acts as a physical barrier to LECs migrating towards the optical axis. A review comparing the effect of sharp-edged to round-edged optics on PCO incidence found a significantly lower rate of PCO when sharp-edged IOLs were used[182]. Nishi *et al*.[183] demonstrated that a sharp capsular bend created at the rectangular edge of the IOL induced contact inhibition of migrating LECs, reducing PCO development regardless of the IOL material. Several studies support these findings, reporting no difference in PCO prevention between IOL models when sharp-edged optics were used, irrespective of the IOL's material composition or enhanced edged design[182,184–187].

In addition to IOL design, lens polymer materials and consequent surface properties can also influence postoperative complications. Several studies have evaluated PCO rate, severity and treatment via neodymium-doped yttrium aluminium garnet (Nd:YAG) laser capsulotomy as a function of IOL material[188]. Nd:YAG is an effective treatment for PCO where a laser is used to cut a hole in the posterior lens capsule[189]. This treatment can lead to further complications, including elevated intraocular pressure and retinal detachment[69]. Auffarth *et al*.[190] found that PCO and

Nd:YAG rates for hydrophobic acrylate IOLs were significantly lower than PMMA, silicone, and hydrophilic acrylate lenses. Another investigation into IOL material biocompatibility found significantly higher PCO rates following implantation with hydrophilic hydrogel IOLs in comparison to hydrophobic acrylates IOLs (n = 95). At the two-year postoperative review, 28 % of the hydrophilic group required Nd:YAG capsulotomy, whereas only 2 % of the hydrophobic group required the treatment[191]. A meta-analysis study evaluated the association of hydrophobic and hydrophilic IOLs with the prevention of PCO and reduction of Nd:YAG rates using data from eleven previous studies. PCO occurrence and Nd:YAG rates were lower following implantation with hydrophobic IOLs, yet visual acuity was similar between both hydrophobic and hydrophilic IOLs[190]. Nevertheless, it has been reported that IOLs with a hydrophilic surface promote LEC proliferation and migration from the equator to the visual axis[192]. It is suggested that hydrophobic acrylate IOLs have superior biocompatibility due to better adhesion to the lens capsule. Linnola *et al*.[193] assessed the adhesion of fibronectin, vitronectin, laminin and collagen to various IOLs including PMMA, silicone, hydrophobic acrylate, and hydrogel-based. Fibronectin and laminin had greater adhesiveness to the hydrophobic acrylate leading to greater attachment to the lens capsule[193–195]. Moreover, the tight attachment of the IOL to the capsule may reduce the space for LEC migration, reducing PCO occurrence[69]. Surface modifications to IOL base-polymers have also been studied to enhance uveal and capsular biocompatibility[42]. For instance, hydrophilic IOLs were functionalised with adhesion containing Arg-Gly-Asp peptides to promote LEC adhesion comparable to hydrophobic IOLs[196]. If MXene coatings are to be considered for use in an AIOL

design, they should first be investigated to confirm they do not provoke a detrimental local response to the ocular environment.

3.1.2 Biocompatibility of $Ti_3C_2T_x$

The safety and efficacy of any new IOL technology must be evaluated to ensure that factors do not negatively influence cellular reactions contributing to postoperative complications, including PCO development. $Ti_3C_2T_x$ is the most studied MXene and although some cell studies have been conducted to investigate cytotoxicity no lens epithelial cell studies or studies considering the interaction of this material with pathways potentially leading to PCO have been conducted to date. It is believed that the initial developmental stages of PCO occur within the first 24 hours post cataract surgery although PCO can develop over months to years. Pro-inflammatory mediator levels are elevated as part of the LEC wound healing response including the upregulation of inflammatory cytokines by monocytes migrating from the uveal layer and residual LECs[179]. Therefore, an initial consideration of $Ti_3C_2T_x$ biocompatibility should consider interaction with these cells and upregulation of cytokine-induced inflammatory pathways. $Ti_3C_2T_x$ has been shown to repress monocyte (THP-1) induced inflammatory marker upregulation for interleukin (IL) 6, tumour necrosis factor-alpha (TNF-α), and IL-8 in a study indicating that $Ti_3C_2T_x$ could be used to benefit the wound healing response through repression of dysregulated hyper-inflammatory mediator interactions[197].

$Ti_3C_2T_x$ cytotoxicity has been assessed in other biological applications and these have indicated a dose and cell line-dependent relationship. $Ti_3C_2T_x$ was exposed to normal

(MRC-5 and HaCaT) and cancerous (A549 and A375) cell lines. The most significant toxicity was observed with A549 cells, while HaCaT cells were non-toxic over the 0 – 500 mg L^{-1} concentration range[198]. Wu *et al.*[199] found that low $Ti_3C_2T_x$ concentrations of 12.5 µg mL^{-1} did not stimulate apoptosis in primary neural stem cells (NSCs) (E14.5). However, apoptotic NSCs were significantly increased with $Ti_3C_2T_x$ concentrations above 25 µg mL^{-1}, supporting the dose-dependent toxicity reported previously. The study verified its findings with live/dead staining, LDH assays, and TEM, strengthening the investigation by indicating the nanosheets were internalised, compromising cell integrity[199]. These conclusions were consistent with several studies that propose that the cytotoxicity of $Ti_3C_2T_x$ is due to reactive oxygen species (ROS) production[200–202]. ROS or oxidative stress occurs when oxygen species and free radicals exceed the cell's ability to respond via its natural anti-oxidant defence system, causing protein and DNA damage, leading to cell death. In human skin malignant melanoma cells (A375), 89 % ROS production was observed when compared to the controls, whereas the non-cancerous cell line (HaCaT) produced 29 %. The authors suggest that these apparent differences in ROS production could be attributed to the differences in the kinetics of intracellular biochemical processes between the relative cell lines[198].

In addition to concentration and cell line dependencies, MXene surface properties are believed to influence ROS generation and hence toxicity[10,203]. Jastrzebska *et al.*[204] investigated $Ti_3C_2T_x$ oxidation as a function of cytotoxicity to better understand how post-treatments such as sonication influence the mechanism of toxicity. The *in vitro* study investigated three different $Ti_3C_2T_x$ types, the first pristine (AS-MX), the second slightly oxidised (SO-MX) through mild sonication and the third thermally oxidised

(TO-MX) through mild sonication heated to 60 °C. Cancer and non-malignant cell lines were used and repeatedly demonstrated selective toxicity towards the cancerous cell lines in viability and ROS investigations, with TO-MX the most lethal at a lower dose of 62.5 mg L^{-1}. XPS data revealed greater Ti_2O_3 on the TO-MX surface, relating directly to the higher degree of toxicity for this $Ti_3C_2T_x$ batch. In another study, collagen-modified $Ti_3C_2T_x$ increased cellular survival compared to pristine $Ti_3C_2T_x$. An MTT assay demonstrated that the reduced cell viability of the modified $Ti_3C_2T_x$ was negligible over the concentration range (0 – 125 mg L^{-1}). Furthermore, a significant decrease in ROS production was observed for the modified $Ti_3C_2T_x$ compared to the pristine $Ti_3C_2T_x$. The addition of collagen reduced cell toxicity by reducing oxidative stress[200].

The literature indicates that the biocompatibility profile of $Ti_3C_2T_x$ is complex and is governed by several factors such as cell line, concentration, and surface functional modifications[205]. Also, variability in study assay protocols could influence results since $Ti_3C_2T_x$ can act as a reductant and can interfere with some colourimetric assays to produce a false positive result in studies not including a $Ti_3C_2T_x$ only control[206]. $Ti_3C_2T_x$ has not been tested using ophthalmic modelling strategies and the interaction of these materials with lens epithelial cell cytotoxic and inflammatory pathways linked to PCO has yet to be investigated. Therefore, before developing the nanomaterial for AIOL design, initial ophthalmic biocompatibility should be investigated.

3.1.3 Aim

Early biomedical studies using MXenes suggest that $Ti_3C_2T_x$ is a compatible material. However, there is some variability in findings across studies using different cell types and the impact of $Ti_3C_2T_x$ on capsular bag lens epithelial cell physiology has yet to be investigated. Furthermore, no ocular models suitable for assessing the biocompatibility of $Ti_3C_2T_x$ within an AIOL device currently exist. The work presented in this chapter aims to evaluate the cytocompatibility and inflammatory profile of a $Ti_3C_2T_x$ coating on an IOL using a human lens epithelial cell (HLE) model following ISO 10993 for the biological evaluation of medical devices, their materials and/or extracts. It will address the hypothesis that the $Ti_3C_2T_x$ coated IOLs have no significant detrimental impact on HLE cell viability and do not exacerbate inflammation and oxidative stress pathways linked to negative outcomes following IOL surgical implantation. The objectives are:

1. To measure the impact of $Ti_3C_2T_x$ coated IOLs on the cell viability characteristics of a human lens epithelial lens cell line.
2. To investigate the potential upregulation of oxidative stress pathways in a monocytic cell line through measurement of ROS generation following exposure of cells to $Ti_3C_2T_x$ coated IOLs.
3. To investigate the propensity for $Ti_3C_2T_x$ coated IOLs to upregulate the secretion of pro-inflammatory markers known to induce inflammation within the capsular bag following cataract surgery.

3.2 Materials and methods

3.2.1 Materials

- Mouse embryo fibroblast (3T3) cell line (NIH-3T3, LGC Standards American Type Culture Collection (ATCC) CRL-1658, UK)
- Human lens epithelial (HLE) cell line (B-3, LGC Standards ATCC CRL-11421, UK)
- Human peripheral blood monocyte (THP-1) cell line (LGC Standards ATCC TIB-202, UK)
- Dulbecco's Modified Eagle Medium (DMEM) (Gibco 41960-029, UK)
- Minimum Essential Media (MEM) (Gibco, UK)
- Roswell Park Memorial Institute 1640 Medium (RPMI) (Gibco 11875-093, UK)
- Fetal bovine serum (FBS) (Sigma Aldrich F0804, UK)
- Non-essential amino acids (NEAA), (Gibco, 11140050, UK)
- Phosphate buffered saline (PBS) (Oxoid BR0014, UK)
- Trypsin-EDTA (0.25%) (Gibco 25200-056, UK)
- Trypan Blue stain (0.4%) (Gibco 15250-061, UK)
- CellTiter 96 Aqueous One Solution Cell Proliferation Assay kit (Promega Corporation G5421, UK)
- Dibutyltin maleate (Hydro Polymers Ltd, UK)
- CytoTox 96 Non-Radioactive Cell Proliferation Assay kit (Promega Corporation G3580, UK)
- Calcein, AM (Sigma Aldrich, UK)
- Penicillin Streptomycin (Fisher Scientific, UK)

- 2', 7'-Dichlorofluorescein diacetate (DCFH-DA) (Sigma Aldrich D6883, UK)
- Hydrogen peroxide (H_2O_2), 30 % purity (Fisher Scientific, UK)
- Opaque walled 96-well plate (Corning CLS3610, UK)
- High affinity binding 96-well plate for enzyme-linked immunosorbent assay (ELISA) (Fisher Scientific 95029330, UK)
- IL-6 ELISA kit (BD OptEIA 555220, UK)
- IL-8 ELISA kit (BD OptEIA 555244, UK)
- TNF-α ELISA kit (BD OptEIA 555212, UK)
- Lipopolysaccharide from *E. coli* O55:B5 (Sigma Aldrich L6529, UK)
- Substrate reagent (BD Opteia 555214, UK)

3.2.2 Cell culture conditions

Cell culture was performed in a Class II biological safety cabinet under aseptic conditions. Mouse embryo fibroblast (3T3), Human lens epithelial (HLE), and Human peripheral blood monocyte (THP-1) cell lines were used. 3T3 cells were grown in Dulbecco's Modified Eagle Medium (DMEM), HLE cells were grown in Minimum Essential Media (MEM) and THP-1 cells were grown in Roswell Park Memorial Institute 1640 Medium (RPMI). The cell lines were stored in liquid nitrogen until required. The frozen cultures were thawed by gentle agitation in a 37 °C water bath, then immediately transferred to a centrifuge tube containing 9 mL of the cell lines required growth medium and centrifuged for 10 minutes (3T3 at 500 *g*, HLE and THP-1 at 125 *g*). The cell pellets were resuspended in 5 mL of fresh media, seeded in 25 cm^2 culture flasks, and incubated at 37 °C at 5 % CO_2 until confluent. Media was replaced when necessary.

3.2.2.1 3T3 cell culture

3T3 cells grown with DMEM containing 10 % (v/v) fetal bovine serum (FBS) in 80 cm^2 flasks. Once 80 % confluent, the cells were passaged. The spent media was aspirated off, and the cells were rinsed with phosphate buffered saline (PBS) to remove any debris. The cells were incubated with 4 mL of trypsin-EDTA at 37 °C at 5 % CO_2 to detach from the flask. This was confirmed with optical microscopy (Carl Zeiss Primovert, UK). 8 mL of DMEM was added to the flask to prevent further trypsinisation. The cell suspension was collected and centrifuged at 500 g for 5 minutes. The supernatant was aspirated, the pellet resuspended in 1 mL of DMEM and reseeded in fresh flasks in the ratio of 1:10. The flasks were incubated at 37 °C at 5 % CO_2 and kept horizontal.

Cell number was calculated using a haemocytometer. A portion of the cell suspension was diluted in PSB, and then 10 µL was transferred to the haemocytometer. The cells were counted and averaged to calculate the cell number shown in equation (3.1).

$$Cell\ number\ (cells\ mL^{-1}) = mean\ cell\ count\ \text{x}\ dilution\ factor\ \text{x}\ 10^4 \qquad (3.1)$$

3.2.2.2 HLE cell culture

HLE cells were grown with MEM, supplemented with 20 % (v/v) fetal bovine serum (FBS) and 1% non-essential amino acids (NEAA), in 80 cm^2 flasks. At 80 % confluence, the cells were passaged. The spent media was aspirated, and cells were washed twice with PBS. 2 mL of trypsin was incubated at 37 °C at 5 % CO_2. Once the

cells had detached from the flask, 4 mL of MEM was added. The suspension was centrifuged for 5 minutes at 125 *g*. The pellet was redispersed in 1 mL of MEM, and a portion of the cell suspension was diluted to be counted using equation (3.1). Cells were reseeded 1:10 in new flasks and incubated horizontally at 37 °C at 5 % CO_2.

3.2.2.3 THP-1 cell culture

THP-1 cells were grown in RPMI with 10 % (v/v) FBS, and the media was topped up by 10 mL on a 3 to 4-day cycle. Cells were passaged when the concentration reached 8 x 10^5 cells mL^{-1}. The cell suspension was collected and centrifuged at 125 *g* for 5 minutes. The pellet was resuspended in 1 mL of RPMI, and a portion diluted in a trypan blue stain to be counted. The cell concentration was calculated using equation (3.1). The cells were reseeded at 4 x 10^5 cells mL^{-1} and incubated at 37 °C at 5 % CO_2 vertically.

3.2.3 Preparation of leachate material

Commercially available IOLs were spin-coated with the MILD method synthesised and delaminated $Ti_3C_2T_x$, described in chapter 2 (2.2.4.2). The coated IOLs were UV sterilised for 1 hour on each side. The IOLs were placed into wells of a 48 well plate with 250 µL of growth medium and then incubated for 24 hours at 37 °C at 5 % CO_2. Following incubation, the leachate media was collected in individual Eppendorf tubes for use as stated in the subsequent assessments. The protocol was repeated for uncoated IOLs as a negative control for the assays.

3.2.4 Cell viability of 3T3 and HLE cells exposed to coated IOLs

The cell viability of $Ti_3C_2T_x$ coated IOLs was assessed using the CellTiter 96 Aqueous One Solution Cell Proliferation Assay kit (MTS) performed on 3T3 and HLE cell lines. The MTS assay allows the quantification of cell viability when a tetrazolium compound is reduced to formazan. NADPH/NADH produced by dehydrogenase enzymes in metabolically active cells reduces the MTS reagent into a coloured formazan product that is soluble in tissue culture medium. The quantity of formazan produced is measured by reading absorbance at 490 nm and is directly proportional to the number of living cells. This assay used material leachate of the coated IOLs and uncoated IOLs that were prepared as described above. Dibutyltin maleate (tin maleate) was used as a positive control owing to its reproducible cytotoxic response[207]. Disks were cut to a surface area comparable to that of the IOLs, and the leachate was prepared following the same protocol as the IOLs. Each cell line was passaged by standard trypsinisation, plated at a seed density of 1 x 10^4 cells per well in a 96 well plate, and incubated at 37 °C, 5 % CO_2 for 24 hours. Following incubation, the spent media was removed from the cells and replaced with 100 µL of the leachate media and incubated at 37 °C, 5 % CO_2 for a further 24 hours. The MTS reagent was prepared according to the manufacturer's instructions, and 100 µL was used to replace the spent leachate media. After a 2-hour incubation of 37 °C, 5 % CO_2, with the MTS reagent, the absorbance at 490 nm was recorded using an ELx800 Universal Microplate reader (Biotek, USA). In each experiment, the conditions were repeated 6 times then the experiment was repeated in triplicate. Cell number was calculated from a standard curve of cell density against absorbance at a wavelength of 490 nm. Cell viability (%) was calculated relative to the cell only control using equation (3.2), where A is the

absorbance of cells exposed to the material or leachate and B is the absorbance of untreated cells (control).

$$Cell\ viability\ (\%) = \frac{A}{B} \text{ x } 100 \qquad (3.2)$$

3.2.5 Cytotoxicity of 3T3 and HLE cells exposed to coated IOLs

Cytotoxicity of the $Ti_3C_2T_x$ coated IOLs was assessed using the CytoTox96 non-radioactive cytotoxicity assay measuring LDH release by lysed cells. When cells are damaged, LDH is released into the culture medium and catalyses the reduction of NAD to NADH. A tetrazolium salt is reduced to a red formazan product, proportional to the number of lysed cells. 3T3 and HLE cells were passaged by standard trypsinisation, plated at a seed density of 1 x 10^4 cells per well in a 96 well plate, and incubated at 37 °C, 5 % CO_2 for 24 hours. Leachate media was prepared and introduced to the seeded cells described in the previous section, and plates were incubated at 37 °C, 5 % CO_2 for 24 hours. 10 µL Lysis solution was incubated with cells to establish maximum LDH release, and plates were then incubated for 45 minutes, 50 µL of media from each well were transferred to a new plate and 50 µL of the substrate mix, prepared according to the manufacturer's instructions, were then added to each well. The plate was incubated at room temperature in the dark for 30 minutes before adding 50 µL of the stop solution to each well. The absorbance at a wavelength of 490nm was recorded using an ELx800 Universal Microplate reader (Biotek, UK). In each experiment, the conditions were repeated 6 times then the experiment was repeated in triplicate. Cytotoxicity (%) was calculated using equation (3.3) relative to the maximum LDH released positive control. A is the LDH

absorbance of cells exposed to the material or leachate and B is the LDH absorbance of the lysed cell control.

$$Cytotoxicity\ (\%) = \frac{A}{B} \text{x}\ 100 \qquad (3.3)$$

3.2.6 Calcein-AM staining of 3T3 cells on coated IOLs

Sterilised, coated, and uncoated IOLs were placed into a 48 well plate. 3T3 cells at a seed density of 2.3 x 10^4 cells per well were incubated to investigate cell adhesion via live staining with calcein-AM. Following incubation of 24 hours at 37 °C, 5 % CO_2, 50 µg of calcein-AM was added in 50 µL of DMSO. 20 µL of the calcein-AM/DMSO solution was added to 10 mL media (DMEM with 10 % FBS and 1 % Penicillin Streptomycin) to produce a 2 µM concentration solution. The spent media was aspirated from the wells, and 250 µL of the stain solution was added to each well and incubated for 30 minutes at 37 °C, 5 % CO_2. The wells were imaged on a confocal microscope (Leica Inverted Confocal Microscope, UK), with excitation at 488 nm and emission 515 nm, argon laser. Cell number across each of 3 fields of view was captured using 6 repeats for each control. Images were processed ImageJ to determine cell number. The following macro was set up to analyse the images:

run("Subtract Background...", "rolling=15 light"); run("32-bit"); setOption("BlackBackground", false); run("Convert to Mask"); run("Watershed"); run("Analyze Particles...", "size=0.01-Infinity show=Outlines display exclude clear summarize");

Each image was compared to the imageJ processed file to confirm that only cells had been accounted for.

3.2.7 Oxidative stress in THP-1 monocytes

ROS generation of THP-1 cells was investigated when exposed to $Ti_3C_2T_x$ coated IOLs for 1-hour and 24-hour. Oxidative stress was evaluated with dichloro-dihydro-fluorescein diacetate (DCFH-DA), a dye that measures the activity of ROS generation in cells. ROS is increased when cells are stressed and therefore is a good measure of material compatibility to mammalian cells. ROS oxidises the non-fluorescent DCFH to DCF that is highly fluorescent and can be readily detected. The coated and uncoated IOLs were sterilised and placed in a 48 well plate. 3 x 10^5 cells mL^{-1} were stained with DCFH-DA at a working concentration of 50 mM for 40 minutes. The cells were washed twice with warm PBS. The cells were redispersed in FBS free RPMI. 300 µL of the cell suspension was added to each well. Hydrogen peroxide (H_2O_2) was used as a positive control as it induces ROS production in cells. A concentration of 0.8 mM of H_2O_2 was added to a cell only condition at time = 0 hours for the 1-hour study and at time = 23 hours for the 24-hour study. The plates were incubated at 37 °C, 5 % CO_2 for their respective time periods. After incubation, 100 µL of the media was transferred into an opaque walled 96 well plate, and fluorescence was measured using a microplate reader (Biotek Synergy HT, UK) at an excitation/emission wavelength 485 nm/528 nm. In each experiment, the conditions were repeated 6 times then the experiment was repeated in triplicate.

3.2.8 Immune response

Inflammatory marker production was quantified following incubation of coated IOLs with monocyte THP-1 cells using an enzyme-linked immunosorbent (ELISA) assay for IL-6, TNF-α, and IL-8. An ELISA is a technique to quantify proteins, antibodies

and peptides. Samples are exposed to the antibody coated on the plate, and the specific antigen under investigation will bind. An additional antibody is introduced, sandwiching the antigen. A solute is added, and the resultant colour is directly proportional to the species present. The absorbance is measured at 450 nm. The coated and uncoated IOLs were sterilised and transferred to 48 well plates. A 1 x 10^6 cells mL^{-1} cell suspension of the THP-1 cells was prepared. 300 µL of the cell suspension was added to each of the control wells and the coated and uncoated IOL wells. 30 µL of lipopolysaccharide (LPS) at a concentration of 20 µg mL^{-1} was added to control cells as a positive control at time = 0 hours. The plate was incubated at 37 °C, 5 % CO_2 for 24 hours. Media from each of the wells was transferred to Eppendorf tubes and centrifuged with a Heraeus™ Pico™ 17 Microcentrifuge (Thermo Fisher Scientific, UK) at 800 *g*. The conditions were analysed using BD ELISA kits, for IL-6, TNF-α and IL-8, according to the manufacturer's protocol. The following dilutions were used for IL-6, TNF-α and IL-8, respectively, 1 in 5, 1 in 5 and 1 in 600. Each condition was repeated 6 times within the experiment, in addition, duplicate repeats of each sample were included in each ELISA, and the experiments were repeated in triplicate.

3.2.9 Control conditions used assays

Table 3-1 – Details of the controls used in the various biocompatibility assays.

Assay	Negative control	Positive control
MTS	IOL only	Tin maleate
LDH	IOL only	Tin maleate
Live staining	IOL only	Tin maleate
ROS activity	IOL only	Hydrogen peroxide
ELISA	IOL only	Lipopolysaccharide

3.2.10 Statistical analysis

The data was processed using GraphPad Prism 7.05 (GraphPad Software Inc., USA) and is reported as mean ± SD, where n = 3. Statistical analysis of the data was evaluated using either a one- or two-way ANOVA, where necessary, followed by a Dunnett post hoc test. Statistical significance was calculated with a p-value less than 0.05.

3.3 Results

Under ISO 10993 the standard procedure for the biological evaluation of medical devices, their materials and/or extracts, cell culture techniques were used to indicate the impact of $Ti_3C_2T_x$ on the ocular environment. This was evaluated through a range of biological assays to determine if coated IOLs have a detrimental impact on cell viability and do not exacerbate inflammation and oxidative stress pathways linked to negative outcomes following IOL surgical implantation. A range of cell lines were explored including the human lens epithelial (HLE) cell line, B-3. The mouse embryo fibroblast cell line 3T3 was also included, although this cell line is not associated with the ocular environment it is widely used in biocompatibility cell culture modelling[208–210]. The human peripheral blood monocyte (THP-1) cell line was selected because of its functional properties, such as the production of pro-inflammatory markers and previous use in MXene studies[211,212].

3.3.1 Cell viability of 3T3 and HLE cells exposed to coated IOLs

3.3.1.1 Cell viability (MTS)

The MTS assay was used to measure viable 3T3 (***Figure 3-1** (a)*) and HLE (***Figure 3-1** (b)*) cells following a 24 hour incubation with $Ti_3C_2T_x$ coated IOL leachate media. This is a standard cell viability assay used to indicate the toxicity in a cell culture technique. No significant difference was observed in cell viability for either cell line comparing $Ti_3C_2T_x$ coated IOLs with the cell only and the uncoated IOL only ($p < 0.05$). In contrast, positive control, tin maleate, significantly reduced viability for 3T3 ($p < 0.0001$) and for HLE ($p < 0.001$) compared to the cell only control.

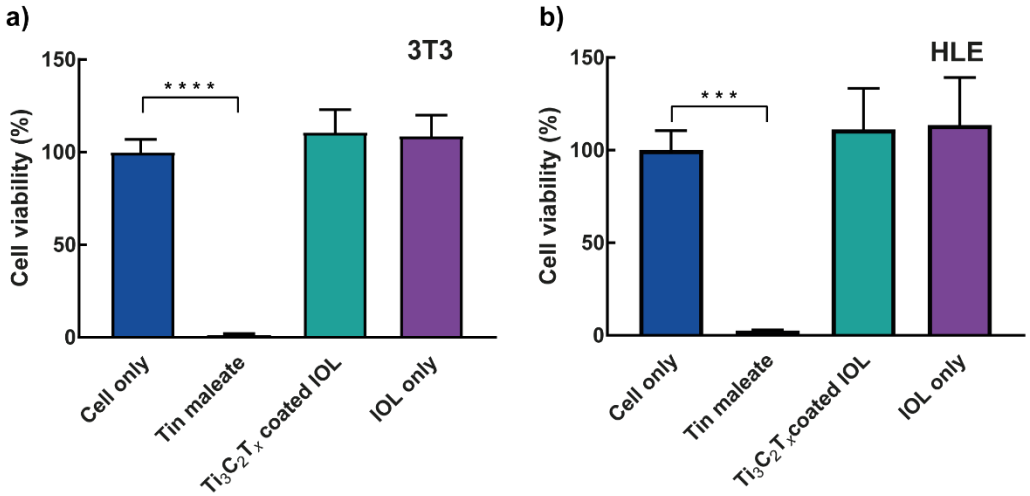

Figure 3-1 – Cell viability (%) via MTS assay when (a) 3T3 and (b) HLE cell lines were exposed to material leachates $Ti_3C_2T_x$ coated IOL, with negative control, IOL only, and positive control, tin maleate. One-way ANOVA, (mean ± SD, n = 3, **** $p < 0.0001$, *** $p < 0.001$).

3.3.1.2 Cell number (MTS)

A calibration curve is shown in ***Figure 3-2*** **(a)** of the cell viability (MTS data) of HLE cells. Linearity of absorbance and cell number is demonstrated. Cell numbers were established as follows, for the cell only $3.5x10^4 \pm 5.1x10^3$, for the $Ti_3C_2T_x$ coated IOLs $3.8x10^4 \pm 5.4x10^3$, and for the uncoated IOL, only $4.1x10^4 \pm 5.4x10^3$. The positive control, tin maleate, a negative value was calculated with the equation from the calibration curve as -1129 ± 118. There is no significant difference in cell number when comparing the $Ti_3C_2T_x$ coated IOLs with the cell only and the uncoated IOL only. However, there is a significance with a *p*-value < 0.0001 between tin maleate and the cell only.

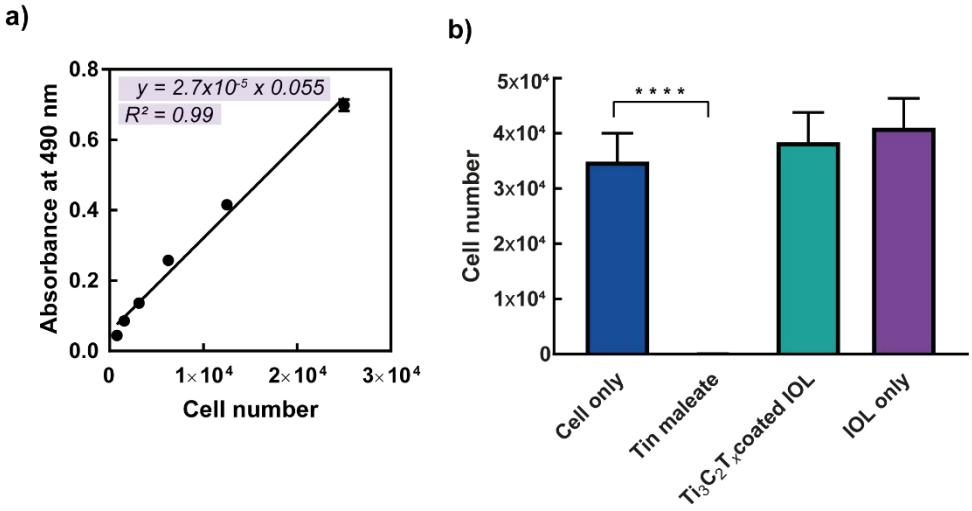

Figure 3-2 – Cell viability measured via an MTS assay, (a) calibration curve of absorbance versus cell number, with a linear relationship where $y = 2.7 \times 10^{-5} \times 0.055$, $R^2 = 0.99$. (b) Cell number of HLE cells exposed to material leachates $Ti_3C_2T_x$ coated IOL, with negative control, IOL only, and positive control, tin maleate. One-way ANOVA, (mean ± SD, n = 3, **** $p < 0.0001$).

3.3.2 Cytotoxicity of 3T3 and HLE cells exposed to coated IOLs

The LDH assay is a widely accepted method for the quantification of cytotoxicity. Following 24-hour incubation of 3T3 (***Figure 3-3*** (a)) and HLE (***Figure 3-3*** (b)) cells with leachates $Ti_3C_2T_x$ coated IOL, with negative control, IOL only, and positive control, tin maleate. There was no significant difference in cytotoxicity of the $Ti_3C_2T_x$ coated IOLs or the uncoated IOL control compared to the cell only control. In contrast, the positive control, tin maleate, displayed 93.5 ± 5.8 % cytotoxicity compared to the cell only control with the 3T3 cell line, and for the HLE cells, tin maleate showed 96.4 ± 10.8 % cytotoxicity, with a significance level of $p < 0.0001$.

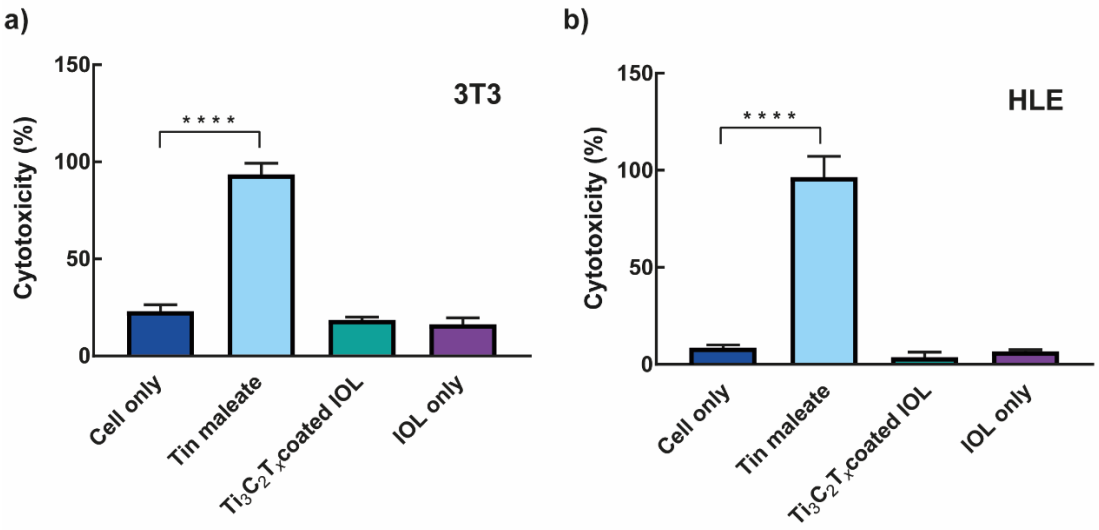

Figure 3-3 – LDH cytotoxicity assay to assess the impact of $Ti_3C_2T_x$ coated IOL leachate on 3T3 and HLE cell lysis and release of LHD compared to IOL only and tin maleate leachate controls. One-way ANOVA, (mean ± SD, n = 3, **** $p < 0.0001$).

3.3.3 Calcein AM staining

Calcein AM was used to observe the cells grown directly onto the $Ti_3C_2T_x$ coated IOLs. 3T3 cells were stained with calcein-AM after a 24-hour incubation in direct

contact with the coated IOLs and the controls. No significant difference in cell count was observed for $Ti_3C_2T_x$ coated IOLs with cell only in a one-way ANOVA (***Figure 3-4***). The cell count for each condition was found to be cell only 144 ± 33, tin maleate 17 ± 7, $Ti_3C_2T_x$ coated IOL 113 ± 41, IOL only 101 ± 36. In contrast, significance at $p < 0.0001$ was demonstrated for tin maleate compared to cell only. Representative images of the analysis are shown in ***Figure 3-5*** of the 3T3 cells on the coated IOLS, stained positive for calcein-AM, which fluoresces green. The positive control used in the assay, tin maleate, shown in ***Figure 3-5*** *(c)* demonstrates the lack of viable cells, hence toxicity of the material.

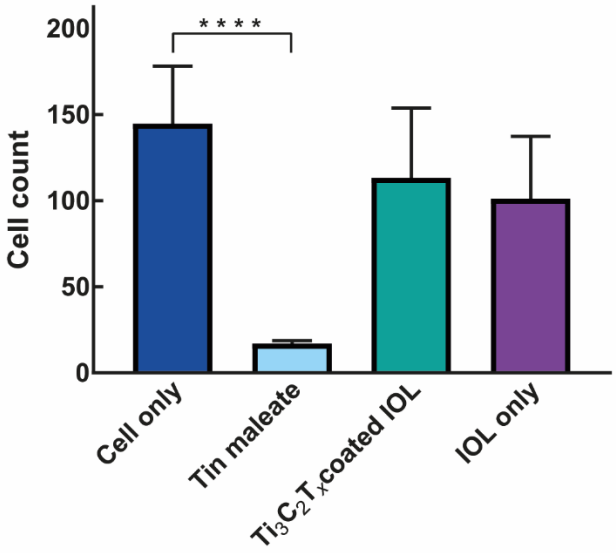

Figure 3-4 – Cell count of calcein-AM stained 3T3 cells following a 24-hour incubation with $Ti_3C_2T_x$ coated IOLs, uncoated IOLs and tin maleate. Statistical analysis by one-way ANOVA, (mean ± SD, n = 6, **** $p < 0.0001$).

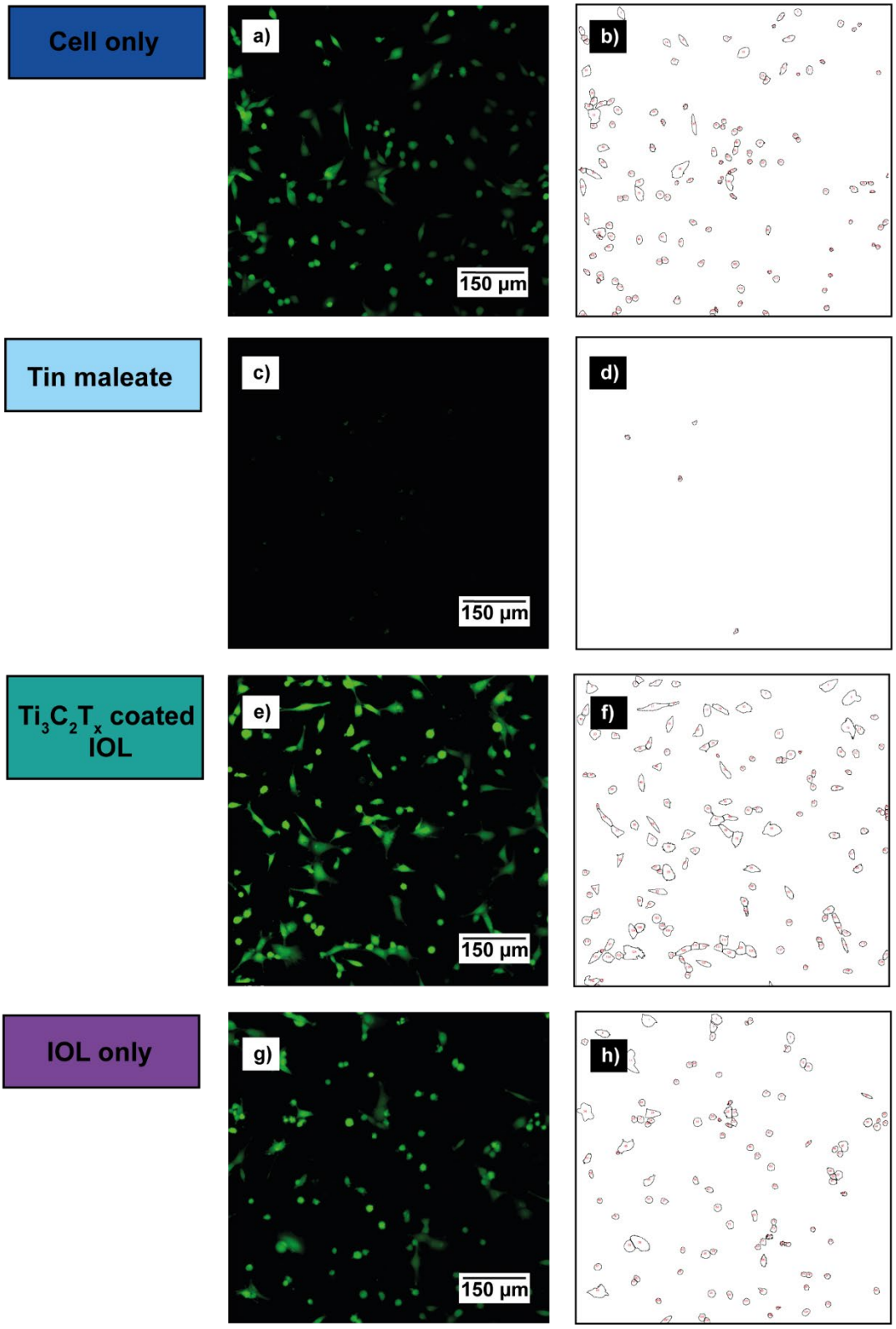

Figure 3-5 – Representative images of calcein-AM staining for viable cells with 3T3 cells in direct contact with (e) $Ti_3C_2T_x$ coated IOLs, (a) cell only (control), (g)

uncoated IOLs (negative control) and (c) tin maleate (positive control) imaged with a confocal microscope (Leica Confocal Microscope, UK) excitation/emission 488/515, argon laser. Image processing with ImageJ (f) $Ti_3C_2T_x$ coated IOLs, (b) cell only, (h) uncoated IOLs and (d) tin maleate (see methods for image processing detail).

3.3.4 Oxidative stress

Following THP-1 cells incubation with $Ti_3C_2T_x$ coated IOLs to evaluate if the coating influenced ROS generation at 1 and 24 hours, no significant difference was observed in ROS production at the 1 hour time period compared to $Ti_3C_2T_x$ coated IOLs with the uncoated IOL and cell only (***Figure 3-6***). This was in contrast to the positive H_2O_2 control, which significantly increased ROS production compared to the cell only control, where $p < 0.0001$. ROS production for the coated IOL was 3.6 ± 0.6 % and the IOL control was 4.0 ± 0.6 %. Similarly, for the 24-hour time period, a significant difference ($p < 0.0001$) was observed between the positive control when compared to the cell only. ROS production for the coated IOLs was 35.0 ± 7.8 %, and the cell only was 33.1 ± 4.4 %. This is a widely used method in the measurement of free radical generation.

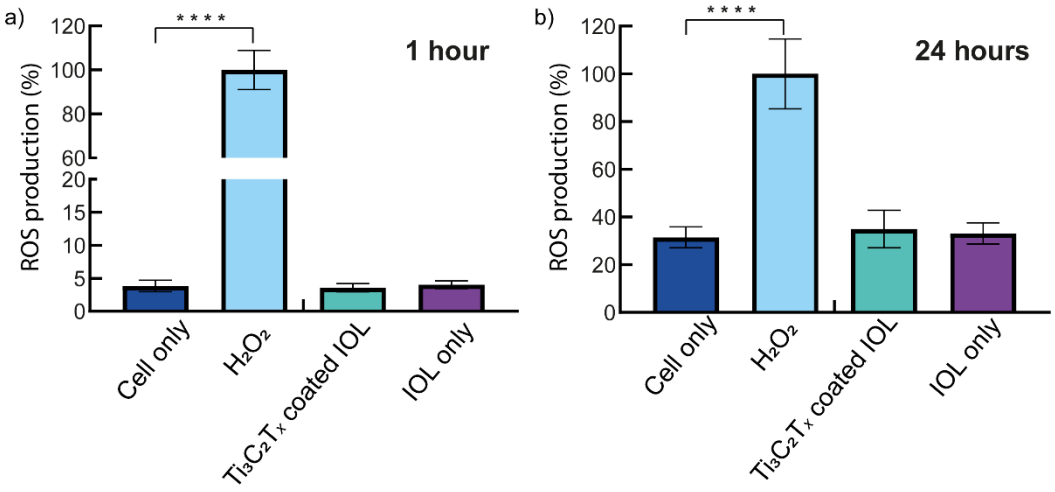

Figure 3-6 – Dichloro-dihydro-fluorescein diacetate (DCFH-DA) assay to assess the propensity of $Ti_3C_2T_x$ coated IOL to upregulate the production of ROS using a monocyte THP-1 cell line at 1 and 24 hours. Statistical test via one-way ANOVA (mean ± SD, n = 3, **** $p < 0.0001$)

3.3.5 Immune response

An ELISA is a commonly used assay for the detection and quantification of antigens, here it was used to explore the activity of pro-inflammatory markers, IL-6, IL-8 and TNF-α. No significant upregulation of each of the inflammatory markers was observed following incubation of a THP-1 monocytic cell line with $Ti_3C_2T_x$ coated IOLs when compared to uncoated and cell only controls (***Figure 3-7***). For each of the cytokines measured, a negligible concentration was detected even using undiluted test samples in additional analysis. In contrast, a significant upregulation of IL-6, IL-8 and TNF-α production occurred following stimulation of THP-1 cells with LPS over time.

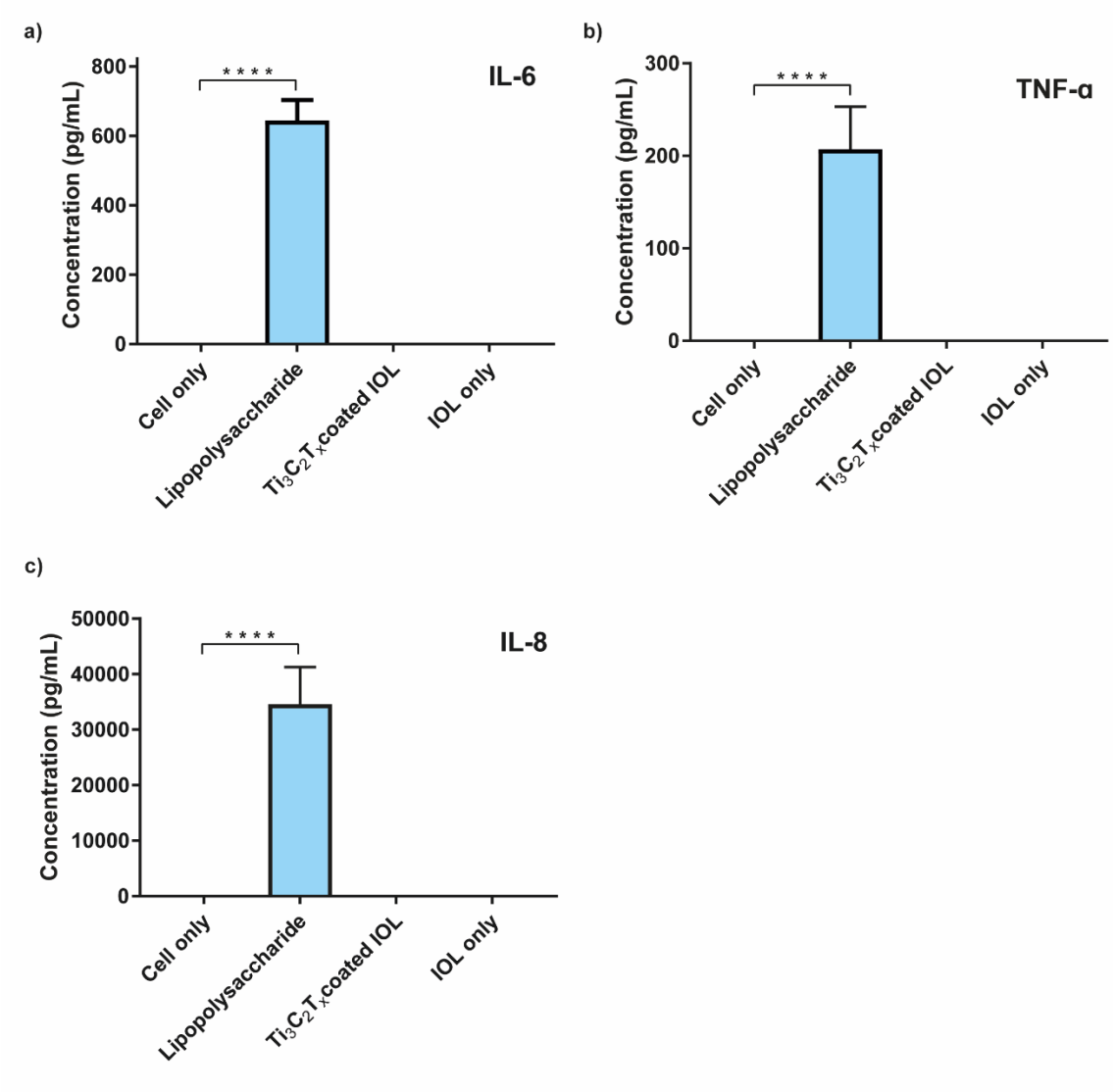

Figure 3-7 – ELISA data of (a) IL-6, (b) TNF- α and (c) IL-8 for $Ti_3C_2T_x$ coated IOLs with THP-1 cell line. Statistical test via one-way ANOVA, (mean ± SD, n = 3, **** $p < 0.0001$).

3.4 Discussion

The research described within this chapter assessed the biocompatibility of the nanomaterial $Ti_3C_2T_x$ as an IOL coating for use within the capsular bag and ocular environment. Many factors, such as cell type, concentration, and surface

modifications, have been found to influence toxicity indicating the importance of developing appropriate cell models to assess ocular biocompatibility. This is the first study to consider the use of $Ti_3C_2T_x$ as a transparent conductive electrode for use in the anterior eye and therefore considered lens epithelial cell interactions as an early indication of biocompatibility issues[199,200,205,213]. The cytotoxicity of $Ti_3C_2T_x$ coated IOLs was evaluated via cell viability and toxicity studies on 3T3 and HLE cell lines through MTS and LDH assays. The toxicity investigation was supported via a live cell count study with calcein-AM staining. The oxidative stress pathways of monocytic THP-1 cells were evaluated following $Ti_3C_2T_x$ coated IOL exposure. Cytokine-induced inflammation was assessed to aid in producing a biocompatibility profile of the $Ti_3C_2T_x$ coated IOLs for the ocular environment to further the development of the AIOL design.

3.4.1 Effect on cell viability and cytotoxicity

The MTS assay found no significant difference in cell viability of both 3T3 and HLE cell lines incubated with $Ti_3C_2T_x$ coated IOLs compared to the cell only, and IOL only controls shown in ***Figure 3-1*** and ***Figure 3-2***. The results indicated that the coating did not induce cytotoxic effects (24 hour, $p > 0.05$). Similarly, Jastrzebska *et al*.[198] used an MTT assay to demonstrate cell viability over a range of concentrations of $Ti_3C_2T_x$ colloidal solutions. The study included two cancerous and two normal cell lines, where viability decreased with increasing concentration of $Ti_3C_2T_x$ and was dependent on the cell line. While higher toxicity was observed in the cancerous cell lines, over the 0 – 500 mg L^{-1} range, the viability of the normal (HaCaT) cell line did not drop below 70 %. According to ISO 10993-5, reducing viability beyond 30 % is

considered a toxic effect[214]. The $Ti_3C_2T_x$ coated IOL leachate did not provoke a toxic effect with either of the included cell lines in the current study confirming the results of previous studies using non-cancerous cell lines and indicating biocompatibility using tissue-appropriate cell types.

The LDH assay supported the MTS analysis through cell lysis measurements to evaluate the induction of $Ti_3C_2T_x$ coating leachate on necrotic cell death. The LDH assay, shown in ***Figure 3-3***, demonstrated no significant cytotoxic effects of the $Ti_3C_2T_x$ coated IOLs when compared to cell only and IOL only controls. The data is in good agreement with the literature, where $Ti_3C_2T_x$ did not significantly impact 3T3 fibroblast cell viability[197]. The results support those for the MTS assay demonstrating the cytocompatibility of the $Ti_3C_2T_x$ coatings and their suitability for contact with ocular cell types. Interestingly, Rasool *et al.*[127] used LDH to present antibacterial properties of $Ti_3C_2T_x$, where a dose-dependent relationship was found following direct exposure of colloidal $Ti_3C_2T_x$ solutions to bacterial species *Escherichia coli* (*E. coli*) and *Bacillus subtilis* (*B. subtilis*). LDH production by the exposed cells increased with increasing $Ti_3C_2T_x$ concentration. The study demonstrated cytotoxicity levels of 38.41 % and 55.24 % for both *E. coli* and *B. subtilis*, which agrees with the previous study and highlights further the issue of cell line/type-dependent cytotoxicity. SEM and TEM showed clear membrane disruption consistent with the LDH analysis. The authors attributed the potential mechanism to oxidative stress[127].

The calcein-AM staining investigation assessed the biocompatibility of the lens coated surface in direct contact with 3T3 cells shown in ***Figure 3-4*** and ***Figure 3-5***. It is known that IOL surface interactions play a considerable role in uveal and capsular biocompatibility[42]. Following 24-hour incubation of the cells with $Ti_3C_2T_x$ coated

IOLs, no significant influence on cell proliferation was demonstrated with cells stained positive for calcein-AM growing across the surface of the coated and uncoated lenses but not over the tin maleate cytotoxic control. The images display regular morphology and growth, characteristic of a fibroblast 3T3 cell line. The toxicity evaluation supports the cytocompatibility of $Ti_3C_2T_x$ coated IOLs as no toxicity was induced.

3.4.2 Oxidative stress and pro-inflammatory activity

Although the cytotoxicity assessment supports the biocompatibility of $Ti_3C_2T_x$ coatings for use in the ocular, capsular bag environment, sub-lethal oxidative stress mechanisms may be upregulated to promote tissue damage despite no evidence of cell death. Oxidative stress is an imbalance of reactive oxygen species where the disturbance can adversely affect cells and surrounding tissue[215]. Non-adherent THP-1 monocyte cells were used for this investigation to determine if $Ti_3C_2T_x$ coated IOLs induced oxidative stress by measuring ROS activity. No significant difference in ROS production was observed when the cells were incubated with the $Ti_3C_2T_x$ coated IOLs for 1 and 24 hours compared to controls indicating no upregulation of oxidative stress pathways by $Ti_3C_2T_x$ (***Figure 3-6***). A previous study presented minimal loss in viability and high ROS production with cells in contact with $Ti_3C_2T_x$ for 24 hours. The authors concluded that cell viability would reduce if the interaction time between the cells and $Ti_3C_2T_x$ flakes was prolonged due to oxidative stress[198]. Here, cell viability and toxicity demonstrated with MTS, LDH and calcein-AM staining assays were evaluated over the same time period, and corroborate the non-toxic effect observed from the oxidative stress assay. Due to the solution processing technique, it is not

feasible to determine the concentration of $Ti_3C_2T_x$ that the cells are exposed to, which makes it challenging to compare to the literature.

In addition to the upregulation of oxidative stress pathways, the impact of the $Ti_3C_2T_x$ coatings on the upregulation of inflammatory cytokine production was also investigated. Surgical trauma following cataract treatment stimulates inflammatory mediators including IL-6, TNF-α, and IL-8 in residual lens epithelial cells and recruits monocytes from surrounding vasculature, although the capsular bag itself is avascular. The persistence and accumulation of inflammatory cytokines result in chronic inflammation, leading to postoperative complications, including PCO. The effect of non-adherent THP-1 monocyte cell incubation with $Ti_3C_2T_x$ coated IOLs on inflammatory cytokine production was therefore investigated to determine if $Ti_3C_2T_x$ caused upregulation of cytokine production and associated inflammatory pathways. No increase in the production of inflammatory cytokines, IL-6, TNF-α, and IL-8 by the cell line was observed in contrast to LPS stimulated positive controls indicating that the $Ti_3C_2T_x$ coatings are unlikely to promote additional inflammatory cytokine production following lens surgical insertion into the capsular bag environment (***Figure 3-7***). Ozulumba *et al.*[197] investigated the suppression of inflammatory cytokine stimulus by flakes over a range of $Ti_3C_2T_x$ concentrations using an *in vitro* THP-1 cytokine induction model and demonstrated a reduction in IL-6, IL-8 and TNF-α following $Ti_3C_2T_x$ incubation. It was suggested that a reduction in cytokine production by cells was a result of physical binding mechanisms and that cytokine binding occurred through $\pi - \pi$ stacking and hydrophobic bonds[197]. Therefore, in ocular environments, it may be possible to use $Ti_3C_2T_x$ coatings to aid in the wound healing response following the physical trauma of cataract surgery by inhibiting inflammatory

mediators. However, the concentrations required for effective inflammatory cytokine suppression may be greater than those necessary to maintain transparency for optical lens-based applications. One alternative consideration for IOL linked suppression of inflammatory pathways leading to PCO could consider anti-inflammatory drug intercalation within the $Ti_3C_2T_x$ layers for slow elution of drug over time.

3.5 Conclusion

In this chapter, the biocompatibility of $Ti_3C_2T_x$ coated lenses on interaction with human lens epithelial cells and inflammatory monocytes present in the capsular bag environment has been considered for the first time. No significant impact on cell viability or cytotoxicity was observed comparing $Ti_3C_2T_x$ (leachate) exposed cells to cell only and tin maleate cytotoxic controls. The coated IOLs did not stimulate an oxidative stress response in a monocyte THP-1 cell line compared to hydrogen peroxide stimulated controls indicating no upregulation of ROS-mediated inflammatory pathways by $Ti_3C_2T_x$ coated lenses. The coated lenses also did not upregulate the production of pro-inflammatory cytokines, IL-6, TNF-α, and IL-8 in THP-1 monocytes in comparison to LSP stimulated positive controls indicating no induction of key drivers of capsular bag lens epithelial cell inflammatory response following $Ti_3C_2T_x$ exposure. Whilst further studies should consider the use of capsular bag models to investigate the interaction of $Ti_3C_2T_x$ on specific pathways in PCO development and the impact of active, conductive materials on cell physiology this chapter provides an early indication that $Ti_3C_2T_x$ is a biocompatible nanomaterial for use in an AIOL design.

Chapter 4

4 *MXene and liquid crystal, refractive index modulating, proof-of-concept design*

4.1 Introduction

IOL technology research is motivated to restore the accommodative function of the crystalline lens. An AIOL aims to deliver a controlled, seamless, fast switching, and reversible change in focus from near to distant vision. Although, no current clinically available lens has achieved the goal of producing true accommodation. Current AIOL approaches such as axial displacement and shape-changing lenses utilise the existing mechanisms of the eye. However, they are limited in their development as they produce little to no accommodative amplitude and are associated with increased postoperative complications[55,62,63,67]. LC smart lenses have the potential to address lens accommodation towards the development of the next generation in AIOL technology and wearable optoelectronics.

4.1.1 Liquid crystal smart lenses

The recently proposed LC smart lenses exploit the electroactive behaviour of LCs[216]. The mechanism of these adjustable focus lenses relies on the refractive index modulation of an LC through external stimulation. Li *et al.*[217] designed LC-based glasses that adaptively change focus through an applied electrical potential. The glasses offer high optical transmittance, fast response time, and operate with low voltages for potential presbyopia treatment, correcting the age-related loss of near vision through tunable light refraction. LC-based contact lenses offer similar

possibilities. Several variations of material and design have been explored in their development. For instance, one group investigated an ITO coated curved lens design that gave 2.00 ± 0.25 dioptre (D) correction[218]. Though this lens demonstrates an important step towards achieving adaptive focus lenses for the ocular environment, some limitations regarding the flexibility of the device remain as ITO electrodes fracture easily, affecting lens conductivity and therefore durability. For that reason, electrode flexibility continues to be of significance for the development of wearable and optoelectronic devices to improve patient outcomes. Another study investigated graphene electrodes in combination with ITO electrodes for LC-based contact lenses[88]. Despite fabrication limitations, the use of graphene introduced nanomaterials for flexible optoelectronic applications, thus presenting two-dimensional materials as realistic candidates for flexible, transparent, and conductive applications.

In addition to presbyopia correction, LC-based lens technology has the potential to address the main drawback in IOL development which is the restoration of lens accommodation in cataract patients. Research has proposed the use of electronically variable LC lenses for IOL application. One design demonstrated up to 4 D of accommodation. However, this design presented similar ITO flexibility limitations. IOL flexibility has considerable importance demonstrated with the evolution in IOL material from rigid to foldable polymers. The flexibility of the IOL base material enables the lens to be implanted through smaller incisions. Brittle TCEs with minimal flexibility require larger incisions leading to more complex procedures, longer recovery times, and increased risk of postoperative complications. Therefore, MXenes' combination of mechanical strength, transparency, and high electrical

conductivity present suitable characteristics for LC-based AIOL design. Furthermore, the investigation of the two-dimensional transition metal carbide, $Ti_3C_2T_x$, as a TCE and bio-suitability within the ocular environment indicate the appropriateness of exploring this member of the MXene family for adjustable focus LC lens design.

4.1.2 Liquid crystals and their properties

LC smart lenses utilise the unique optical and electronic characteristics of LCs. The elongated structure of LC molecules or mesogens gives rise to their anisotropic behaviour, shown in ***Figure 4-1*** *(b)*. They flow similarly to a liquid with the orientational ordering of a crystalline solid[219]. The two main LC families are classified as lyotropic and thermotropic. Lyotropic exhibit a liquid crystalline state as a function of concentration when combined with a solvent. Whereas thermotropic LCs show anisotropy over a temperature range specific to their composition[220]. When heating and cooling thermotropic LCs, mesomorphic phase changes occur, which vary from material to material. These mesophases are characterised by their ordering: nematic, smectic, and cholesteric[221]. The nematic phase is the simplest form of LC phase, with long-range orientational order, the molecules align approximately parallel to one another, shown in ***Figure 4-1*** *(b)*. The molecules have a rigid core and flexible alkyl side chains that influence their orientation in a preferred direction. The average order is represented by a unit vector, known as the director '*n*', shown in ***Figure 4-1*** *(b)*[219]. The nematic LC phase behaves uniaxially with its centre of symmetry. Hence, the director's orientation can be manipulated through external stimuli such as mechanical, electric, or magnetic fields. The LC behaves differently depending on the initial orientation of the director relative to the applied field.

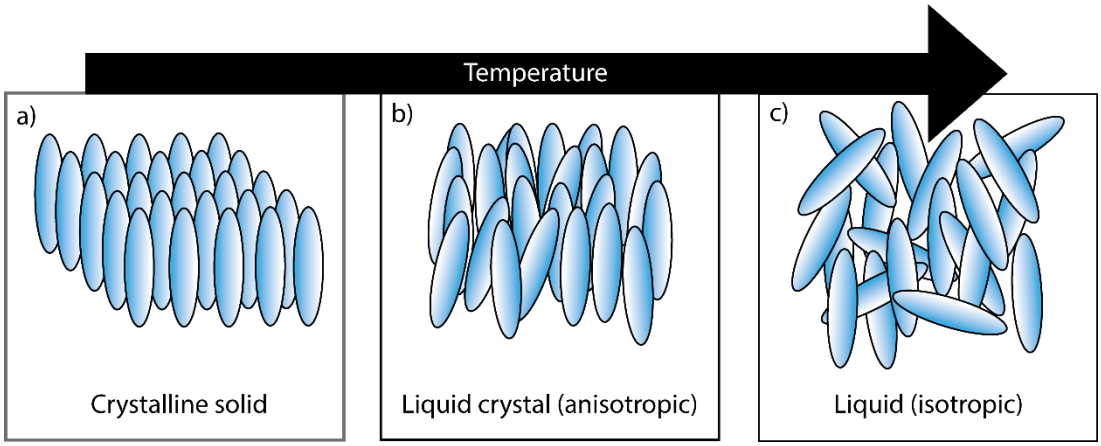

Figure 4-1 – Schematic of liquid crystal rod-like molecules demonstrating the stepwise transition from (a) a crystalline solid, (b) to a liquid crystal, (c) and an isotropic liquid upon heating. The degree of order decreases with increasing temperature transitioning from the crystalline solid state, past the melting point, to an anisotropic liquid crystalline state, overcoming the clearing point and moving to an isotropic liquid. The arrows demonstrate the orientational order of the phase, for liquid crystals, the average direction of the molecules is known as the director '*n*'.

Optoelectronic applications utilise the anisotropic characteristics of LCs. Their optical anisotropy results in birefringence, meaning they have double refraction. When light is incident on an LC, the wave splits into two orthogonally polarised components, known as the ordinary and extraordinary rays, demonstrated in ***Figure 4-2***. The differing refractive indices of the two rays indicate birefringence.

$$\Delta n = n_e - n_o = n_{\parallel} - n_{\perp} \tag{4.1}$$

The ordinary refractive index 'n_o' is independent of the orientation of the incident ray entering the LC[222]. Whereas the extraordinary refractive index 'n_e' is dependent on the angle between the incident ray and the direction of the director[223]. Positive birefringence, approximately 0.2, is necessary for most LC display applications[224].

Due to the temperature dependence of thermotropic LCs, birefringence decreases with increasing temperature as the nematic LC transitions to the isotropic liquid state, overcoming the clearing point and decreasing its degree of order. Moreover, birefringence depends on the LC's chemical composition and structure, which also influence the dielectric permittivity and elastic constants.

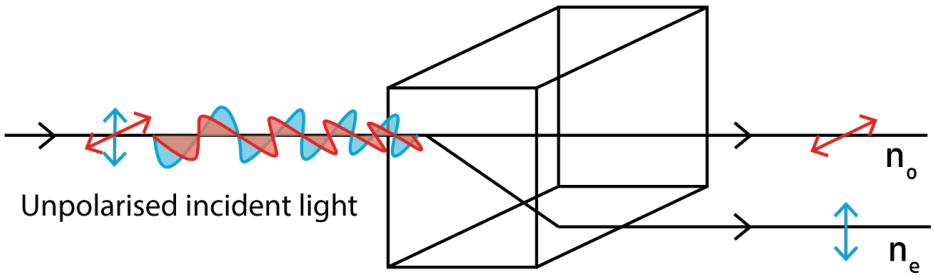

Figure 4-2 – Schematic representation of birefringence showing incoming unpolarised incident light through a birefringent medium that splits the light into the ordinary (n_o) and extraordinary (n_e) rays.

4.1.3 Optoelectronic liquid crystal applications

One of the most common applications to utilise the electronic light-modulating properties of nematic LCs are liquid crystal displays (LCDs), found in many everyday devices, including computer monitors, calculators, watches, and smartphones. LCDs are constructed of two glass panels with a thin layer of LC sandwiched between, forming the LC cavity[225]. The anisotropy allows molecular reorientation when an external electrical potential is applied. The glass panels are coated with a TCE, typically ITO. A surface treatment anchors and aligns the LC molecules in a twisted nematic (TN) arrangement, shown in ***Figure 4-3***[226]. In the 'OFF' state, in the absence of an electric field, light incident on the device is polarised by the filter. The light

passes through the 90° twist of the LC (***Figure 4-3*** *(left)*). In the 'ON' state, precise and controlled realignment occurs when the field is applied. Induced dipole moments cause the polarisation effects to be diminished and disappear entirely if the voltage (V) is significant, greater than the threshold (V^{th}), $V > V_{th}$[227]. Resulting in light being blocked by the filter (***Figure 4-3*** *(right)*).

The dielectric anisotropy of the molecules refers to the difference in parallel and perpendicular permittivities[220]. For instance, an LC with positive dielectric anisotropy orients from planar to vertically aligned with the applied field. Applied forces elastically deform the molecules in patterns described as splay, twist, and bend, (k_{11}, k_{22}, and k_{33}), respectively[228]. The elastic constants are molecular parameters that characterise the restoring forces on the molecules therefore, they influence the LCs response and relaxation times, contributing to optoelectronic performance. The dielectric parameter and the splay elastic constant are used to establish the minimum voltage required to reorient the molecules using the Fréedricks transition.

$$V_{th} = \pi \sqrt{K_{11}/\varepsilon_0 \Delta\varepsilon} \qquad (4.2)$$

where K_{11} is the splay elastic constant, ε_0 is the permittivity of free space, and $\Delta\varepsilon$ dielectric parameter. The director remains undistorted until the threshold is achieved. Gradually as the voltage increases, the director starts to deform until it is aligned with the field[229].

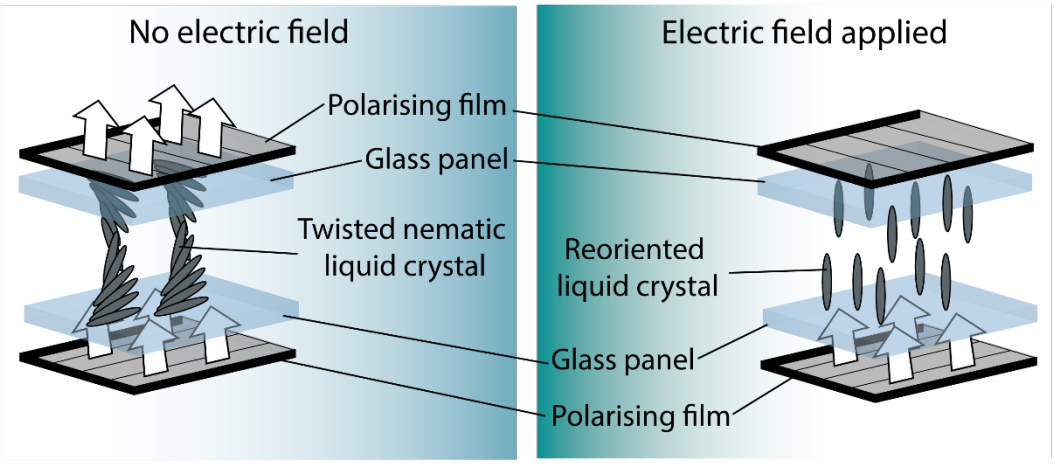

Figure 4-3 – Schematic representation of a single liquid crystal pixel to demonstrate the twisted nematic arrangement of the liquid crystals, no electric field applied (left) and the reoriented liquid crystal arrangement with an electric field used (right).

Similar designs have been considered for ophthalmic applications, exploiting the anisotropy of LCs through external stimuli. As with LCDs, they are composed of two solid substrates coated with a TCE, alignment layers and an LC layer which resides between, shown in ***Figure 4-4***. Sato,[230] presented the first variable focus LC lens in 1979. The study demonstrated that the path of light propagating through the LC layer could be altered, causing torque on the induced dipole moments of the LC molecules, and the change in path difference led to a change in focal length. Therefore, the pathway of the propagating light depends on the LC's composition and the polarisation and angle of the incident light with regards to the LC director. Sato also discussed problems related to LC lens design, such as LC cavity thickness, response, and recovery time, as well as the temperature dependence of the refractive index of nematic LCs.

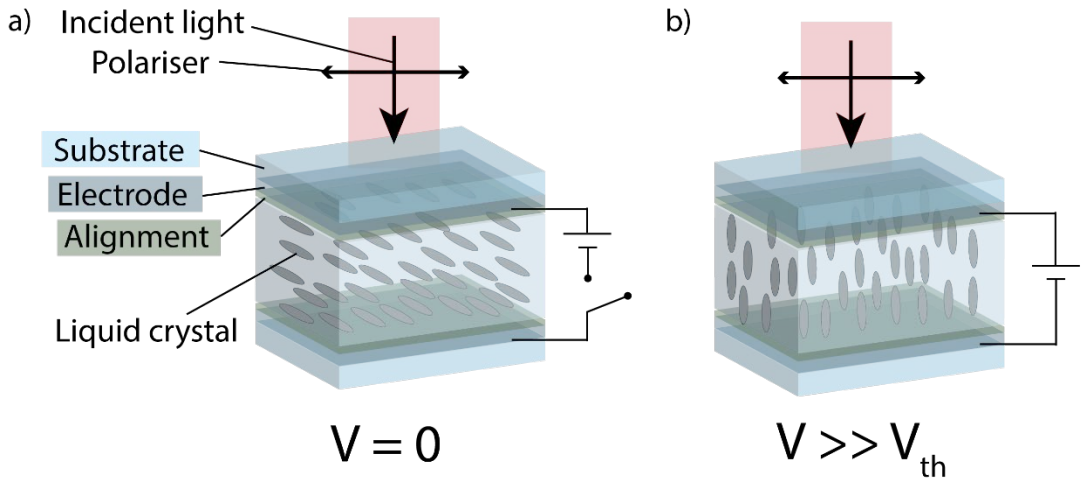

Figure 4-4 – A schematic of the general operating principle for liquid crystal lenses, a) 'OFF' state, 0 V, showing the polarised incident light passing through the liquid crystal, the light experiences the ordinary refractive index, b) 'ON' state, the voltage sufficiently exceeds the threshold voltage the polarised incident light passes through the liquid crystal, the light experiences the extraordinary refractive index as the electric field reorients the molecules.

4.1.4 Aim

IOL technology has made significant advances in treatment for cataract patients, though the need to address a more suitable accommodative mechanism for AIOL design is at an all-time high due to the ageing population. Current AIOL approaches have not been successful in restoring true lens accommodation. However, LC smart lenses offer an adjustable focus mechanism with tunable electrical stimulation. The use of $Ti_3C_2T_x$ as the TCE provides a possible solution to the flexibility restraints of existing LC lenses. The previous chapters support the suitability of $Ti_3C_2T_x$ for use as a TCE and demonstrate the biosafety within the ocular environment. In addition, LC

lenses have the potential to mitigate concerns associated with the weakening of ciliary muscles and fibrosis of the capsular bag by relying less on these natural mechanisms. This chapter aims to demonstrate the use of $Ti_3C_2T_x$ as a TCE in an LC test cell to reorient the director through the external stimulus. Moreover, it is hypothesised that $Ti_3C_2T_x$ TCE coatings are able to promote controlled and reversible modulations in LC refractive indices through external electrical stimulation. The objectives are:

1. To fabricate an LC test cell with $Ti_3C_2T_x$ as a TCE.
2. To determine if $Ti_3C_2T_x$ can facilitate molecular reorientation of a nematic LC in a test cell by measuring the extraordinary ray's refractive index with a purpose-built in-line laser refractometer.
3. To investigate the optical dynamics of the LC and the $Ti_3C_2T_x$ TCE in the test cell.

4.2 Materials and methods

4.2.1 Materials

- Superfrost plus microscope slides (VWR international, UK)
- 4’-Pentyl-4-cyanobiphenyl (5CB), 98 % purity (Sigma-Aldrich, UK)
- Poly(vinyl alcohol) (PVA) 8-88 M_w ~67,000 (Sigma-Aldrich, UK)
- Double-sided tape (Tesa Tesa 64621) (RS components, UK)
- Conductive paint (Electrolube) (RS components, UK)
- Copper tape (Hi-Bond HB 720A) (RS components, UK)

4.2.2 Ordinary refractive index measurement of the liquid crystal

4'-Pentyl-4-cyanobiphenyl, or 5CB, was selected due to its large dielectric anisotropy and optical birefringence in the nematic phase. The ordinary refractive index of the 4'-Pentyl-4-cyanobiphenyl, (5CB) nematic LC was measured using a Bellingham and Standley Abbe 5 refractometer. The measurement was performed in triplicate at 24 °C.

4.2.3 Fabrication of the $Ti_3C_2T_x$/liquid crystal test cell

$Ti_3C_2T_x$ was synthesised via the MILD method with LiF/HCl over 24 hours, as described in section 2.2.2.

4.2.3.1 Solid substrate pre-treatment

For the proof-of-concept design, a $Ti_3C_2T_x$/LC test cell was fabricated. Test cells are used to investigate LC properties for display applications, here the test cell was used to observe the optoelectronic properties of the $Ti_3C_2T_x$ electrode and determine the suitability for refractive index modulation of the 5CB LC. Glass microscope slides were used as solid supports in the test cell. The substrates were subjected to a 10-minute treatment of pure oxygen plasma at 100 W and 10 cm^3 min^{-1} using a Henniker plasma etcher (Henniker plasma, UK). The treatment cleaned the glass surface and increased the hydrophilicity to allow an even, continuous, and thin $Ti_3C_2T_x$ coating.

4.2.3.2 Spin coating of $Ti_3C_2T_x$ onto the solid substrates

500 µL of a 5 mg mL^{-1} $Ti_3C_2T_x$ solution was deposited onto the microscope slides. $Ti_3C_2T_x$ was spin-coated onto the substrates through the same two-step method described in section 2.2.4.2. The microscope slides were transferred to the oven for 24 hours at 80 °C to allow the coating to anneal.

4.2.3.3 Preparation and coating of the alignment layer

A 3 % PVA solution was prepared by heating 100 mL of DI water to 90 °C and adding 3 g of PVA over 5 minutes with constant stirring. After 30 minutes of stirring at 90 °C, the solution was cooled to room temperature. Additional DI water was added if needed to account for any loss through evaporation. The 3 % PVA solution was spin-coated onto the $Ti_3C_2T_x$ coated microscope slides following their 24 hour annealing stage (section 4.3.2.3). The PVA coating forms the alignment layer. The spin coating method used was 1500 rpm for 1 minute, then the substrates were transferred to the oven for 1 hour to allow annealing of this alignment layer. The PVA coated $Ti_3C_2T_x$ microscope slides were rubbed with a microfibre cloth parallel to the long edge of the slides to introduce microgrooves, for alignment of the LC.

4.2.3.4 $Ti_3C_2T_x$/Liquid crystal cell fabrication

The coated microscope slides were attached at the edges with a double-sided adhesive to construct the test cell. The adhesive formed a cavity in the test cell's centre that was filled with 5CB LC through capillary action. Copper tape was placed onto the $Ti_3C_2T_x$

coating, and wires connected a Keithley SMU 2450 Source meter (Tektronix, USA) as the power supply to provide the electric field.

4.2.4 Refractive index measurements of the $Ti_3C_2T_x$/liquid crystal test cell

The refractive index of the test cell was measured in the presence and absence of an electric field using a purpose-built in-line laser refractometer. The experimental setup, presented in ***Figure 4-5***, was composed of a diode laser (Thorlabs CPS405, USA) emitting a beam at 405 nm, a 100 µm precision pinhole to clip the laser beam, translation, and rotation stages to position the microscope slide assembly, and a CMOS camera (Basler ace acA1920-40gm, Germany) to record the beam's position shift. The position of the laser beam was recorded both with and without applying a 20 V electric field, allowing the beam shift to yield the change in the refractive index using Snell's law.

$$n_1 sin\theta_1 = n_2 sin\theta_2 \tag{4.3}$$

The beam shift was measured by sub-pixel affine image registration using the script detailed in Appendix 1 – Beam shift MATLAB script. The script takes an average of 200 reference images and 200 refracted images. The reference images have no applied electrical potential, hence 0 V. The refracted images are with the applied field at 20 V. Prior to analysis of the beam's translation, the noise and any diffraction are cleaned from the images. The images are also cropped to speed up the image processing. The image registration transform is performed by the MATLAB script, to yield the *x* and *y* beam displacement induced by the change in refraction.

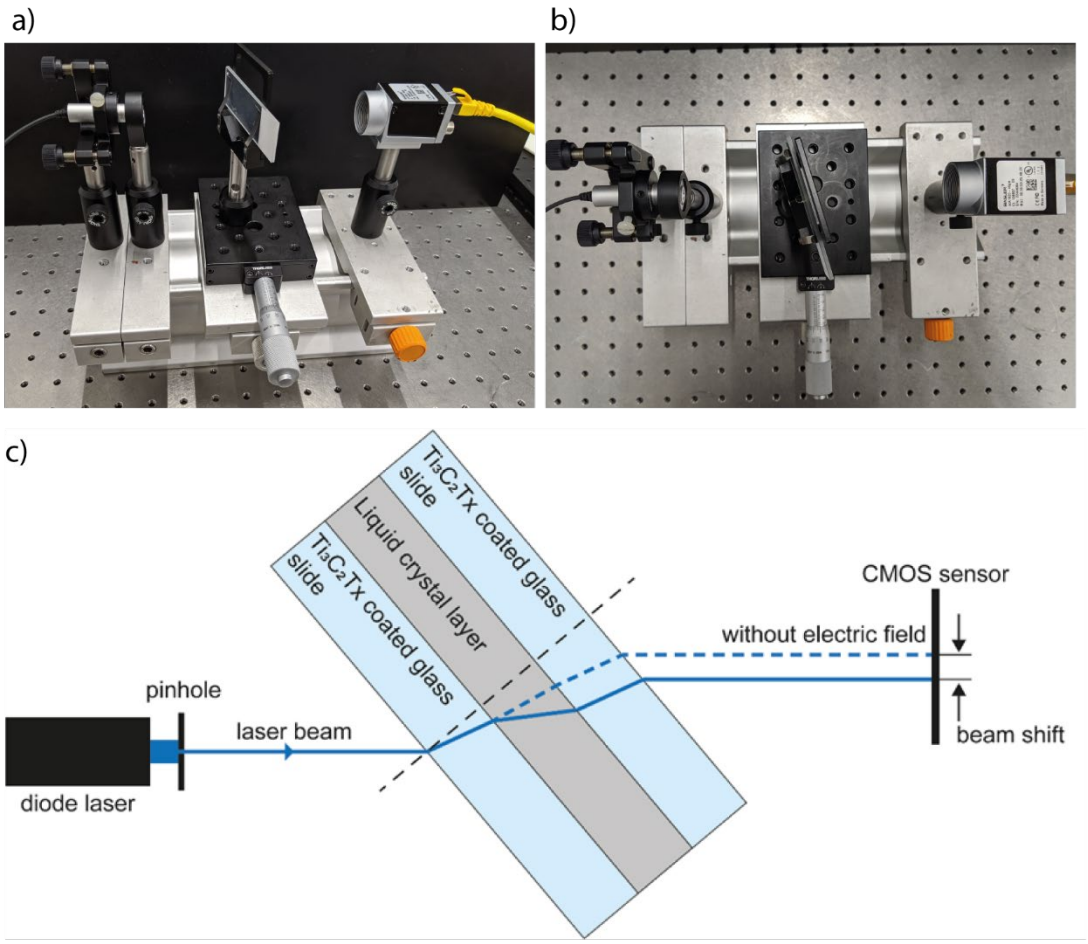

Figure 4-5 – Digital images (a-b) and schematic of the purpose-built in-line laser refractometer (c). The position of the laser beam is recorded on a CMOS sensor both with and without applying a 20 V electric field. The change in refractive index is calculated from the beam shift (measured by sub-pixel affine image registration).

The angle of the test cell (sample) holder relative to the laser beam was precisely measured by replacing the test cell with a sapphire optical flat and computing its angle from the induced laser beam shift. ***Figure 4-6*** demonstrates the displacement of the beam and was calculated using the trigonometric ratios of r the refracted beam path, t the thickness of the sample, and d_2 the displacement of the beam relative to the

incident beam. Equation (4.4) was determined from the blue triangle represented in ***Figure 4-6*** and was rearranged regarding the refracted beam path to give equation (4.5). Equation (4.6) was established from the red triangle in ***Figure 4-6*** and was rearranged with respect to the displacement of the beam resulting in equation (4.7). Equation (4.5) was substituted into equation (4.7) to give equation (4.8), eliminating one of the unknown variables. Snell's law expressed in equation (4.3) was rearranged for $sin\theta_2$, giving equation (4.9), which was then rearranged for θ_2, leading to equation (4.10). Equation (4.10) was substituted into equation (4.8) to form equation (4.11) which leaves the only unknown variable as θ_1, the angle of the test cell holder in equation (4.11) and the angle at which the incident light hits the test cell.

$$cos\theta_2 = \frac{t}{r} \tag{4.4}$$

$$r = \frac{t}{cos\theta_2} \tag{4.5}$$

$$sin(\theta_1 - \theta_2) = \frac{d_2}{r} \tag{4.6}$$

$$d_2 = r\, sin(\theta_1 - \theta_2) \tag{4.7}$$

$$d_2 = t\, \frac{sin(\theta_1 - \theta_2)}{cos\theta_2} \tag{4.8}$$

$$sin\theta_2 = \frac{n_1}{n_2}\, sin\theta_1 \tag{4.9}$$

$$\theta_2 = sin^{-1}\left[\frac{n_1}{n_2}\, sin\theta_1\right] \tag{4.10}$$

$$d_2 = t\, \frac{\sin\left(\theta_1 - sin^{-1}\left[\frac{n_1}{n_2} sin\theta_1\right]\right)}{\cos\left(sin^{-1}\left[\frac{n_1}{n_2} sin\theta_1\right]\right)} \tag{4.11}$$

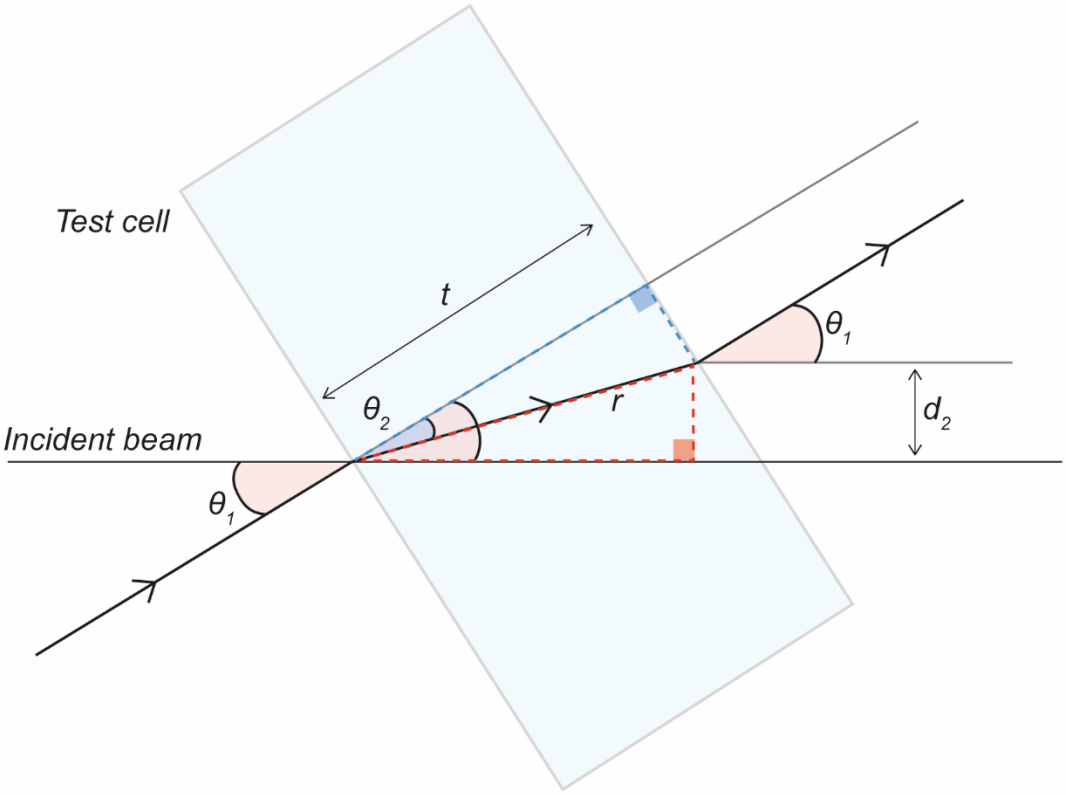

Figure 4-6 – A diagram of the purpose-built in-line laser refractometer to establish beam displacement at the interface, providing reference to θ_1 the angle of incidence of the beam, θ_2 the angle of the refracted beam path, r refracted beam path, t the thickness of the sample (the sample being the sapphire optical flat or the test cell), and d_2 the displacement of the beam.

Once the angle of the test cell holder was determined with the sapphire optical flat, the test cell was investigated. As with the optical flat equation (4.11) was used to evaluate the test cell's angle relative to the incident beam (θ_1), the only remaining unknown in the beam shift calculation is the refractive index of the LC layer in the test cell. Although the laser beam had a gaussian profile, microscopic-scale refractive index gradients within the LC disrupted the radial energy distribution of the beam. The

aberration was corrected by applying a frequency filter to the distorted beam profile images so that the beam shift could be accurately measured.

4.2.5 Optical evaluation

The optical focus of the test cell was investigated when an electric field was applied, and the changes were observed. An Olympus em10ii camera connected to a M.Zuiko 12-40 mm f/2.8 Pro lens was used to capture the data. ***Figure 4-7*** shows a schematic of the experimental setup, with the text being viewed through a lens, then through the test cell, by the camera. The object, lens and test cell were all set at fixed distances in order to observe the expected change in optical power and, therefore, focal length. The electric field was applied to the test cell using a Keithley SMU 2450 Source meter (Tektronix, USA). A voltage range was applied incrementally and held for 15 seconds before each image was captured. The investigation of the optical effects over time was performed on 10, 15 and 30 V, the voltage was applied for 30 seconds. The camera was set to record for 1 minute to allow the initial switching time to be observed and the molecular relaxation time.

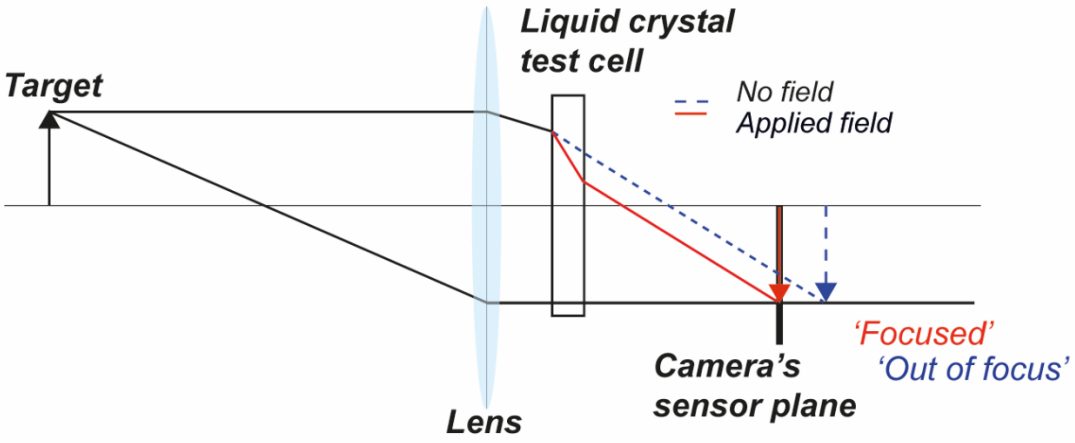

Figure 4-7 – Schematic of the setup for capturing the focusing performance of the test cell. Text is viewed through the camera passing through the lens and test cell. When the electric field is applied the light is refracted differently than when no field is applied, due to molecular reorientation of the liquid crystal, resulting in a change in focus, and therefore a change in optical power.

4.2.5.1 Digital image processing

The data was processed using a Laplacian differential function of the OpenCV 4.2.0 library written in Python Appendix 2 – Laplacian operator. All image frames were aligned before the processing. Examples are shown in ***Figure 4-8*** as controls to demonstrate the function of the operator with examples of high and low variance where the images are in and out of focus, respectively. An example of the image processing from the operator can be seen in ***Figure 4-9***.

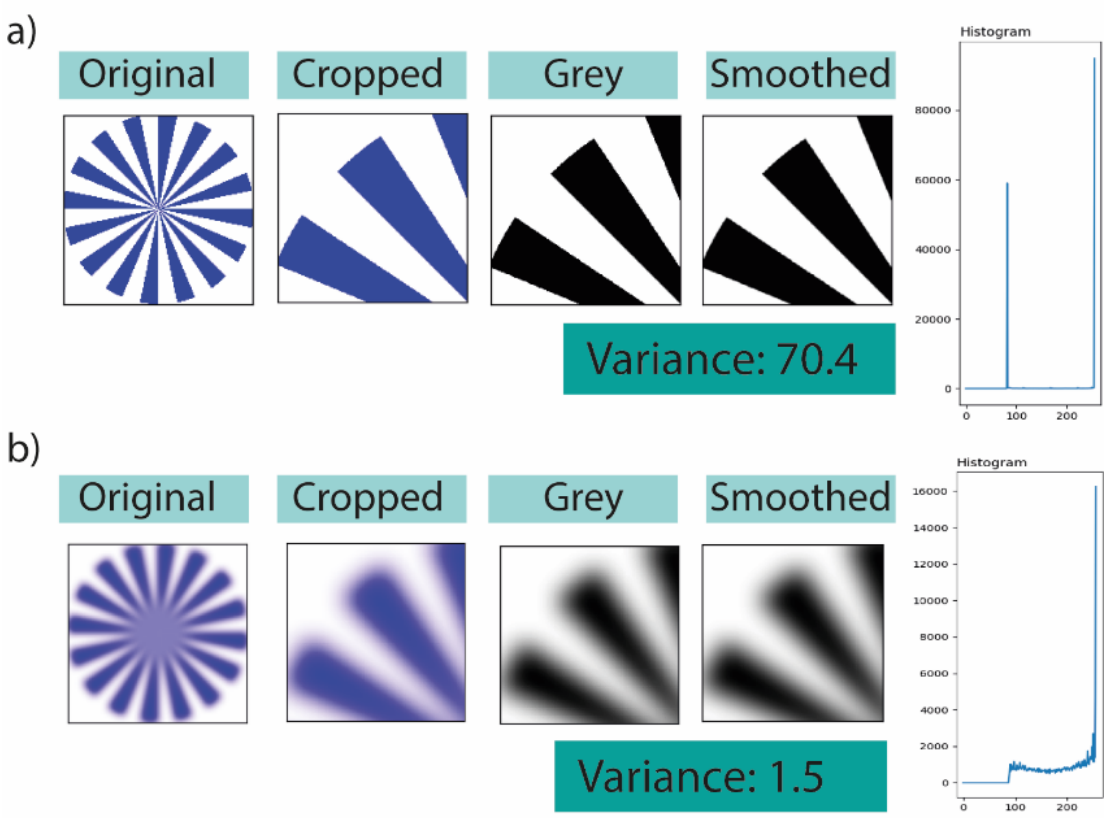

Figure 4-8 – Laplacian operator outputs. The script crops the original image that is then processed to greyscale, and a gaussian filter is applied to minimise the noise in the image (smoothed image). A histogram shows the frequency distribution of the image's overall pixel greyscale intensity, and the variance of these intensities is computed. (a) Validation exercise showing the focused image with a variance value of 70.4. (b) Validation exercise showing the out of focus image with a variance value of 1.5.

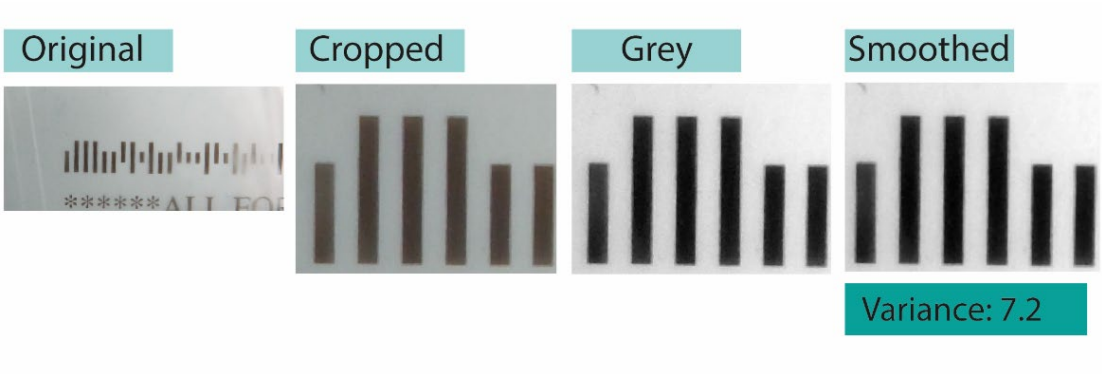

Figure 4-9 – Laplacian operator output for the lines observed throughout the analysis seen in Figure 4b-c.

4.3 Results

An electroactive AIOL mechanism was investigated with the aim of producing controlled and reversible adjustments in lens focus at all distances. The novel approach involves the use of the transparent, conductive, and flexible $Ti_3C_2T_x$ to perform as the TCE to facilitate molecular reorientation of a nematic LC. The electronically controlled alterations in LC orientation led to switchable refractive index and, therefore, changes in focal length (m^{-1} or D). Systematically, the ordinary refractive index of the LC was determined, a $Ti_3C_2T_x$/LC test cell was fabricated, and then a method to measure the electronically induced refractive index change was developed. The adjustments in focus were observed, and image processing was used to qualitatively evaluate the mechanism.

4.3.1 Ordinary refractive index measurement of the liquid crystal

The anisotropic physical properties of LCs lend themselves to complex lens applications. 4'-Pentyl-4-cyanobiphenyl, or 5CB, is a commonly used LC for such

applications due to its large dielectric anisotropy and optical birefringence in the nematic phase. It is composed of two benzene rings and two terminal groups shown in ***Figure 4-10***. It is nematic at room temperature and undergoes an isotropic phase transition at 35 °C[231]. The ordinary refractive index of 5CB was measured at 24 °C using an Abbe refractometer before the test cell fabrication. It was determined to be 1.5354 ± 0.0002 verified by values within the literature[231,232].

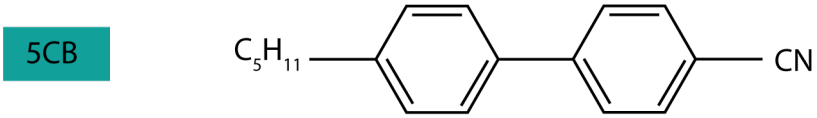

Figure 4-10 – The structure of 5CB, including two benzene rings and two functional groups, C_5H_{11} and CN.

4.3.2 Fabrication of the $Ti_3C_2T_x$/liquid crystal test cell

Figure 4-11 shows the fabrication of the $Ti_3C_2T_x$/LC test cell constructed similarly to an LCD, with TCE-coated solid substrates, PVA alignment layer, and the LC sandwiched between. The thin PVA layer was rubbed linearly with a microfibre cloth to induce planar alignment of the LC molecules with a 90° twist from one substrate to the other, creating the twisted nematic orientation. The predetermined alignment of the LC molecules confined between the substrates was demonstrated in ***Figure 4-11*** *(d-e)*, where the polarising film allowed the orientation set by the PVA layer to be observed. The polarising film was placed above and below the test cell. First, ***Figure 4-11*** *(d)*, the films were positioned in the same orientation, where the LC cavity presented a dark region of the cell. Polarising films filter light as it passes through.

The dark region demonstrates that when light passed through the first film, it was polarised in one direction, then as it passed through the transparent LC cavity, the molecules twisted the light through 90°, resulting in the molecules aligned in the opposite direction to the orientation of the polarising films. In ***Figure 4-11*** *(e)*, the filters were arranged opposite to one another, hence cross polarised. The LC cavity displayed bright in this example as the molecules again twist the light, causing the bright region. It is important to note that these observations are demonstrated in the absence of the electric field, the test cell is not powered. These results solely demonstrate the predetermined order of the molecules director and the homogeneity of the planar alignment.

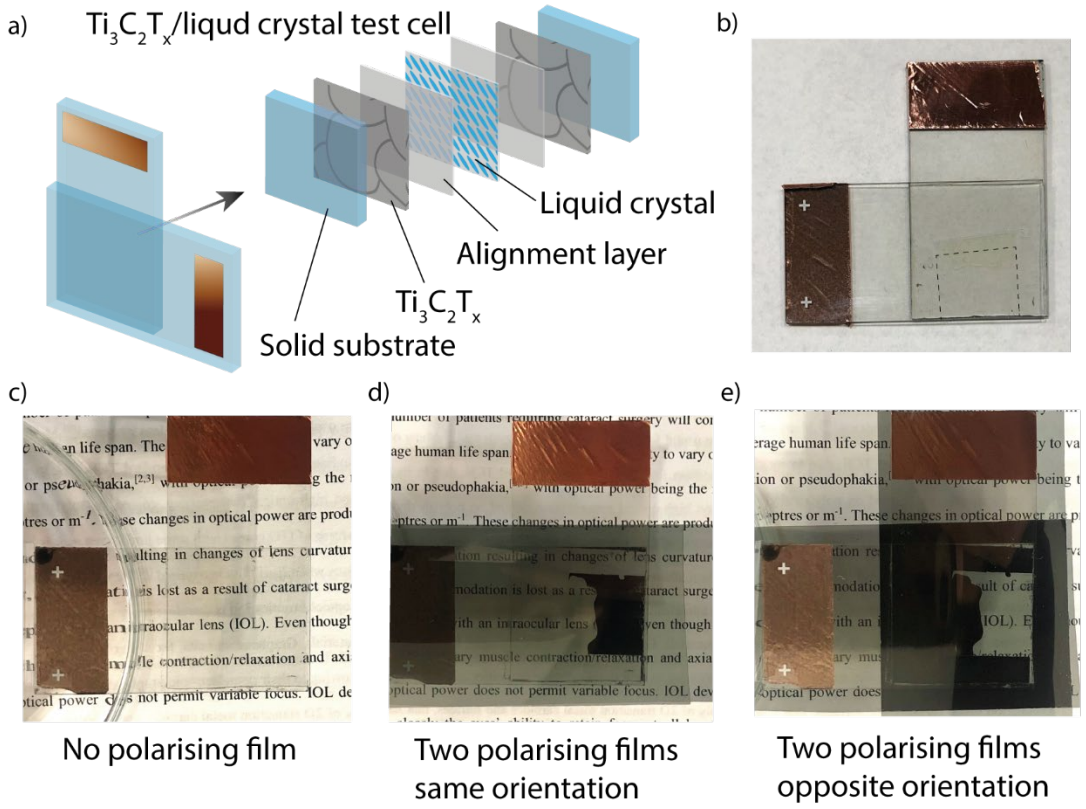

Figure 4-11 – $Ti_3C_2T_x$/LC test cell. (a) schematic of the cell assembly demonstrating $Ti_3C_2T_x$ coated microscope slides, PVA alignment layers, and 5CB LC cavity. (b) digital photo of a $Ti_3C_2T_x$/LC test cell. (c) The test cell is placed over text to demonstrate optical transparency. d) The test cell is placed over text sandwiched between two polarising films in the same direction, showing the LC cavity blocking light (dark region). e) The test cell is placed over text sandwiched between two polarising films in the opposite directions, showing the LC cavity allowing the passage of light (bright region).

4.3.3 Refractive index measurements of the $Ti_3C_2T_x$/liquid crystal test cell

The mechanism was evaluated in the fabricated test cell to address the hypothesis and determine if $Ti_3C_2T_x$ could facilitate the molecular reorientation of a nematic LC with an electric field. The external electric field was connected, and the refractive index modulation was measured with a purpose-built in-line laser refractometer. The

refractometer was set up with the laser emitting a beam through the test cell, and the relative displacement between the powered and unpowered test cell (in the presence and absence of the electric field) was captured with a camera. The test cell was held in a rotation stage at a specific angle to the beam. Equation (4.11) was used to calculate the refractive index of the test cell, though the precise angle at which the beam was incident on the test cell was required. A sapphire optical flat was used as a control material of known refractive index and thickness to determine the incident angle.

4.3.3.1 The specific angle of the purpose-built refractometer rotation stage

The angle of the rotation stage was determined using a sapphire optical flat. The theoretical beam shift of the sapphire flat was calculated using equation (4.11). Forming a linear relationship between the displacement of the beam and the angle of the rotation stage, demonstrated in ***Figure 4-12***. The same equation was used to determine the angle of the stage with the measured beam shift of the refractometer, plotted in red. The beam shift of the sapphire allowed the angle of the rotation stage to be measured as 38.42°. Moreover, equation (4.11) repeated below, involves the displacement (d_2) that is measured through beam shift, measured thickness (t) of the sample, the refractive index of the first (n_1) and second (n_2) interfaces and the incidence angle of the beam (θ_1), meaning that the refractive index of the second interface is the only unknown component of the equation as $\theta_1 = 38.42°$.

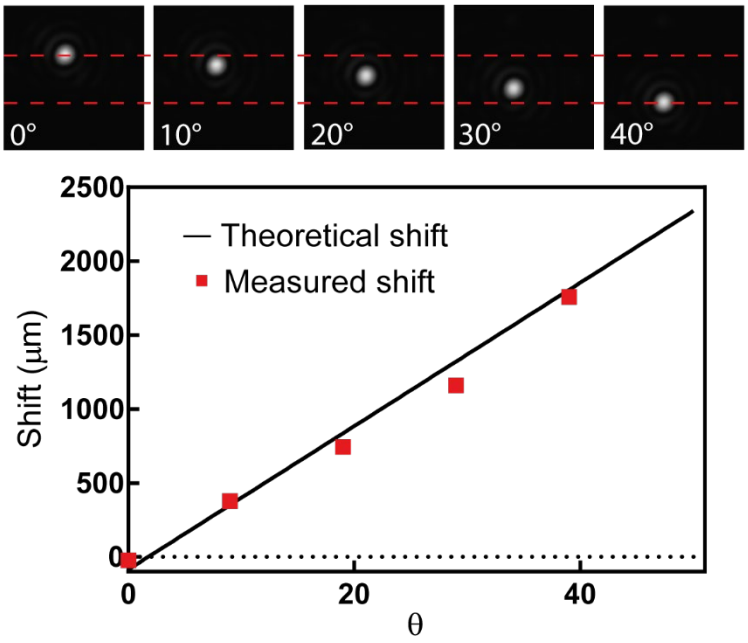

Figure 4-12 – Beam profile images of a laser beam (405 nm) through a sapphire optical flat at angles 0 – 40° from left to right using a CMOS camera (Basler ace acA1920-40gm, Germany). The plot of the calculated beam shift as a function of the angle (θ).

4.3.3.2 Test cell refractive index measurements with the purpose-built refractometer

The refractive index modulation of the $Ti_3C_2T_x$/LC test cell was investigated using the refractometer that was specifically constructed for the study. The laser was incident on the test cell in the presence and absence of the electric field. The images were processed to measure the beam displacement using a MATLAB script. The displacement was used to calculate the refractive index using equation (4.11). In the presence of the 20 V electric field, the refractive index was 1.7280 ± 0.0479 (mean ± SD, n = 3). In agreement with the literature, the refractive index measured corresponds to and is described as the extraordinary refractive index of 5CB[233,234]. The measurement of a significant change in the refractive index under the influence of an

electric field supports the hypothesis that $Ti_3C_2T_x$ is a suitable alternative transparent conductive electrode, not only for lens applications but also for LCDs.

4.3.4 Optical evaluation

The $Ti_3C_2T_x$/LC test cell demonstrated molecular reorientation, switching between the ordinary and extraordinary refractive indices in the unpowered and powered states. To observe the optical changes as a function of the test cell's ability to focus, a lens was added to the setup and images processed.

4.3.4.1 Optical evaluation of test cell with edge detection operator

The test cell was set up to observe a printed target (the logos of the University of Brighton and Drexel University) with and without an electric field. The digital images were processed with a Laplacian operator to distinguish the focus of the images captured through the test cell. The derivative operator detects edges in an image by comparing the intensities of neighbouring pixels and reporting the variance. ***Figure 4-13*** shows the target a) without an electric field, and b) with an electric field. In the absence of the field, the logos are blurry and not focused. In the presence of the field, the logos are focused, the histograms in ***Figure 4-13*** display the output following processing with the Laplacian operator. The output shows distinct differences in the greyscale histograms of the two images: in the absence of the field, more counts were recorded between 100 – 150 of the pixel's grey level, corresponding to a variance value of 3.7. Whereas, in the presence of the field, more counts were observed at 50 – 75 of

the grey level resulting in larger frequency distribution and corresponding to a greater variance of 24.3.

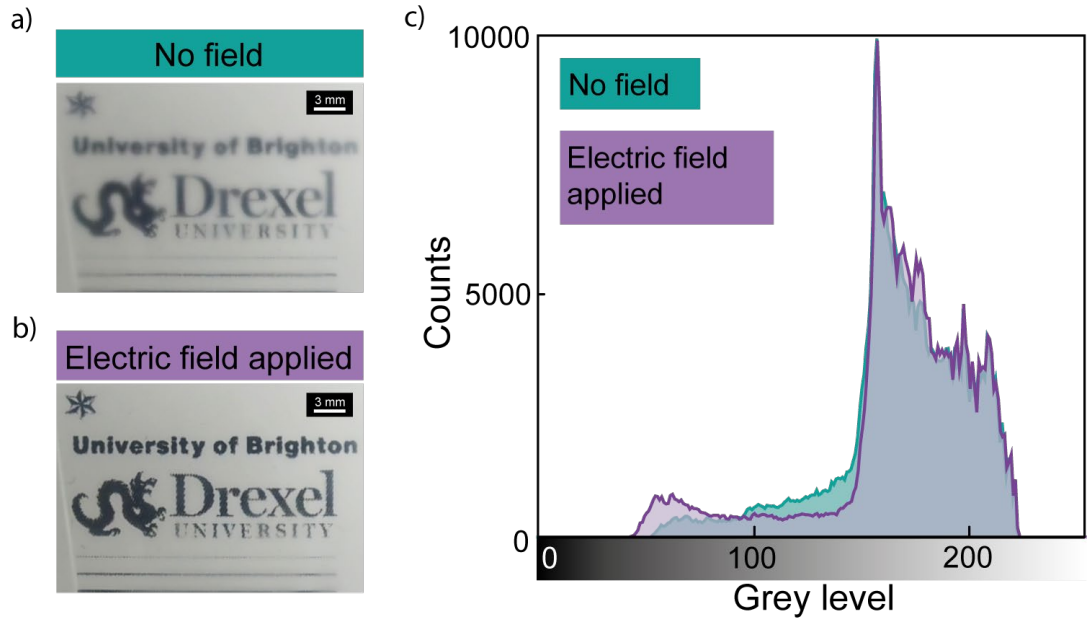

Figure 4-13 – Optical evaluation of the test cell with digital image processing using the Laplacian operator. (a) The University of Brighton and Drexel University logos were observed with no electric field applied through the test cell. (b) The logos were observed with the electric field applied through the test cell. (c) Histograms of pixel intensity, no field (green) with an electric field (purple) with a larger frequency distribution of the applied electric field demonstrating a larger variance.

4.3.4.2 The effect of the electric field on the test cell

The test cell's focusing ability was assessed as a function of the electric field, and the images were processed using the edge detection operator discussed above. ***Figure 4-14*** demonstrates that the greyscale variance increases with increased voltage, indicating that an increase in the applied electrical potential leads to a greater sharpness of the observed target through the test cell.

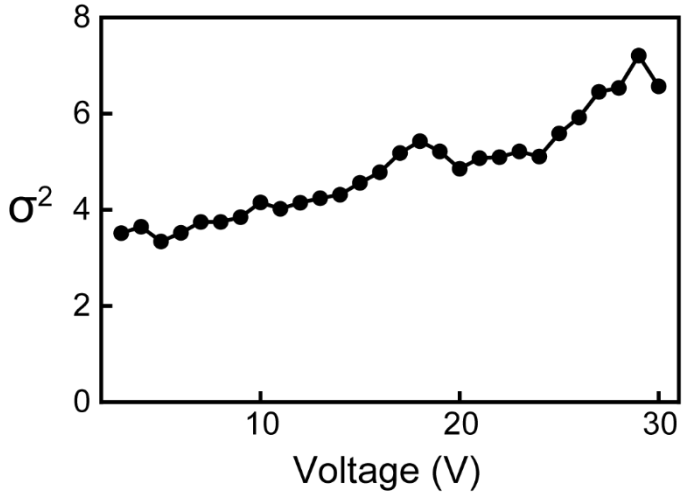

Figure 4-14 – Optical evaluation of the test cell with digital image processing to provide variance (σ^2) of image pixel's greyscale intensity for a range of voltages. A target was observed through the test cell with the applied voltage held for 15 seconds before capturing the image. A Laplacian edge detection operator was used for image processing, demonstrating greater variance in pixel greyscale with increased voltage.

4.3.4.3 Dynamic liquid crystal orientation

To investigate the dynamics of the test cell, the variance was plotted as a function of time, as shown in ***Figure 4-15***. The refractive index of the LC within the test cell switched from ordinary to extraordinary as the applied field reoriented the molecules. The time for LC reorientation was calculated by subtracting the time at which the minimum variance value was observed from the time that the maximum variance value was observed. For 10, 15, and 30 V the switching times were calculated as; 2.30, 1.04, and 0.26 seconds, respectively. With an increasing voltage, the time taken for reorientation decreased.

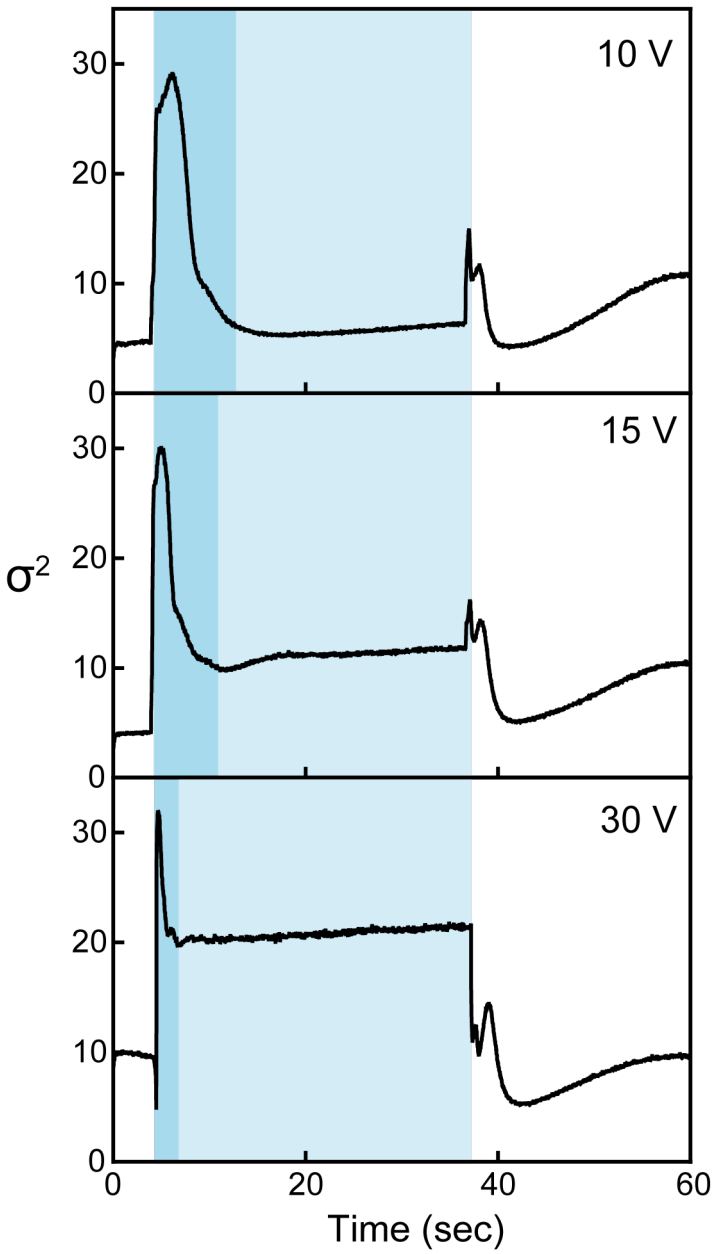

Figure 4-15 – An evaluation of the test cell's response to an applied electric field over time. 10, 15, and 30 V were applied to the test cell, a target was observed through the test cell and images were recorded over time. The images were processed using an edge detection operator to provide variance (σ^2) of image pixels' greyscale intensity over the range of voltages as a function of time. The time for the liquid crystal in the test cell to switch from the ordinary refractive index to the extraordinary refractive is identified as the darker blue region in each plot, and the time the electric field was applied is the whole of the blue region.

4.4 Discussion

This chapter demonstrated the potential use of $Ti_3C_2T_x$ as a TCE in developing an alternative approach to an adjustable focus mechanism for AIOL design. Current commercially available AIOLs have not provided true accommodation. A proof-of-concept $Ti_3C_2T_x$/LC test cell was fabricated, and the index of refraction measured in the presence and absence of an external electric field. The $Ti_3C_2T_x$/LC cell dynamics were evaluated as a function of applied voltage and the optical characteristics observed.

4.4.1 Fabrication of the $Ti_3C_2T_x$/liquid crystal test cell

The electroactive $Ti_3C_2T_x$/LC test cell was fabricated, as shown in ***Figure 4-11***. The purpose of the test cell was to establish the capability of $Ti_3C_2T_x$ to reorient the LC molecules, hence modulating the medium's refractive index leading to changes in focal length. Although flexibility has been identified as a key restraint regarding AIOL and smart lens progression, a systematic approach was employed to assess $Ti_3C_2T_x$'s suitability for the present application. Thus, the TCE was investigated on solid substrates.

When an LC is confined between two substrates, with the absence of any external forces, i.e. an electric field, the bulk orientation of the director is dependent on the chemical and physical properties of the LC and substrate interface. A spin-coated thin polymer layer can be added to the substrate to predetermine the director's orientation by anchoring the LC molecules at the substrate and LC boundary. Hence, the bound molecules at the interface orient the neighbouring molecules and, as a result

transferring the local order to the bulk director due to the long-range orientational properties of nematic LCs[235]. PVA and polyimide are typical polymers used and, once coated, rubbed to produce homeotropic (perpendicular) or planar (parallel) alignment. PVA rubbed with planar alignment was used in the test cell. Cui *et al*. [236] demonstrated that anchoring strength is directly correlated to polymer layer thickness. Thus, the coating parameters used in the $Ti_3C_2T_x$/LC test cell were in accordance with the study's findings, and a 3 % weight concentration PVA solution was used. The substrates were arranged to form a TN orientation of the LC molecules, meaning a 90° twist was set from one substrate to the other. The TN orientation has been used in LCD technology since its discovery in the 1970s, offering fast switching and lower operating voltages. ***Figure 4-11*** *(d-e)* displays images of the test cell to evidence the highly ordered LC cavity using polarising filters. The test cell is not connected to the electric field. When two polarising films are crossed, they filter the light in the *x* and y direction, and no light is able to pass through the films. However, when the test cell is placed between the cross polarised films, the LC molecules twist the light and present a bright, transparent region. ***Figure 4-11*** *(d-e*) demonstrates the homogenously ordered cavity before investigating the refractive index measurement. These findings illustrate the quality of the test cell with the absence of defects in the respective bright and dark regions.

4.4.2 Refractive index measurements of the $Ti_3C_2T_x$/liquid crystal test cell

The in-line laser refractometer was set up to determine the refractive index of the test cell with an applied electrical potential measured through the relative displacement of the beam. The validity of the refractometer was assessed using a sapphire optical flat

to identify the displacement of the beam concerning the angle of the sample holder. The optical flat of known thickness and index of refraction allowed the beam shift to be theorised and measured as a function of the angle. The sample holder angle was measured at 38.42° and used to calculate the refractive index of the $Ti_3C_2T_x$/LC test cell. Using Snell's law, equation (4.11) expresses the beam's displacement at the interface. While Snell's law is limited to computing details relative to one interface, equation (4.11) allows two interfaces to be investigated and rather than focusing on the respective beam angles, the calculation provides the output displacement as a function of the incident angle, the thickness of the sample and two refractive indices. The refractive index of the test cell with the applied 20 V electric field was measured as 1.7280 ± 0.0479 (mean ± SD, n = 3) at 24 °C, λ = 405 nm. A study investigating the effects of temperature on the refractive indices of 5CB for a range of wavelengths of the EM spectrum found the ordinary and extraordinary refractive indices to be n_o = 1.5411 and n_e = 1.7232 at 25.4 °C, λ =546 nm, hence Δn = 0.1821[224]. Another study identified the birefringence of 5CB as 0.2 ± 0.02 in the 0.2 – 1.0 THz frequency range, with the ordinary and extraordinary refractive indices being 1.58 and 1.77, respectively[234]. In agreement with the literature, the present study calculated Δn = 0.1926, despite comparable magnitudes of birefringence for 5CB, the literature expresses the anisotropic properties' temperature dependence and wavelength sensitivity. The observed refractive index modulation of the LC within the test cell supports the hypothesis that $Ti_3C_2T_x$ has the optoelectronic capabilities to facilitate the adjustable focus mechanism for developing an AIOL design. The refractive index modulation was controlled and reversible, regulated by the electrical potential of the external stimuli via the $Ti_3C_2T_x$ electrodes.

4.4.3 Optical evaluation of the $Ti_3C_2T_x$/liquid crystal test cell

The optical effects of the $Ti_3C_2T_x$/LC test cell were evaluated with and without the applied electric field by observing various target objects through the test cell and a biconvex lens. The external stimuli of the electric field were used to modulate the orientation of the LC molecules and, therefore, the refractive index allowing the observed targets to come in and out of focus. As a metric to observe and quantify the dynamics of the test cell, the digital images were processed using a Laplacian differential operator. The operator is used to identify edges in images by computing the second-order derivative of the neighbouring pixel's greyscale intensity[237]. When an edge is detected, the second differential identifies a sharp difference between neighbouring pixels, which goes from a positive to a negative value, where the zero-crossing recognised as the edge. The rapid changes in greyscale intensity are reported as variance (σ^2), therefore, if the greyscale values are similar between pixels, no edge is detected[238]. Laplacian is an accepted edge detection method, hence a measure of focus for image processing[239].

Printed targets observed through the test cell, shown in ***Figure 4-13*** *(a-b)*, demonstrate the dynamic modulation of the LCs refractive index with the applied potential. The computed variance value from the Laplacian for the image with no field applied was 3.7, and the image with the field was 24.3. The values support the observations that the image was out of focus with no field applied and corresponded to a low variance value. Whereas the image with the field applied was more focused and was reflected in a higher variance value. Moreover, fewer edges were detected with no field applied, compared to more edges that were detected with the field applied. Thus, the optical

change was attributed to the change from ordinary to extraordinary refractive index. The uniform and consistent $Ti_3C_2T_x$ electrode provided a direct path for the electrons to flow through the LC medium. Coating issues, such as the presence of defects, would present optical differences causing light to be scattered due to the inhomogeneous orientation of the molecules, thus, refractive index.

The focusing power of the test cell was evaluated as a function of the applied electrical potential. To increase the efficiency of image processing using the edge detection operator, simple black lines were used as the target, shown in ***Figure 4-9***. ***Figure 4-14*** shows an incremental increase in the computed variance value with an increase in voltage applied. The results indicate that the image became more focused with the gradual increase in the field. The average order of alignment of the molecules is described by the director, when the external force applied exceeds the critical field strength, the director orients with the field. Fréedericksz transitions are used to explain this behaviour. The dielectric anisotropy of LCs allows molecular re-orientation in the presence of the field. Hence, a gradual increase in the force exerted on the director leads to progressive changes until, eventually, it is aligned with the field. Moreover, the observations suggest tunable molecular orientation through slight adjustments in the magnitude of the field.

The dynamics of the test cell were also evaluated using the differential edge detection operator, and the variance value was plotted as a function of time at different applied voltages, as shown in ***Figure 4-15***. Edges were detected in the presence of the field, and a decrease in time taken for reorientation with increasing voltage was observed. The literature discusses LC cavity thickness and geometry as parameters that influence the response and recovery time of the change from the induced to the original

refractive index. It is well understood that the larger the aperture of the lens, the slower the change. Likewise, the thicker the cavity, the slower the change due to the elastic forces applied to the molecules[230]. There is a necessity to optimise the response and recovery time for LC lenses as they work together with the existing mechanisms of the eye to supply information to the brain. Studies indicate that the visual system can process information from visual input as quickly as 13 milliseconds[240]. However, the data presented in this study (shown in ***Figure 4-15***), is limited by its experimental set up. The voltage was applied for just over 30 seconds, in the absence of the field, the molecules relaxed back to their original state due to their intrinsic elastic properties. Moreover, the analysis period did not capture the point at which the molecules had fully recovered to their original position, thus conclusions can be made regarding the recovery.

The current proof-of-concept design demonstrates molecular modulation of a nematic LC using the two-dimensional transition metal carbide $Ti_3C_2T_x$. This framework provides a potential approach to an AIOL mechanism for use in the eye. Although, several factors could be optimised to enhance the performance of the mechanism to contend with the capability of the visual system.

4.5 Conclusion

A $Ti_3C_2T_x$/LC test cell was fabricated to determine its potential use in a refractive index modulating application toward developing an AIOL design. Studies have demonstrated advancements in LC smart lens technology that present suitability for AIOL applications as the anisotropy of LCs is exploited for adaptive focus[218,241].

Current axial displacement and shape-changing AIOLs do not produce true accommodation; therefore, a $Ti_3C_2T_x$ electroactive refractive index modulating approach presents potential. A $Ti_3C_2T_x$/LC test cell was fabricated, and molecular reorientation of the LC was observed in the presence of an external field demonstrated by the change in refractive index, indicating the transparent conductive abilities of the $Ti_3C_2T_x$ coating. The proof-of-concept design was further evaluated on its focusing ability where it displayed controlled, reversible, and fast switching between the refractive indices. The dynamic reorientation of the LC molecules displays faster switching with increasing voltages, 10, 15, and 30 V, 2.30, 1.04, and 0.26 seconds, respectively. Parameters, such as cavity thickness, could optimise response/relaxation times. Nevertheless, the $Ti_3C_2T_x$/LC test cell demonstrates the ability of $Ti_3C_2T_x$ to perform as an effective TCE in the refractive index modulation of a nematic LC and introduces a suitable mechanism for AIOL design.

Chapter 5

5 *MXene and liquid crystal change of focus mechanism for accommodating intraocular lens design*

5.1 Introduction

The optical anisotropy of LCs has been utilised in electronically controlled lenses. The electroactive mechanism has been proposed to treat presbyopia, investigated in glasses and contact lenses, and has the potential to lend itself to AIOL design[216]. The electroactive LC mechanism requires a transparent and conductive material to facilitate the optical change; the two-dimensional, $Ti_3C_2T_x$, has suitable characteristics for LC-based AIOL design. The studies undertaken in the previous chapters have supported the hypothesis that $Ti_3C_2T_x$ can function as a TCE in an AIOL design. The proof-of-concept $Ti_3C_2T_x$/LC test cell demonstrated the refractive index modulating mechanism, indicating the potential to explore a lens-based design for an adaptive focus AIOL explored in this chapter.

5.1.1 Liquid crystal lens basic operating principles

The literature reports a range of LC lens designs and operating principles. Lin *et al.* categorised the main operating principles as curved and gradient index (GRIN)[242]. ***Figure 5-1*** *(a-b)* shows an example of a curved LC lens where the LC cavity is inhomogeneous. Typically, the lens requires linearly polarised incident light, a concave glass lens, and a glass panel coated in a TCE, followed by an alignment layer that is buffed to induce homogenous alignment of the LC, an electric field, and an LC layer. The electrically tunable refractive indices of the LC layer, coupled with the glass

lens curvature, result in a variable focus lens. Hence, the focal length can be adjusted by changing the radius of curvature of the glass lens.

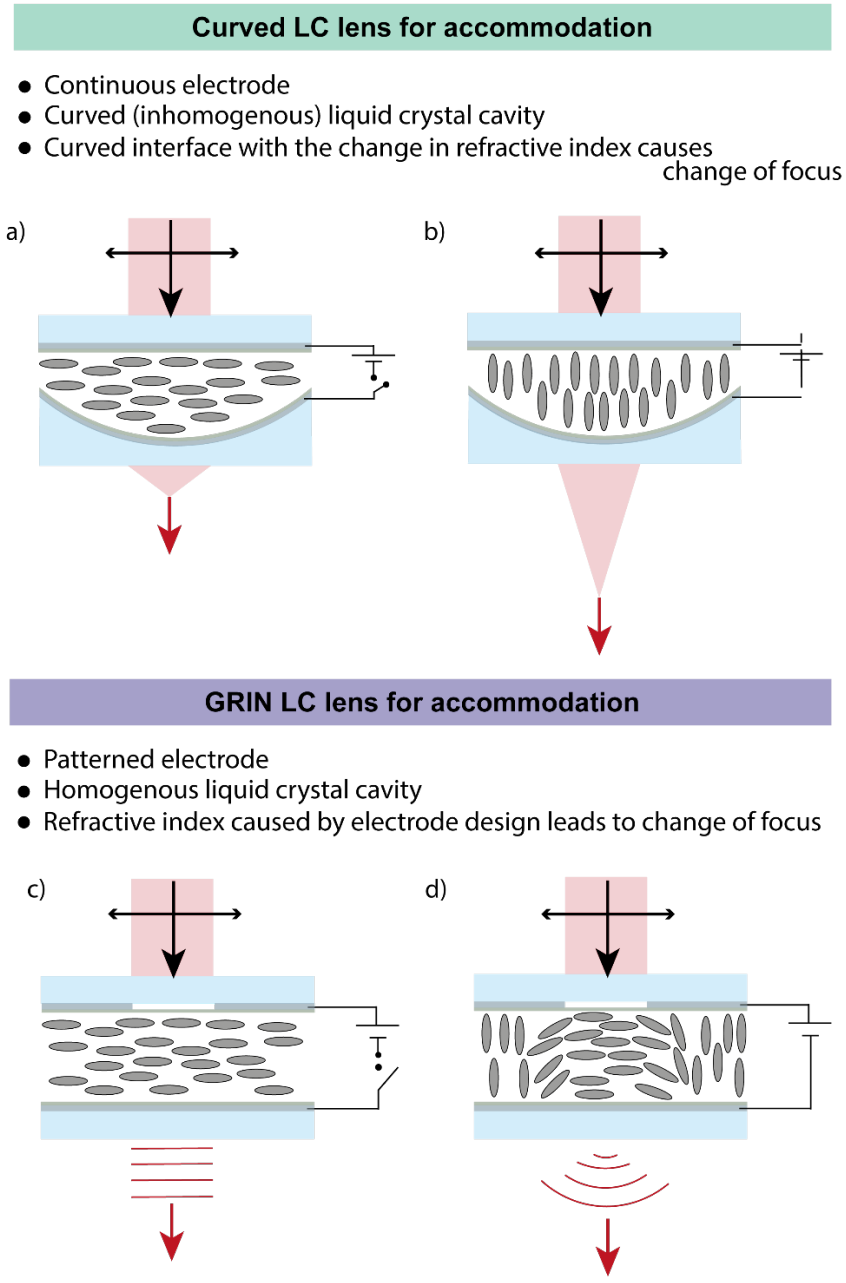

Figure 5-1 – A schematic demonstrating the operating principles of liquid crystal lenses. (a-b) An example of a curved liquid crystal lens to demonstrate the operating method, the electrode and alignment layers are present on both the flat and curved surfaces, (a) 'OFF' state, (b) 'ON' state. (c-d) An example of a gradient index liquid crystal lens to show the general operating procedure, (c) 'OFF' state the wavefront of

the incident light passes through the liquid crystal experiencing extraordinary refractive index, (d) ‘ON’ state, the patterned electrode forms a refractive index gradient.

GRIN LC lenses are another approach demonstrated in ***Figure 5-1*** *(c-d)*. These lenses differ from curved lenses by having a homogenous LC cavity. Therefore, they experience variable focus through distributions in their directors across the cavity, established through inhomogeneous electric fields. Inhomogeneous electric fields are achieved through patterned, circular, and curved electrode arrays. With the exception of electrode geometry, GRIN lenses are composed in the same manner as curved LC lenses with two flat glass panels, TCE, alignment layers and an LC layer. Many factors influence lens performance, making it challenging to compare individual features that contribute to the functionality. ***Table 5-1*** compares a range of LC lenses with electroactive optics for glasses and contact lenses.

Table 5-1 – Comparison of different liquid crystal lenses, their operating principle, and key features.

Ref	Liquid crystal lens type	Details	Cell gap (μm)	Accommodative change (dioptres)	Voltage (v_{rms})
[230]	Curved	Investigation of response/recovery times and temperature dependence of refractive index.	9-800	1	10
[243]	GRIN	Lens design with planoconvex glass, ITO, homogeneously aligned polyimide layers and reorientation were found to be greater at the edge to produce a bell-like distribution.	300	0.23	40, 55
[244]	GRIN	Contact or implantable lens with two electrodes where one is a conductive ring. Three wireless principles are introduced.	25, 50	3	7
[245]	GRIN	Homogeneous LC cavity with a spherical and planar electrode. A UV curable polymer to fill the sag area. The switching speed was ~1 sec at room temperature.	40	1.67	40
[217]	Fresnel	Photolithographically patterned thin diffractive lens with a large aperture.	1	1	2
[246]	GRIN	A lens design with spherical and flat electrodes and a centrosymmetric refractive index. The sag region was filled with a range of materials and evaluated.	25	1.04	140

[247]		An implantable lens design with a wireless radio-frequency control compact receiver.	40	2.51	2.83
[218]	Curved	A PMMA contact lens design with a negative LC lens meniscus produces a negative power LC layer. The 'OFF' state of the lens experiences extraordinary refractive index and then reduces to ordinary in the 'ON' state.	50-67	2	5
[248]	Curved	A PMMA contact lens with a vertically aligned homeotropic alignment layer.	3.6	2	7.1
[88]	Curved	A PMMA contact lens with a CVD grown graphene electrode.	50	0.7	7.1
[241]	Curved	A PMMA contact lens with PEDOT:PSS, and an investigation into planar and homeotropic alignment.	2.3	3.3	6
[249]	GRIN	A lens design with a float electrode.	50	3.5	4.1

5.1.2 Liquid crystal lens design and performance

The LC lens research provides an alternative approach to variable focus optics, although the design and performance depend on several factors. For instance, LC composition determines the medium's birefringence, and typically $\Delta n = 0.2$ is required for most lenses to observe a significant change in focal length. Ren *et al*.[245] prepared a higher birefringent LC mixture, where $\Delta n = 0.4$ at $\lambda = 633$ nm and filled the 40 μm thick LC cavity designed to produce a positive lens. In the absence of the electric field, the focal length was at infinity; once the field was applied, it shifted from infinity to approximately 0.6 m, corresponding to a dioptre change of ~ 0.19 D. The response time of the lens was approximately 1 second at room temperature. Whereas Milton *et al*.[250] reported a 2.00 D shift for a 5CB filled contact lens design. The positive optical power lens substrates formed a negative LC cavity meniscus. The authors observed the extraordinary refractive index in the 'OFF' state and ordinary when 'ON'. Therefore, the refractive index was at its maximum when 'OFF' and reduced to its minimum when 'ON', causing an overall increase in optical power.

Response and recovery times are also influential factors concerning lens performance. For most LC lens examples, the objective is to produce a mechanism with a similar switching time to the subsecond accommodative speed of the crystalline lens. In the presence of a field, the molecules reorient from one refractive index to the other, the time it takes to reach the induced refractive index is the response time. Whereas, in the absence of the field, the molecules return to their original orientation, and refractive index, which is described as the retardation or recovery time[225]. It is known that response/recovery times are not only influenced by LC composition but also by cavity thickness and geometry[230]. Lenses that require a larger aperture are known to

be significantly challenging regarding performance[216]. For designs with a curved cavity, thicker regions are present at the centre or periphery depending on the optic design, influencing response/recovery times, affecting lens performance as the regions switch at differing speeds.

The predetermined alignment of the director further influences lens performance. In the absence of external stimuli, the director's bulk orientation is fixed with a thin polymer layer, buffed in a set direction, planar or homeotropic. The preferred orientation is set based upon the birefringence of the LC, the design of the optic. Surface interactions of the alignment layer anchor the LC molecules in place. The angle at which the alignment is set is the pre-tilt angle. Most LC lens designs set a low pretilt angle between 0 – 5° as research has demonstrated that a wider angle has a negative impact on the response time of the lens[251].

Temperature is another important aspect that impacts lens performance. The temperature dependence of nematic LCs used for adaptable focus applications stems from their thermotropic quality, meaning they operate over a specific temperature range[232]. When the temperature exceeds the clearing point, the LC transitions from anisotropic to isotropic, at this point, the molecules are disordered and no longer birefringent[230]. Moreover, fluctuations in temperature result in unwanted optical effects that impact the resultant change in refractive index and overall change in focal length. Some lens designs have exploited the temperature dependency of LCs through thermally controlled methods where the phase transitions between nematic and isotropic experience a difference in their bulk refractive indices[252].

A significant obstacle identified from the reported lens designs is the electrode material. ITO remains the most commonly used TCE for lens applications due to its

high optical transparency and electrical conductivity, although it is inherently brittle and will eventually hinder future developmental possibilities where flexibility is required. Furthermore, the progression from ITO to a flexible material was introduced with a graphene layer in a poly(methyl methacrylate) (PMMA) contact lens[88]. The design was constructed from two lens substrates with a 50 μm thick LC cavity filled with the nematic LC MLC-6648. One of the lens substrates had an ITO electrode and the other a graphene electrode. The chemical vapour deposition (CVD) synthesised graphene layer was transferred from the copper foil it was formed on, to the contact lens substrate through a three-step roll-to-roll transfer process, which involved the adhesion of PMMA to the graphene film, etching of the copper layer and release of graphene to the contact lens[161]. The lens provided a 0.7 D change in optical power in the presence of 7.1 V_{rms}. Although the design introduced the potential of two-dimensional materials, the mechanism relied on the presence of ITO. In addition, the synthesis and incorporation of graphene into the design were complex. Moreover, there is an opportunity to investigate the use of $Ti_3C_2T_x$ for LC lens applications in AIOL design.

5.2 Aim

Adjustable focus LC lenses have been investigated for presbyopia, although this technology has potential use in developing IOL technology for cataract patients to address the inevitable loss of accommodation. The electrically tunable focusing mechanism offers substantial possibilities for AIOL design, mitigating reliance on the existing mechanism of the eye, unlike current commercially available approaches. $Ti_3C_2T_x$ has demonstrated potential in biomedicine and optoelectronic applications,

therefore suited to the investigation into an electroactive AIOL design. The work presented in this chapter aims to construct a $Ti_3C_2T_x$/LC lens that generates a change in focus through external stimuli. First, a glass-based lens design was constructed, and an optical evaluation was made, then a polymer-based lens design was investigated. The work addresses the hypothesis that transparent conductive $Ti_3C_2T_x$ coatings are able to facilitate a change in focus in an LC-based AIOL design through refractive index modulation. The objectives are:

1. To construct a glass-based $Ti_3C_2T_x$/LC lens that modulates the refractive index.
2. To evaluate lens performance through optical assessments in the presence and absence of the electric field.
3. To investigate a poly(methyl methacrylate) (PMMA) lens design for the fabrication of a $Ti_3C_2T_x$/LC AIOL.

5.3 Materials and methods

5.3.1 Materials

- 4'-Pentyl-4-cyanobiphenyl (5CB) (Sigma-Aldrich, UK)
- Bi-convex lens, LB1471, plano-concave lens (LC1220) and planoconvex lens (LA1131) (Thorlabs, UK)
- 25 μm double-sided adhesive (8211) (Digi-key, UK)
- Silicone (egs10c-20g) (Digi-key, UK)
- Conductive paint (Electrolube) (RS components, UK)

- MG Chemicals Cold Solder Solid Adhesive (RS Components, UK)
- Poly(vinyl alcohol) (PVA) 8-88 M_w ~67,000 (Sigma-Aldrich, UK)
- Poly(methyl methacrylate) (PMMA) lenses (Contamac, UK)
- Acrylic acid (Sigma-Aldrich, UK)

5.3.2 Fabrication of a glass-based $Ti_3C_2T_x$/liquid crystal lens

5.3.2.1 Synthesis, coating of $Ti_3C_2T_x$ and alignment layer on the glass lenses

$Ti_3C_2T_x$ was synthesised through the MILD method, described in section 2.2.2. Three BK7 glass lenses were used to construct the $Ti_3C_2T_x$/LC lens. Lens 1 was bi-convex, lens 2, plano-concave and lens 3 plano-convex, shown in ***Figure 5-2***. Lenses 1 and 2 were subjected to a 10-minute treatment of pure oxygen plasma at 100 W and 10 cm^3 min^{-1} using a Henniker plasma etcher (Henniker plasma, UK), to clean and increase the hydrophilicity of the lens surface. The lenses were spin-coated with the synthesised $Ti_3C_2T_x$ using an Ossila spin coater (Ossila, UK) in a two-step program, at 5000 rpm for 2 minutes and 6000 rpm for 1 minute. The lenses were transferred to the oven for 24 hours at 80 °C to anneal. Silver conductive paint was applied to the lenses to create contacts for wires to be added later. The 3 % PVA solution was prepared, as described in section 4.2.3.4, and spin-coated onto the $Ti_3C_2T_x$-coated lenses using an Ossila spin coater at 1500 rpm for 1 minute. The lenses were returned to the 80 °C oven for 1 hour. The PVA/$Ti_3C_2T_x$-coated lenses were buffed with a microfibre cloth to cause planar alignment.

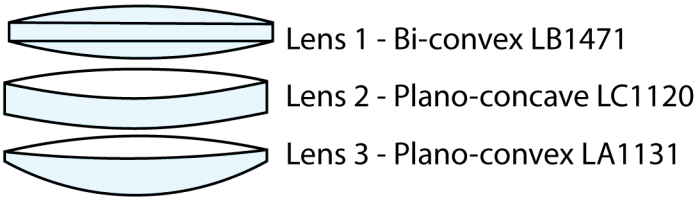

Figure 5-2 – BK7 glass lenses, used to fabricate the $Ti_3C_2T_x$/liquid crystal lens. Lens 1 was a bi-convex lens, lens 2 was a plano-concave lens, and lens 3 was a plano-convex lens (Thorlabs LB1471, LC1220, and LA1131, respectively).

5.3.2.2 Glass-based $Ti_3C_2T_x$/liquid crystal lens assembly

Two double-sided adhesive sections were added to lens 2 to form the cavity for the LC to reside. Lens 1 was placed carefully onto lens 2 to configure the 90° TN alignment of the LC molecules, described with the test cell in the previous chapter. The now combined lenses 1 and 2 were filled with 3-5 µL of 5CB via capillary action, and a silicone sealant was applied around the lenses' perimeter. Lens 3 was glued to the plano side of lens 2. Conductive epoxy connected wires to the lens. Later, once the epoxy was set, the wires were connected to a Keithley SMU 2450 Source meter (Tektronix, USA), the power supply for the lens during the investigation.

5.3.3 Optical evaluation of the glass-based $Ti_3C_2T_x$/liquid crystal lens

5.3.3.1 Experimental setup of the optical bench

Figure 5-3 details the experimental setup of the optical bench used to evaluate the fabricated $Ti_3C_2T_x$/LC lens. The following components were mounted onto the optical rail: a CMOS camera (Basler ace acA1920-40gm, Germany), an iris, a mount to hold the $Ti_3C_2T_x$/LC lens, a target holder on a translation stage, a diffuser, a collimating

lens, and an LED. The camera was set up to record 10 frames per second. The iris reduced the amount of scattered light from the environment to the camera. The collimating lens and the diffuser were used to capture and focus the light from the LED to provide a uniform gaussian-like distribution.

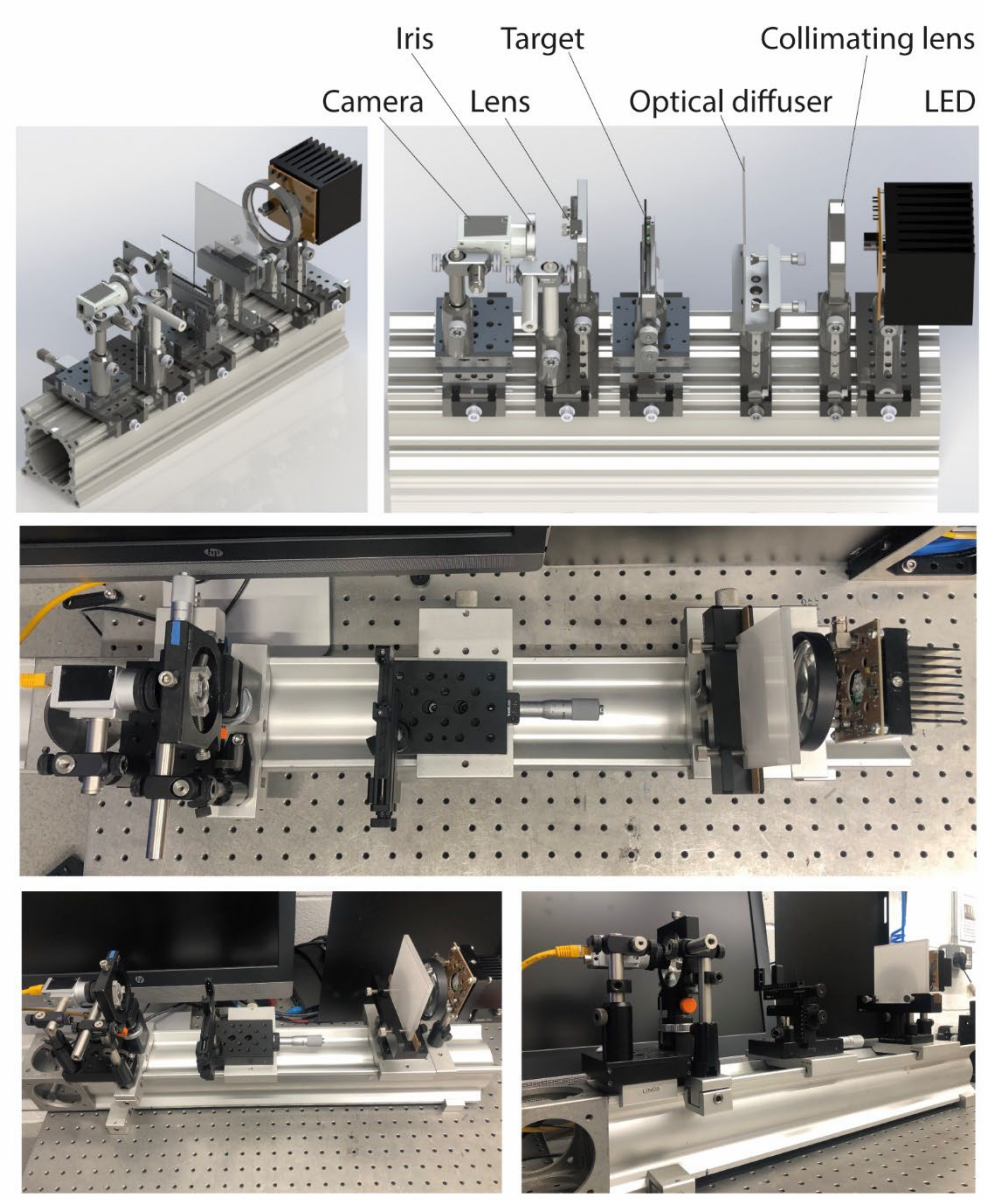

Figure 5-3 – Schematic and digital images of the experimental setup of the optical bench used to evaluate the $Ti_3C_2T_x$/liquid crystal lens, detailing the camera, iris, lens target holder on a translation stage, diffuser, collimating lens, and LED.

The power supply was a Keithley SMU 2450 Source meter (Tektronix, USA). The $Ti_3C_2T_x$/LC lens and the camera were triggered simultaneously using a purpose-built trigger generator. An overview of the setup is demonstrated in ***Figure 5-4***. The trigger generator was connected to the pulse generator (Quantum Composers model 9614), connected to the camera. The power supply, the trigger and pulse generators were connected to an oscilloscope (LeCroy WaveSurfer 424) to monitor the signal of each component.

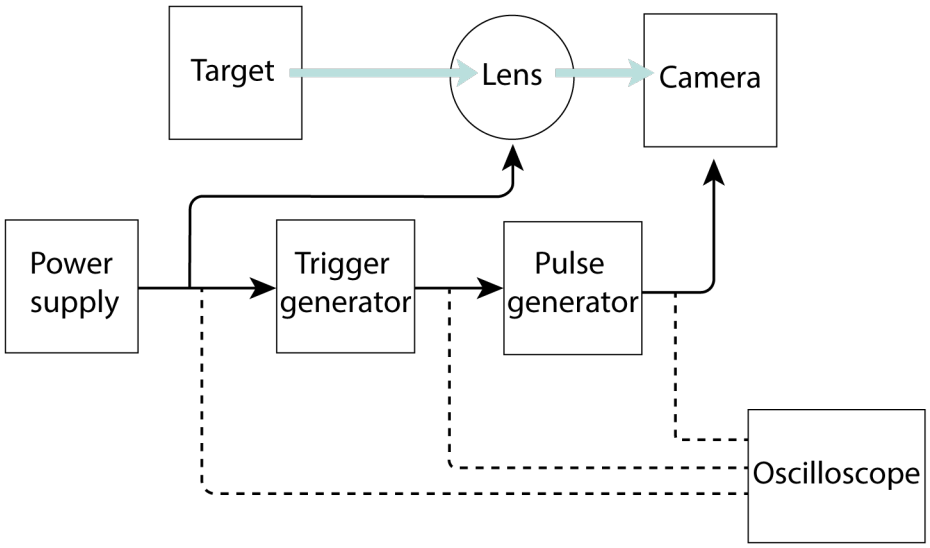

Figure 5-4 – Schematic of the experimental setup for the optical measurements detailing the power supply connected to the lens and the trigger generator, connected to the pulse generator, connected to the camera. The power supply, the trigger and pulse generators were connected to an oscilloscope.

5.3.3.2 Change of focus of the $Ti_3C_2T_x$/liquid crystal lens

The focus position of the $Ti_3C_2T_x$/LC lens was evaluated in the presence and absence of the external field using a 5 cy mm^{-1} Ronchi ruling that was mounted in the target

holder tilted at a 45° angle along the optical axis, shown in ***Figure 5-5***. The Ronchi target is a series of equally spaced opaque lines. 0 – 40 V was investigated and for each magnitude of the applied field, 100 frames were analysed. The data was processed using the script detailed in Appendix 3 – Ronchi focus position MATLAB script.

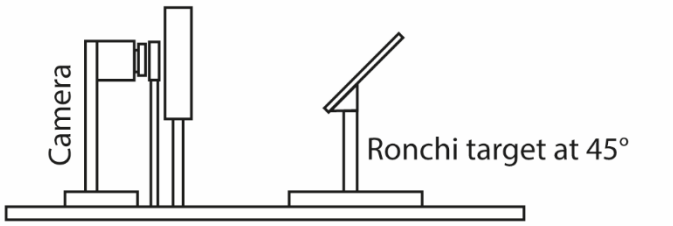

Figure 5-5 – Schematic of the optical evaluation setup for the change of focus investigation to demonstrate the position of the Ronchi ruling tilted at a 45° angle to the optical axis.

5.3.3.3 The optical quality of the $Ti_3C_2T_x$/liquid crystal lens

The optical quality of the $Ti_3C_2T_x$/LC lens was assessed by evaluating the modulation transfer function (MTF) using the slanted edge, ISO 12233 compatible, target and using a Siemens star target. The slanted edge data was processed using the script found in Appendix 4 – Slanted edge MTF MATLAB script.

5.3.4 Design and development of a polymer-based $Ti_3C_2T_x$/liquid crystal lens

A PMMA lens was designed using the lens makers formula shown below (Equation 5.1).

$$P = \frac{1}{f} = (n-1)[\frac{1}{R_1} - \frac{1}{R_2} + \frac{(n-1)t}{nR_1R_2}] \quad (5.1)$$

Where P is optical power measured in dioptres (D), f is the focal length, n is the refractive index, R_1 and R_2 are the radii of curvature of the anterior and posterior lens surfaces, and t is the centre thickness of the lens.

The lens was designed in two halves (lens 1 and 2) and lathed using a 100 A Dac lathe. The lens halves were plasma-treated with a 10-minute treatment of pure oxygen plasma at 100 W and 10 cm^3 min^{-1} using a Henniker plasma etcher (Henniker plasma, UK). Then spin-coated with $Ti_3C_2T_x$ in the two-step spin coating method at 5000 rpm for 2 minutes followed by 6000 rpm for 1 minute with an Ossila spin coater (Ossila, UK) and incubated for 24 hours at 80 °C. Contact points were added with silver conductive paint, then spin-coated with 3 % PVA, and returned to the oven for 1 hour at 80 °C. Microgrooves were introduced to align the LC molecules using a microfibre cloth. The 25 µm thick double-sided adhesive was applied to lens 2, and 3 – 5 µL of 5CB LC was pipetted into the LC cavity (in the optic). Lens 1 was placed on lens 2 and secured in place. Wires were attached to connect to the power supply for investigation.

5.3.4.1 Protocol development of the polymer-based $Ti_3C_2T_x$/liquid crystal lens

The PMMA lenses were lathed and polished using an aluminium oxide polishing slurry for 24 hours at 100 rpm. The lenses were plasma treated and coated with $Ti_3C_2T_x$ following the protocol described above. The coating was examined with light

microscopy and SEM (Zeiss Supra 50VP, Germany) with a 5 kV accelerating voltage. The lenses were not sputter coated.

The $Ti_3C_2T_x$ coating procedure was investigated further. PMMA lenses were lathed, polished, and plasma treated as described above. The spin speed was varied over the following range 4000 – 6000 rpm. The coated lenses were imaged with (SEM) microscopy and qualitative energy dispersive x-ray (EDX) (Oxford Instruments, Aztec 2.2, XMax80) point selection analysis was performed. The accelerating voltage was 10 keV, working distance 8.5 mm, 30-micron aperture, and a 5 second scan.

5.3.4.2 Fabrication of a polymer-based $Ti_3C_2T_x$/liquid crystal test cell

A flat sheet of PMMA was cut into 50 mm by 20 mm sections to construct a PMMA test cell. The PMMA slides were plasma treated and coated following the test cell fabrication protocol detailed in section 4.2.3. Another batch of PMMA slides were functionalised with acrylic acid (AAc). The plasma polymerisation of AAc to the PMMA surface was applied with a 3-minute plasma treatment at 200 W using a Henniker plasma etcher (Henniker plasma, UK). $Ti_3C_2T_x$ was spin-coated onto the PMMA-AAc through a two-step method, 5000 rpm for 2 minutes and 6000 rpm for 1 minute, then transferred to the 80 °C oven for 24 hours to anneal. The contact angle of the PMMA-AAc was compared to PMMA. A 5 μL syringe (Hamilton Company, USA) was filled with deionised water and deposited controlled volumes onto the sample surface with the sessile drop method. The contact angle of the deposited water was measured (DataPhysics Instruments OCA15, Germany). The analysis was repeated in triplicate. After annealing, the fabrication of the PMMA-AAc test cell followed the standard test cell protocol, adding the PVA alignment layer, introducing

the microgrooves to set the alignment, followed by assembly and filling with 5CB, see section 4.2.3.2 – 4.2.3.4 for more details.

5.3.5 Statistics

GraphPad prism (9.3.1) (GraphPad Software Inc., USA) was used for the statistical analysis of the Ronchi data. Descriptive statistics and normality tests were performed, and the non-parametric Friedman test with multiple comparisons post hoc Dunn's test was carried out. Prism was also used in the PMMA coating protocol analysis, where a one-way ANOVA and Tukey's multiple comparisons tests were performed.

5.4 Results

A $Ti_3C_2T_x$/LC lens was fabricated to develop an AIOL design for cataract patients. The $Ti_3C_2T_x$ nanomaterial provides the possibility of progression to a flexible and implantable lens. The work presented in this thesis demonstrates that the two-dimensional material is conductive, transparent, flexible, biocompatible in an ocular model and is capable of facilitating molecular reorientation of an LC. This chapter investigated the next steps in developing an adaptive focus $Ti_3C_2T_x$/LC lens by assessing if $Ti_3C_2T_x$ could facilitate a change in focus.

5.4.1 Fabrication of a glass-based $Ti_3C_2T_x$/liquid crystal lens

The glass-based $Ti_3C_2T_x$/LC lens was constructed the same way as the test cell. The lens substrates and operating principles were selected based on their geometry and

accessibility. ***Figure 5-6*** shows lenses 1 and 2 coated with $Ti_3C_2T_x$ and PVA on the inner surface. The alignment was set at 90° in the TN orientation, and silver conductive paint was applied to connect the $Ti_3C_2T_x$ electrode coating to the power supply. The double-sided adhesive set the cavity thickness and attached lenses 1 and 2 to one another, and lens 3 was adhered with glue. ***Figure 5-6*** also demonstrates the ordered LC cavity in the digital images where polarising filters were placed above and below the lens. The dark region of the image on the left identifies the LC molecules were aligned in the opposite direction to the polarising filters, the LC twists the light in the opposite direction to the polarising filter. Further demonstrated in the right image, as the crossed polar films present dark, the cavity is bright, and light can pass through. The observations were made before incorporating the external stimuli to view the molecule's alignment and check for inconsistencies and defects that would result in unwanted optical aberrations.

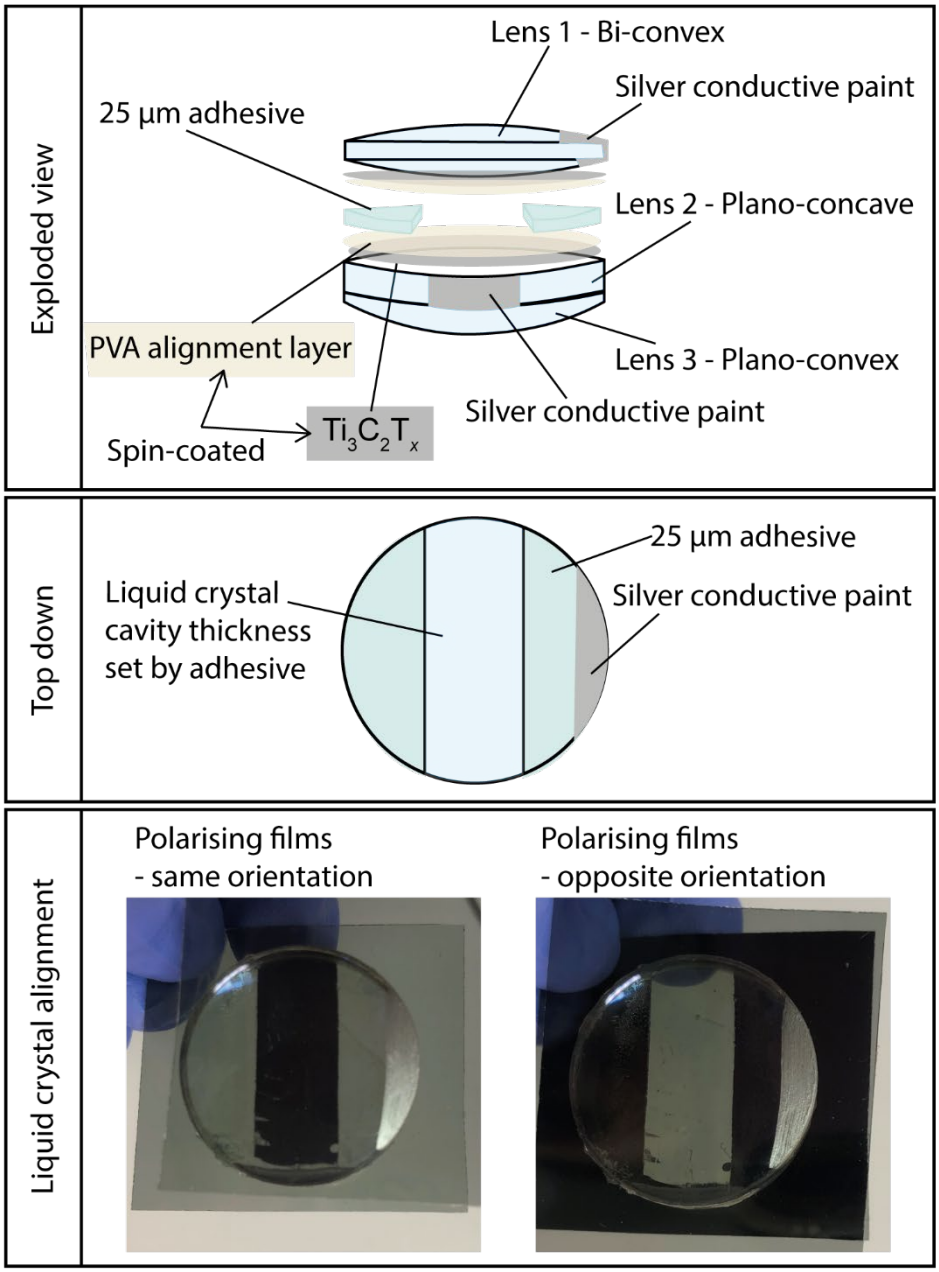

Figure 5-6 – Schematic and digital images of the $Ti_3C_2T_x$/liquid crystal lens. The exploded view shows the three lenses used to construct the final lens. Lens 1 and 2 are spin-coated with $Ti_3C_2T_x$ and PVA for the alignment. The double-sided adhesive stuck the lenses (1 and 2) together and formed the cavity for the LC. Contacts were added with silver conductive paint to connect to the power supply. The top-down view displays the LC cavity and the silver paint connection. The liquid crystal alignment section shows digital images of the $Ti_3C_2T_x$/liquid crystal lens between two polarising

films in the same direction, demonstrating that the LC cavity is blocking light (dark region left image) and the $Ti_3C_2T_x$/liquid crystal lens between two polarising films in the opposite directions, showing the LC cavity allowing the passage of light (bright region right).

5.4.2 Optical evaluation of the glass-based $Ti_3C_2T_x$/liquid crystal lens

The optical evaluation of the glass-based $Ti_3C_2T_x$/LC lens used several optical targets, including a Ronchi ruling, a slanted edge MTF, and Siemens star, to assess optical performance and image quality. The investigation required a purpose-built trigger generator to allow the power supply and the camera to be activated simultaneously. Timings were of particular interest. Specifically, the relationship between the voltage applied to the lens and the individual frame exposures were controlled using a pulse generator as the camera required a trigger edge for each exposure that the trigger could not produce. The Keithley 2450 SourceMeter supplied 5 – 40 V to the trigger generator that converted the output to 5 V to trigger the pulse generator without damaging it. The trigger generator was composed of a resistor, a diode and a Zener diode to form a Zener regulator. The pulse generator triggered the camera on the rising edge of the signal, capturing 10 frames per second.

5.4.2.1 Change of focus of the $Ti_3C_2T_x$/liquid crystal lens

The change of focus of the $Ti_3C_2T_x$/LC lens was first investigated as part of the optical evaluation. A Ronchi ruling was used to observe if there was a difference in focus position in the presence or absence of the electric potential. ***Figure 5-7*** illustrates that

the focus position can be obtained when the target is angled, showing the centre of the target in focus and the periphery out of focus.

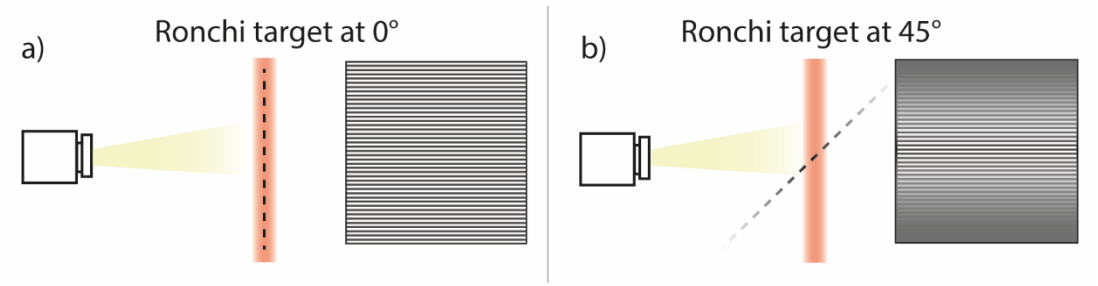

Figure 5-7 – Schematic representation of how the focus is determined using the Ronchi ruling target. (a) The target is at 0°, and the whole target is focused. (b) The target tilted at a 45° angle to the optical axis, causing the centre to be in focus and the periphery out of focus.

Three lenses were fabricated for the evaluation, lenses A, B, and C. The Ronchi ruling analysis of lens A is demonstrated in ***Figure 5-8***, (a) shows an example of the MATLAB analysis on a single frame with 0 V applied. The black crosses indicate the best local focus position, and the red line illustrates the median focus position over the whole frame, 100 frames were analysed for each condition. ***Figure 5-8*** (b-e) shows the focus position for 10, 20, 30, and 40 V, respectively. Lens A's focus position at varying voltages was plotted as a function of time, shown in ***Figure 5-8*** (f-g). At 0.1 s, the focus position for the lens with 10 V applied was 1.558 mm, and by 0.2 s, the position reached 2.287 mm, where it remained stable over the period the field was applied. The application of 20, 30, and 40 V demonstrated consistent focus positions from the first measurement. ***Figure 5-8*** (h) shows the relationship between the lens's

focus position and the applied voltage. A significant difference was observed when comparing the absence of the field to the application of the field for each voltage applied ($p < 0.0001$). The largest change observed was 0 V compared to 10 V, with a 2.285 ± 0.076 mm (mean ± SD, $n = 100$) difference. As the voltage was increased to 20, 30 and 40 V, the focus position saw a rise in each example, with values of 2.298 ± 0.013 mm, 2.300 ± 0.007 mm, and 2.307 ± 0.005 mm, respectively (mean ± SD, $n = 100$), indicating that the refractive index switch occurred between 0 V and 10 V.

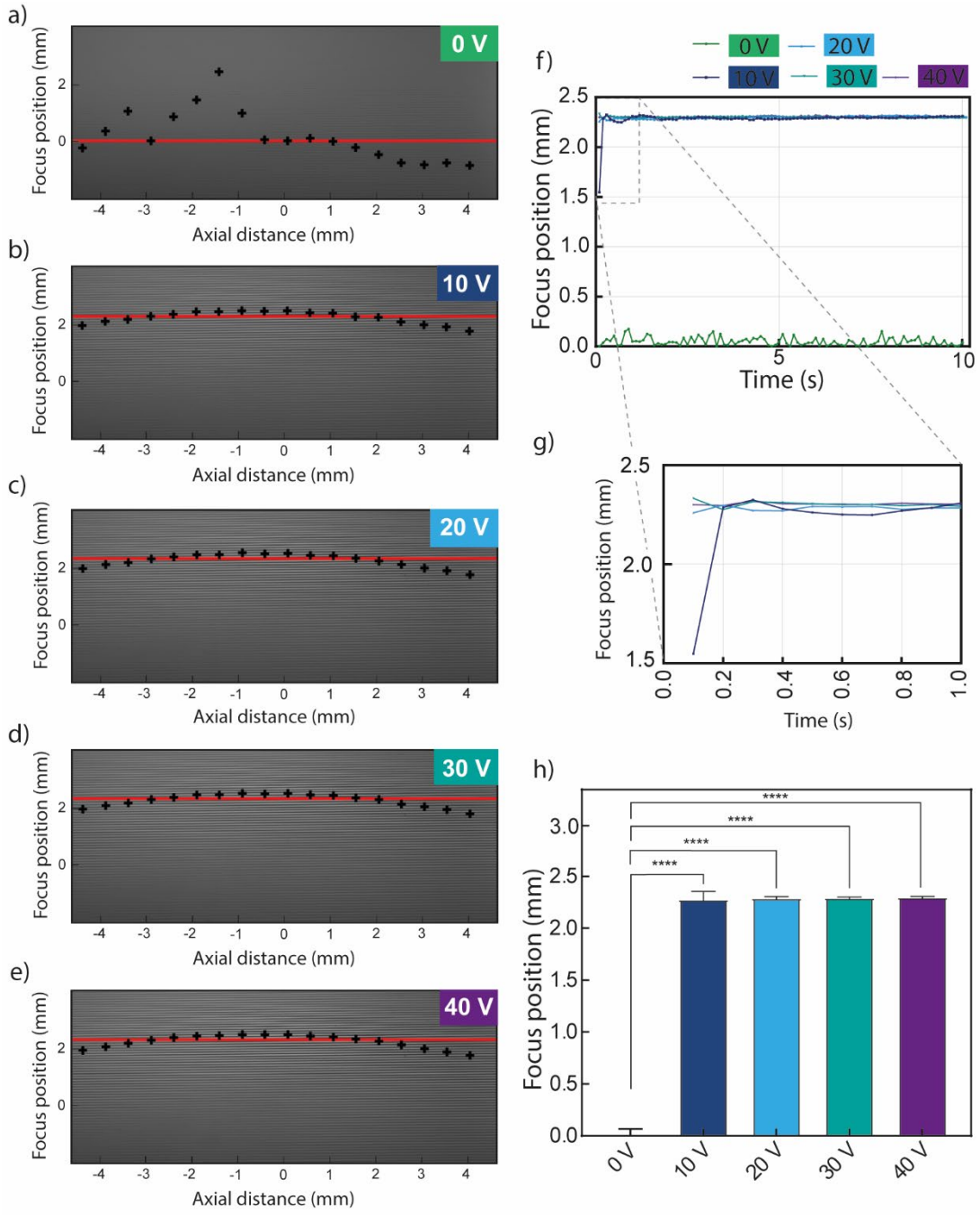

Figure 5-8 – Change of focus evaluation of lens A in the presence and absence of the electric field using a Ronchi ruling target tilted at a 45° angle to the optical axis. The voltage was increased in 10 V increments from 0 to 40 V. (a-e) A single measurement for the specified electrical potential applied. The black crosses identify the best local focus position, and the red line indicates the median focus position over the whole frame. (f) Focus position as a function of time. (g) An enlarged section of the focus

position as a function of time plot to highlight the initial focus positions. (h) Focus position with respect to the voltage applied (mean ± SD, n = 100, **** $p < 0.0001$).

The Ronchi ruling analysis of lens B, shown in ***Figure 5-9***, demonstrates the change in focus position with and without the electric field, (a-e) are examples of a single frame and the MATLAB analysis for the frame at the particular voltage. The analysis observed the change in focus over time, presented in ***Figure 5-9*** *(f-g)*. A more consistent and stable measurement was established with a larger electrical potential applied to the lens. For example, with 10 V applied, the measurement from the first frame was 0.844 mm, then by the second frame 0.934 mm and, with 20 V applied, an initial spike was observed in the first measurement that then decreased until it stabilised after 0.4 s to 0.896 mm. ***Figure 5-9*** *(h)* demonstrates the relationship between the field applied and focus position. A significant difference was displayed between the application of the field and not. The greatest change in focus was observed when 0 V was compared to 10 V, and the position changed by 0.875 ± 0.013 mm. The focus positions with 20, 30, and 40 V applied were 0.945 ± 0.015 mm, 0.958 ± 0.009 mm and 0.963 ± 0.008 mm, respectively (mean ± SD, n = 100).

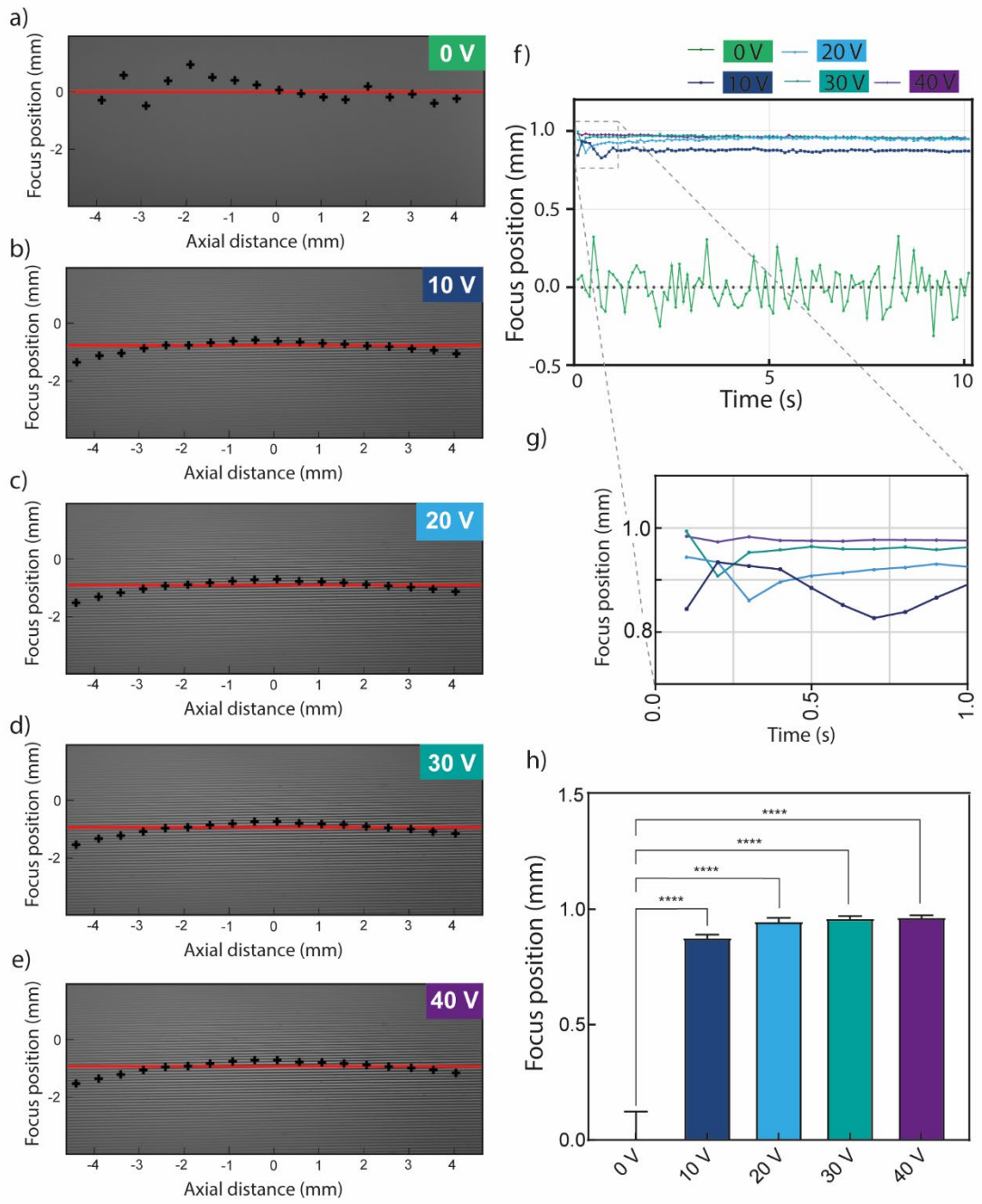

Figure 5-9 – Change of focus evaluation of lens B in the presence and absence of the electric field using a Ronchi ruling target tilted at a 45° angle to the optical axis. The voltage was increased in 10 V increments from 0 to 40 V. (a-e) A single measurement for the specified electrical potential applied. The black crosses identify the best local focus position, and the red line indicates the median focus position over the whole frame. (f) Focus position as a function of time. (g) An enlarged section of the focus

position as a function of time plot to highlight the initial focus positions. (h) Focus position with respect to the voltage applied (mean ± SD, n = 100, **** $p < 0.0001$).

The focus change analysis of Lens C using the Ronchi target is displayed in ***Figure 5-10***. The target was angled at 45°, and the electric field was applied incrementally. Plots (a-e) show a single frame of the MATLAB analysis used to determine the focus position of the lens in the presence/absence of the field. Lens focus as a function of time is shown in ***Figure 5-10*** (f-g). When 10 V was applied to the lens, the first measurement was 0.533 mm, then spiked to 0.755 mm at 0.2 s. After the rise, the focus position dropped to 0.467 mm at 1.0 s. A similar trend was observed for 20 V, where the measurement spiked to 0.741 mm, then decreased to 0.411 mm at 0.6 s. For 30 and 40 V, a spike and then a small drop was observed, with a slight resemblance to the trend exhibited by the lower voltages. ***Figure 5-10*** *(h)* displays the average focus position for the applied field. As with lenses A and B, lens C also demonstrated a significant difference in change of focus in the presence compared to the absence of the field. The greatest shift observed was with the application of 10 V when compared to 0 V, with a focus position of 0.673 ± 0.062 mm, while 20, 30 and 40 V were found to be 0.695 ± 0.051 mm, 0.743 ± 0.027 mm and 0.748 ± 0.022 mm, respectively (mean ± SD, n = 100).

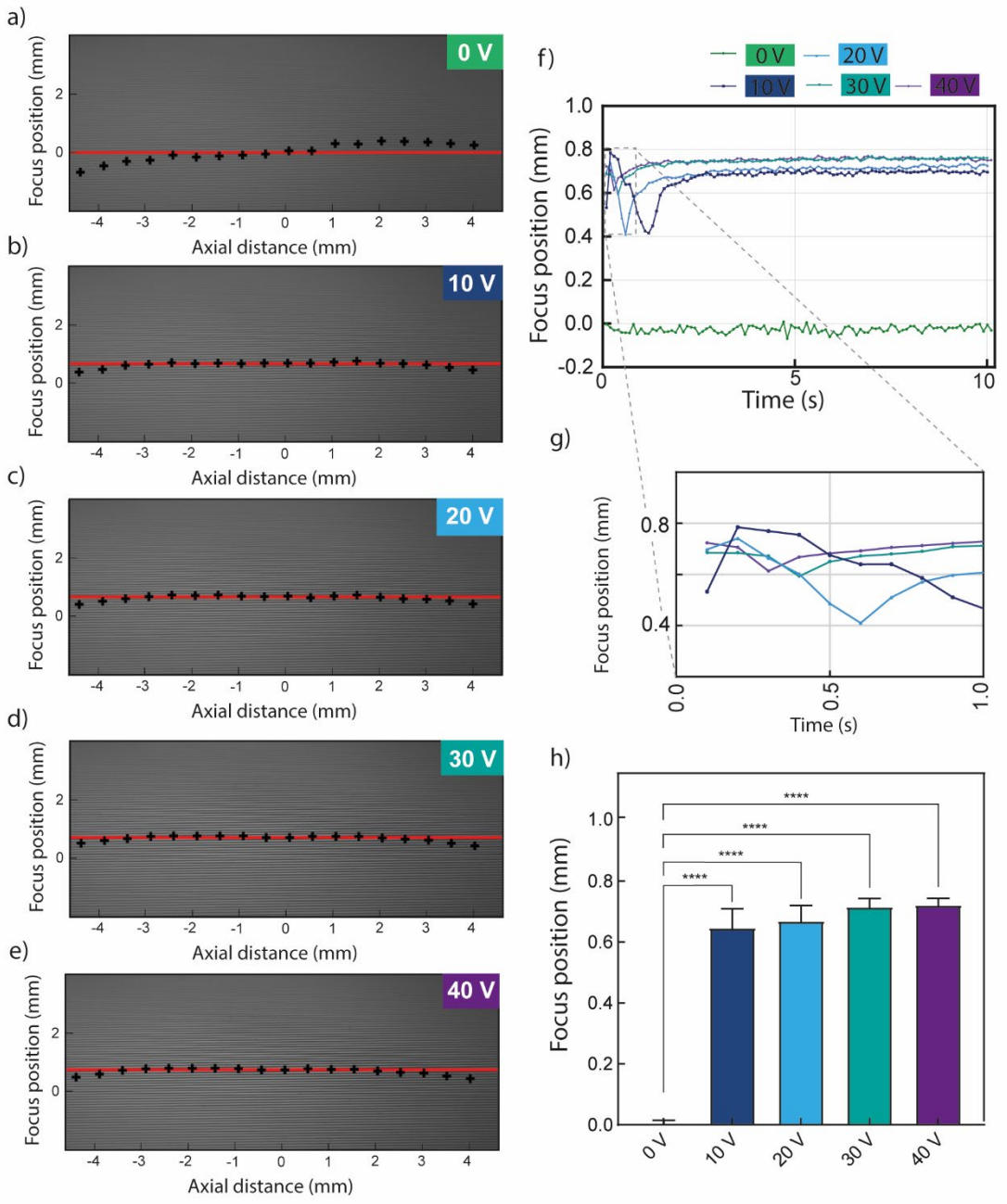

Figure 5-10 – Change of focus evaluation of lens C in the presence and absence of the electric field using a Ronchi ruling target tilted at a 45° angle to the optical axis. The voltage was increased in 10 V increments from 0 to 40 V. (a-e) A single measurement for the specified electrical potential applied. The black crosses identify the best local focus position, and the red line indicates the median focus position over the whole frame. (f) Focus position as a function of time. (g) An enlarged section of the focus

position as a function of time plot to highlight the initial focus positions. (h) Focus position with respect to the voltage applied (mean ± SD, n = 100, **** $p < 0.0001$).

5.4.2.2 The optical quality of the $Ti_3C_2T_x$/liquid crystal lens

The optical quality of the $Ti_3C_2T_x$/LC lens was evaluated by assessing resolution and performance through MTF measurements. The MTF measures the ability of the lens to transfer contrast information at a particular resolution from the object to the image.[167] Spatial frequency is expressed in line pairs (lp mm^{-1}), with one pair consisting of one black and one white line. The resolution of a lens is its ability to differentiate spatial frequencies. High-resolution images experience minimal blurring and large amounts of detail, whereas low-resolution images display a greater degree of image blurring and lack fine detail. The contrast or modulation of an imaging lens is how accurately the minimum and maximum intensity values are transferred from the object to the image. Furthermore, the MTF estimation of an optical system is a method of analysis that combines resolution and contrast into a single metric. Several methods can measure MTF, including the slanted edge technique, which uses an opaque edge[253]. This approach is widely accepted and recognised by ISO 12233 as the standard for characterising the optical resolution of lenses.

The MTF target was imaged with lens A, over a range of distances, as demonstrated in ***Figure 5-11***. The distance was established by observing the lens in the presence of the field whilst translating the target along the optic axis to include the target presenting out of focus, in then out again. The working distance was varied over 10 mm, from 100 to 110 mm, to determine the maximum spatial frequency at MTF50 (cy mm^{-1}). The greatest MTF value measured was at 104 mm, demonstrating that with the

applied field, the lens is most focused at this position. Whereas in the absence of the field, the MTF50 value was slightly higher at 100 mm compared to 110 mm, indicating the possibility that the focal point was closer than demonstrated over the working distance investigated. ***Figure 5-11*** shows images of the target at 104 mm in the presence and absence of the field. The MTF50 was 0.677 ± 0.002 and 6.627 ± 0.014 cy mm^{-1} for 0 and 40 V, respectively (mean ± SD, n = 30). The difference in MFT50 value demonstrates an increase in contrast and spatial resolution of lens A in the presence of the field.

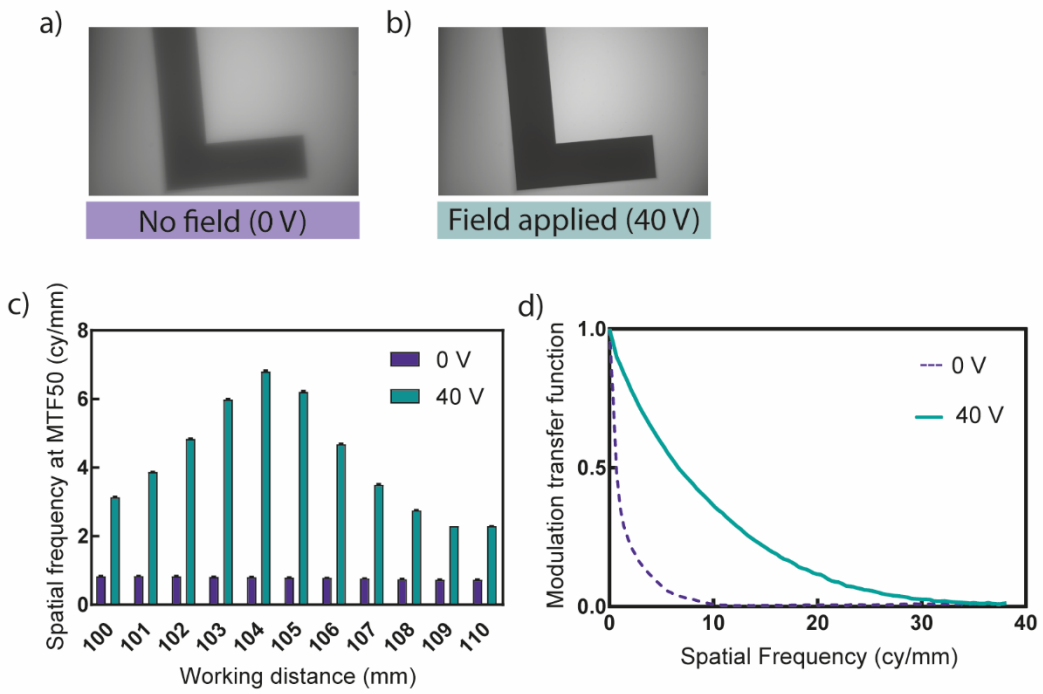

Figure 5-11 – Modulation transfer function (MTF) of lens A. (a) Image of the slanted edge MTF target observed through lens A in the absence of the field at 104 mm. (b) Image of the slanted edge MTF target observed through lens A in the presence of 40 V at 104 mm. (c) The spatial frequency at MTF50 (cy mm^{-1}) as a function of the working distance (mm). (d) MTF of lens A in the presence (40 V) and absence (0 V)

of the electric field, MTF50 was 6.627 ± 0.014 and 0.677 ± 0.002, respectively (mean ± SD, n = 30).

The MTF of lens B was investigated in the same way as lens A, demonstrated in ***Figure 5-12***. The working distance was investigated from 92 to 102 mm. The maximum MTF value in the presence of the field was at 96 mm, demonstrating the most focused position for lens B. Similarly to lens A, a slightly higher MTF50 value was observed at 92 mm compared to 102 mm, suggesting that the best focus position could be closer than the distance range observed here in the absence of the field. Images shown in ***Figure 5-12*** of the target at 96 mm were imaged with the lens in the presence and absence of the field. The MTF50 was 0.491 ± 0.002 and 4.706 ± 0.209 cy mm^{-1} for 0 and 40 V, respectively (mean ± SD, n = 30). An increase in contrast and resolution was observed in the presence of the field, demonstrating that the refractive index switched from ordinary to extraordinary, improved image quality at this focal length.

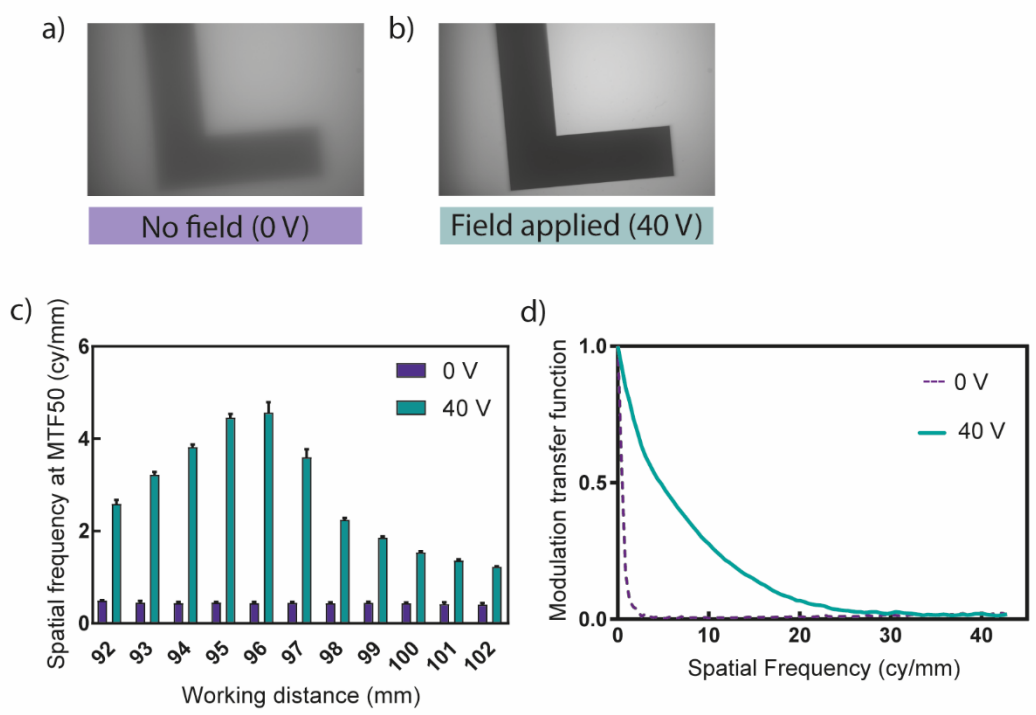

Figure 5-12 – Modulation transfer function (MTF) of lens B. (a) Image of the slanted edge MTF target observed through lens B in the absence of the field. (b) image of the slanted edge MTF target observed through lens B in the presence of 40 V. (c) The spatial frequency at MTF50 (cy mm^{-1}) as a function of the working distance. (d) MTF of lens B in the presence (40 V) and absence (0 V) of the electric field, MTF50 was 4.706 ± 0.209 and 0.491 ± 0.002, respectively (mean ± SD, n = 30).

The MTF of lens C was evaluated in ***Figure 5-13***. The working distance was investigated from 97 to 107 mm, where the maximum MTF value with the field was at 102 mm, displaying the most focused position with the field. In the absence of the field, it is evident that the most focused position was closer than the working distance range investigated, indicated by the increase in MTF50 as the distance approaches 97 mm. ***Figure 5-13*** displays images of the target at 102 mm imaged with the lens in the presence and absence of the field. The MTF50 was 1.030 ± 0.001 and 2.968 ± 0.351

cy mm^{-1} for 0 and 40 V, respectively (mean ± SD, n = 30). The increase in contrast and resolution in the presence of the field, shows how the switched refractive index improved image quality at 102 mm.

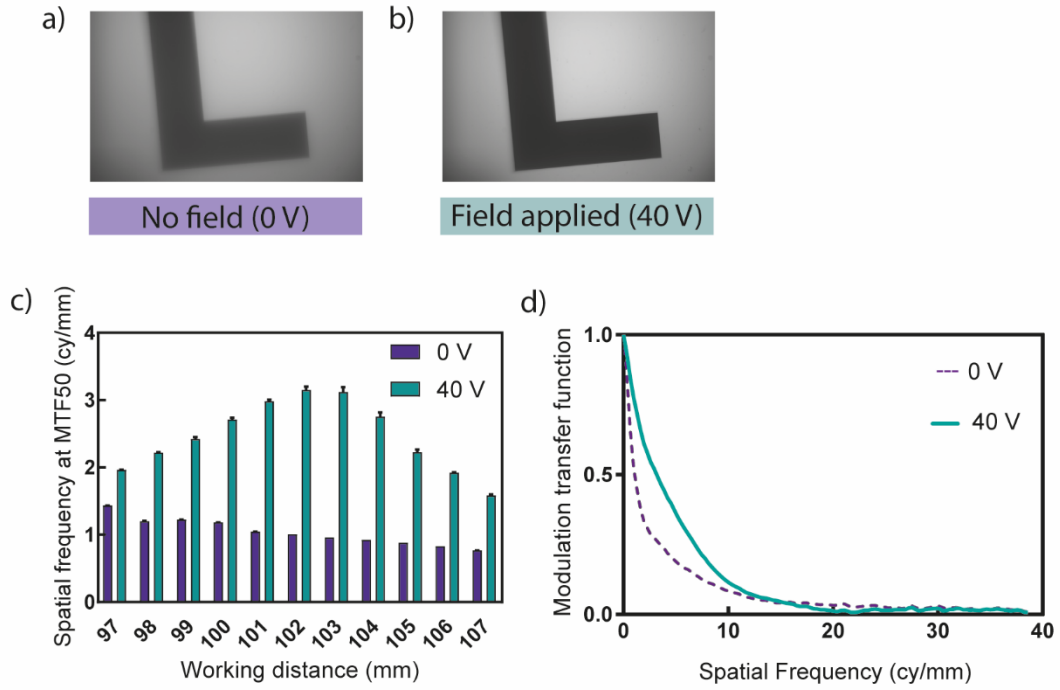

Figure 5-13 – Modulation transfer function (MTF) of lens C. (a) Image of the slanted edge MTF target observed through lens C in the absence of the field. (b) image of the slanted edge MTF target observed through lens C in the presence of 40 V. (c) The spatial frequency at MTF50 (cy mm^{-1}) as a function of the working distance, (30 frames). (d) MTF of lens C in the presence (40 V) and absence (0 V) of the electric field, MTF50 was 2.968 ± 0.351 and 1.030 ± 0.001, respectively (mean ± SD, n = 30).

The Siemens star target was used to assess the image quality of the lenses shown in ***Figure 5-14***. The target consists of bright and dark spokes that gradually become narrower until they meet at the centre point. This optical target is used to evaluate the presence of contrast reversal, which can significantly degrade the optical performance

of an optical system. The target was placed at the working distance identified during the MTF evaluation for A, B, and C at 104 mm, 96 mm and 102 mm, respectively. All three lenses demonstrated superior image quality in the presence of the field with fewer aberrations, and no discernible contrast reversal (i.e. the correct black/white pattern is maintained across the star pattern).

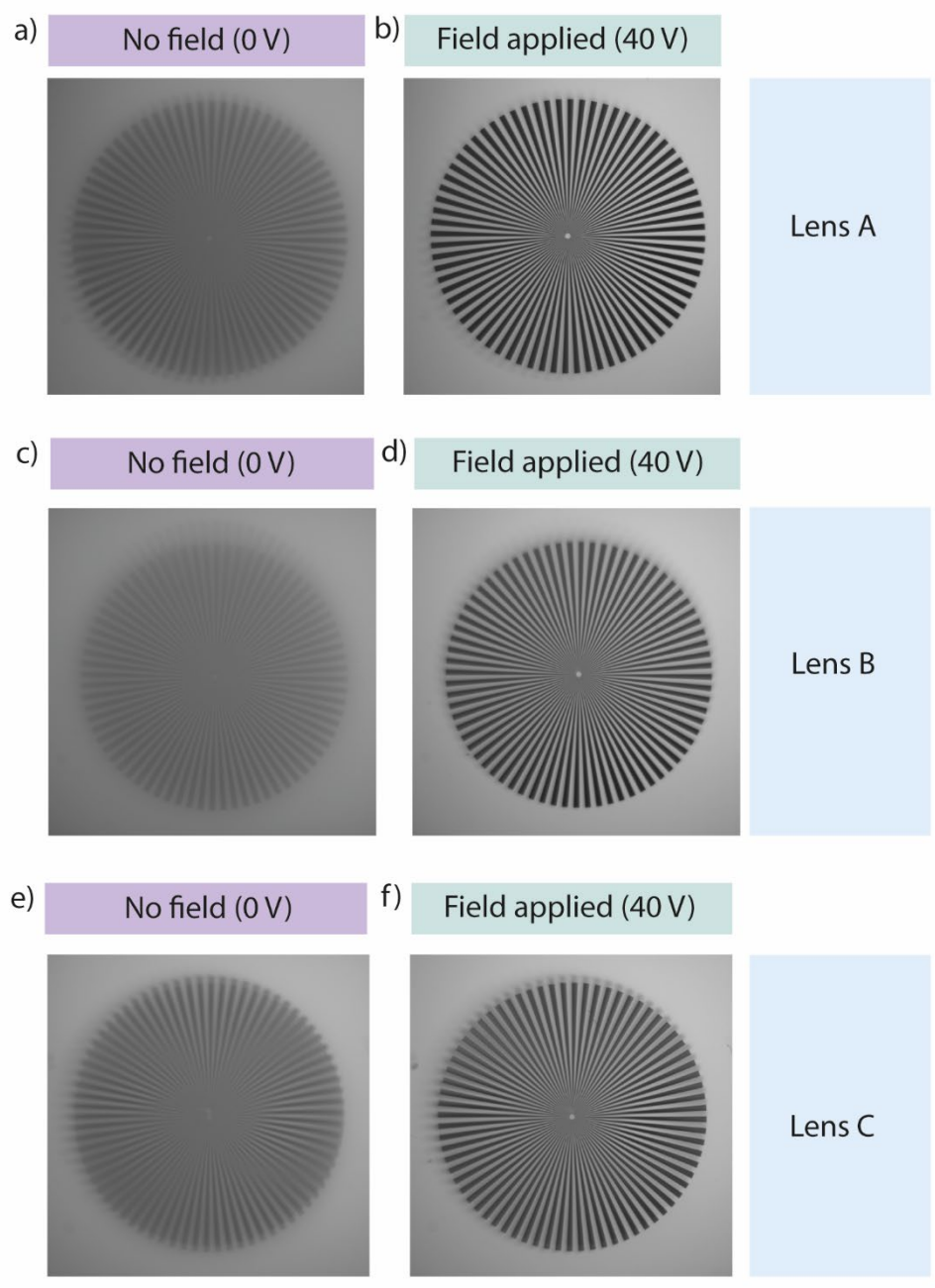

Figure 5-14 – Image quality evaluation of the fabricated $Ti_3C_2T_x$/liquid crystal lenses A, B, and C using a Siemens star target. (a) Lens A 0 V applied. (b) Lens A 40 V applied. (c) Lens B 0 V applied. (d) Lens B 40 V applied. (e) Lens C 0 V applied. (f) Lens C 40 V applied.

5.4.3 Design and development of a polymer-based $Ti_3C_2T_x$/liquid crystal lens

Whilst a change in focus was demonstrated with the glass $Ti_3C_2T_x$/LC lens, the substrate lacks suitability for use in eye as an IOL, thus a PMMA design was explored. The lens makers formula (Equation 5.1) was used to design the lens, an overview of the design is shown in ***Figure 5-15***, optical power calculations in the absence of the field are shown in ***Table 5-2***, and optical power calculations in the presence of the field are shown in ***Table 5-3***. The lens was designed to produce 3 D of accommodative amplitude. The computed optical power of the lens without the field applied was 20.01 D and with the field 23.52 D.

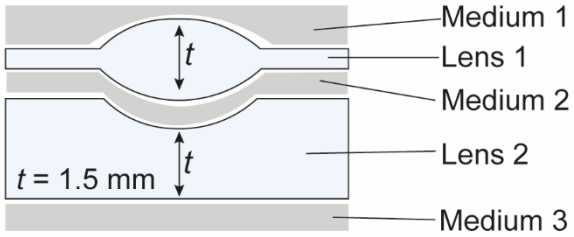

Figure 5-15 – Schematic of the PMMA lens to support the lens calculations displayed in tables 5-2 and 5-3 by defining medium 1, lens 1, medium 2, lens 2, and medium 3.

Table 5-2 – PMMA lens optical power calculations, demonstrated in the absence of the electric field.

	Material	Index of refraction	Surface	Radius of curvature (mm)	Optical power at each surface (D)
Medium 1	Water	1.333	1	8.260	19.25
Lens 1	PMMA	1.492	2	-5.500	-7.82
Medium 2	Liquid crystal	1.535	3	-5.090	8.45
Lens 2	PMMA	1.492	4	10000	-0.02
Medium 3	Water	1.333		Power lens 1	11.58
				Power lens 2	8.43
				Total power (D)	20.01

Table 5-3 – PMMA lens optical power calculations, demonstrated in the presence of the electric field.

	Material	Index of refraction	Surface	Radius of curvature (mm)	Optical power at each surface (D)
Medium 1	Water	1.333	1	8.260	19.25
Lens 1	PMMA	1.492	2	-5.500	-42.91
Medium 2	Liquid crystal	1.728	3	-5.090	46.37
Lens 2	PMMA	1.492	4	10000	-0.02
Medium 3	Water	1.333		Power lens 1	-22.83
				Power lens 2	46.35
				Total power (D)	23.52

The lathed PMMA lens halves can be seen in ***Figure 5-16***, with lens 1 as the top half of the PMMA/$Ti_3C_2T_x$/LC lens and lens 2 as the bottom half. ***Figure 5-16*** (a-b) also highlights one of the issues that occurred during the fabrication of the PMMA lens. The digital images show a constructed PMMA/$Ti_3C_2T_x$/LC lens with an air bubble in the centre of the optic in the LC cavity. Unlike the test cell and the glass-based lens, the cavity could no longer be filled through capillary forces. A known volume of the LC was pipetted onto the cavity of lens 2 and lens 1 was positioned with great caution

to prevent the introduction of air bubbles. Regardless of the care taken during assembly, switching of the refractive index was not observed.

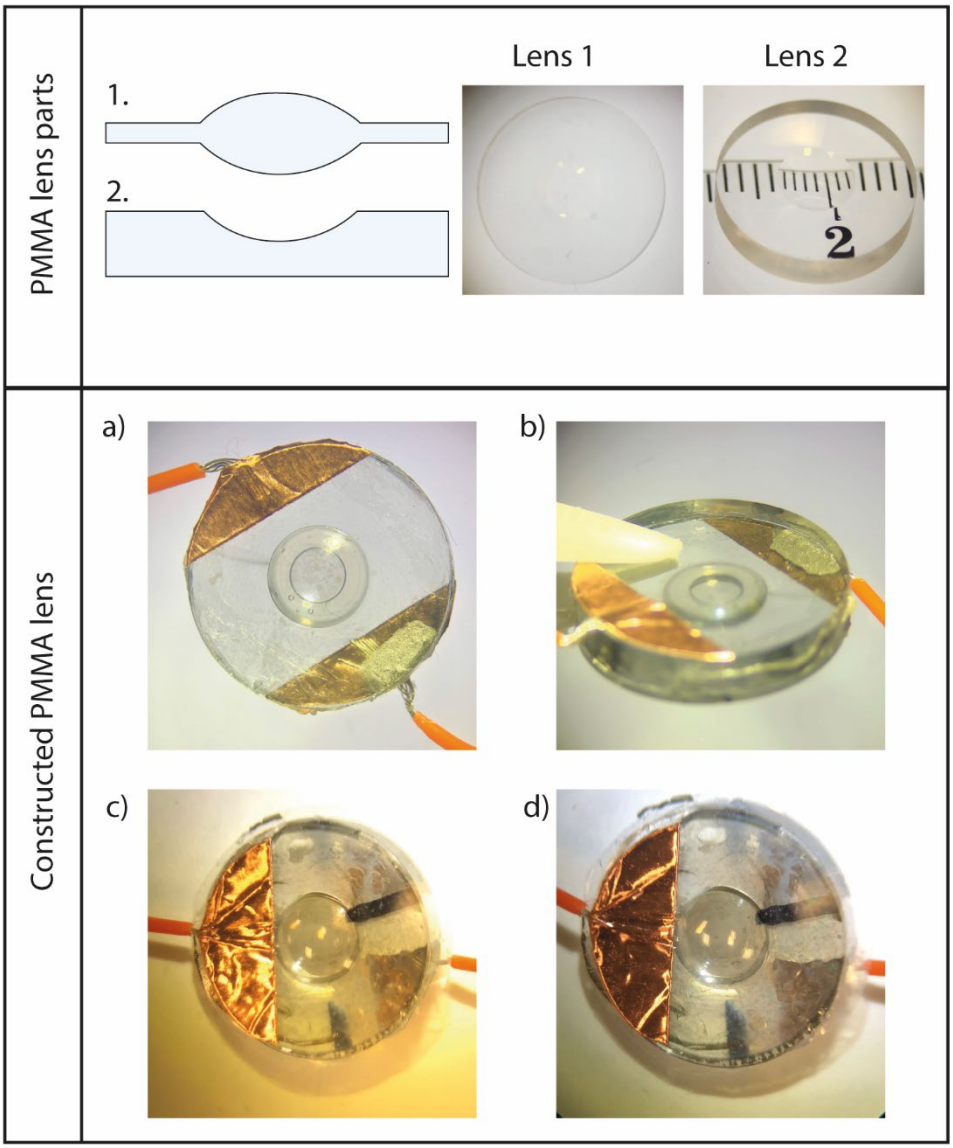

Figure 5-16 – Schematic and digital images of the Poly(methyl methacrylate) (PMMA) $Ti_3C_2T_x$/liquid crystal lens. PMMA lens parts, demonstrating lens 1 as the top half of the lens and lens 2 as the bottom half of the lens. (a-b) Digital images of a constructed PMMA $Ti_3C_2T_x$/liquid crystal lens with an air bubble in the liquid crystal cavity. (c-d) Digital images of a constructed PMMA $Ti_3C_2T_x$/liquid crystal lens, no air bubble.

5.4.3.1 Protocol development of the polymer-based $Ti_3C_2T_x$/liquid crystal lens

In the first instance, the electrical connection was examined, and an issue with the $Ti_3C_2T_x$ coating was observed. ***Figure 5-17*** shows digital images of lens 2, the bottom half of the PMMA lens, coated with $Ti_3C_2T_x$. The images (a-c) identified clumping and inconsistencies in the electrode coating. The protocol was reassessed, and the lathed lenses were polished, following Rayner's standard method used in their manufacturing process before coating with $Ti_3C_2T_x$. The coating appeared to be more uniform, though some inconsistencies remained across the optic.

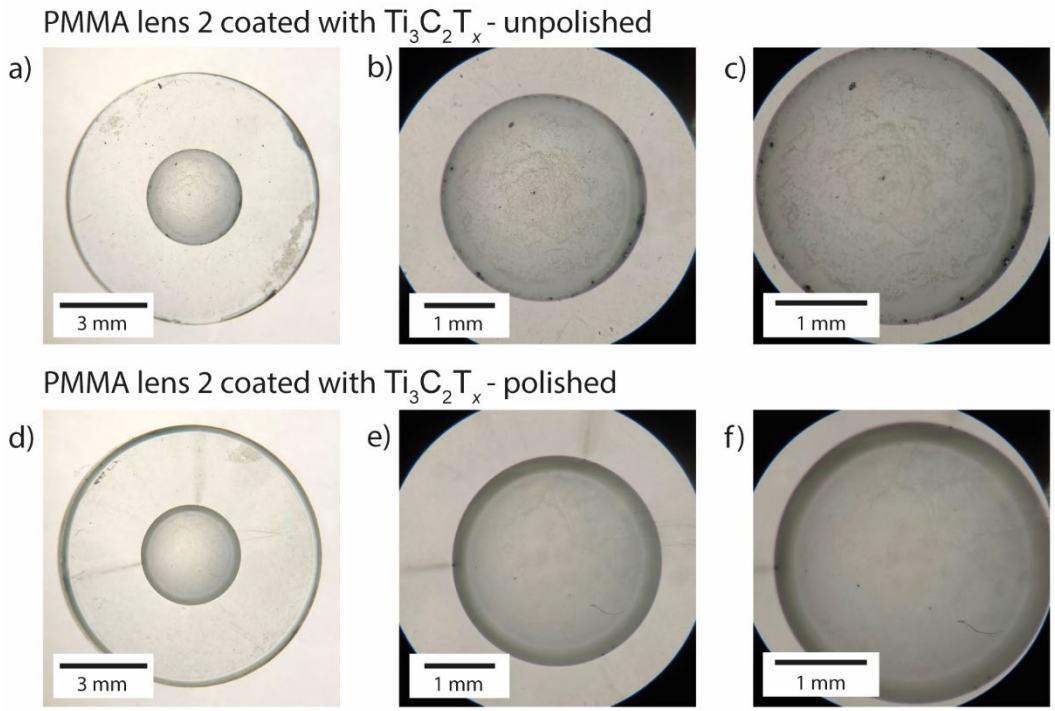

Figure 5-17 – Digital images to show the $Ti_3C_2T_x$ coating quality on the PMMA lens 2. (a-c) Images show clumping and non-uniform $Ti_3C_2T_x$ coating the half lens. The lens was lathed, washed, plasma-treated and spin-coated with $Ti_3C_2T_x$. (d-f) Images

show the $Ti_3C_2T_x$ coating on the lens. The lens was polished after it was lathed, and the coating was more consistent overall, yet some clumping was apparent on the optic.

In addition to the nonuniformity of the coating across the optic, rings of $Ti_3C_2T_x$ form around the perimeter and at the edge of the concave section of the optic with lens 2, illustrated in ***Figure 5-18***. These artefacts are speculated as being caused by radial displacement and surface tension of the $Ti_3C_2T_x$ solution. The lens is formed of an outermost edge and an inner edge where the concave area meets the flat section of the lens. Beading of the $Ti_3C_2T_x$ solution in these areas causes thicker layers to form, resulting in radial artefacts.

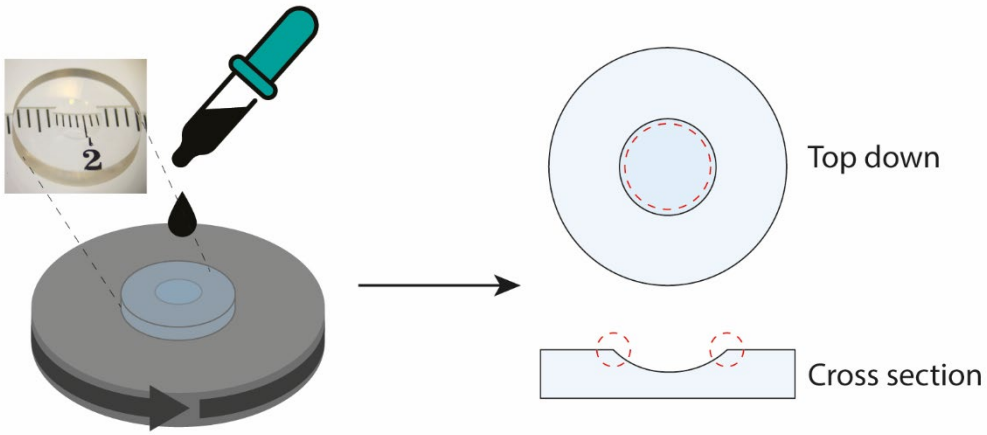

Figure 5-18 – Schematic of the bottom half of the PMMA lens (2) to illustrate spin-coating of $Ti_3C_2T_x$ and display the location of the ring.

SEM was used to investigate the artefacts around the perimeter and the optic edge of lens 2, to determine if there was a relationship between spin speed and the irregular radial patterns. ***Figure 5-19*** demonstrates the difference in titanium (Ti) levels,

corresponding to the amount of $Ti_3C_2T_x$ present on the lens. Spectrum 1 was placed on the flat region of the lens, spectrum 2 was arranged on the ring close to the edge of the optic, and spectrum 3 towards the centre of the optic. A higher percentage of Ti was identified on spectrum 2, suggesting a greater degree of $Ti_3C_2T_x$ was coated in this region.

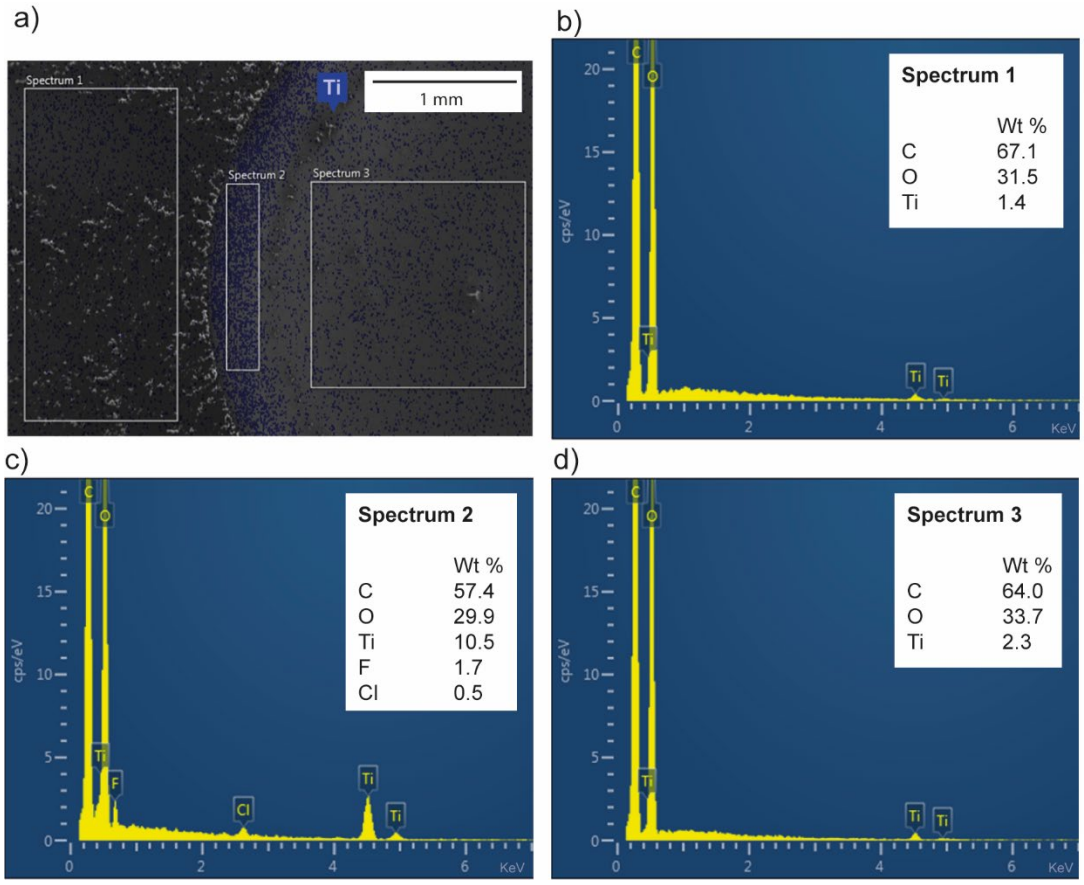

Figure 5-19 – SEM and EDS of the $Ti_3C_2T_x$ coated PMMA lens 2. (a) SEM image of the PMMA lens with areas selected that correlate to the EDS spectra (1, 2, and 3). (b) EDS spectrum 1 shows 1.4 % titanium. (c) EDS spectrum 2 shows 10.5 % titanium. (d) EDS spectrum 3 shows 2.3 % titanium.

The high-resolution images shown in ***Figure 5-20***, produced with SEM, demonstrate an inversely proportional correlation between the thickness of the ring pattern and spin

speed. A decrease in thickness was observed with an increase in speed. However, the results did not provide any further understanding of why switching of the LC's refractive index was not observed.

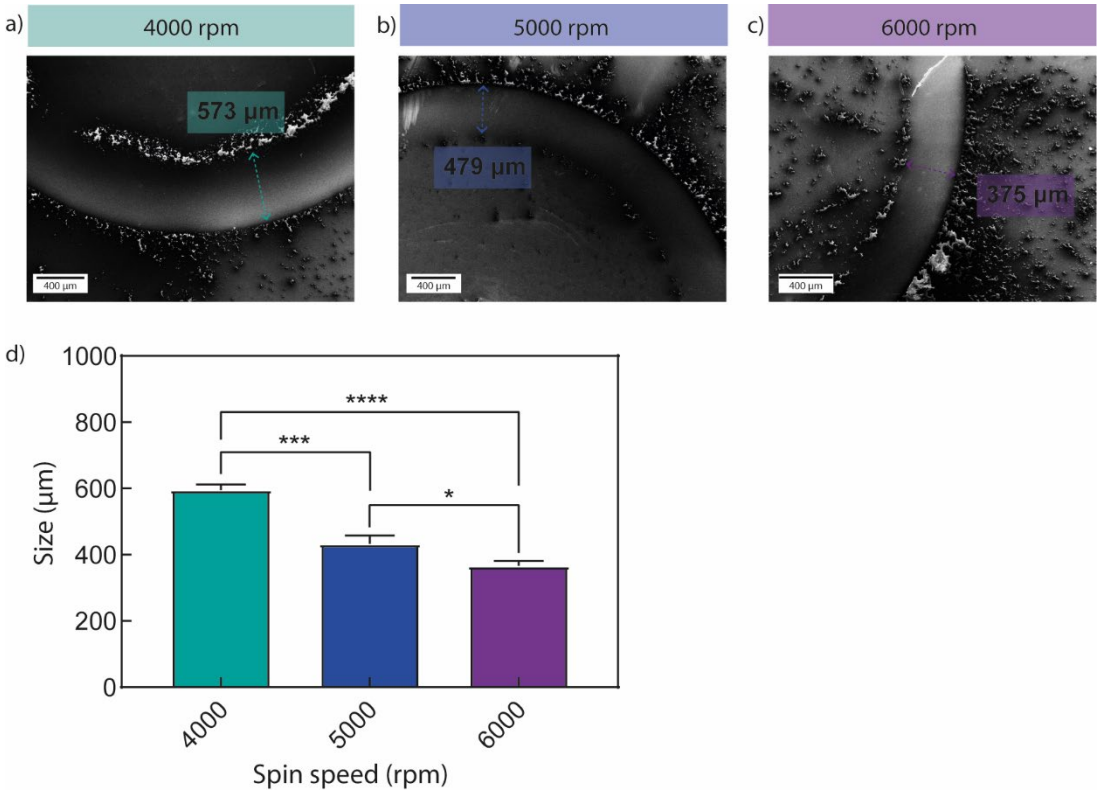

Figure 5-20 – Spin-coating speed investigation. (a-c) High-resolution SEM images (5 kV accelerating voltage) of PMMA lens 2 spin-coated with $Ti_3C_2T_x$ at varying speeds (4000, 5000 and 6000 rpm). (d) Size measurement of the ring observed, an artefact from coating with $Ti_3C_2T_x$ on the PMMA lens 2 (mean ± SD, n = 3, **** $p < 0.0001$, *** $p = 0.0001$, * $p = 0.0145$).

5.4.3.2 Fabrication of a polymer-based $Ti_3C_2T_x$/liquid crystal test cell

To better understand the lack of switching, a PMMA test cell was constructed, yet, no switching was observed. It was hypothesised that the failure of the LC molecules to

reorient was due to poor adhesion of $Ti_3C_2T_x$ to the PMMA surface. $Ti_3C_2T_x$ was lifting off the polymer into the LC, disrupting the electrical connection. Therefore, acrylic acid (AAc) was plasma polymerised onto the PMMA slides. The surface modifications aimed to increase adherence of $Ti_3C_2T_x$ to the polymer. Contact angle demonstrated the presence of the AAc coating with an increase in the hydrophilicity of the surface. The PMMA slide measured 60.2° ± 1.0, and AAc-PMMA measured 45.2° ± 1.2 (mean ± SD, n = 3). With the coating confirmed, $Ti_3C_2T_x$ was then spin-coated onto the PMMA blanks to fabricate a test cell. ***Figure 5-21*** shows the PMMA test cell where switching of the refractive index was observed.

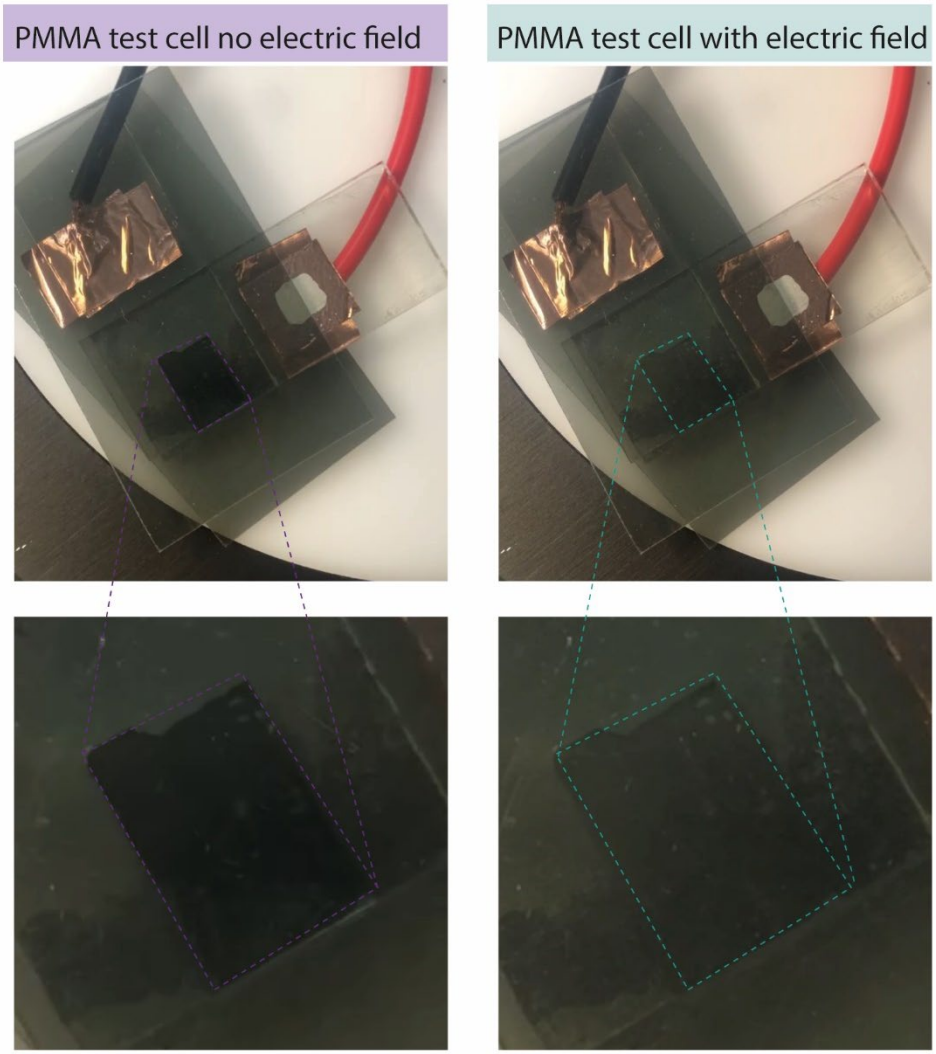

Figure 5-21 – Digital images of a fabricated PMMA/$Ti_3C_2T_x$/liquid crystal test cell with polarising filters placed above and below the test cell in the same orientation to observe the refractive index change in the presence and absence of the field. (left) Without the electric field, the LC is dark as the molecules are oriented in the opposite direction to the polarising filters. (right) With the electric field applied, the LC is brighter as the molecules have reoriented.

5.5 Discussion

AIOL development is limited by current approaches not meeting the fundamental requirements of mimicking the accommodative ability of the eye. However, the two-dimensional transition metal, $Ti_3C_2T_x$, has a unique combination of characteristics, including optical transparency in the visible spectrum, high electrical conductivity, flexibility, hydroxide/oxide surface chemistry and hydrophilicity that lend themselves to the investigation of an optoelectronic AIOL approach. Smart LC lens technology has the potential to address lens accommodation through refractive index modulation. This chapter explored the construction of a glass-based $Ti_3C_2T_x$/LC lens and assessed its performance and optical quality in the presence and absence of an external stimulus. A polymer-based $Ti_3C_2T_x$/LC lens was designed, and a fabrication protocol was developed.

5.5.1 Fabrication and optical evaluation of a glass-based $Ti_3C_2T_x$/liquid crystal lens

The refractive index modulation of a nematic LC was demonstrated in the previous chapter with the proof-of-concept $Ti_3C_2T_x$/LC test cell, presenting the possibility of the mechanism to provide adjustable focus. Although the test cell evidenced the concept, for AIOL design, a quantifiable change of focus is essential, given that the overall goal of an AIOL is to produce controlled, reversible, and seamless changes in focus for near and far objects. Moreover, a $Ti_3C_2T_x$/LC lens was constructed from commercially available glass lenses and assessed.

The purpose of any lens is to form an image, real or virtual, from an observed object, and its optical performance is determined by assessing the image quality. First, the lenses were evaluated using a Ronchi ruling that was titled to a 45° angle to allow the position of focus to be observed and address the hypothesis that $Ti_3C_2T_x$ can facilitate a change in focus in an AIOL design. The three fabricated lenses, A, B, and C displayed fast switching and a significant difference in focus position when the field was applied to the system. The change in focus indicates that molecular reorientation of the LC's director occurred in the presence of the electric field, as the LC switched from its ordinary to extraordinary refractive index. Thus, a change in the lens' focal length was observed, as demonstrated in ***Figure* 5-8**, ***Figure* 5-9**, and ***Figure* 5-10**. With the field applied, the focus positions were compared, and between 20, 30, and 40 V, slight differences in focus were measured. However, the greatest difference was observed when 0 V, no field, was compared to 10 V. These outcomes indicate that the threshold voltage, meaning the voltage at which the director orients with the applied field, lies between 0 and 10 V. As the external force exceeds the critical field strength, the induced dipole moments cause the molecules to align in the direction of the electrical potential through Fréedericksz transitions[227].

The optical quality of the lenses was evaluated through MTF measurements using the slanted edge method. This method measures the MTF as a function of the horizontal and vertical spatial frequencies imaging an infinitely sharp step in object intensity.[253] Each of the lenses displayed significantly higher MTF values in the presence of the field, indicating that at the specified working distances, a higher degree of detail was transferred from the object to the image (***Figure 5-11***, ***Figure 5-12***, and ***Figure 5-13***). Therefore, the application of the field and reorientation of the LC director produced

higher quality images than without the field at their respective positions. For each lens, the maximum MTF value in the absence of the field was not established. A comparison between the lens' maximum MTF values in the presence and absence of the field would have made a more ideal evaluation. In practice, degraded images are formed due to light scattering, aberrations and diffraction. Some rays do not reach the image from the object through reflection losses, refracting surfaces, and scattering from inhomogeneities in the transparent media. Nonetheless, all three lens examples displayed improved image quality in the presence of the field. Moreover, the electronically controlled switch in the refractive index resulted in optical quality changes. The findings were supported by the quality assessment with the Siemens star target. All the lenses exhibited better contrast and resolution with the electric field applied.

Throughout the evaluation, the three fabricated lenses presented comparable performance and image quality trends. However, the investigation demonstrated the high sensitivity of the lens fabrication protocol, evidenced by the minor differences measured in absolute values of focus and MTF. Factors that influence lens to lens variability include the assembly and positioning of the lenses with regard to the optical axis. For instance, the placement of the bi-convex, plano-concave, and plano-convex lenses must be precisely aligned with the optical plane, as the lack of congruency will lead to optical aberrations and changes in the focal point. Additionally, poor lens assembly could introduce unintentional inequalities in the LC cavity thickness. LC cavity thickness has been well-studied for LCDs, such that micro-scale variations impact focusing characteristics[254]. Lens and LC cavity thickness was measured during fabrication. However, inconsistencies and unaccountable fluctuations were

observed that were thought to have been attributed to the thermal expansion of the glass lenses. BK7 has a high thermal expansion coefficient and is consequently sensitive to temperature changes affecting its thickness[255].

In addition to the susceptibility to variation in the lens assembly, several elements could be optimised to enhance lens performance. A mould could be developed for use during lens construction to preserve the alignment of the individual parts. LC cavity thickness could also be improved. Glass bead spacers, as small as 2.3 μm, are widely used in LC lens technology and LCDs to set the thickness of the cavity[241]. The incorporation of glass spacers would increase the homogeneity of the LC layer, leading to greater reproducibility and minimise variation. As smaller glass beads could be used, the thickness of the cavity could be decreased, resulting in fast response/relaxation times. The orientation of the LC molecules with respect to the lens surface is known to produce significant changes in optical properties. Furthermore, it is a parameter used to design the lens and is influenced by the birefringence of the LC. The focal length of an LC lens is altered electrically through reorienting the director, and the predetermined order of the molecules is set with the alignment layer, either planarly or vertically. Whilst both alignment configurations achieve molecular reorientation, planar alignment has demonstrated superior changes in focus, thus optical power[241]. Alternatively, to the TN planar orientation presented throughout this thesis, planar and anti-planar could be investigated to reduce the potential of light scatter introduced in the 90° twist. The lens could be further optimised by reducing the working voltage required to switch the LC's refractive index. Research has investigated nematic LCs doped with nanomaterials. Incorporating a two-dimensional material lowers the threshold voltage by improving the dielectric anisotropy. Several

studies have doped 5CB with low concentrations of materials, such as graphene and demonstrated significant reductions in the voltage required to reorient the director[256–259]. Many of the factors described could improve lens performance for additional optimisation of the LC lens to further develop the study into the use of $Ti_3C_2T_x$ coatings to facilitate a change of focus for AIOL design.

5.5.2 Design and development of a polymer-based $Ti_3C_2T_x$/liquid crystal lens

The glass-based $Ti_3C_2T_x$/liquid crystal lens successfully demonstrates the ability of $Ti_3C_2T_x$ to be used in an adjustable focus lens. However, a more suitable IOL base material was investigated in the development of a truly AIOL. The first IOL to be manufactured was made from PMMA, this material can be lathed to any design, is biologically inert and has been used in other LC contact lens designs. The PMMA/$Ti_3C_2T_x$/LC lens was designed as a 20.01 D lens in the OFF state, whilst ON, in the presence of the field, the lens would provide 23.52 D of optical power as a high optical power value corresponds to a higher degree of refraction, required to focus on closer objects, for near vision.

The fabrication protocol used to construct the glass-based lens had to be amended to assemble the PMMA/$Ti_3C_2T_x$/LC lens. The LC had to be incorporated before the top lens was added, which led to a high incidence of air bubbles confined in the cavity (***Figure 5-16***). The assembly technique was adjusted to construct an air bubble-free lens, but switching the refractive index was not achieved. Several factors could have caused the failure to modulate the refractive index. The lens displayed inconsistencies and radial artefacts in $Ti_3C_2T_x$ coating shown in ***Figure 5-17***. A polishing step was

introduced to the protocol, which made the coating less clumpy in areas specifically across the optic. The radial artefacts of the coating process were investigated by exploring different spin speeds, demonstrating an increase in ring thickness with decreasing speed (***Figure 5-20***).

The glass- and PMMA-based lens designs were compared to establish the parameters that had been modified, as switching was observed with the glass design. The major alterations were the material and geometry of the lens. The material was investigated by producing a PMMA-based test cell in the same way as the $Ti_3C_2T_x$/LC test cell. No switching of the refractive index was observed. It was speculated that the LC was disrupting the $Ti_3C_2T_x$ coating. Therefore, AAc was plasma polymerised to the PMMA before coating the $Ti_3C_2T_x$. Research shows that surface modifications using plasma polymerised AAc improve wettability, surface topography, and chemical composition[260,261]. The AAc functionalised PMMA/$Ti_3C_2T_x$/LC test cell demonstrated switching of the LC displayed in ***Figure 5-21***. This finding suggests that $Ti_3C_2T_x$ adhesion to PMMA contributed to the lack of refractive index modulation in the PMMA lens.

5.6 Conclusion

A glass-based $Ti_3C_2T_x$/LC lens was constructed and successfully modulated the refractive index of the nematic LC, 5CB. The optical performance evaluation confirmed a difference in focus and image quality in the presence of the field compared to the absence of the field. The changes observed resulted from the field-induced switch from the ordinary to the extraordinary refractive index in conjunction

with the optic of the lens. Factors to decrease variability and optimise the glass-based $Ti_3C_2T_x$/LC lens were introduced and discussed. A PMMA lens was designed, and a protocol was created to construct the lens in a more suitable material for AIOL development. Fabrication issues included the introduction of air bubbles into the LC cavity and adherence of $Ti_3C_2T_x$ to the PMMA substrate. An AAc functionalised PMMA test cell successfully modulated the LC's refractive index. Further work would functionalise the PMMA lens and construct the PMMA/$Ti_3C_2T_x$/LC lens. An optical evaluation would be performed on the lens to observe a change of focus from distant to near vision. Alternative polymers, such as Rayner's hydrophobic polymer, would be considered to develop $Ti_3C_2T_x$ AIOL further. This chapter contributes to the field by demonstrating that $Ti_3C_2T_x$ coatings are able to facilitate changes in focus in an AIOL design through refractive index modulation.

Chapter 6

6 General discussion

An AIOL aims to restore adaptive focus for patients following crystalline lens removal during cataract surgery. As an age-related disorder, cataracts, and cataract surgery, impose increasing strain on healthcare services and this will continue to grow along with an increasingly aged population. The increasing demand to improve patient outcomes stems from the need to mimic more closely the crystalline lens, providing continuous focus at all distances. Current AIOL approaches, including axial displacement and adjustments in lens curvature, rely heavily on ciliary contraction. However, it is understood that ageing of the ciliary tissues and fibrosis dampen responses and reduce the sensitivity required to operate these mechanisms. Despite the use of different approaches to resolving the challenge of lens accommodation in AIOL design, no clinically effective AIOL currently exists. Key challenges include the absence of a sensitive and stable, transparent conductive material with properties appropriate for long-term function within the physiological environment of the lens in the ocular capsular bag.

A new class of two-dimensional transition metal carbides and/or nitrides called MXenes have emerged with favourable characteristics for developing an AIOL design. Since their discovery, MXenes have experienced rapid growth in a diverse range of interdisciplinary applications due to their attractive optical, electronic, and mechanical properties. The MXene family is continually expanding with the synthesis of new MXene variants through novel techniques to explore their potential. To date, the majority of MXene research has been carried out on $Ti_3C_2T_x$ demonstrating its biosafety, electrical conductivity, and optical characteristics for applications including

energy storage[105,106], electromagnetic interference shielding[107,108], gas and pressure sensors[103,104], water purification[7,109], and biomedicine[130–132]. However, this widely investigated member of the MXene family has yet to be considered for use as a transparent conductive electrode within an ophthalmic smart lens device to address current challenges in AIOL technology.

This thesis addressed the gap in knowledge regarding the suitability of MXene $Ti_3C_2T_x$ by investigating the hypothesis that MXenes can be incorporated into an AIOL design to produce a transparent, flexible, biocompatible, highly electrically conductive coating coupled with a liquid crystal (LC) layer to develop an adaptive focus implantable lens[262]. While exploring the hypothesis, a series of research objectives were employed. First, the synthesis and deposition of $Ti_3C_2T_x$ coatings were investigated to determine if the nanomaterial could retain its transparency, conductivity, and flexibility when coated onto an IOL polymer. Second, the effect of $Ti_3C_2T_x$ coated IOLs on human lens epithelial cell viability and inflammation within the ocular environment was considered. Next, the incorporation of $Ti_3C_2T_x$ coatings within a nematic LC was investigated to assess if $Ti_3C_2T_x$ could facilitate refractive index modulation of the LC in a proof-of-concept design. Finally, the integration of $Ti_3C_2T_x$ and the LC into the lens to enable a change in focus through external electrical stimuli was investigated. This research was the first to explore MXenes for ocular applications developing an adjustable focus mechanism.

6.1 MXene synthesis, solution processing, and physical characterisation

The initial stages of the study explored $Ti_3C_2T_x$ synthesis to achieve high-quality, single flakes with large lateral size. The minimally intensive layer delamination

(MILD) method produced colloidal $Ti_3C_2T_x$ solutions by selectively etching MAX phase with LiF and HCl. Physical characterisation through techniques such as XRD, XPS and UV-Vis confirmed the synthesis of the $Ti_3C_2T_x$ product (section 2.2.3). The average lateral flake size was identified as 1250 nm with bulk conductivity of ~6000 S cm^{-1} demonstrated in ***Figure 2-7*** and ***Table 2-3***, respectively. A solution processing spin-coating technique was used to apply thin and uniform $Ti_3C_2T_x$ coatings onto commercially available IOLs. The optoelectronic evaluation characterised the sheet resistance of the coatings that ranged from 0.2 – 1.0 kΩ sq^{-1}, corresponding to a transmittance of 50 – 80 % shown in ***Figure 2-12***, demonstrating the high conductivity and transparency. Coating flexibility was displayed when sufficient conductivity was maintained following manual distortion (***Figure 2-13***). In addition, the $Ti_3C_2T_x$ coatings did not negatively influence lens performance, assessed through optical power or MTF measurements before and after coating demonstrated as no significant difference was observed ($p < 0.05$). The findings in this chapter supported the hypothesis that $Ti_3C_2T_x$ is an appropriate TCE material for use within an investigation into a $Ti_3C_2T_x$-based AIOL design. The chapter also contributes to the wider field of wearable electronic device applications, demonstrating its favourable characteristics as an effective transparent electrode. These properties could also be implemented into future developments in IOL sensor technology.

6.2 Biocompatibility of MXene coated intraocular lens

Biomedical research using $Ti_3C_2T_x$ suggests compatibility for a range of applications. However, since surgical trauma, as a result of cataract surgery, stimulates an immune response, there is a requirement to evaluate the response of the ocular environment

exposed to $Ti_3C_2T_x$ to ensure the material does not exacerbate the immune response leading to chronic inflammation or other postoperative complications. In particular, an excessive inflammatory response is linked to the development of the primary complication associated with cataracts over months to years, posterior capsular opacification (PCO), in which human lens epithelial cells are activated to migrate across the posterior IOL to form a fibrous secondary cataract requiring further surgical intervention. The findings from the cell viability assay showed no significant difference ($p < 0.05$) to cells exposed to $Ti_3C_2T_x$ compared to the cell only for fibroblast (3T3) and human lens epithelial (HLE) cell lines (***Figure 3-1*** and ***Figure 3-2***). Calcein AM staining demonstrated no influence on cell proliferation when 3T3 cells were incubated with $Ti_3C_2T_x$ for 24 hours ($p < 0.05$). The cytotoxicity assay, presented in ***Figure 3-3***, was in agreement with the viability assessment as exposure to $Ti_3C_2T_x$ did not impact HLE cell toxicity. Oxidative stress pathways, thought of as potential mechanisms promoting tendency to PCO were not found to be activated by $Ti_3C_2T_x$ through measurement of ROS generation following monocytic cell line exposure to $Ti_3C_2T_x$ for 1 and 24 hours (***Figure 3-6***). Pro-inflammatory mediators IL-6, TNF-α, and IL-8 were investigated to determine if the exposure to $Ti_3C_2T_x$ led to an upregulation of these common ocular inflammatory markers. No significant difference was exhibited between the cell only and $Ti_3C_2T_x$ exposed cells shown in ***Figure 3-7*** ($p < 0.05$). This chapter evaluates the cytocompatibility and inflammatory profile of $Ti_3C_2T_x$ coatings on IOL polymers in the ocular environment. This biological investigation presents a platform for IOL technology by introducing functional properties for use in eye and introduces the potential to explore other MXene variants for a wider variety of ophthalmic applications.

6.3 MXene and liquid crystal, refractive index modulating, proof-of-concept design

An important focus of current IOL technology-based research is to address the loss of accommodation through the development of AIOLs, aiming to produce controlled, reversible, and seamless adjustments in focus. Although advancements have been made in the field, commercially available AIOLs display low accommodative amplitude and are associated with postoperative complications. LC smart lenses have been investigated to treat presbyopia by offering adaptive focus controlled through an external stimulus, such as an electric field. LC technology has the potential to address IOL accommodation. Furthermore, the desirable properties of $Ti_3C_2T_x$, including flexibility, which is a key property not present in other TCE materials, indicate suitability for use in an electroactive mechanism. A $Ti_3C_2T_x$/LC test cell was fabricated, shown in ***Figure 4-11***. The test cell demonstrated switching between the LC's refractive indices in the presence and absence of the electric field. The refractive index was measured with a purpose-built refractometer that determined the field-induced extraordinary refractive index as $n_e = 1.7280 \pm 0.0479$, and in the absence of the field, the ordinary refractive index was $n_o = 1.5354 \pm 0.0002$. Following the observed molecular reorientation of the LC director, an optic was incorporated to determine if $Ti_3C_2T_x$ could facilitate adjustments in focus. Edge detection image processing was used to assess focus with and without the field. A higher degree of focus was observed with increasing voltage applied, and switching time decreased. This chapter introduces an alternative adaptive focus mechanism using $Ti_3C_2T_x$ and a nematic LC in a test cell, which displayed molecular reorientation of the director in

the presence of the field, demonstrating the potential for use in an AIOL design. This work also contributes to the field of optoelectronics as the MXene/LC mechanism offers possibilities for small optics applications such as cameras for mobile phones.

6.4 MXene and liquid crystal change of focus mechanism

This chapter transferred the proof-of-concept mechanism into a lens design to determine if the $Ti_3C_2T_x$/LC approach could change focus through molecular reorientation of the LC director with the field. Three glass-based $Ti_3C_2T_x$/LC lenses were constructed, and their optical performance evaluation showed switching between the ordinary and extraordinary refractive indices corresponding to a change in focus in the presence and absence of the electric field (***Figure 5-8***, **Figure 5-9**, and ***Figure* 5-10**). The lenses demonstrated field-induced improvements in image quality consistent with the focus measurements (***Figure* 5-11**, ***Figure 5-12***, ***Figure 5-13***, and ***Figure 5-14***). In developing an AIOL, a more suitable polymer-based material was investigated. A PMMA lens was designed to provide 20.01 D of optical power in the absence of the field and 23.52 D with the field. Fabrication of the lens was challenging, and an issue was identified with the adherence of $Ti_3C_2T_x$ to the PMMA substrates. Therefore, a PMMA/$Ti_3C_2T_x$/LC test cell was constructed to investigate the issue. Acrylic acid (AAc) was plasma polymerised to the PMMA surface before coating with $Ti_3C_2T_x$ and assembling the test cell. The AAc coated test cell successfully switched between the LC's refractive indices with and without the applied field. The work presented in this chapter demonstrated the first use of $Ti_3C_2T_x$ as a TCE to facilitate the molecular reorientation of a nematic LC in a lens resulting in changes in focus following stimulation with an external electric field. The $Ti_3C_2T_x$/LC lens makes a

contribution to the advancement of new approaches in AIOL design. As such it presents a contribution toward improvements in AIOL and IOL technology.

Whilst the proof-of-concept and fabricated lens data is a significant contribution to potentially advancing AIOL technology it was not possible to produce a polymer-based lens to measure an absolute optical power change due to the challenges with MXene/polymer adhesion with the introduction of the liquid crystal. In addition, the biological modelling was limited to isolated human lens epithelial cell studies.

6.5 Limitations

The work presented in this thesis demonstrated the potential use of MXenes as a TCE in an ocular application. Although the investigation was successful in introducing this adjustable focus mechanism, it was limited by several factors. In terms of biocompatibility, the study performed was an *in vitro* cell culture-based investigation on immortalised cell lines. To improve the emphasis of the findings primary ocular cell lines would be used. With further development of the lens, producing a prototype, animal models would need to be considered. Further limitations include issues with lens manufacture. Assembly must be optimised to gain greater control and minimise variability between lenses. This could be achieved through the use of jigs and templates.

6.6 Future work

The next steps in developing this work would be to functionalise the PMMA lens with AAc before coating it with $Ti_3C_2T_x$ increasing MXene adhesion to the polymer

substrate and minimising disruption to the TCE in the presence of the LC. The lens would be constructed, and performance would be assessed to confirm the 3 D shift in optical power. Foldable polymers would be investigated to progress the rigid PMMA model to a more suitable design in keeping with the development of IOL technology. Optical performance would be optimised following the success of incorporating the $Ti_3C_2T_x$/LC mechanism into a foldable polymer. A wireless approach to trigger the modulation could be incorporated. A lower working voltage could be achieved by doping the LC with a nanomaterial. For example, low concentrations of $Ti_3C_2T_x$ could be added to improve the dielectric anisotropy[256]. Alternative LCs should be considered that have more suitable transition temperature ranges to the temperature of the eye. The change of focus trigger could be investigated, by researching applications such as photovoltaic cells and photosensors that use light to stimulate the mechanism[263]. In this approach, the eye's pupillary dilation would activate the accommodative function. It would be useful to develop a capsular bag model to allow an accurate performance evaluation of the adaptive focus trigger mechanism, whether it be light-activated or through a mechanical trigger. A capsular bag model would also present opportunities for further biological modelling. In addition to investigating an adaptive focus $Ti_3C_2T_x$ mechanism for IOLs, further functionalisation could be introduced. A multifunctional, adaptive focus and intraocular pressure (IOP) sensing implantable lens design could be explored. As IOP is a significant indicator for the early diagnosis and monitoring of glaucoma, such a multifunctional device offers advancements for two ocular disorders that contribute significantly to the world's blind population.

6.7 Conclusion

This work is the first to demonstrate the use of two-dimensional $Ti_3C_2T_x$ (MXene) as a transparent conductive electrode with ocular biocompatibility and ability to induce a change in optical power on incorporation into a prototype AIOL device. The material retained transparency, conductivity, and flexibility when spin-coated onto IOL polymers. $Ti_3C_2T_x$ displayed biocompatibility with cells appropriate to the ocular environment and did not upregulate inflammatory cytokines linked to progression of pathways leading to PCO. In a proof-of-concept adaptive focus design, $Ti_3C_2T_x$ performed as an effective TCE to facilitate the molecular reorientation of a nematic LC. The mechanism was developed into a lens, and the change in focus on the application of an electrical stimulus evidenced the ability of $Ti_3C_2T_x$ to be used in an AIOL design. While this research was the first application of MXene in an ocular application, further work is required to optimise $Ti_3C_2T_x$ lens polymer interaction, incorporate a trigger mechanism, and assess performance in a capsular bag model.

References

[1] R. R. A. Bourne *et al.*, "Causes of blindness and vision impairment in 2020 and trends over 30 years, and prevalence of avoidable blindness in relation to VISION 2020: the Right to Sight: an analysis for the Global Burden of Disease Study," *The Lancet Global Health*, vol. 9, no. 2, pp. e144–e160, Feb. 2021, doi: 10.1016/S2214-109X(20)30489-7.

[2] D. Allen and A. Vasavada, "Cataract and surgery for cataract.," *BMJ*, vol. 333, no. 7559, pp. 128–132, Jul. 2006, doi: 10.1136/bmj.333.7559.128.

[3] J. A. Venter, M. Pelouskova, B. M. Collins, S. C. Schallhorn, and S. J. Hannan, "Visual outcomes and patient satisfaction in 9366 eyes using a refractive segmented multifocal intraocular lens ASCRS and ESCRS ARTICLE," *Journal of Cartaract & Refractive Surgery*, vol. 39, pp. 1477–1484, 2013, doi: 10.1016/j.jcrs.2013.03.035.

[4] M. Naguib, M. W. Barsoum, and Y. Gogotsi, "Ten Years of Progress in the Synthesis and Development of MXenes," *Advanced Materials*, vol. 33, no. 39, p. 2103393, Oct. 2021, doi: 10.1002/ADMA.202103393.

[5] H. Tang *et al.*, "MXene–2D layered electrode materials for energy storage," *Progress in Natural Science: Materials International*, vol. 28, no. 2, pp. 133–147, Apr. 2018, doi: 10.1016/J.PNSC.2018.03.003.

[6] B. Anasori, M. R. Lukatskaya, and Y. Gogotsi, "2D metal carbides and nitrides (MXenes) for energy storage," *Nature Reviews Materials*, vol. 2, no. 2, p. 16098, Feb. 2017, doi: 10.1038/natrevmats.2016.98.

[7] K. Rasool, R. P. Pandey, P. A. Rasheed, S. Buczek, Y. Gogotsi, and K. A. Mahmoud, "Water treatment and environmental remediation applications of two-dimensional metal carbides (MXenes)," *Materials Today*, vol. 30, pp. 80–102, Jun. 2019, doi: 10.1016/J.MATTOD.2019.05.017.

[8] H. Lin, X. Wang, L. Yu, Y. Chen, and J. Shi, "Two-Dimensional Ultrathin MXene Ceramic Nanosheets for Photothermal Conversion," *Nano Lett*, vol. 17, no. 1, pp. 384–391, Jan. 2017, doi: 10.1021/ACS.NANOLETT.6B04339.

[9] Z. Xie *et al.*, "Biocompatible Two-dimensional Titanium Nanosheets for Efficient Plasmonic Photothermal Cancer Therapy," *ACS Applied Materials & Interfaces*, vol. 11, no. 25, pp. 22129–22140, May 2019, doi: 10.1002/((please).

[10] M. Soleymaniha, M. A. Shahbazi, A. R. Rafieerad, A. Maleki, and A. Amiri, "Promoting Role of MXene Nanosheets in Biomedical Sciences: Therapeutic and Biosensing Innovations," *Advanced Healthcare Materials*, vol. 8, no. 1, p. 1801137, Jan. 2019, doi: 10.1002/ADHM.201801137.

[11] L. Wu *et al.*, “2D transition metal carbide MXene as a robust biosensing platform for enzyme immobilization and ultrasensitive detection of phenol,” *Biosensors and Bioelectronic*, vol. 107, no. February, pp. 69–75, 2018, doi: 10.1016/j.bios.2018.02.021.

[12] J. F. Koretz and G. H. Handelman, “How the Human Eye Focuses,” *Sci Am*, vol. 259, no. 1, pp. 92–99, 1988, doi: 10.2307/24989163.

[13] H. Martin, R. Guthoff, T. Terwee, and K. P. Schmitz, “Comparison of the accommodation theories of Coleman and of Helmholtz by finite element simulations,” *Vision Research*, vol. 45, no. 22, pp. 2910–2915, Oct. 2005, doi: 10.1016/j.visres.2005.05.030.

[14] T. E. Lockhart and W. Shi, “Effects of age on dynamic accommodation,” *Ergonomics*, vol. 53, no. 7, pp. 892–903, 2010, doi: 10.1080/00140139.2010.489968.

[15] M. A. Wride, “Lens fibre cell differentiation and organelle loss: Many paths lead to clarity,” *Philosophical Transactions of the Royal Society B: Biological Sciences*, vol. 366, no. 1568, pp. 1219–1233, Apr. 2011, doi: 10.1098/rstb.2010.0324.

[16] J. Feher, “Vision,” in *Quantitative Human Physiology*, Academic Press, 2012, pp. 386–400. doi: 10.1016/B978-0-12-382163-8.00041-4.

[17] D. R. Whikehart, *Biochemistry of the eye*, vol. 2. Butterworth-Heinemann, 2003.

[18] S. E. Skalicky, *Ocular and Visual Physiology: Clinical Application*. Singapore: Springer, 2016. doi: 10.1007/978-981-287-846-5_24.

[19] S. M. Salvi, S. Akhtar, and Z. Currie, “Ageing changes in the eye,” *Postgraduate Medical Journal*, vol. 82, no. 971. BMJ Publishing Group, pp. 581–587, Sep. 2006. doi: 10.1136/pgmj.2005.040857.

[20] J. L. Alió, J. L. Alió Del Barrio, and A. Vega-Estrada, “Accommodative intraocular lenses: where are we and where we are going,” *Eye and Vision*, vol. 4, no. 16, 2017, doi: 10.1186/s40662-017-0077-7.

[21] R. A. Schachar, “Treatment Of Presbyopia And Other Eye Disorders - Patent number 5354331,” Jul. 15, 1992

[22] D. Allen and A. Vasavada, “Cataract and surgery for cataract,” *BMJ BMJ (Clinical research ed.)*, vol. 333, no. 7559, pp. 128–132, 2006, Accessed: Mar. 11, 2018. [Online]. Available: https://www.ncbi.nlm.nih.gov/pmc/articles/PMC1502210/pdf/bmj33300128.pdf

[23] K. J. Lampi *et al.*, “Age-related Changes in Human Lens Crystallins Identified by Two-dimensional Electrophoresis and Mass Spectrometry,” *Experimental Eye Research*, vol. 67, no. 1, pp. 31–43, Jul. 1998, doi: 10.1006/EXER.1998.0481.

[24] S. H. Heruye *et al.*, “Current trends in the pharmacotherapy of cataracts,” *Pharmaceuticals*, vol. 13, no. 1. MDPI AG, Jan. 01, 2020. doi: 10.3390/ph13010015.

[25] K. Banerjee, “Per-operative and post-operative complications small incision cataract surgery,” Rajiv Gandhi University of Health Sciences, Karnataka, 2006. Accessed: Mar. 11, 2018. [Online]. Available: https://web.archive.org/web/20140605064801/http://14.139.159.4:8080/jspui/bitstream/123456789/1638/1/CDMOPTH00032.pdf

[26] Y.-C. Liu, M. Wilkins, T. Kim, B. Malyugin, and J. S. Mehta, “Cataracts,” *The Lancet*, vol. 390, no. 10094, pp. 600–612, 2017, doi: 10.1016/S0140-6736(17)30544-5.

[27] J. Knight, R. Bates, J. Dellar, and B. Anderson, “Eye Health Needs Assessment,” London, May 2018. Accessed: Jun. 29, 2022. [Online]. Available: www.facebook.com/PublicHealthEngland

[28] S. K. West, C. T. Valmadrid, S. K. West, and C. T. Valmadrid, “Epidemiology of risk factors for age-related cataract.,” *Surv Ophthalmol*, vol. 39, no. 4, pp. 323–34, Jan. 1995, doi: 10.1016/S0039-6257(05)80110-9.

[29] D. Allen, “Cataract.,” *BMJ Clinical Evidence*, vol. 2011, Feb. 2011, Accessed: Oct. 30, 2021. [Online]. Available: https://www.ncbi.nlm.nih.gov/pmc/articles/pmid/21718561/?tool=EBI

[30] M. Khairallah *et al.*, “Number of People Blind or Visually Impaired by Cataract Worldwide and in World Regions, 1990 to 2010,” *Investigative Opthalmology & Visual Science*, vol. 56, no. 11, p. 6762, Oct. 2015, doi: 10.1167/iovs.15-17201.

[31] S. Coronini-Cronberg, H. Lee, A. Darzi, and P. Smith, “Evaluation of clinical threshold policies for cataract surgery among English commissioners,” *J Health Serv Res Policy*, vol. 17, no. 4, pp. 241–247, Oct. 2012, doi: 10.1258/JHSRP.2012.012023.

[32] G. Davis, “The Evolution of Cataract Surgery,” *Missouri Medicine*, vol. 113, no. 1, p. 58, Jan. 2016, doi: 10.1097/apo.0b013e31829df4bf.

[33] H. Y. Lee, Y. J. Choy, and J. S. Park, “Comparison of OVD and BSS for maintaining the anterior chamber during IOL implantation.,” *Korean J Ophthalmol*, vol. 25, no. 1, pp. 15–21, Feb. 2011, doi: 10.3341/KJO.2011.25.1.15.

[34] D. B. Moore, A. Harris, and B. Siesky, “The world through a lens: the vision of Sir Harold Ridley,” *British Journal of Ophthalmology*, vol. 94, no. 10, pp. 1277–1280, Oct. 2010, doi: 10.1136/bjo.2009.163956.

[35] K. Singh, A. Misbah, P. Saluja, and A. Singh, “Review of manual small-incision cataract surgery,” *Indian Journal of Ophthalmology*, vol. 65, no. 12, p. 1281, Dec. 2017, doi: 10.4103/IJO.IJO_863_17.

[36] J. D. Stein, “Serious adverse events after cataract surgery.1. Stein JD. Serious adverse events after cataract surgery. Curr Opin Ophthalmol [Internet]. 2012 May [cited 2017 Nov 1];23(3):219–25. Available from: http://www.ncbi.nlm.nih.gov/pubmed/22450221,” *Curr Opin Ophthalmol*, vol. 23, no. 3, pp. 219–25, May 2012, doi: 10.1097/ICU.0b013e3283524068.

[37] C. Pérez-Vives, “Biomaterial Influence on Intraocular Lens Performance: An Overview,” vol. 2018, no. January 2000, 2018, doi: 10.1155/2018/2687385.

[38] D. Tripti, R. S. Haldar, S. Geetha, U. K. Niyogi, and R. K. Khandal, “Materials for intraocular lenses (IOLs): Review of developments to achieve biocompatibility,” *E-Polymers*, vol. 9, no. 1, p. 124, 2009, doi: 10.1515/epoly.2009.9.1.1466.

[39] M. Lombardo, M. P. de Santo, G. Lombardo, R. Barberi, and S. Serrao, “Analysis of intraocular lens surface properties with atomic force microscopy,” *J Cataract Refract Surg*, vol. 32, pp. 1378–1384, 2006, doi: 10.1016/j.jcrs.2006.02.068.

[40] O. Findl, “Intraocular Lens Materials and Design,” in *Achieving Excellence in Cataract Surgery A Step-by-Step Approach*, D. M. Colvard, Ed. Loa Angeles, 2009, pp. 95–108.

[41] D. J. A. James A. Davison, Guy Kleinmann, Yoel Greenwald, “Intraocular Lenses,” *Ophthalmology*, 2016. https://entokey.com/intraocular-lenses-2/ (accessed Jun. 03, 2018).

[42] Q. Huang, G. P. M. Cheng, K. Chiu, and G. Q. Wang, “Surface Modification of Intraocular Lenses,” *Chin Med J (Engl)*, vol. 129, no. 2, pp. 206–214, Jan. 2016, doi: 10.4103/0366-6999.173496.

[43] C. Krutzler, K. Lux, and M. Prinz, *Recent developments in modeling innovative intraocular lenses*, vol. 45, no. 18. IFAC, 2012. doi: 10.3182/20120829-3-HU-2029.00022.

[44] P. Kanclerz, F. Toto, A. Grzybowski, and J. L. Alio, “Extended Depth-of-Field Intraocular Lenses: An Update,” *Asia-Pacific Journal of Ophthalmology (Philadelphia, Pa.)*, vol. 9, no. 3, p. 194, 2020, doi: 10.1097/APO.0000000000000296.

[45] K. Cao *et al.*, “Multifocal versus monofocal intraocular lenses for age-related cataract patients: a system review and meta-analysis based on randomized controlled trials,” *Survey of Ophthalmology*, vol. 64, no. 5, pp. 647–658, Sep. 2019, doi: 10.1016/j.survophthal.2019.02.012.

[46] P. Pérez-Merino *et al.*, “Aberrometry in patients implanted with accommodative intraocular lenses,” *Am J Ophthalmol*, vol. 157, no. 5, 2014, doi: 10.1016/J.AJO.2014.02.013.

[47] K. v. Zamora-Alejo, S. P. Moore, D. G. A. Parker, K. Ullrich, A. Esterman, and M. Goggin, “Objective accommodation measurement of the Crystalens HD compared to monofocal intraocular lenses,” *J Refract Surg*, vol. 29, no. 2, pp. 133–139, Feb. 2013, doi: 10.3928/1081597X-20130117-09.

[48] S. Vilupuru, L. Lin, and J. S. Pepose, “Comparison of Contrast Sensitivity and Through Focus in Small-Aperture Inlay, Accommodating Intraocular Lens, or Multifocal Intraocular Lens Subjects,” *Am J Ophthalmol*, vol. 160, no. 1, pp. 150-162.e1, Jul. 2015, doi: 10.1016/J.AJO.2015.04.023.

[49] Food and Drug Administration, “Summary of safety and effectiveness data for Crystalens™ Model AT-45 Accommodating Intraocular Lens,” 2003. Accessed: Dec. 29, 2021. [Online]. Available: https://www.accessdata.fda.gov/cdrh_docs/pdf3/p030002b.pdf

[50] J. S. Cumming *et al.*, “Clinical evaluation of the Crystalens AT-45 accommodating intraocular lens. Results of the U.S. Food and Drug Administration clinical trial,” *Journal of Cataract and Refractive Surgery*, vol. 32, no. 5, pp. 812–825, May 2006, doi: 10.1016/j.jcrs.2006.02.007.

[51] M. Sadoughi, B. Einollahi, D. Roshandel, M. Sarimohammadli, and S. Feizi, “Visual and Refractive Outcomes of Phacoemulsification with Implantation of Accommodating versus Standard Monofocal Intraocular Lenses,” *Journal of Ophthalmic & Vision Research*, vol. 10, no. 4, p. 370, Oct. 2015, doi: 10.4103/2008-322X.176896.

[52] D. R. Sanders and M. L. Sanders, “Visual Performance Results after Tetraflex Accommodating Intraocular Lens Implantation,” *Ophthalmology*, vol. 114, no. 9, pp. 1679–1684, Sep. 2007, doi: 10.1016/j.ophtha.2006.12.017.

[53] M. D. Nijkamp, M. G. T. Dolders, J. de Brabander, B. van den Borne, F. Hendrikse, and R. M. M. A. Nuijts, “Effectiveness of multifocal intraocular lenses to correct presbyopia after cataract surgery: a randomized controlled trial.,” *Ophthalmology*, vol. 111, no. 10, pp. 1832–9, Oct. 2004, doi: 10.1016/j.ophtha.2004.05.023.

[54] I. L. Ossma, A. Galvis, L. G. Vargas, M. J. Trager, M. R. Vagefi, and S. D. McLeod, “Synchrony dual-optic accommodating intraocular lens. Part 2: pilot clinical evaluation,” *J Cataract Refract Surg*, vol. 33, no. 1, pp. 47–52, Jan. 2007, doi: 10.1016/J.JCRS.2006.08.049.

[55] J. L. Alio *et al.*, “Visual Outcomes and Accommodative Response of the Lumina Accommodative Intraocular Lens,” *Am J Ophthalmol*, vol. 164, pp. 37–48, Apr. 2016, doi: 10.1016/J.AJO.2016.01.006.

[56] J. L. Alio *et al.*, “Visual Outcomes and Accommodative Response of the Lumina Accommodative Intraocular Lens,” *American Journal of Ophthalmology*, vol. 164, pp. 37–48, 2016, doi: 10.1016/j.ajo.2016.01.006.

[57] A. Dhital, D. J. Spalton, and K. B. Gala, “Comparison of near vision, intraocular lens movement, and depth of focus with accommodating and monofocal intraocular lenses,” *J Cataract Refract Surg*, vol. 39, no. 12, pp. 1872–1878, Dec. 2013, doi: 10.1016/J.JCRS.2013.05.049.

[58] N. Tan, D. Zheng, and J. Ye, “Comparison of visual performance after implantation of 3 types of intraocular lenses: Accommodative, multifocal, and monofocal,” *European Journal of Ophthalmology*, vol. 24, no. 5, pp. 693–698, 2014, doi: 10.5301/ejo.5000425.

[59] H. S. Ong, J. R. Evans, and B. D. S. Allan, “Accommodative intraocular lens versus standard monofocal intraocular lens implantation in cataract surgery.,” *Cochrane Database Syst Rev*, no. 5, p. CD009667, May 2014, doi: 10.1002/14651858.CD009667.pub2.

[60] Y. L. Liang and S. B. Jia, “Clinical application of accommodating intraocular lens,” *International Journal of Ophthalmology*, vol. 11, no. 6. International Journal of Ophthalmology (c/o Editorial Office), pp. 1028–1037, 2018. doi: 10.18240/ijo.2018.06.22.

[61] D. Brown, P. Dougherty, J. P. Gills, J. Hunkeler, D. R. Sanders, and M. L. Sanders, “Functional reading acuity and performance : Comparison of 2 accommodating intraocular lenses,” *Journal of Cartaract & Refractive Surgery*, vol. 35, no. 10, pp. 1711–1714, 2009, doi: 10.1016/j.jcrs.2009.05.023.

[62] J. S. Cumming *et al.*, “Clinical evaluation of the Crystalens AT-45 accommodating intraocular lens. Results of the U.S. Food and Drug Administration clinical trial,” *Journal of Cataract and Refractive Surgery*, vol. 32, no. 5, pp. 812–825, 2006, doi: 10.1016/j.jcrs.2006.02.007.

[63] P. Buckhurst, “Evaluation of modern intraocular lenses,” Aston University, 2011. Accessed: Aug. 02, 2020. [Online]. Available: https://publications.aston.ac.uk/id/eprint/19544/1/Studentthesis-2011.pdf

[64] S. D. McLeod, V. Portney, and A. Ting, “A dual optic accommodating foldable intraocular lens,” *British Journal of Ophthalmology*, vol. 87, no. 9, pp. 1083–1085, Sep. 2003, doi: 10.1136/bjo.87.9.1083.

[65] J. Tomás-Juan and A. Murueta-Goyena Larrañaga, “Axial movement of the dual-optic accommodating intraocular lens for the correction of the presbyopia: Optical performance and clinical outcomes,” *Journal of Optometry*, vol. 8, no. 2. Spanish Council of Optometry, pp. 67–76, Apr. 01, 2015. doi: 10.1016/j.optom.2014.06.004.

[66] C. Peris-Martínez, A. Díez-Ajenjo, and C. García-Domene, “Short-term results with the Synchrony lens implant for correction of presbyopia following cataract surgery,” *J Emmetropia*, vol. 4, pp. 137–143, 2013.

[67] J. L. Alió, A. B. Plaza-Puche, R. Montalban, and P. Ortega, “Near visual outcomes with single-optic and dual-optic accommodating intraocular lenses,” *Journal of Cataract and Refractive Surgery*, vol. 38, no. 9, pp. 1568–1575, 2012, doi: 10.1016/j.jcrs.2012.05.027.

[68] J. S. Pepose, J. S. Burke, and M. A. Qazi, “Accommodating Intraocular Lenses,” pp. 350–357, 2017, doi: 10.22608/APO.2017198.

[69] C. Pérez-Vives, “Biomaterial Influence on Intraocular Lens Performance: An Overview,” *Journal of Ophthalmology*, vol. 2018, pp. 1–17, 2018, doi: 10.1155/2018/2687385.

[70] J. S. Wolffsohn *et al.*, “Subjective and objective performance of the Lenstec KH-3500 ‘accommodative’ intraocular lens,” *Br J Ophthalmol*, vol. 90, no. 6, pp. 693–696, Jun. 2006, doi: 10.1136/BJO.2006.090951.

[71] P. Studeny, D. Krizova, and J. Urminsky, “Clinical experience with the WIOL-CF accommodative bioanalogic intraocular lens: Czech national observational registry,” *Eur J Ophthalmol*, vol. 26, no. 3, pp. 230–235, May 2016, doi: 10.5301/EJO.5000653.

[72] A. Salahieh, C. P. Argento, T. Saul, B. Vaughane, R. Willis, and A. Salahieh, “US20160058553A1 - Accommodating intraocular lens,” US 2016/0058553 A1, Apr. 03, 2016 Accessed: Jun. 29, 2022. [Online]. Available: https://patentimages.storage.googleapis.com/6a/ea/c0/16e204ed3c059f/US20160058553A1.pdf

[73] H. J. Kim, J. W. Seo, S. J. Shin, and S. K. Chung, “Visual Outcome and Stability of Hydrogel Full-Optics Accommodative Intraocular Lens,” *Journal of the Korean Ophthalmological Society*, vol. 52, no. 12, p. 1448, Dec. 2011, doi: 10.3341/jkos.2011.52.12.1448.

[74] I. G. Pallikaris, D. M. Portaliou, G. D. Kymionis, S. I. Panagopoulou, and G. A. Kounis, “Outcomes after accommodative bioanalogic intraocular lens implantation,” *J Refract Surg*, vol. 30, no. 6, pp. 402–406, 2014, doi: 10.3928/1081597X-20140520-01.

[75] P. Studeny, D. Krizova, and J. Urminsky, “Clinical experience with the WIOL-CF accommodative bioanalogic intraocular lens: Czech national observational registry.,” *Eur J Ophthalmol*, vol. 26, no. 3, pp. 230–5, 2016, doi: 10.5301/ejo.5000653.

[76] B. Cheskin, “FluidVision: Designed to Restore True Accommodation,” *Ophthalmology Innovation Source*, 2016. https://ois.net/fluidvision-designed-to-restore-true-accommodation/ (accessed Jun. 18, 2018).

[77] J. S. Pepose, “Design Strategies for New Accommodating IOLs,” *Catarcat & Refractive Surgery Today*, pp. 39–44, Jan. 2009. Accessed: Feb. 06, 2022. [Online]. Available: https://crstoday.com/wp-content/themes/crst/assets/downloads/CRST0109_07.pdf

[78] K. Michalska-Małecka *et al.*, “Results of cataract surgery in the very elderly population.,” *Clin Interv Aging*, vol. 8, pp. 1041–6, 2013, doi: 10.2147/CIA.S44834.

[79] M. Walckling, R. Beck, O. Stachs, and R. F. Guthoff, “Subjective and objective accommodation of the Crystalens Advanced Optics (AO) in patients 6 months after bilateral implantation,” *Ophthalmology Journal*, vol. 3, no. 2, pp. 29–36, Nov. 2018, doi: 10.5603/OJ.2018.0034.

[80] X. Chen *et al.*, “A Dual-Functional Graphene-Based Self-Alarm Health-Monitoring E-Skin,” *Advanced Functional Materials*, vol. 29, no. 51, p. 1904706, Oct. 2019, doi: 10.1002/adfm.201904706.

[81] K. Choi and H. G. Park, “Smart Reinvention of the Contact Lens with Graphene,” *ACS Nano*, vol. 11, no. 6, pp. 5223–5226, Jun. 2017, doi: 10.1021/acsnano.7b03180.

[82] C. Choi *et al.*, “Human eye-inspired soft optoelectronic device using high-density MoS 2 -graphene curved image sensor array,” *Nature Communications*, vol. 8, no. 1, p. 1664, 2017, doi: 10.1038/s41467-017-01824-6.

[83] T. Hwang *et al.*, “Transparent actuator made with few layer graphene electrode and dielectric elastomer, for variable focus lens,” *Applied Physics Letters*, vol. 103, no. 2, p. 023106, Jul. 2013, doi: 10.1063/1.4812982.

[84] ISO/TS 80004-1:2015(en), “Nanotechnologies, Vocabulary - Part 1:Core terms” Accessed: Jun. 29, 2022. [Online]. Available: https://www.iso.org/obp/ui/#iso:std:iso:ts:80004:-1:ed-2:v1:en

[85] F. A. Maulvi *et al.*, “Controlled bimatoprost release from graphene oxide laden contact lenses: In vitro and in vivo studies,” *Colloids Surf B Biointerfaces*, vol. 208, Dec. 2021, doi: 10.1016/J.COLSURFB.2021.112096.

[86] S. Lee *et al.*, “Smart Contact Lenses with Graphene Coating for Electromagnetic Interference Shielding and Dehydration Protection,” *ACS Nano*, vol. 11, no. 6, pp. 5318–5324, Jun. 2017, doi: 10.1021/acsnano.7b00370.

[87] Y. Zhang *et al.*, “High resolution non-invasive intraocular pressure monitoring by use of graphene woven fabrics on contact lens,” *Microsystems and Nanoengineering*, vol. 5, no. 1, 2019, doi: 10.1038/s41378-019-0078-x.

[88] S. Kaur *et al.*, “Graphene electrodes for adaptive liquid crystal contact lenses,” *Optics Express*, vol. 24, no. 8, p. 8782, 2016, doi: 10.1364/oe.24.008782.

[89] E. Lueder, “Electro-Optic Effects in Twisted Nematic Liquid Crystals,” in *Liquid Crystal Displays*, John Wiley & Sons, Ltd, 2010, pp. 57–82. doi: 10.1002/9780470688342.ch4.

[90] Y. Volkov, J. McIntyre, and A. Prina-Mello, “Graphene toxicity as a double-edged sword of risks and exploitable opportunities: a critical analysis of the most recent trends and developments,” *2D Materials*, vol. 4, no. 2, p. 022001, Jan. 2017, doi: 10.1088/2053-1583/AA5476.

[91] X. Hu and Q. Zhou, “Health and ecosystem risks of graphene,” *Chem. Rev.*, vol. 113, no. 5, pp. 3815–3835, May 2013, doi: 10.1021/cr300045n.

[92] A. Bianco and M. Prato, “Safety concerns on graphene and 2D materials: a Flagship perspective,” *2D Materials*, vol. 2, no. 3, p. 030201, Jun. 2015, doi: 10.1088/2053-1583/2/3/030201.

[93] J. N. Coleman, P. J. King, U. Khan, M. Lotya, and S. De, “Improvement of Transparent Conducting Nanotube Films by Addition of Small Quantities of Graphene,” *Acs Nano*, vol. 4, no. 7, pp. 4238–4246, 2010.

[94] C. J. Zhang *et al.*, “Transparent, Flexible, and Conductive 2D Titanium Carbide (MXene) Films with High Volumetric Capacitance,” *Advanced Materials*, vol. 29, no. 36, p. 1702678, Sep. 2017, doi: 10.1002/adma.201702678.

[95] F. Shahzad *et al.*, “2D Transition Metal Carbides (MXenes): Applications as an Electrically Conducting Material,” *Advanced Materials*, vol. 32, no. 51, p. 2002159, Dec. 2020, doi: 10.1002/ADMA.202002159.

[96] M. Naguib *et al.*, “Two-dimensional nanocrystals produced by exfoliation of Ti3AlC2,” *Advanced Materials*, vol. 23, no. 37, pp. 4248–4253, Oct. 2011, doi: 10.1002/adma.201102306.

[97] B. Anasori, M. R. Lukatskaya, and Y. Gogotsi, “2D metal carbides and nitrides (MXenes) for energy storage,” *Nature Reviews Materials*, vol. 2, p. 16098, 2017, doi: 10.1038/natrevmats.2016.98.

[98] H. Kim and H. N. Alshareef, “MXetronics : MXene enabled electronic and photonic devices,” *ACS Materials Letters*, vol. 2, no. 1, pp. 55–70, 2020, doi: 10.1021/acsmaterialslett.9b00419.

[99] Z. Fu *et al.*, “Rational Design of Flexible Two-Dimensional MXenes with Multiple Functionalities,” *Chemical Reviews*, vol. 119, no. 23, pp. 11980–12031, 2019, doi: 10.1021/acs.chemrev.9b00348.

[100] A. Lipatov *et al.*, “Elastic properties of 2D Ti3C2Tx MXene monolayers and bilayers,” *Science Advances*, vol. 4, no. 6, p. 0491, Jun. 2018, doi: 10.1126/sciadv.aat0491.

[101] A. D. Dillon *et al.*, “Highly Conductive Optical Quality Solution-Processed Films of 2D Titanium Carbide,” *Advanced Functional Materials*, vol. 26, no. 23, pp. 4162–4168, Jun. 2016, doi: 10.1002/adfm.201600357.

[102] K. Hantanasirisakul *et al.*, “Fabrication of Ti3C2Tx MXene Transparent Thin Films with Tunable Optoelectronic Properties,” *Advanced Electronic Materials*, vol. 2, no. 6, p. 1600050, Jun. 2016, doi: 10.1002/aelm.201600050.

[103] S. J. Kim *et al.*, “Metallic Ti3C2Tx MXene Gas Sensors with Ultrahigh Signal-to-Noise Ratio,” *ACS Nano*, vol. 12, pp. 986–993, 2018, doi: 10.1021/acsnano.7b07460.

[104] Y. Cai *et al.*, “Stretchable Ti3C2Tx MXene/Carbon Nanotube Composite Based Strain Sensor with Ultrahigh Sensitivity and Tunable Sensing Range,” *ACS Nano*, vol. 12, no. 1, pp. 56–62, Jan. 2018, doi: 10.1021/ACSNANO.7B06251.

[105] Y.-Y. Peng *et al.*, “All-MXene (2D titanium carbide) solid-state microsupercapacitors for on-chip energy storage,” *Energy & Environmental Science*, vol. 9, no. 9, pp. 2847–2854, Aug. 2016, doi: 10.1039/C6EE01717G.

[106] M. R. Lukatskaya *et al.*, “Ultra-high-rate pseudocapacitive energy storage in two-dimensional transition metal carbides,” *Nature Energy*, vol. 2, no. 8, p. 17105, Jul. 2017, doi: 10.1038/nenergy.2017.105.

[107] F. Shahzad *et al.*, “Electromagnetic interference shielding with 2D transition metal carbides (MXenes),” *Science (1979)*, vol. 353, no. 6304, pp. 1137–1140, Sep. 2016, doi: 10.1126/science.aag2421.

[108] R. Bian, G. He, W. Zhi, S. Xiang, T. Wang, and D. Cai, “Ultralight MXene-based aerogels with high electromagnetic interference shielding performance,” *Journal of Materials Chemistry C*, vol. 7, no. 3, pp. 474–478, 2019, doi: 10.1039/c8tc04795b.

[109] J. Saththasivam, K. Wang, W. Yiming, Z. Liu, and K. A. Mahmoud, “A flexible Ti3C2Tx (MXene)/paper membrane for efficient oil/water separation,” *RSC Advances*, vol. 9, no. 29, pp. 16296–16304, May 2019, doi: 10.1039/C9RA02129A.

[110] A. Sarycheva *et al.*, “Two-Dimensional Titanium Carbide (MXene) as Surface-Enhanced Raman Scattering Substrate,” *Journal of Physical Chemistry C*, vol. 121, no. 36, pp. 19983–19988, Sep. 2017, doi: 10.1021/ACS.JPCC.7B08180.

[111] Z. Ling *et al.*, “Flexible and conductive MXene films and nanocomposites with high capacitance,” *Proceedings of the National Academy of Sciences*, vol. 111, no. 47, pp. 16676–16681, Nov. 2014, doi: 10.1073/pnas.1414215111.

[112] B. Anasori *et al.*, “Two-Dimensional, Ordered, Double Transition Metals Carbides (MXenes),” *ACS Nano*, vol. 9, no. 10, pp. 9507–9516, Oct. 2015, doi: 10.1021/acsnano.5b03591.

[113] K. Hantanasirisakul and Y. Gogotsi, “Electronic and Optical Properties of 2D Transition Metal Carbides and Nitrides (MXenes),” *Advanced Materials*, vol. 30, no. 52, p. 1804779, Dec. 2018, doi: 10.1002/adma.201804779.

[114] T. S. Mathis *et al.*, “Modified MAX Phase Synthesis for Environmentally Stable and Highly Conductive Ti3C2 MXene,” *ACS Nano*, vol. 15, no. 4, pp. 6420–6429, Apr. 2021, doi: 10.1021/ACSNANO.0C08357.

[115] J. Gonzalez-Julian, “Processing of MAX phases: From synthesis to applications,” *Journal of the American Ceramic Society*, vol. 104, no. 2, pp. 659–690, Feb. 2021, doi: 10.1111/JACE.17544.

[116] B. Anasori and Y. Gogotsi, *2D Metal Carbides and Nitrides (MXenes)*. Berlin: Springer, 2019. doi: 10.1007/978-3-030-19026-2.

[117] M. Alhabeb *et al.*, “Guidelines for Synthesis and Processing of Two-Dimensional Titanium Carbide (Ti3C2Tx MXene),” *Chemistry of Materials*, vol. 29, no. 18, pp. 7633–7644, Sep. 2017, doi: 10.1021/acs.chemmater.7b02847.

[118] Y. Yang *et al.*, “Distinguishing electronic contributions of surface and sub-surface transition metal atoms in Ti-based MXenes,” *2D Materials*, vol. 7, no. 2, Feb. 2020, doi: 10.1088/2053-1583/ab68e7.

[119] B. Fu *et al.*, “MXenes: Synthesis, Optical Properties, and Applications in Ultrafast Photonics,” *Small*, vol. 17, no. 11, p. 2006054, Mar. 2021, doi: 10.1002/SMLL.202006054.

[120] M. Han *et al.*, “Tailoring electronic and optical properties of MXenes through forming solid solutions,” *J Am Chem Soc*, vol. 142, no. 45, pp. 19110–19118, Nov. 2020, doi: 10.1021/JACS.0C07395/ASSET/IMAGES/LARGE/JA0C07395_0004.JPEG.

[121] G. R. Berdiyorov, “Optical properties of functionalized Ti3C2T2 (T = F, O, OH) MXene: First-principles calculations,” *AIP Advances*, vol. 6, no. 5, p. 055105, May 2016, doi: 10.1063/1.4948799.

[122] A. Sarycheva, A. Polemi, Y. Liu, K. Dandekar, B. Anasori, and Y. Gogotsi, “2D titanium carbide (MXene) for wireless communication,” *Science Advances*, vol. 4, no. 9, p. eaau0920, Sep. 2018, doi: 10.1126/sciadv.aau0920.

[123] K. Montazeri, M. Currie, L. Verger, P. Dianat, M. W. Barsoum, and B. Nabet, “Beyond Gold: Spin-Coated Ti3C2-Based MXene Photodetectors,” *Advanced Materials*, vol. 31, no. 43, Oct. 2019, doi: 10.1002/ADMA.201903271.

[124] J. Halim *et al.*, “Transparent conductive two-dimensional titanium carbide epitaxial thin films,” *Chemistry of Materials*, vol. 26, no. 7, pp. 2374–2381, Apr. 2014, doi: 10.1021/CM500641A/SUPPL_FILE/CM500641A_SI_001.PDF.

[125] P. Salles, D. Pinto, K. Hantanasirisakul, K. Maleski, C. E. Shuck, and Y. Gogotsi, “Electrochromic Effect in Titanium Carbide MXene Thin Films Produced by Dip-Coating,” *Advanced Functional Materials*, vol. 29, no. 17, pp. 1–9, 2019, doi: 10.1002/adfm.201809223.

[126] H. Lashgari, M. R. Abolhassani, A. Boochani, S. M. Elahi, and J. Khodadadi, “Electronic and optical properties of 2D graphene-like compounds titanium carbides and nitrides: DFT calculations,” *Solid State Communications*, vol. 195, pp. 61–69, Oct. 2014, doi: 10.1016/J.SSC.2014.06.008.

[127] K. Rasool, M. Helal, A. Ali, C. E. Ren, Y. Gogotsi, and K. A. Mahmoud, “Antibacterial Activity of Ti3C2Tx MXene,” *ACS Nano*, vol. 10, no. 3, pp. 3674–3684, Mar. 2016, doi: 10.1021/acsnano.6b00181.

[128] X. Yu, X. Cai, H. Cui, S. W. Lee, X. F. Yu, and B. Liu, “Fluorine-free preparation of titanium carbide MXene quantum dots with high near-infrared photothermal performances for cancer therapy,” *Nanoscale*, vol. 9, no. 45, pp. 17859–17864, 2017, doi: 10.1039/c7nr05997c.

[129] Q. Xue *et al.*, “Photoluminescent Ti3C2 MXene Quantum Dots for Multicolor Cellular Imaging,” *Advanced Materials*, vol. 29, no. 15, p. 1604847, Apr. 2017, doi: 10.1002/adma.201604847.

[130] Z. Liu *et al.*, “2D magnetic titanium carbide MXene for cancer theranostics,” *Journal of Materials Chemistry B*, vol. 6, no. 21, pp. 3541–3548, 2018, doi: 10.1039/c8tb00754c.

[131] X. Han *et al.*, “Therapeutic mesopore construction on 2D Nb2C MXenes for targeted and enhanced chemo-photothermal cancer therapy in NIR-II biowindow.,” *Theranostics*, vol. 8, no. 16, pp. 4491–4508, 2018, doi: 10.7150/thno.26291.

[132] G. Liu *et al.*, “Surface Modified Ti3C2 MXene Nanosheets for Tumor Targeting Photothermal/Photodynamic/Chemo Synergistic Therapy,” *ACS Applied Materials & Interfaces*, vol. 9, no. 46, pp. 40077–40086, Nov. 2017, doi: 10.1021/acsami.7b13421.

[133] K. Rasool, K. A. Mahmoud, D. J. Johnson, M. Helal, G. R. Berdiyorov, and Y. Gogotsi, “Efficient Antibacterial Membrane based on Two-Dimensional Ti3C2Tx (MXene) Nanosheets.,” *Sci Rep*, vol. 7, no. 1, p. 1598, May 2017, doi: 10.1038/s41598-017-01714-3.

[134] K. Rasool, M. Helal, A. Ali, C. E. Ren, Y. Gogotsi, and K. A. Mahmoud, "Antibacterial Activity of Ti3C2Tx MXene," *ACS Nano*, vol. 10, no. 3, pp. 3674–3684, Mar. 2016, doi: 10.1021/acsnano.6b00181.

[135] S. Kumar, Y. Lei, N. H. Alshareef, and K. N. Salama, "Biofunctionalized Two-Dimensional Ti 3 C 2 MXenes for Ultrasensitive Detection of Cancer Biomarker," *Biosensors and Bioelectronic*, vol. 121, pp. 243–249, 2018, doi: 10.1016/j.bios.2018.08.076.

[136] Z. Wang, J. Xuan, Z. Zhao, Q. Li, and F. Geng, "Versatile Cutting Method for Producing Fluorescent Ultrasmall MXene Sheets," *ACS Nano*, vol. 11, no. 11, pp. 11559–11565, Nov. 2017, doi: 10.1021/ACSNANO.7B06476.

[137] Z. Guo *et al.*, "Fluorescent Ti3C2 MXene quantum dots for an alkaline phosphatase assay and embryonic stem cell identification based on the inner filter effect," *Nanoscale*, vol. 10, no. 41, pp. 19579–19585, Nov. 2018, doi: 10.1039/C8NR05767B.

[138] C. Dai, H. Lin, G. Xu, Z. Liu, R. Wu, and Y. Chen, "Biocompatible 2D Titanium Carbide (MXenes) Composite Nanosheets for pH-Responsive MRI-Guided Tumor Hyperthermia," *Chemistry of Materials*, vol. 29, no. 20, pp. 8637–8652, Oct. 2017, doi: 10.1021/acs.chemmater.7b02441.

[139] H. Lin, Y. Wang, S. Gao, Y. Chen, and J. Shi, "Theranostic 2D Tantalum Carbide (MXene)," *Adv Mater*, vol. 32, no. 42, Oct. 2020, doi: 10.1002/ADMA.202003085.

[140] Y. Lei *et al.*, "A MXene-Based Wearable Biosensor System for High-Performance In Vitro Perspiration Analysis," *Small*, vol. 15, no. 19, pp. 1–10, 2019, doi: 10.1002/smll.201901190.

[141] B. Xu *et al.*, "Ultrathin MXene-Micropattern-Based Field-Effect Transistor for Probing Neural Activity," *Advanced Materials*, vol. 28, no. 17, pp. 3333–3339, 2016, doi: 10.1002/adma.201504657.

[142] M. S. Artiles, C. S. Rout, and T. S. Fisher, "Graphene-based hybrid materials and devices for biosensing," *Advanced Drug Delivery Reviews*, vol. 63, no. 14–15, pp. 1352–1360, Nov. 2011, doi: 10.1016/J.ADDR.2011.07.005.

[143] N. Driscoll *et al.*, "Two-Dimensional Ti3C2 MXene for High-Resolution Neural Interfaces," *ACS Nano*, vol. 12, no. 10, pp. 10419–10429, 2018, doi: 10.1021/acsnano.8b06014.

[144] K. M. Kang *et al.*, "Selective Molecular Separation on Ti3C2Tx Graphene Oxide Membranes during Pressure Driven Filtration: Comparison with Graphene Oxide and MXenes," *ACS Applied Materials & Interfaces*, vol. 9, no. 51, pp. 44687–44694, Dec. 2017, doi: 10.1021/acsami.7b10932.

[145] Y. Gogotsi, “Chemical vapour deposition: Transition metal carbides go 2D,” *Nature Materials*, vol. 14, no. 11, pp. 1079–1080, Nov. 2015, doi: 10.1038/NMAT4386.

[146] M. Naguib, V. N. Mochalin, M. W. Barsoum, and Y. Gogotsi, “25th Anniversary Article: MXenes: A New Family of Two-Dimensional Materials,” *Advanced Materials*, vol. 26, no. 7, pp. 992–1005, Feb. 2014, doi: 10.1002/adma.201304138.

[147] P. Srivastava, A. Mishra, H. Mizuseki, K. R. Lee, and A. K. Singh, “Mechanistic Insight into the Chemical Exfoliation and Functionalization of Ti3C2 MXene,” *ACS Appl Mater Interfaces*, vol. 8, no. 36, pp. 24256–24264, Sep. 2016, doi: 10.1021/ACSAMI.6B08413.

[148] O. Mashtalir *et al.*, “Intercalation and delamination of layered carbides and carbonitrides,” *Nature Communications*, vol. 4, p. 1716, Apr. 2013, doi: 10.1038/ncomms2664.

[149] J. Halim *et al.*, “Transparent conductive two-dimensional titanium carbide epitaxial thin films,” *Chemistry of Materials*, vol. 26, no. 7, pp. 2374–2381, Apr. 2014, doi: 10.1021/CM500641A/SUPPL_FILE/CM500641A_SI_001.PDF.

[150] M. Ghidiu, M. R. Lukatskaya, M. Q. Zhao, Y. Gogotsi, and M. W. Barsoum, “Conductive two-dimensional titanium carbide ‘clay’ with high volumetric capacitance,” *Nature*, vol. 516, no. 7529, pp. 78–81, Dec. 2014, doi: 10.1038/NATURE13970.

[151] X. Sang *et al.*, “Atomic defects in monolayer titanium carbide (Ti3C2Tx) MXene,” *ACS Nano*, vol. 10, no. 10, pp. 9193–9200, Oct. 2016, doi: 10.1021/acsnano.6b05240.

[152] S. Abdolhosseinzadeh, X. Jiang, H. Zhang, J. Qiu, and C. (John) Zhang, “Perspectives on solution processing of two-dimensional MXenes,” *Materials Today*, vol. 48, pp. 214–240, Sep. 2021, doi: 10.1016/J.MATTOD.2021.02.010.

[153] C. B. Hatter, J. Shah, B. Anasori, and Y. Gogotsi, “Micromechanical response of two-dimensional transition metal carbonitride (MXene) reinforced epoxy composites,” *Composites Part B: Engineering*, vol. 182, p. 107603, Feb. 2020, doi: 10.1016/j.compositesb.2019.107603.

[154] S. Uzun *et al.*, “Knittable and Washable Multifunctional MXene-Coated Cellulose Yarns,” *Advanced Functional Materials*, vol. 29, no. 45, p. 1905015, Nov. 2019, doi: 10.1002/adfm.201905015.

[155] S. Seyedin *et al.*, “MXene Composite and Coaxial Fibers with High Stretchability and Conductivity for Wearable Strain Sensing Textiles,” *Advanced Functional Materials*, vol. 30, no. 12, p. 1910504, Mar. 2020, doi: 10.1002/adfm.201910504.

[156] S. Abdolhosseinzadeh, X. Jiang, H. Zhang, J. Qiu, and C. (John) Zhang, "Perspectives on solution processing of two-dimensional MXenes," *Materials Today*, vol. 48, pp. 214–240, Sep. 2021, doi: 10.1016/J.MATTOD.2021.02.010.

[157] E. Quain *et al.*, "Direct Writing of Additive-Free MXene-in-Water Ink for Electronics and Energy Storage," *Advanced Materials Technologies*, vol. 4, no. 1, p. 1800256, Jan. 2019, doi: 10.1002/admt.201800256.

[158] C. (John) Zhang *et al.*, "Additive-free MXene inks and direct printing of micro-supercapacitors," *Nature Communications*, vol. 10, no. 1, pp. 1–9, Dec. 2019, doi: 10.1038/s41467-019-09398-1.

[159] C. (John) Zhang *et al.*, "Additive-free MXene inks and direct printing of micro-supercapacitors," *Nature Communications 2019 10:1*, vol. 10, no. 1, pp. 1–9, Apr. 2019, doi: 10.1038/s41467-019-09398-1.

[160] Z. Chen, W. Li, R. Li, Y. Zhang, G. Xu, and H. Cheng, "Fabrication of highly transparent and conductive indium-tin oxide thin films with a high figure of merit via solution processing," *Langmuir*, vol. 29, no. 45, pp. 13836–13842, Nov. 2013, doi: 10.1021/LA4033282.

[161] C. (John) Zhang and V. Nicolosi, "Graphene and MXene-based transparent conductive electrodes and supercapacitors," *Energy Storage Materials*, vol. 16, pp. 102–125, Jan. 2019, doi: 10.1016/J.ENSM.2018.05.003.

[162] S. De and J. N. Coleman, "Are there fundamental limitations on the sheet resistance and transmittance of thin graphene films?," *ACS Nano*, vol. 4, no. 5, pp. 2713–2720, May 2010, doi: 10.1021/NN100343F/SUPPL_FILE/NN100343F_SI_001.PDF.

[163] K. Hantanasirisakul and Y. Gogotsi, "Electronic and Optical Properties of 2D Transition Metal Carbides and Nitrides (MXenes)," *Advanced Materials*, vol. 30, no. 52, p. 1804779, Dec. 2018, doi: 10.1002/adma.201804779.

[164] H. A. Becerril, J. Mao, Z. Liu, R. M. Stoltenberg, Z. Bao, and Y. Chen, "Evaluation of solution-processed reduced graphene oxide films as transparent conductors," *ACS Nano*, vol. 2, no. 3, pp. 463–470, Mar. 2008, doi: 10.1021/NN700375N.

[165] M. Mariano *et al.*, "Solution-processed titanium carbide MXene films examined as highly transparent conductors," *Nanoscale*, vol. 8, no. 36, pp. 16371–16378, Sep. 2016, doi: 10.1039/C6NR03682A.

[166] G. Ying, A. D. Dillon, A. T. Fafarman, and M. W. Barsoum, "Transparent, conductive solution processed spincast 2D Ti2CTx (MXene) films," *Materials Research Letters*, vol. 5, no. 6, pp. 391–398, Nov. 2017, doi: 10.1080/21663831.2017.1296043/SUPPL_FILE/TMRL_A_1296043_SM1894.DOCX.

[167] G. D. Boreman, “Modulation transfer function in optical systems,” in *Modulation transfer function in optical and electro-optical systems*, SPIE Press, 2001, p. 120.

[168] I. Miccoli, F. Edler, H. Pfnur, and C. Tegenjamp, “The 100th anniversary of the four-point probe technique: the role of probe geometries in isotropic and anisotropic systems,” *J. Phys.: Condens. Matter*, vol. 27, p. 223201, 2015, doi: 10.1088/0953-8984/27/22/223201.

[169] V. Natu, M. Benchakar, C. Canaff, A. Habrioux, S. Célérier, and M. W. Barsoum, “A critical analysis of the X-ray photoelectron spectra of Ti3C2Tz MXenes,” *Matter*, vol. 4, no. 4, pp. 1224–1251, Apr. 2021, doi: 10.1016/J.MATT.2021.01.015.

[170] K. Hantanasirisakul *et al.*, “Effects of Synthesis and Processing on Optoelectronic Properties of Titanium Carbonitride MXene,” *Chemistry of Materials*, vol. 31, no. 8, pp. 2941–2951, Apr. 2019, doi: 10.1021/ACS.CHEMMATER.9B00401/SUPPL_FILE/CM9B00401_SI_001.PDF.

[171] M. Ghidiu, M. R. Lukatskaya, M. Q. Zhao, Y. Gogotsi, and M. W. Barsoum, “Conductive two-dimensional titanium carbide ‘clay’ with high volumetric capacitance,” *Nature*, vol. 516, no. 7529, pp. 78–81, Dec. 2014, doi: 10.1038/NATURE13970.

[172] D. Magne, V. Mauchamp, S. Célérier, P. Chartier, and T. Cabioc’h, “Site-projected electronic structure of two-dimensional Ti3C2 MXene: the role of the surface functionalization groups,” *Physical Chemistry Chemical Physics*, vol. 18, no. 45, pp. 30946–30953, Nov. 2016, doi: 10.1039/C6CP05985F.

[173] F. Du *et al.*, “Environmental Friendly Scalable Production of Colloidal 2D Titanium Carbonitride MXene with Minimized Nanosheets Restacking for Excellent Cycle Life Lithium-Ion Batteries,” *Electrochimica Acta*, vol. 235, pp. 690–699, May 2017, doi: 10.1016/J.ELECTACTA.2017.03.153.

[174] M. C. Biesinger, L. W. Lau, A. R. Gerson, and R. StC Smart, “Resolving surface chemical states in XPS analysis of first row transition metals, oxides and hydroxides: Sc, Ti, V, Cu and Zn,” *Applied Surface Science*, vol. 257, pp. 887–898, 2010, doi: 10.1016/j.apsusc.2010.07.086.

[175] L. Å. Naslund, P. O. Å. Persson, and J. Rosen, “X-ray Photoelectron Spectroscopy of Ti3AlC2, Ti3C2Tz, and TiC Provides Evidence for the Electrostatic Interaction between Laminated Layers in MAX-Phase Materials,” *The Journal of Physical Chemistry C*, vol. 124, no. 50, pp. 27732–27742, Dec. 2020, doi: 10.1021/ACS.JPCC.0C07413.

[176] J. K. El-Demellawi, S. Lopatin, J. Yin, O. F. Mohammed, and H. N. Alshareef, “Tunable Multipolar Surface Plasmons in 2D Ti3C2Tx MXene Flakes,” *ACS Nano*, vol. 12, no. 8, pp. 8485–8493, Aug. 2018, doi: 10.1021/acsnano.8b04029.

[177] K. Maleski, C. E. Ren, M.-Q. Zhao, B. Anasori, and Y. Gogotsi, “Size-Dependent Physical and Electrochemical Properties of Two-Dimensional MXene Flakes,” *ACS Applied Materials & Interfaces*, vol. 10, no. 29, pp. 24491–24498, Jun. 2018, doi: 10.1021/acsami.8b04662.

[178] P. Özyol, E. Özyol, and F. Karel, “Biocompatibility of Intraocular Lenses,” *Turkish Journal of Ophthalmology*, vol. 47, no. 4, p. 221, 2017, doi: 10.4274/TJO.10437.

[179] G. Cooksley, J. Lacey, M. K. Dymond, and S. Sandeman, “Factors Affecting Posterior Capsule Opacification in the Development of Intraocular Lens Materials,” *Pharmaceutics 2021, Vol. 13, Page 860*, vol. 13, no. 6, p. 860, Jun. 2021, doi: 10.3390/PHARMACEUTICS13060860.

[180] X. Tan *et al.*, “Improvement of Uveal and Capsular Biocompatibility of Hydrophobic Acrylic Intraocular Lens by Surface Grafting with 2-Methacryloyloxyethyl Phosphorylcholine-Methacrylic Acid Copolymer,” *Scientific Reports 2017 7:1*, vol. 7, no. 1, pp. 1–13, Jan. 2017, doi: 10.1038/srep40462.

[181] P. G. Ursell *et al.*, “Three-year incidence of Nd:YAG capsulotomy and posterior capsule opacification and its relationship to monofocal acrylic IOL biomaterial: a UK Real World Evidence study,” *Eye (Lond)*, vol. 32, no. 10, pp. 1579–1589, Oct. 2018, doi: 10.1038/S41433-018-0131-2.

[182] O. Findl, W. Buehl, P. Bauer, and T. Sycha, “Interventions for preventing posterior capsule opacification,” *Cochrane Database Syst Rev*, vol. 2017, no. 2, Feb. 2010, doi: 10.1002/14651858.CD003738.PUB3.

[183] O. Nishi, K. Nishi, J. Akura, and T. Nagata, “Effect of round-edged acrylic intraocular lenses on preventing posterior capsule opacification,” *J Cataract Refract Surg*, vol. 27, no. 4, pp. 608–613, Apr. 2001, doi: 10.1016/S0886-3350(00)00644-1.

[184] T. Kohnen *et al.*, “Optic edge design as long-term factor for posterior capsular opacification rates,” *Ophthalmology*, vol. 115, no. 8, 2008, doi: 10.1016/J.OPHTHA.2008.01.002.

[185] O. Nishi, K. Nishi, and Y. Osakabe, “Effect of intraocular lenses on preventing posterior capsule opacification: design versus material,” *J Cataract Refract Surg*, vol. 30, no. 10, pp. 2170–2176, Oct. 2004, doi: 10.1016/J.JCRS.2004.05.022.

[186] C. Leydolt, S. Schriefl, E. Stifter, A. Haszcz, and R. Menapace, “Posterior capsule opacification with the iMics1 NY-60 and AcrySof SN60WF 1-piece hydrophobic acrylic intraocular lenses: 3-year results of a randomized trial,” *Am J Ophthalmol*, vol. 156, no. 2, 2013, doi: 10.1016/J.AJO.2013.04.007.

[187] R. Mencucci, E. Favuzza, C. Boccalini, J. J. Gicquel, and L. Raimondi, “Square-edge intraocular lenses and epithelial lens cell proliferation: Implications on

posterior capsule opacification in an in vitro model," *BMC Ophthalmology*, vol. 15, no. 1, pp. 1–5, Jan. 2015, doi: 10.1186/1471-2415-15-5/FIGURES/4.

[188] Y. Zhao, K. Yang, J. Li, Y. Huang, and S. Zhu, "Comparison of hydrophobic and hydrophilic intraocular lens in preventing posterior capsule opacification after cataract surgery: An updated meta-analysis," *Medicine*, vol. 96, no. 44, Nov. 2017, doi: 10.1097/MD.0000000000008301.

[189] S. Kumar. Khokhar and Chirakshi. Dhull, *Essentials of pediatric cataract surgery*. Singapore: Springer, 2021.

[190] G. U. Auffarth *et al.*, "Comparison of Nd : YAG capsulotomy rates following phacoemulsification with implantation of PMMA, silicone, or acrylic intra-ocular lenses in four European countries," *Ophthalmic Epidemiol*, vol. 11, no. 4, pp. 319–329, Oct. 2004, doi: 10.1080/09286580490515116.

[191] K. Hayashi and H. Hayashi, "Posterior capsule opacification after implantation of a hydrogel intraocular lens," *The British Journal of Ophthalmology*, vol. 88, no. 2, p. 182, Feb. 2004, doi: 10.1136/BJO.2003.023580.

[192] M. W. Dorey *et al.*, "Proposed pathogenesis for the delayed postoperative opacification of the hydroview hydrogel intraocular lens," *Am J Ophthalmol*, vol. 135, no. 5, pp. 591–598, May 2003, doi: 10.1016/S0002-9394(02)02154-2.

[193] R. J. Linnola, L. Werner, S. K. Pandey, M. Escobar-Gomez, S. L. Znoiko, and D. J. Apple, "Adhesion of fibronectin, vitronectin, laminin, and collagen type IV to intraocular lens materials in pseudophakic human autopsy eyes. Part 2: explanted intraocular lenses," *J Cataract Refract Surg*, vol. 26, no. 12, pp. 1807–1818, 2000, doi: 10.1016/S0886-3350(00)00747-1.

[194] R. J. Linnola, "Sandwich theory: bioactivity-based explanation for posterior capsule opacification," *J Cataract Refract Surg*, vol. 23, no. 10, pp. 1539–1542, 1997, doi: 10.1016/S0886-3350(97)80026-0.

[195] R. J. Linnola, M. Sund, R. Ylönen, and T. Pihlajaniemi, "Adhesion of soluble fibronectin, laminin, and collagen type IV to intraocular lens materials," *J Cataract Refract Surg*, vol. 25, no. 11, pp. 1486–1491, Nov. 1999, doi: 10.1016/S0886-3350(99)00238-2.

[196] Y. S. Huang *et al.*, "RGD Surface Functionalization of the Hydrophilic Acrylic Intraocular Lens Material to Control Posterior Capsular Opacification," *PLOS ONE*, vol. 9, no. 12, p. e114973, Dec. 2014, doi: 10.1371/JOURNAL.PONE.0114973.

[197] T. Ozulumba, G. Ingavle, Y. Gogotsi, and S. Sandeman, "Moderating cellular inflammation using 2-dimensional titanium carbide MXene and graphene variants," *Biomaterials Science*, vol. 9, no. 5, pp. 1805–1815, Mar. 2021, doi: 10.1039/D0BM01953D.

[198] A. Jastrzębska, AM, Szuplewska, A, Wojciechowski, T, Chudy, M, Ziemkowska, W, Chlubny, L, Rozmysłowska, A, Olszyna, "In vitro studies on cytotoxicity of delaminated Ti3C2 MXene," *Journal of Hazardous Materials*, vol. 339, pp. 1–8, Oct. 2017, doi: 10.1016/J.JHAZMAT.2017.06.004.

[199] W. Wu *et al.*, "Evaluating the Cytotoxicity of Ti3C2 MXene to Neural Stem Cells," *Chemical Research in Toxicology*, vol. 33, no. 12, pp. 2953–2962, Dec. 2020, doi: 10.1021/ACS.CHEMRESTOX.0C00232.

[200] A. Rozmysłowska-Wojciechowska *et al.*, "A simple, low-cost and green method for controlling the cytotoxicity of MXenes," *Materials Science and Engineering: C*, vol. 111, p. 110790, Jun. 2020, doi: 10.1016/J.MSEC.2020.110790.

[201] B. Sui, X. Liu, and J. Sun, "Biodistribution, inter-/intra-cellular localization and respiratory dysfunction induced by Ti3C2 nanosheets: Involvement of surfactant protein down-regulation in alveolar epithelial cells," *Journal of Hazardous Materials*, vol. 402, p. 123562, Jan. 2021, doi: 10.1016/J.JHAZMAT.2020.123562.

[202] B. Scheibe *et al.*, "Cytotoxicity Assessment of Ti–Al–C Based MAX Phases and Ti3C2Tx MXenes on Human Fibroblasts and Cervical Cancer Cells," *ACS Biomaterials Science & Engineering*, vol. 5, no. 12, pp. 6557–6569, Dec. 2019, doi: 10.1021/ACSBIOMATERIALS.9B01476.

[203] H. Lin, Y. Chen, J. Shi, H. Lin, Y. Chen, and J. Shi, "Insights into 2D MXenes for Versatile Biomedical Applications: Current Advances and Challenges Ahead," *Advanced Science*, vol. 5, no. 10, p. 1800518, Oct. 2018, doi: 10.1002/ADVS.201800518.

[204] A. M. Jastrzębska *et al.*, "On tuning the cytotoxicity of Ti3C2 (MXene) flakes to cancerous and benign cells by post-delamination surface modifications," *2D Materials*, vol. 7, no. 2, 2020, doi: 10.1088/2053-1583/AB6A60.

[205] G. P. Lim *et al.*, "Cytotoxicity of MXene-based nanomaterials for biomedical applications: A mini review," *Environmental Research*, vol. 201, p. 111592, Oct. 2021, doi: 10.1016/J.ENVRES.2021.111592.

[206] T. Jennifer Ozulumba, "Two-dimensional nanomaterials for use in medical devices for remediation of biological toxins," University of Brighton, Brighton, 2020.

[207] G. C. Ingavle *et al.*, "Affinity binding of antibodies to supermacroporous cryogel adsorbents with immobilized protein A for removal of anthrax toxin protective antigen," *Biomaterials*, vol. 50, no. 1, pp. 140–153, 2015, doi: 10.1016/J.BIOMATERIALS.2015.01.039.

[208] S. Mullick Chowdhury, G. Lalwani, K. Zhang, J. Y. Yang, K. Neville, and B. Sitharaman, "Cell specific cytotoxicity and uptake of graphene nanoribbons,"

Biomaterials, vol. 34, no. 1, pp. 283–293, Jan. 2013, doi: 10.1016/J.BIOMATERIALS.2012.09.057.

[209] C. Romo-valera, P. Guerrero, J. Arluzea, J. Etxebarria, K. de la Caba, and N. Andollo, "Cytocompatibility and Suitability of Protein-Based Biomaterials as Potential Candidates for Corneal Tissue Engineering," *International Journal of Molecular Sciences*, vol. 22, no. 7, Apr. 2021, doi: 10.3390/IJMS22073648.

[210] F. Meng *et al.*, "MXene Sorbents for Removal of Urea from Dialysate: A Step toward the Wearable Artificial Kidney," *ACS Nano*, vol. 12, no. 10, pp. 10518–10528, 2018, doi: 10.1021/ACSNANO.8B06494.

[211] W. Chanput, J. J. Mes, and H. J. Wichers, "THP-1 cell line: An in vitro cell model for immune modulation approach," *International Immunopharmacology*, vol. 23, no. 1, pp. 37–45, 2014, doi: 10.1016/J.INTIMP.2014.08.002.

[212] T. Ozulumba, G. Ingavle, Y. Gogotsi, and S. Sandeman, "Moderating cellular inflammation using 2-dimensional titanium carbide MXene and graphene variants," *Biomater Sci*, vol. 9, no. 5, pp. 1805–1815, Mar. 2021, doi: 10.1039/D0BM01953D.

[213] A. M. Jastrzębska *et al.*, "In vitro studies on cytotoxicity of delaminated Ti3C2 MXene," *Journal of Hazardous Materials*, vol. 339, pp. 1–8, Oct. 2017, doi: 10.1016/J.JHAZMAT.2017.06.004.

[214] International Organization for Standardization (ISO) 10993-5, "Biological evaluation of medical devices," 2009. Accessed: Jan. 30, 2022. [Online]. Available: http://nhiso.com/wp-content/uploads/2018/05/ISO-10993-5-2009.pdf

[215] T. Dutta *et al.*, "ROS generation by reduced graphene oxide (rGO) induced by visible light showing antibacterial activity: Comparison with graphene oxide (GO)," *RSC Advances*, vol. 5, no. 98, pp. 80192–80195, Sep. 2015, doi: 10.1039/c5ra14061g.

[216] H. C. Lin, M. S. Chen, and Y. H. Lin, "A Review of Electrically Tunable Focusing Liquid Crystal Lenses," *undefined*, vol. 12, no. 6, pp. 234–240, Dec. 2011, doi: 10.4313/TEEM.2011.12.6.234.

[217] G. Li *et al.*, "Switchable electro-optic diffractive lens with high efficiency for ophthalmic applications.," *Proc Natl Acad Sci U S A*, vol. 103, no. 16, pp. 6100–6104, Apr. 2006, doi: 10.1073/PNAS.0600850103.

[218] H. E. Milton, P. B. Morgan, J. H. Clamp, and H. F. Gleeson, "Electronic liquid crystal contact lenses for the correction of presbyopia," *Optics Express*, vol. 22, no. 7, p. 8035, 2014, doi: 10.1364/oe.22.008035.

[219] I. C. Khoo, *Liquid Crystals: Second Edition*, 2nd ed. Wiley, 2006. doi: 10.1002/0470084030.

[220] I. W. Hamley, *Introduction to Soft Matter: Synthetic and Biological Self-Assembling Materials*. John Wiley and Sons, 2007. doi: 10.1002/9780470517338.

[221] D. Andrienko, "Introduction to liquid crystals," *Journal of Molecular Liquids*, vol. 267, pp. 520–541, 2018, doi: 10.1016/j.molliq.2018.01.175.

[222] C. W. Fowler and E. S. Pateras, "Liquid crystal lens review," *Ophthalmic and Physiological Optics*, vol. 10, no. 2, pp. 186–194, 1990, doi: 10.1111/j.1475-1313.1990.tb00974.x.

[223] R. G. Horn, "Refractive indices and order parameters of two liquid crystals," *Journal de Physique*, vol. 39, no. 1, pp. 105–109, 1978, doi: 10.1051/jphys:01978003901010500ï.

[224] J. Li, "Refractive Indices Of Liquid Crystals And Their Applications In Display And Photonic Devices," 2005. Accessed: Nov. 26, 2019. [Online]. Available: http://library.ucf.edu

[225] M. Schadt, "Liquid crystal materials and liquid crystal displays," 1997.

[226] J. Stöhr and M. G. Samant, "Liquid crystal alignment by rubbed polymer surfaces: A microscopic bond orientation model," *Journal of Electron Spectroscopy and Related Phenomena*, vol. 98–99, pp. 189–207, 1999.

[227] Y.-H. Lin, H.-S. Chen, and M.-S. Chen, "Electrically-tunable liquid crystal lenses and applications," *Emerging Liquid Crystal Technologies VIII*, vol. 8642, pp. 65–76, 2013, doi: 10.1117/12.2005580.

[228] D. K. Yang and S. T. Wu, *Fundamentals of Liquid Crystal Devices*. Wiley, 2014. doi: 10.1002/9781118751992.

[229] A. Bogi and S. Faetti, "Elastic, dielectric and optical constants of 4′-pentyl-4-cyanobiphenyl," *Liquid Crystals*, vol. 28, no. 5, pp. 729–739, 2001, doi: 10.1080/02678290010021589.

[230] S. Sato, "Liquid-Crystal Lens-Cells with Variable Focal Length," *Japanese Journal of Applied Physics*, vol. 18, no. 9, p. 1679, Sep. 1979, doi: 10.1143/JJAP.18.1679.

[231] P. Yeh and Claire. Gu, *Optics of liquid crystal displays*. Wiley, 2010.

[232] R. P. Pan, T. R. Tsai, C. Y. Chen, and C. L. Pan, "Optical constants of two typical liquid crystals 5CB and PCH5 in the THz frequency range," in *Journal of Biological Physics*, 2003, vol. 29, no. 2–3, pp. 335–338. doi: 10.1023/A:1024485918938.

[233] J. Li, C. H. Wen, S. Gauza, R. Lu, and S. T. Wu, "Refractive indices of liquid crystals for display applications," *IEEE/OSA Journal of Display Technology*, vol. 1, no. 1, pp. 51–61, 2005, doi: 10.1109/JDT.2005.853357.

[234] R. P. Pan, C. F. Hsieh, C. L. Pan, and C. Y. Chen, “Temperature-dependent optical constants and birefringence of nematic liquid crystal 5CB in the terahertz frequency range,” *Journal of Applied Physics*, vol. 103, no. 9, p. 093523, May 2008, doi: 10.1063/1.2913347.

[235] X. Li *et al.*, “Engineering the anchoring behavior of nematic liquid crystals on a solid surface by varying the density of liquid crystalline polymer brushes,” *Soft Matter*, vol. 14, no. 37, pp. 7569–7577, Sep. 2018, doi: 10.1039/C8SM00991K.

[236] Y. Cui *et al.*, “Alignment Layers with Variable Anchoring Strengths from Polyvinyl Alcohol,” *Chemical Physics Publications Department of Chemical Physics*, vol. 111, no. 6, 2012, doi: 10.1063/1.3697680.

[237] S. Y. Lee, Y. Kumar, J. M. Cho, S. W. Lee, and S. W. Kim, “Enhanced autofocus algorithm using robust focus measure and fuzzy reasoning,” *IEEE Transactions on Circuits and Systems for Video Technology*, vol. 18, no. 9, pp. 1237–1246, 2008, doi: 10.1109/TCSVT.2008.924105.

[238] X. Wang, “Laplacian operator-based edge detectors,” *IEEE Transactions on Pattern Analysis and Machine Intelligence*, vol. 29, no. 5, pp. 886–890, 2007, doi: 10.1109/TPAMI.2007.1027.

[239] M. Riaz, S. Park, M. B. Ahmad, W. Rasheed, and J. Park, “Generalized Laplacian as focus measure,” in *Lecture Notes in Computer Science*, 2008, vol. 5101 LNCS, no. PART 1, pp. 1013–1021. doi: 10.1007/978-3-540-69384-0_106.

[240] M. C. Potter, B. Wyble, C. E. Hagmann, and E. S. McCourt, “Detecting meaning in RSVP at 13 ms per picture,” *Attention, Perception, & Psychophysics 2014 76:2*, vol. 76, no. 2, pp. 270–279, Dec. 2013, doi: 10.3758/S13414-013-0605-Z.

[241] J. Bailey, S. Kaur, P. B. Morgan, H. F. Gleeson, J. H. Clamp, and J. C. Jones, “Design considerations for liquid crystal contact lenses,” *Journal of Physics D: Applied Physics*, vol. 50, no. 48, p. 485401, Nov. 2017, doi: 10.1088/1361-6463/aa9358.

[242] Y. H. Lin, Y. J. Wang, and V. Reshetnyak, “Liquid crystal lenses with tunable focal length,” *Liquid Crystals Reviews*, vol. 5, no. 2, pp. 111–143, 2017, doi: 10.1080/21680396.2018.1440256.

[243] B. Wang, M. Ye, M. Honma, T. Nose, and S. Sato, “Liquid crystal lens with spherical electrode,” *Japanese Journal of Applied Physics, Part 2: Letters*, vol. 41, no. 11 A, p. L1232, Nov. 2002, doi: 10.1143/JJAP.41.L1232/XML.

[244] A. Naumov, G. Vdovin, and M. Loktev, “On the possibility of intraocular adaptive optics,” *Optics Express, Vol. 11, Issue 7, pp. 810-817*, vol. 11, no. 7, pp. 810–817, Apr. 2003, doi: 10.1364/OE.11.000810.

[245] H. Ren, Y. H. Fan, S. Gauza, and S. T. Wu, “Tunable-focus flat liquid crystal spherical lens,” *Applied Physics Letters*, vol. 84, no. 23, p. 4789, May 2004, doi: 10.1063/1.1760226.

[246] H. Ren and S.-T. Wu, “Adaptive liquid crystal lens with large focal length tunability.,” *Opt Express*, vol. 14, no. 23, p. 11292, 2006, doi: 10.1364/OE.14.011292.

[247] A. N. Simonov, G. Vdovin, and M. Loktev, “Liquid-crystal intraocular adaptive lens with wireless control,” *Optics Express*, vol. 15, no. 12, p. 7468, 2007, doi: 10.1364/oe.15.007468.

[248] I. M. Syed *et al.*, “Novel switching mode in a vertically aligned liquid crystal contact lens,” *Optics Express*, vol. 23, no. 8, p. 9911, 2015, doi: 10.1364/oe.23.009911.

[249] A. Galstian, T., Asatryan, K., Presniakov, V., Zohrabyan, “Electrically variable liquid crystal lenses for ophthalmic distance accommodation,” *Opt Express*, vol. 27, no. 13, pp. 18803–18817, 2019.

[250] H. E. Milton, H. F. Gleeson, P. B. Morgan, J. W. Goodby, S. Cowling, and J. H. Clamp, “Switchable liquid crystal contact lenses: dynamic vision for the ageing eye,” *Emerging Liquid Crystal Technologies IX*, vol. 9004, p. 90040H, 2014, doi: 10.1117/12.2044676.

[251] X. Nie, H. Xianyu, R. Lu, T. X. Wu, and S. T. Wu, “Pretilt angle effects on liquid crystal response time,” *Journal of Display Technology*, vol. 3, no. 3, pp. 280–283, Sep. 2007, doi: 10.1109/JDT.2007.900926.

[252] Y.-J. Lee, C.-J. Yu, J.-H. Lee, J.-H. Baek, Y. Kim, and J.-H. Kim, “Optically isotropic switchable microlens arrays based on liquid crystal,” *Applied Optics*, vol. 53, no. 17, 2014, doi: 10.1364/AO.53.003633.

[253] K. Masaoka *et al.*, “Modified slanted-edge method and multidirectional modulation transfer function estimation,” *Optics Express, Vol. 22, Issue 5, pp. 6040-6046*, vol. 22, no. 5, pp. 6040–6046, Mar. 2014, doi: 10.1364/OE.22.006040.

[254] T. Iwase, J. Onaka, A. Emoto, D. Koyama, and M. Matsukawa, “Relationship between liquid crystal layer thickness and variable-focusing characteristics of an ultrasound liquid crystal lens,” *Japanese Journal of Applied Physics*, vol. 61, p. SG1013 1-SG1013 4, Mar. 2022, doi: 10.35848/1347-4065/AC48D1.

[255] C. L. Tien and T. W. Lin, “Out-of-plane thermal expansion coefficient and biaxial young’s modulus of sputtered ITO thin films,” *Coatings*, vol. 11, no. 2, pp. 1–11, Feb. 2021, doi: 10.3390/COATINGS11020153.

[256] Z. G. Özdemir, N. Yilmaz Canli, M. Okutan, and B. Bilgin Eran, “Dielectric Anisotropy Properties of BAC-Doped 5CB Liquid Crystal,” *Molecular Crystals and*

Liquid Crystals, vol. 616, no. 1, pp. 102–111, Jul. 2015, doi: 10.1080/15421406.2014.990283.

[257] S. Al-Zangana, M. Iliut, M. Turner, A. Vijayaraghavan, and I. Dierking, "Properties of a Thermotropic Nematic Liquid Crystal Doped with Graphene Oxide," *Advanced Optical Materials*, vol. 4, no. 10, pp. 1541–1548, 2016, doi: 10.1002/adom.201600351.

[258] G. B. Hadjichristov, Y. G. Marinov, A. G. Petrov, L. Marino, and N. Scaramuzza, "Dielectric and electrical characterization of 5CB nematic liquid crystal doped with silver nanoparticles," *Journal of Physics: Conference Series*, vol. 682, no. 1, p. 012015, 2016, doi: 10.1088/1742-6596/682/1/012015.

[259] M. Mrukiewicz, K. Kowiorski, P. Perkowski, R. Mazur, and M. Djas, "Threshold voltage decrease in a thermotropic nematic liquid crystal doped with graphene oxide flakes," *Beilstein Journal of Nanotechnology*, vol. 10, no. 1, pp. 71–78, 2019, doi: 10.3762/bjnano.10.7.

[260] R. Bitar *et al.*, "Acrylic acid plasma polymerization for biomedical use," *ApSS*, vol. 448, pp. 168–185, Aug. 2018, doi: 10.1016/J.APSUSC.2018.04.129.

[261] M. Ji, A. Jagodar, E. Kovacevic, L. Benyahia, and F. Poncin-Epaillard, "Characterization of functionalized coatings prepared from pulsed plasma polymerization," *Materials Chemistry and Physics*, vol. 267, 2021, doi: 10.1016/j.matchemphys.2021.124621ï.

[262] E. J. Ward *et al.*, "2D Titanium Carbide (Ti3C2Tx) in Accommodating Intraocular Lens Design," *Advanced Functional Materials*, vol. 30, no. 47, p. 2000841, Nov. 2020, doi: 10.1002/adfm.202000841.

[263] F. A. Hayden, "Electronic IOLs : The future of cataract sugery," *EyeWorld*, no. February 2012, pp. 2011–2013, 2012.

Appendices

Appendix 1 – Beam shift MATLAB script

```
function iol_xc

% requires imfreq.m
% refracted beam is assumed to be left of the reference beam

%% define variables
simulate_refraction = 0; % [pix] set to zero to process refracted images, set to a pixel shift to simulate
refraction
image_file_extension = 'tiff';
default_path = '\\university\store\AEC\Projects\Live\Spray Lab 3\Experiments\2019 Emma';
background = 100; % [-] value (0-255) for backgound thresholding
frequency_filter = [0 30];
beam_radius = 100; % [pix] used to define the cropping window
pixel_size = 5.86; % [µm/pix] the camera's pixel size (=5.86µm for the Basler acA1920-40gm)
beam_shift_coarse = 0;

%% get files to process
% get file paths from user and find all image files
reference_files = get_files(default_path, image_file_extension, 'Select reference beam folder');
if simulate_refraction == 0
    refracted_files = get_files(default_path, image_file_extension, 'Select refracted beam folder');
end

%% pre-process images
% compute average images
reference_image = average_image(reference_files);
if simulate_refraction == 0
    refracted_image = average_image(refracted_files);
else
    refracted_image = imtranslate(reference_image, [-simulate_refraction 0]);
end

% filter images (thresholding and frequency filter)
reference_image_filtered = filter_image(reference_image);
refracted_image_filtered = filter_image(refracted_image);

% find optimum crop to speed up cross-correlation
[reference_image_filtered_cropped, refracted_image_filtered_cropped, crop_rect] =
crop_images(reference_image_filtered, refracted_image_filtered);

%% process and output results
% perform cross-correlation
[refraction_tx, refraction_ty, refraction_tform] = register_images(reference_image_filtered_cropped,
refracted_image_filtered_cropped);
```

```
% compute unrefracted image
unrefracted_image = imwarp(refracted_image_filtered_cropped, refraction_tform,
'OutputView',imref2d(size(reference_image_filtered_cropped)));

display_results;


%% nested functions
    function file_list = get_files(initial_path, file_extension, title)
        % returns a dir structure
        if ~isfolder(initial_path)
            initial_path = '';
        end

        path = uigetdir(initial_path, title);
        if path==0
            % user cancelled
            error('get_files', 'User cancelled folder selection');
        end

        % find all image files
        file_list = dir(fullfile(path, ['*.' file_extension]));
    end

    function avg_img = average_image(image_files)
    % average_image computes the mean image from all images in image_files
    % image_files is a dir structure

    n = numel(image_files);

    % Load waitbar
    h = waitbar(0,'1','Name','Processing images...', 'CreateCancelBtn', 'setappdata(gcbf,"canceling",1)');
    setappdata(h,'cancelling',0)

    % Initialise M as double precision floating point
    avg_img = double(0);

    %% Process images
    % Open images and compute average image sequentially
    for i = 1:n
        % Check for Cancel button press on waitbar
        if getappdata(h,'canceling')
            delete(h);
            error('Processing cancelled by user.')
        end

        % Report progress in the waitbar's message field
        waitbar(i/n,h,sprintf('Processing file %i of %i...',i,n))

        %% Read image data and store it as double
        % Load image data as double precision
        I = double(imread(fullfile(image_files(i).folder, image_files(i).name)));

        %% Update mean
        % Update mean, sum and sum of the squares
        avg_img = (avg_img*(i-1) + I)/i;
    end
```

```
    delete(h);

    end

    function image_filtered = filter_image(image)
        % thresholding to remove background noise
        image_filtered = image-background;
        image_filtered(image_filtered<0) = 0;

        % frequency filter to remove noise and diffraction
        image_filtered = imfreq(image_filtered, frequency_filter);
    end

    function [image1_cropped, image2_cropped, crop_rect] = crop_images(image1, image2)
        % find max intensity in both images and crop both images while
        % keeping both beams in final crop
        max_pixel_index_refe = find(image1==max(image1(:)));
        [max_pixel_refe_y, max_pixel_refe_x] = ind2sub(size(image1), max_pixel_index_refe);
        max_pixel_index_refr = find(image2==max(image2(:)));
        [max_pixel_refr_y, max_pixel_refr_x] = ind2sub(size(image2), max_pixel_index_refr);

        crop_pixel_y = min(max_pixel_refe_y, max_pixel_refr_y) -beam_radius;
        crop_pixel_x = min(max_pixel_refe_x, max_pixel_refr_x) -beam_radius;
        crop_pixel_h = max(max_pixel_refe_y, max_pixel_refr_y) -crop_pixel_y +beam_radius;
        crop_pixel_w = max(max_pixel_refe_x, max_pixel_refr_x) -crop_pixel_x +beam_radius;

        % check if beam seperation is too large for imregtform to converge
        if crop_pixel_w > 3*beam_radius
            beam_shift_coarse = crop_pixel_w-3*beam_radius;
        else
            beam_shift_coarse = 0;
        end

        crop_rect = [crop_pixel_x crop_pixel_y crop_pixel_w crop_pixel_h];
        image1_cropped = imcrop(image1, crop_rect - [-beam_shift_coarse 0 beam_shift_coarse 0]);
        image2_cropped = imcrop(image2, crop_rect - [0 0 beam_shift_coarse 0]);
    end

    function [dx, dy, tform] = register_images(image1, image2)
        % compute translation transform
        [optimizer, metric] = imregconfig('monomodal'); % 'monomodal' because both images were
recorded using same sensor
        tform = imregtform(image2, image1, 'translation', optimizer, metric, 'DisplayOptimization',true);

        % extract translation values
        dx = tform.T(3,1) + beam_shift_coarse;
        dy = tform.T(3,2);
    end

    function display_results
        figure('Units','normalized','Position', [0,0,1,1]);

        m=2; n=3;
        ax1 = subplot(m,n,1);
        imshowpair(reference_image, refracted_image)
        title('mean images');

        % display processed images
```

```
        ax4 = subplot(m,n,4);
        imshowpair(imcrop(reference_image,crop_rect), imcrop(refracted_image,crop_rect))
        title('cropped images');

        ax5 = subplot(m,n,5);
        imshowpair(reference_image_filtered_cropped, refracted_image_filtered_cropped)
        title('denoised images');

        ax6 = subplot(m,n,6);
        imshowpair(reference_image_filtered_cropped, unrefracted_image)
        title('unrefracted image');

        linkaxes([ax4,ax5,ax6],'xy')

        str = sprintf("%s\n%s\n\n",reference_files(1).folder, refracted_files(1).folder);
        str = [str sprintf('translation x = %.4f µm (%.4f pixels)\n', refraction_tx*pixel_size,
refraction_tx)];
        str = [str sprintf('translation y = %.4f µm (%.4f pixels)\n', refraction_ty*pixel_size,
refraction_ty)];
        refraction_d = sqrt(refraction_tx^2 + refraction_ty^2);
        str = [str sprintf('translation = %.4f µm (%.4f pixels)\n', refraction_d*pixel_size, refraction_d)];
        dim = [.4 .5 .3 .3];
        annotation('textbox',dim,'String',str,'FitBoxToText','on', 'FontSize', 14, 'LineStyle', 'none');

        disp(str)

    end

end
```

Appendix 2 – Laplacian operator

```
import cv2
import os
import csv
from matplotlib import pyplot as plt

# Set up some variables
directory = 'images'
laplacianVariance = []
fig = plt.figure(None, [12, 6])
count = 1

# Get the list of images
lst = os.listdir(directory)
lst.sort()

# Loop through all the images
for filename in lst:
    if filename.endswith((".JPG", ".jpg", ".JPEG", ".jpeg", ".PNG", ".png")):
```

```
        # Load the image
        mxImage = cv2.imread(directory+'/'+filename, )
        b, g, r = cv2.split(mxImage)  # get b, g, r
        mxImage = cv2.merge([r, g, b])  # switch it to r, g, b

        # Set the points for cropped image
        left = 50
        top = 50
        right = 450
        bottom = 450

        # Crop the image
        masked_mxImage = mxImage[top:bottom, left:right].copy()

        # Convert to gray scale
        masked_mxImage_gray = cv2.cvtColor(masked_mxImage, cv2.COLOR_BGR2GRAY)

        # Remove noise with Gaussian blur
        masked_mxImage_gray_img = cv2.GaussianBlur(masked_mxImage_gray, (3, 3), 0)

        # Get Laplacian variance from the image
        laplacian_mxImage = cv2.Laplacian(masked_mxImage_gray_img, cv2.CV_16S).var()

        # Create a Histogram
        hist_mxImage = cv2.calcHist([masked_mxImage_gray_img], [0], None, [256], [0, 256])

        # Plot the figure
        fig.subplots_adjust(bottom=0.025, left=0.025, top=0.975, right=0.975)

        plt.subplot(1, 5, 1), plt.title('Original', loc='left'), plt.imshow(mxImage), plt.xticks(
            []), plt.yticks([])
        plt.subplot(1, 5, 2), plt.title('Cropped', loc='left'), plt.imshow(masked_mxImage), plt.xticks(
            []), plt.yticks([])
        plt.subplot(1, 5, 3), plt.title('Grey', loc='left'), plt.imshow(masked_mxImage_gray, cmap='gray'),
plt.xticks(
            []), plt.yticks([])
        plt.subplot(1, 5, 4), plt.title('Smoothed', loc='left'), plt.text(-130, 560,
                                                    'Variance: ' + str(laplacian_mxImage),
                                                    style='italic',
                                                    bbox={'facecolor': 'red', 'alpha': 0.5,
                                                          'pad': 10}), plt.imshow(
            masked_mxImage_gray_img, cmap='gray'), plt.xticks([]), plt.yticks([])
        plt.subplot(1, 5, 5), plt.title('Histogram', loc='left'), plt.plot(hist_mxImage)
        plt.tight_layout()

        # Add variance to array
        fileAndVariance = [count, filename, laplacian_mxImage]
        laplacianVariance.append(fileAndVariance),

        # Save the figure
        plt.savefig('output/figures/'+filename+'.png')
        plt.clf()

        # Save Histogram as CSV
        with open('output/data/histogram'+filename+'.csv', 'w') as varianceList:
            wr = csv.writer(varianceList, quoting=csv.QUOTE_ALL, )
            wr.writerows(hist_mxImage)
```

```
        # Add on to the count
        count += 1
        continue
    else:
        continue

# Add variance to csv if is exists
if laplacianVariance:
    with open('output/data/laplacianVariance.csv', 'w') as varianceList:
        wr = csv.writer(varianceList, quoting=csv.QUOTE_ALL, )
        wr.writerows(laplacianVariance
```

Appendix 3 – Ronchi focus position MATLAB script

```
% Ronchi Analysis Loop
%
% Insert your source images in to the images folder organised by lens
% and then voltage.
%
% For example:
% 'images/Lens1/0v'
% 'images/Lens1/40v'
% 'images/Lens2/0v'
% 'images/Lens2/40v'
% '...'
%

% Include other scripts in lib folder
addpath('lib');

% Specify the images location
folder = 'images';

% Specify the image format
imageType = 'tiff';

% scales
RonchiFreq = 5; % [cycles/mm]
RonchiAngle = 45; % [deg]
mmPerPix = 0.007730; % scale factor [mm/pix] calculated assuming ronchi was at 45 deg
DefocusOffset = 0; % defocus offset

% Intro Banner
fprintf('\n');
fprintf('----------------------\n');
fprintf('--- RONCHI ANALYSIS ---\n');
fprintf('----------------------\n\n');

% Find any files that match the image format within in folder variable
```

```
filePattern = fullfile(folder, ['**/*.' imageType]);
fprintf('Looking for .%s files in %s/%s...\n\n', imageType, pwd, folder);
srcFiles = dir(filePattern);

% Count the number of files
numFiles = length(srcFiles);

% Create the data table and a temp table
dataTable = table();
tempDataTable = table();

if numFiles == 0
  message = sprintf('There are no %s files are in folder:\n%s', imageType, folder);
  uiwait(warndlg(message));
else
  fprintf('There are %d files in %s:\n\n', numFiles, folder);
  for k = 1 : numFiles

    % Get the lens and voltage from the image folder directory
    folder = strsplit(srcFiles(k).folder, filesep);
    lens = folder{end-1};
    voltage = folder{end};

    % Print useful info
    fprintf('Processing: %s at %s - %s\n', lens, voltage,srcFiles(k).name);

       % Read the image
    file = [srcFiles(k).folder '/' srcFiles(k).name];
    I = imread(file);
    [rows, cols, planes] = size(I);
    rect = [fix(cols*0.00) , fix(rows*0.00) , fix(cols*1.00) , fix(rows*0.50)];
    I = imcrop(I , rect);
    I = double(rot90(I));

    %% generate world coordinates
    mmPerPixY = mmPerPix*tand(RonchiAngle);
    SpatialReferencing = imref2d(size(I), mmPerPix, mmPerPixY);
    SpatialReferencing.XWorldLimits=SpatialReferencing.XWorldLimits-size(I,2)/2*mmPerPix;
    SpatialReferencing.YWorldLimits=SpatialReferencing.YWorldLimits-
size(I,1)/2*mmPerPixY+DefocusOffset;

    %% find focus point for every 64pixel column, using a gaussian fit of the gradient image
    [~,Gy] = imgradientxy(I,'Prewitt');
    xs = 1:size(I,1);
    focus = zeros(1,floor(size(I,2)/64));
    for col = 1:floor(size(I,2)/64)
       ys = mean(Gy(:,(col-1)*64+1:col*64),2);
       [~,mu,~]=mygaussfit(xs, abs(ys), .4);
       focus(col) = mu;
    end

    % convert from pixels to mm
    [~, MedianFocus] = intrinsicToWorld(SpatialReferencing,0, median(focus));
    StdFocus = std(focus) * mmPerPixY;

    %% save outputs
    frames(file) = file;
    defocusmed(file) = -MedianFocus;
```

```
    defocusstd(file) = StdFocus;

    %% display image
    hFig = figure;
    imshow(I, SpatialReferencing, [0 250]);
    hold on

    % plot median focal depth
    [Xw, Yw] = intrinsicToWorld(SpatialReferencing, [1 size(I,2)], [median(focus) median(focus)]);
    plot(Xw, Yw, '-r', 'LineWidth',2);
    % plot local focus points
    [Xw, Yw] = intrinsicToWorld(SpatialReferencing, 64*(1:floor(size(I,2)/64))-32, focus);
    plot(Xw, Yw, '+k', 'LineWidth',2);

    hAxes = gca;
    % tick marks every 0.2mm
%     hAxes.XTick = hAxes.XTick(1):0.2:hAxes.XTick(end);
%     hAxes.YTick = hAxes.YTick(1):0.2:hAxes.YTick(end)+0.2;
    hAxes.YTickLabel=-str2double(hAxes.YTickLabel); % invert Y-axis values

    % annotations
    titlestr = sprintf('median defocus = %2.2fmm', MedianFocus);
    title(titlestr, 'Interpreter', 'none');
    xlabel('Axial distance [mm]')
    ylabel('Defocus [mm]')
    axis square;
    hAxes.Position(2) = hAxes.Position(2)+0.024;

    % Save the charts
    fileName = ['charts/' lens '/' voltage '/' srcFiles(k).name '_processed' ];
    SaveMyPlot([fileName '.png'], 200, hFig);

    tempDataTable.Lens = string(lens);
    tempDataTable.Voltage = string(voltage);
    tempDataTable.MedianFocus = MedianFocus;
    tempDataTable.FileName = srcFiles(k).name;
    dataTable = [dataTable;tempDataTable]; %#ok<AGROW> - ignore prealloaction warning as we
don't know the size of the data

    % Close the figure
    close

    % New Line
    fprintf('\n');
  end

% Write the data table
writetable(dataTable,'data-tables/data-table.xls')
fprintf('---FINISHED---\n');

end

function SaveMyPlot(SaveFileName, DPI, figureToSave)
    [path,~,ext] = fileparts(SaveFileName);

    switch lower(ext)
        case '.png'
            % set resolution if missing
```

```
        if ~exist('DPI', 'var'); DPI = 300; end
        % save as png
        fileResolution = ['-r' int2str(DPI)];
        fileFormat = '-dpng';
    case '.eps'
        % save as colour vectorial eps
        fileFormat = '-depsc';
        fileResolution = '';
    otherwise
        error('Use EPS or PNG for the file''s extension')
end

% check directory exists, otherwise print will fail
if ~strcmp(path, '') && ~exist(path, 'dir')
    mkdir(path)
    disp(['Created path for you: ' path])
end

% save it
print(figureToSave, fileFormat, fileResolution, SaveFileName)
disp(['File saved as: <a href="' SaveFileName '">' SaveFileName '</a>'])
end
```

Appendix 4 – Slanted edge MTF MATLAB script

```
% MTF Analysis Loop
%
% Requires sfrmat4 http://burnsdigitalimaging.com/software/sfrmat/
%
% Insert your source images in to the images folder organised by distance
% and then voltage.
%
% For example:
% 'images/100mm/0v'
% 'images/100mm/40v'
% 'images/90mm/0v'
% 'images/90mm/40v'
% '...'
%
% Folder names are important for final table output
%

% Add sfrmat library
addpath('sfrmat4v5');

% Specify the images location
folder = 'images';

% Specify the image format
imageType = 'tiff';

% Specify the crop of the images
crop = [535.5 275.5 241 407];

% Intro Banner
fprintf('\n');
fprintf('------------------------------\n');
fprintf('--- MTF ANALYSIS PRO v1.1 ---\n');
fprintf('------------------------------\n\n');

% Find any files that match the image format within in folder variable
filePattern = fullfile(folder, ['**/*.' imageType]);
fprintf('Looking for .%s files in %s/%s...\n\n', imageType, pwd, folder);
srcFiles = dir(filePattern);

% Count the number of files
numFiles = length(srcFiles);

% Create the data table and a temp table
dataTable = table();
tempDataTable = table();
rawXDataTable = [];
rawYDataTable = [];

if numFiles == 0
  message = sprintf('There are no %s files are in folder:\n%s', imageType, folder);
  uiwait(warndlg(message));
else
  fprintf('There are %d files in %s:\n\n', numFiles, folder);
```

```
for k = 1 : numFiles

  % Get the distance and voltage from the image folder directory
  folder = strsplit(srcFiles(k).folder, filesep);
  distance = folder{end-1};
  voltage = folder{end};

  % Print useful info
  fprintf('Processing: %s at %s - %s\n', distance, voltage,srcFiles(k).name);

  % Read the image
  file = [srcFiles(k).folder '/' srcFiles(k).name];
  img = imread(file);

  % Crop image
  img = imcrop(img, crop);
  imshow(img);

  % Make the image grey
  imgGray = im2gray(img);

  % Run the image through sfrmat4
  [status, dat, fitme] = sfrmat4(1,1,1,0,imgGray);

  % Extract the y data
  yData = dat(:,2);

  % Apply a threshold to filter artifacts from y
  threshhold = 0.20;
  yRowCount = length(yData);
  rowsToRemove = int16(yRowCount * threshhold);
  yData = yData(1:end-rowsToRemove,:);

  % Find nearest corresponding x value when y ~= 0.5
  n = double(0.5);
  tmp = abs(yData - n);
  [~, idx] = min(tmp);
  val = yData(idx);
  fprintf('Closest y value to 0.5 at row %d\n', idx);

  % Spacial frequency mtf50
  a = dat(idx-1,1);
  b = dat(idx-1,2);
  c = dat(idx,1);
  d = dat(idx,2);
  sfmtf50 = c - (0.5 - d) * (c-a) / (b-d) ;

  % Useful debug information
  fprintf('sfmtf50 calculation (to 3 decimal places)\n');
  fprintf('%.3f - (0.5-%.3f) * (%.3f-%.3f) / (%.3f-%.3f) = %.3f\n', c, d, c, a, b, d, sfmtf50);

  % Create the figure
  %plot(dat(:,1), dat(:,2));

  % Write the CSV
  %csvFile = ['csvs/chart-' srcFiles(k).name '.csv'];
  %csvwrite(csvFile,dat);
```

```
    % Create a table with the above values
    tempDataTable.Distance = string(distance);
    tempDataTable.Voltage = string(voltage);
    tempDataTable.SFMTF50 = sfmtf50;
    tempDataTable.FileName = srcFiles(k).name;
    dataTable = [dataTable;tempDataTable]; %#ok<AGROW> - ignore prealloaction warning as we
don't know the size of the data

    % Create a table with the raw mtf data

    rawXDataHeader = ['Frame' k '-' string(distance) string(voltage) 'X-Axis'];
    xData = [strjoin(rawXDataHeader); dat(:,1)];
    rawXDataTable = [rawXDataTable xData]; %#ok<AGROW> - ignore prealloaction warning as we
don't know the size of the data

    rawYDataHeader = ['Frame' k '-' string(distance) string(voltage) 'Y-Axis'];
    yData = [strjoin(rawYDataHeader);  dat(:,2)];
    rawYDataTable = [rawYDataTable yData]; %#ok<AGROW> - ignore prealloaction warning as we
don't know the size of the data

    % Create a pdf of the chart (Requires R2020a or later)
    %chartFile = ['charts/chart-' srcFiles(k).name '.pdf'];
    %exportgraphics(gcf,chartFile,'ContentType','vector');

    % New Line
    fprintf('\n');
  end

% Write the CSV
csvFile = 'csvs/data-table-sfmtf50.csv';
writetable(dataTable,csvFile);

% Write the CSV
xlsFile = 'csvs/data-table-raw-frame-data.xls';
writematrix(rawXDataTable,xlsFile, 'Sheet', 1);
writematrix(rawYDataTable,xlsFile, 'Sheet', 2);

fprintf('---FINISHED---\n');

end
```

Appendix 5 – Publications and Dissemination

1. Accommodative Intraocular Lens Design, *E. J. Ward, J. Lacey, M. K. Dymond, C. Crua, Y. Gogotsi, S. Sandeman,* (Abstract and poster presentation) – 11th World Biomaterials Congress (11th -15th December 2020) Virtual.
2. $Ti_3C_2T_x$ in Adjustable Focus, Implantable Lens Design, *E. J. Ward, K. Hantanasirisakul, J. Lacey, M. K. Dymond, C. Crua, Y. Gogotsi, S. Sandeman,* (Abstract and poster presentation) – MXene 2020: 10 Years Later (3rd -7th August 2020) Virtual.
3. 2D Titanium Carbide ($Ti_3C_2T_x$) in Accommodating Intraocular Lens Design, *E. J. Ward, J. Lacey, C. Crua, M. K. Dymond, K. Maleski, K. Hantanasirisakul, Y. Gogotsi, S. Sandeman*, Adv. Funct. Mater. 2020, 30, 2000841. https://doi.org/10.1002/adfm.202000841.
4. Two-Dimensional Titanium Carbide (MXene) in Accommodating Lens Design, *E. J. Ward, J. Lacey, Y. Gogotsi, S. Sandeman,* (Abstract and poster presentation) – MXene at the Frontier of the 2D Materials World Beilstein Nanotechnology Symposium (15th -19th October 2019) Mainz, Germany.
5. Intraocular lenses, Smart lenses and Wearable Electronics, *E. J. Ward, J. Lacey, Y. Gogotsi, S. Sandeman,* (Abstract and poster presentation) – Festival of Postgraduate Research (22nd May 2019) Brighton, United Kingdom.
6. Two- Dimensional Titanium Carbide (MXene) in Accommodating Lens Design, *E. J. Ward, J. Lacey, Y. Gogotsi, S. Sandeman,* (Abstract and poster presentation) – Materials Research Society (25th -30th November 2018) Boston, United States of America.

Appendix 6 – Publication

FULL PAPER

ADVANCED FUNCTIONAL MATERIALS
www.afm-journal.de

Check for updates

2D Titanium Carbide ($Ti_3C_2T_x$) in Accommodating Intraocular Lens Design

*Emma J. Ward, Joseph Lacey, Cyril Crua, Marcus K. Dymond, Kathleen Maleski, Kanit Hantanasirisakul, Yury Gogotsi, and Susan Sandeman**

While intraocular lenses (IOL) are used to restore visual acuity in cataract patients, they are limited in their development as no clinically available lens can effectively mimic the accommodative function of the eye's natural lens. The optoelectronic properties of 2D transition metal carbides and/or nitrides (MXenes), including high electronic conductivity, optical transparency, flexibility, biocompatibility, and hydrophilicity, suggest potential use within an accommodating IOL. This study investigates the use of $Ti_3C_2T_x$ (MXene) as a transparent, conductive electrode to allow changes in optical power. $Ti_3C_2T_x$ is synthesized and spin-coated on hydrophobic acrylate IOLs, achieving a sheet resistance ranging from 0.2–1.0 kΩ sq^{-1} with 50–80% transmittance in the visible region. Human lens epithelial and monocytic cells show no cytotoxic nor inflammatory response to the coated lenses. An adjustable focus test cell is fabricated using a liquid crystal (LC) layer sandwiched between $Ti_3C_2T_x$ coatings on a solid support. Molecular reorientation of the LC layer, through an applied electric field, results in changes in optical power as objects viewed through the test cell appeared in and out of focus. This study is the first step toward the use of $Ti_3C_2T_x$ within an accommodative IOL design through demonstration of reversible, controlled, adjustable focus.

1. Introduction

Cataracts, formed by the aggregation of proteins on the crystalline lens of the eye, degrade visual acuity over time.[1] This age-related disorder accounts for the majority of the visually impaired population. The number of patients requiring cataract surgery will continue to rise with an increase in the average human life span. The eye's natural ability to vary optical power is known as accommodation or pseudophakia,[2,3] with optical power being the reciprocal of focal length measured in dioptres or m^{-1}. These changes in optical power are produced through ciliary muscle contraction and relaxation resulting in changes of lens curvature to provide continuous focus.[4] However, accommodation is lost as a result of cataract surgery when the eye's lens is removed and replaced with an intraocular lens (IOL). Even though the existing mechanisms of the eye, such as ciliary muscle contraction/relaxation and axial movement remain, the IOL of fixed optical power does not permit variable focus. IOL development is motivated to mimic more closely the eye's ability to retain focus at all lengths. Current accommodative intraocular lens (AIOL) approaches utilize the existing mechanisms of the eye. However, the main limitation associated with these methods is producing a reliable change in optical power. The ideal AIOL aims to have a controlled, reversible, and fast switching mechanism to seamlessly move from near to distant vision and vice versa. No clinically available AIOL reported to date truly restores accommodation.[5–7] In this article, a new transparent and conductive 2D material (MXene) was investigated for AIOL design.

A recent development in the field of optoelectronics is smart contact lenses.[8] They are wearable optoelectronic devices, proposed for the correction of presbyopia; an age-related disorder effecting the eye's accommodative function as the lens hardens and loses elasticity. These devices operate similarly to liquid crystal (LC) displays, where the optical anisotropy of a nematic LC is controlled by an electric field using transparent conductive electrodes (TCE).[9] LCs are mesogenic phases of matter, intermediate between solids and liquids and their average long-range orientational order is defined by their average direction, known as the director. Due to their orientational order, they have two refractive indices—parallel and perpendicular—that can be

E. J. Ward, Dr. M. K. Dymond, Dr. S. Sandeman
School of Pharmacy and Biomolecular Sciences
University of Brighton
Brighton, BN2 4GJ, UK
E-mail: S.Sandeman@brighton.ac.uk
Dr. J. Lacey
Rayner Intraocular Lenses Limited
The Ridley Innovation Centre
Worthing, BN14 8AQ, UK
Prof. C. Crua
Advanced Engineering Centre
University of Brighton
Brighton, BN2 4GJ, UK
Dr. K. Maleski, K. Hantanasirisakul, Prof. Y. Gogotsi
Department of Material Science and Engineering
A. J. Drexel Nanomaterials Institute
Drexel University
Philadelphia, PA 19104, USA
The ORCID identification number(s) for the author(s) of this article can be found under https://doi.org/10.1002/adfm.202000841.

DOI: 10.1002/adfm.202000841

manipulated through external stimuli such as, mechanical, electric, or magnetic fields, allowing molecular reorientation of the director. This allows switchable refractive indices making them useful for adjustable focus lens systems.[10] Many of the proposed smart contact lenses use indium tin oxide (ITO), a standard TCE, due to its characteristics of low sheet resistance and high optical transparency, coated on poly(methyl methacrylate) (PMMA).[11] However, the use of ITO comes with some limitations as it is brittle and therefore not suitable for wearable optoelectronic applications when flexibility is required.[12] 2D nanomaterials, with high flexibility and electronic conductivity, may be better suited Graphene variants, for example, have gained interest in wearable device applications owing to their optoelectronic properties and biocompatibility.[13–16] MXenes are a newer family of 2D transition metal carbides and nitrides, that have also shown potential for optoelectronic applications. These materials have a unique blend of mechanical, electrical, and physical properties including transparency in the visible spectrum, high electronic conductivity (up to 15000 S cm^{-1}), flexibility, hydroxide/oxide-like surface chemistry, and hydrophilicity.[17–20]

MXenes are synthesized from selective etching of layered precursors, such as ternary carbides and nitrides (MAX phases).[21] With the general formula $M_{n+1}AX_n$, M represents an early transition metal, A is an element from group 13 or 14 of the periodic table and X represents carbon and/or nitrogen.[17] MXenes can be produced through wet chemical approaches, selectively etching away the A-element, resulting in the formation of $M_{n+1}X_nT_x$ where T_x are terminating groups whose abundance and type are dependent on the etching process.[22] More than 30 MXenes have been synthesized, since their discovery in 2011, and many more variants are theorized to exist.[23–26] This family of materials has demonstrated outstanding potential in energy storage,[27,28] electromagnetic interference (EMI) shielding,[29,30] and water purification.[31,32] Even though MXene research for biomedical applications remains in its infancy, they have been used for a number of applications such as, diagnostic imaging,[33,34] biosensing,[35–37] as antibacterial materials,[38,39] and in theranostics.[40–42] The most investigated MXene, $Ti_3C_2T_x$, has shown low cytotoxicity to normal cells when compared to cancerous cells lines.[43]

Deposition techniques of MXenes, including spray-, spin-, and dip-coating, produce high-functioning transparent and flexible coatings.[24,44] For example, $Ti_3C_2T_x$ antennas that were bent through a series of different curvatures saw no change in performance or structure.[45] The study shows the flexibility and stability of the coatings, properties that are useful for electrode applications. $Ti_3C_2T_x$ electrodes for neural interfaces have been investigated for sensing applications demonstrating low impedance, high signal-to-noise ratio, and biocompatibility with regard to neuron cell viability.[46] However, MXenes have not yet been proposed for an AIOL design or any ophthalmic medical device application.

Herein, we describe the synthesis and characterization of $Ti_3C_2T_x$ colloidal solution. Once spin-coated onto a hydrophobic IOL (**Figure 1a**), its optoelectronic properties were investigated and biological interactions were assessed. As a proof of concept design, an adjustable focus lens was fabricated within a solid support. It was constructed with a LC layer sandwiched between $Ti_3C_2T_x$ spin-coated glass slides and, through electric field induced molecular reorientation, a change in refractive index and therefore optical power was observed (Figure 1b). The switchable focus demonstrates the incorporation of MXene for an adjustable focus lens. This is the first study investigating

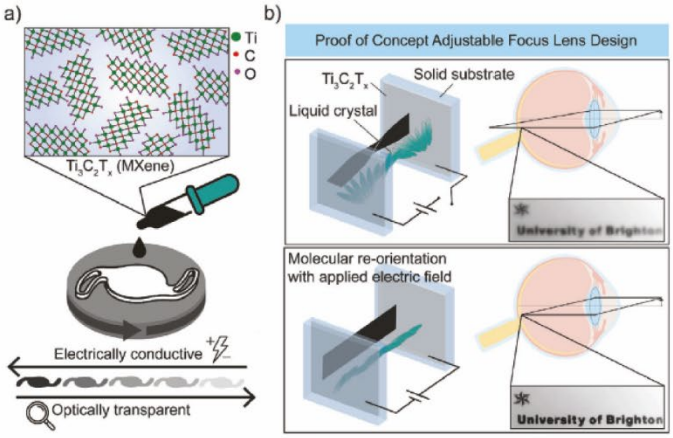

Figure 1. Accommodative intraocular lens (AIOL) design. a) A schematic of $Ti_3C_2T_x$ (MXene) spin coated onto an acrylate IOL (Rayner Intraocular Lenses Ltd, UK) showing fundamental properties of electrical conductivity and optical transparency. b) A schematic of a proof of concept design for an adjustable focus lens. The fabricated test cell was constructed with $Ti_3C_2T_x$ spin coated glass slides assembled to sandwich a liquid crystal (5CB) layer in twisted nematic orientation. With no electric field applied the image is out of focus. When the electric field is applied the image is in focus due to molecular reorientation of the liquid crystal layer.

the application of a 2D titanium carbide in optoelectronic AIOL design. Furthermore, the MXene fabricated IOL contributes to the field of ophthalmology and wearable electronics as currently no IOL designs involving MXenes have been explored.

2. Results and Discussion

2.1. Synthesis and Physical Characterization of $Ti_3C_2T_x$ (MXene)

$Ti_3C_2T_x$ was synthesized by chemical exfoliation of the MAX phase precursor, Ti_3AlC_2. Solvated lithium ions from the lithium fluoride (LiF) and hydrochloric acid (HCl) etchant facilitated the intercalation of multi-layered $Ti_3C_2T_x$ to delaminate into 2D $Ti_3C_2T_x$ flakes, resulting in stable colloidal solutions. A known volume of the solutions was vacuum-filtered to produce a free-standing film composed of $Ti_3C_2T_x$ flakes. The cross-section of the film was captured with scanning electron microscopy (SEM) (Figure S1, Supporting Information) showing the alignment of single flakes compacted as a result of the filtration. X-ray diffraction (XRD) patterns of the free-standing film along with the powdered precursor Ti_3AlC_2 (MAX) are shown in Figure S2, Supporting Information. The (002) peak of the Ti_3AlC_2 MAX powder and free-standing $Ti_3C_2T_x$ film are 9.5° and ≈7.1°. The interlayer spacing was calculated to be 18.6 and ≈25 Å, respectively. The increase observed in the *c* lattice parameter was a result of the removal of Al and the introduction of surface termination and intercalated water molecules. X-ray photoelectron spectroscopy (XPS) of the free-standing film was used to analyze the chemical composition of $Ti_3C_2T_x$ as shown in Figure S3, Supporting Information. Titanium and carbon were identified as core elements as well as oxygen and fluorine as terminating groups. Aluminum is absent in each analysis, consistent with the conversion of MAX to MXene. Dynamic light scattering (DLS) was used to provide flake size estimations. One peak was identified on the DLS distribution (Figure S4, Supporting Information) with an average size of 1250 nm and a polydispersity index (PDI) of 0.5. UV–vis spectroscopy was performed (Figure S5, Supporting Information), and a peak in the near infrared region was observed for $Ti_3C_2T_x$. Corresponding with the literature, the broad peak at 700–800 nm is characteristic of a transverse surface plasmon mode in $Ti_3C_2T_x$.[47] The extinction coefficient was calculated from a plot of absorbance versus concentration (inset of Figure S5, Supporting Information) as 31.34 L g^{-1} cm^{-1}.

2.2. Coating and Physical Characterization of $Ti_3C_2T_x$ Coated Lens

The key attributes of transparent electrodes are to be optically transparent and conductive, allowing the passage of light while permitting the flow of electrons. $Ti_3C_2T_x$ was deposited onto the lens and the coating's ability to perform as a TCE was evaluated. Commercially available, hydrophobic acrylate IOLs (Rayner IOL ltd) were used for this study. First, the lenses were treated with oxygen plasma to increase the hydrophilicity of the surface which improves the uniformity of the coatings. $Ti_3C_2T_x$ was deposited onto the treated lenses by spin-coating. The optical transmittance of the coated lenses showed a broad peak at 700–800 nm, consistent with the UV–vis peak observed for the colloidal solution as described in Section 2.1. By varying coating thickness, the optical transmittance can be optimized (**Figure 2a**). Nanoscale thickness of the coatings was optimized by a combination of varying the spin speed and concentration of the solution being coated and by layering the coatings. A numerical formula, $A = 0.005t$,[24] A being absorbance and t thickness in nm, was used to approximate the MXene coating thickness (Figure S6, Supporting Information).

$Ti_3C_2T_x$ coated lenses were evaluated as electrodes by measurement of sheet resistance. The bulk conductivity of the $Ti_3C_2T_x$ free-standing film (Figure S1, Supporting Information) was ≈6000 S cm^{-1}, indicating high quality of the 2D flakes produced. Sheet resistance of the coated lenses was measured using a four-point probe technique; the experimental setup, and calculations are shown in Figure S7, Supporting Information. Coatings with varied thicknesses were measured and their sheet resistance was found to range from 0.2–1.0 kΩ sq^{-1} with optical transmittance of 50–80% (Figure 2b). An effective means of evaluation for TCEs is through their electrical figure of merit (FoM) which is defined as the ratio between electrical conductivity (σ_{DC}) and optical conductivity (σ_{Op}).[48] The FoM for the MXene-coated lens was calculated as 1.8 (Figure S8, Supporting Information). The substrate surface could be a limiting factor with regards to increasing the FoM. When spin-coated, the centrifugal force orients the $Ti_3C_2T_x$ flakes in plane with the substrate that could increase resistance and affect electron flow. The $Ti_3C_2T_x$-coated IOLs were evaluated for optoelectronic performance as a TCE. Future efforts will be made to enhance performance for the desired high optical transparency and low sheet resistance.

The purpose of an IOL is to allow good visual acuity for the patient following the removal of a cataract. Visual acuity must not be diminished when a coating is introduced to the lens. Therefore, the $Ti_3C_2T_x$-coated lenses were assessed to determine the impact of the coating on lens' optical performance in terms of optical power and spatial resolution. Since IOLs are manufactured for the specific requirements of each individual patient, the axial length of the eye is measured to determine the optical power required. Standard characterization and quality tests that are used in the industrial manufacture of IOLs were performed. Here, no significant difference in optical power was observed on a series of lenses measured before and after coating (Figure 2c). Modulation transfer function (MTF) provides a universal metric based on a lens system's contrast and resolution abilities across the optic.[49] No significant difference was observed in MTF before and after coating (Figure 2d). The $Ti_3C_2T_x$ coatings did not significantly affect the optical performance or quality of the lens. This showcases the advantage of using $Ti_3C_2T_x$ as a conductive coating since it can provide sufficiently high electrical conductivity at low coating thicknesses and thus minimally affect the optical performance of the lens.

2.3. Biocompatibility of $Ti_3C_2T_x$ Coated Lens

To further assess the suitability of $Ti_3C_2T_x$ as a coating for AIOL design, the biocompatibility was evaluated through

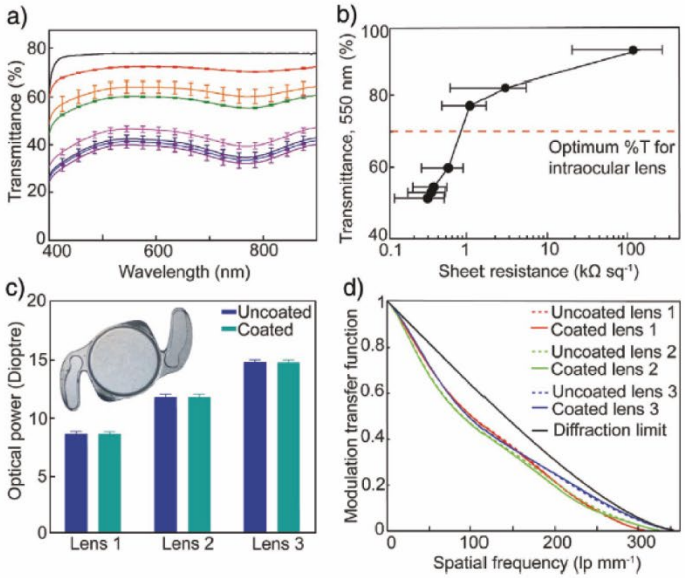

Figure 2. Optoelectronic characterization a) Transmittance spectra of $Ti_3C_2T_x$ coated lenses (black, no coating, colored etc. sequential coatings) mean ± SD, $n = 3$. b) Sheet resistance versus transmittance at 550 nm mean ± SEM, $n = 3$, error bars for transmittance are too small to be visible on the plot. c) Optical power measurement on 3 different lens powers before and after coating with $Ti_3C_2T_x$ for each type $n = 5$, mean ± SD, analyzed by one-way ANOVA, $p < 0.05$. Inset (c) Optical image of spin coated intraocular lens. d) Modulation transfer function (MTF) measurement on three different lens powers before and after coating with $Ti_3C_2T_x$ for each type $n = 5$. Both measurements made using a NIMO (NIMO TR0815, Lambda-X, Belgium).

cytotoxicity testing using (3-(4,5-dimethylthiazol-2-yl)-5-(3-carboxymethoxyphenyl)-2-(4-sulfophenyl)-2H-tetrazolium) MTS and lactate dehydrogenase (LDH) assays. The results of the MTS assay (**Figure 3**a) indicated no significant difference in percent cell viability for human lens epithelial cells (HLEs) incubated with $Ti_3C_2T_x$ coated IOLs when compared to the cell and lens only controls indicating no cytotoxic effects. Findings were supported by the data from the LDH assay (Figure 3b), showing no significant cytotoxic effects by $Ti_3C_2T_x$ coated IOLs compared to cell only controls. These findings demonstrate the cytocompatibility of $Ti_3C_2T_x$ coatings and their suitability for contact with ocular cell types. However, for IOL design, capsular and uveal biocompatibility is essential. Understanding the full biocompatibility profile for IOL applications requires assessment of potential interactions with inflammatory pathways which may be activated following exposure to a biomaterial. Since optoelectronic films such as $Ti_3C_2T_x$ have potential for electron transfer, it is thought that these materials may interact with biological systems with the ability to drive harmful processes such as oxidative stress through reactive oxygen species (ROS) production.[50] In order to explore this potential, both immunological activation studies and ROS production were investigated. Non-adherent THP-1 cells were used to investigate if $Ti_3C_2T_x$ coated IOLs induced oxidative stress by measuring the generation of ROS. No significant difference in ROS production throughout the study period was observed (Figure 3c). This demonstrates that under biological conditions, $Ti_3C_2T_x$ coatings do not provoke an increase in ROS production, supporting the MTS and LDH data indicating that the coatings were non-cytotoxic, and confirming the suitability of these nanomaterials for wider biological applications. The results of immunological cellular studies also supported this conclusion, with no increase in production of common ocular inflammatory cytokines IL-6, IL-8, and TNF-α by THP-1 monocytes in the presence of $Ti_3C_2T_x$ coated IOLs in contrast to LPS stimulated THP-1 controls (Figure 3d–f).

2.4. A Proof of Concept Accommodative Focus Lens Design

To assess the potential use of $Ti_3C_2T_x$ as a TCE in an adjustable focus lens system, a test cell was fabricated as a proof of concept design, (Figure S9, Supporting Information). The test cell, similar to a LC display, was constructed by a LC layer, of known thickness, sandwiched between $Ti_3C_2T_x$ spin-coated glass slides, with twisted nematic alignment (Figure 1b). By applying an electric field, a change in refractive index of the LC was observed due to the reorientation of molecules, producing a change in optical power of the lens. A typical thermotropic LC, 4'-Pentyl-4-cyanobiphenyl (5CB) was used. The

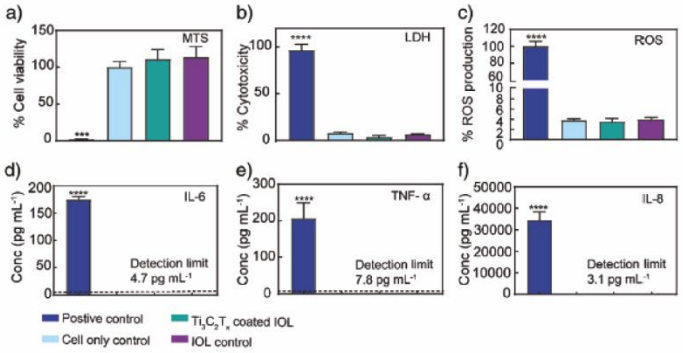

Figure 3. Biological evaluation for $Ti_3C_2T_x$ coated lenses a) % Cell viability via MTS assay for $Ti_3C_2T_x$ coated lens with HLE cell line, mean ± SEM, $n = 3$, $p < 0.05$. b) % Cytotoxicity by LDH assay for $Ti_3C_2T_x$ coated lens with HLE cell line, mean ± SEM, $n = 3$, $p < 0.05$. c) ROS activity of $Ti_3C_2T_x$ coated lens with THP-1 cell line, mean ± SEM, $n = 3$, $p < 0.05$. d–f) ELISA data of IL-6, TNF- α, and IL-8, respectively for $Ti_3C_2T_x$ coated lens with THP-1 cell line, mean ± SEM, $n = 3$, $p < 0.05$.

optical effects observed for 5CB are due to its nematic behavior at room temperature, positive dielectric anisotropy, and high birefringence. The alignment of the LCs director field defines the perpendicular (ordinary "n_o") or parallel (extraordinary "n_e") refractive index.[51] The refractive index of the test cell, with the electric field applied, was measured to be 1.7280 ± 0.0479 (mean ± SD, $n = 3$) at 24 °C, $\lambda = 405$ nm (Figure S10, Supporting Information). A study investigating the effects of temperature on the refractive indices of 5CB for a range of wavelengths of the EM spectrum found $n_e = 1.7232$ at 25.4 °C, $\lambda = 546$ nm,[52] confirming the test cell with the electric field applied experienced parallel orientation.

The optical effects of the test cell were observed showing focused and out of focus objects using the set up detailed in Section 4.6 and Figure S11, Supporting Information. As a means of quantifying the switchable focus of the test cell, data were captured and processed using a Laplacian operator for edge detection. Differential edge detection operators are used to provide edge information, for digital image analysis, through rapid changes in pixel greyscale intensity.[53] The operator compares the greyscale between neighboring pixels and reports the overall variance (σ^2); if the greyscale values are similar between pixels then it is assumed that at that point no edge is present.[54] For the purpose of this study, the variance of the image's pixel greyscale was used as a metric for focus, since an image that is in focus will have a higher degree of change in pixel greyscale than an out of focus image and therefore a higher computed variance value. The inset of **Figure 4**a shows two digital images taken with (top image) and without (bottom image) the 30 V electric field applied. It is clear from the image that it changed from out of focus to in focus state when the voltage was applied, as a result of the realignment of the LC. Figure 4a shows the histograms of each of the image's greyscale intensities. There are distinct differences between the plots for each image. The in focus state (electric field applied) shows a larger frequency distribution, spread over more dark pixels, whilst the out of focus state has less of a range. The corresponding variance values for the out of focus and in focus state are 3.7 and 24.3, respectively. For simplicity of image processing, the following investigations were performed on a series of small black lines (Figure S12, Supporting Information). Variance was plotted as a function of applied voltage as shown in Figure 4b. As voltage increased, a gradual increase in the variance value was observed, implying that the image became more in focus with the applied electric field. Fréedericksz transitions explain how the dielectric anisotropy of LCs allow molecular re-orientation when an electric field is applied.

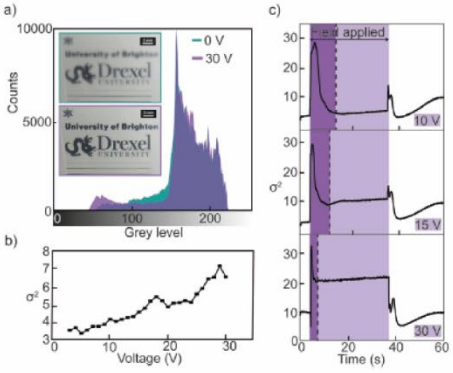

Figure 4. Digital image processing using the Laplacian operator for the proof of concept adjustable focus lens design a) Histograms of pixel greyscale for the inset (a) images of institute logos viewed through the fabricated test cell. b) Image processing to provide variance (σ^2) of image pixels greyscale intensity for a range of voltages. c) Image processing to provide variance (σ^2) of image pixels greyscale intensity for a range of voltages as a function of time, with the switching time (dark purple) and time the electric field was applied highlighted (light purple).

To investigate the dynamic of LC orientation, the variance value was plotted as a function of time at different applied voltages, as shown in Figure 4c. The time for LC reorientation was calculated by subtracting the time at which the minimum variance value was observed, from the time that the maximum variance value was observed. For 10, 15, and 30 V, the switching times were calculated as 2.30, 1.04, and 0.26 s, respectively, demonstrating a decrease in time taken for reorientation as the applied voltage was increased.

The purpose of the study was to achieve a change in optical power through a MXene/liquid crystal lens design. This is the framework for an AIOL design to allow optical changes as seamlessly as the natural lens. A number of factors could be investigated in further work to optimize the performance of the test cell. These include improvements in electrode efficiency through a reduction in the sheet resistance of the $Ti_3C_2T_x$ coating which can be achieved through an increase in the bulk conductivity of the initial $Ti_3C_2T_x$ solution. It has already been shown that $Ti_3C_2T_x$ free-standing films composed of larger flakes have greater conductivity than films produced with smaller flakes. These smaller flakes have lower sheet resistance, due to electron flow and less flake to flake electron hopping.[55] Larger $Ti_3C_2T_x$ flakes can be isolated after the delamination step described in Section 2.1.

Next, unwanted optical aberrations could be reduced by minimizing point defects at the substrate surface, ensuring uniformity of surface anchoring of the PVA alignment layer. The thickness of the LC layer determines the voltage required for reorientation, by decreasing the spacing between the electrodes and therefore the LC layer. This means less voltage is required. The threshold voltage required for reorientation of LC in test cell arrangements is a well-investigated topic and studies have shown that doping LC with nanoparticles, such as graphene oxide, decreases the voltage required to allow reorientation.[56] The data presented in this study shows the potential for the $Ti_3C_2T_x$ coating to act as a TCE for an adaptive focus lens application.

3. Conclusion

The first attempt to use a MXene thin film coating as an optically transparent electrode for an accommodative intraocular lens design was evaluated. The study demonstrates a synthesis and coating method by which a transparent, conductive $Ti_3C_2T_x$ thin film can be coated onto an acrylate polymer IOL surface using an approach which can be further optimized to increase electrical FoM. The study shows the first use of $Ti_3C_2T_x$ in an adjustable focus lens. Furthermore, $Ti_3C_2T_x$ coatings did not negatively affect human lens epithelial cell viability, stimulate upregulation of reactive oxygen species or inflammatory cytokine expression in THP-1 monocytes, demonstrating the biocompatibility of $Ti_3C_2T_x$ thin films coatings for this application. The $Ti_3C_2T_x$ coatings did not alter image quality of the lenses with respect to lens power or spatial resolution. The study demonstrates the use of $Ti_3C_2T_x$ as a TCE in the first step toward an accommodating lens design following further optimization of MXene properties for improved sensitivity.

4. Experimental Section

Reagents: MAX phase Ti_3AlC_2 (A.J. Drexel Nanomaterials Institute, Drexel University, USA), lithium fluoride (LiF) (powder 300 mesh) (Sigma-Aldrich, UK), hydrochloric acid (HCl) (Sigma-Aldrich, UK).

Synthesis of $Ti_3C_2T_x$ (MXene): Hydrofluoric acid (HF), formed in situ, when 0.8 g of LiF dissolved in 10 mL 9 M HCl. 0.5 g Ti_3AlC_2 was added gradually over 5 min, etched with continuous stirring for 24 h at 35 °C. Reaction byproducts were removed by washing with deionized (DI) water (200 mL) and repeatedly centrifuging (5 min, 3500 rpm) using an ALC PK 120R Centrifuge. Once a pH of 5–6 was achieved the sediment was redispersed and hand shaken for 15 min, then centrifuged for 1 h at 3500 rpm to delaminate. The delaminate product was decanted, and a known volume of the solution was vacuum-filtered and weighed to establish concentration (mg mL^{-1}). During storage the solution was frozen at −20 °C.

Physical Characterization of $Ti_3C_2T_x$ Solution: The $Ti_3C_2T_x$ solutions bulk composition was analyzed by XRD with a powder diffractometer (Rigaku SmartLab, USA) using CuKα radiation (λ = 1.54 Å) with θ–2θ continuous scan with 0.02° 2θ step size, 1 s step time, and 10 × 10 mm^2 window slit. Ultraviolet–visible (UV–vis) spectroscopy was carried out using an Evolution 201 UV–vis spectrophotometer (Thermo Scientific, USA) to characterize optical properties in the wavelength range of 200–1100 nm. Particle size analysis was carried out on MXene solutions using dynamic light scattering (DLS) (Zetasizer Nano ZS, Malvern Panalytical, UK). Scanning electron microscopy (SEM) (Zeiss Supra 50VP, Germany) was used to image MXene flakes using a MXene film as the sample produced by vacuum filtering at low concentration solution onto a porous membrane (Anodisk inorganic filter membrane, Whatman). No sputter coating was required for the samples. A four-point probe stand SR-4 (1 mm probe spacing) and Keithley SMU 2450 Source meter (Tektronix, USA) were used to measure the sheet resistance of the $Ti_3C_2T_x$ free-standing films produced. The bulk conductivity was calculated using the measured sheet resistance and the crossectional thickness measured with SEM.

$Ti_3C_2T_x$ Spin Coating onto an Intraocular Lens Material: In order to produce a uniform coating on a hydrophobic lens polymer substrate (Rayner Intraocular Lenses Ltd, UK), surface pre-treatment was required in the form of oxygen plasma using a Henniker plasma etcher (Henniker plasma, UK). The substrate was subject to a 3-min treatment of pure oxygen plasma at 100 W and 10 cm^3 min^{-1}. The treatment cleaned the surface and increased the hydrophilicity to allow the $Ti_3C_2T_x$ an adequate coating. 20 µL of a 5 mg mL^{-1} MXene solution was deposited on to the substrate. A two-step spin coating method was used with an Ossila spin coater (Ossila, UK), 5000 rpm for 2 min to evenly deposit the coating followed by 6000 rpm for 1 min to ensure drying of the coating.

Physical Characterization of $Ti_3C_2T_x$ Coated Lens: The properties of the coated lens surface were characterized by XPS (Physical Electronics VersaProbe 5000, USA) and SEM. XPS spectra were collected using an Al Kα X-ray beam. Dual beam stabilizer was used for charge neutralization. High-resolution scans were obtained with a pass energy of 23.5 eV. Spectral transmission of the coated lens was measured using a UV–vis spectrometer in the wavelength range of 300–1100 nm (Shimadzu, UV–vis Spectrophotometer, UV-2600, Japan) with an integrating sphere to collect any light scattered by the lens optic. The $Ti_3C_2T_x$ coatings were applied incrementally to the polymer lens (n = 3). Sheet resistance was measured using an electrical transport option (ETO) puck. A four-point probe orientation was made on the $Ti_3C_2T_x$ coating on the lens using silver wire and silver conductive paint. The puck was fitted to a circuit that was connected to the source meter described above. Three measurements were made per lens and the average values (n = 3) were reported. Lens quality was assessed through optical measurements of lens power and MTF using a NIMO measurement system (NIMO TR0815, Lambda-X, Belgium). These measurements were performed before and after deposition to ensure that the $Ti_3C_2T_x$ coating did not affect the lens optically or interfere with resolution or contrast.

Biocompatibility of the $Ti_3C_2T_x$ Coated Lens–Cell Viability: Cell viability following exposure to material leachate was assessed using the

CellTiter 96 AQueous One Solution Assay (MTS reagent) (Promega, USA). A human lens epithelial (HLE) cell line (B-3, ATCC CRL-11421) was purchased from the American Type Culture Collection (ATCC) and cultured in growth medium Minimum Essential Medium (MEM) supplemented with 20% FBS and 1% non-essential amino acids (NEAA) at 37 °C, 5% CO_2. Cells were passaged by standard trypsinization, plated at a seed density of 5 x 10^4 cells per well in a 96 well plate and were incubated at 37 °C, 5% CO_2 for 24 h. Material leachate was prepared using lenses coated with $Ti_3C_2T_x$ (detailed in Section 4.4). Coated lenses and controls were sterilized with ultraviolet (UV) light, allowing 60 min per side. Uncoated lenses were used as a negative control. Tin maleate coated polymer discs were cut to a surface area comparable to that of the lenses and were used as a positive control. Each material type was placed into the wells of a 48 well plate, 250 µL of medium was added, and plates were incubated at 37 °C, 5% CO_2 for 24 h. Following incubation, the material leachate was removed from the wells, 100 µL of it was then added to the plated cells. Plates were incubated at 37 °C, 5% CO_2 for a further 24 h. The MTS reagent was prepared according to manufacturer's instructions and 100 µL was used to replace the spent leachate media. After an incubation of 2 h at 37 °C, 5% CO_2, the absorbance at 490 nm was recorded using an ELx800 Universal Microplate reader (Biotek, USA). The experiment was repeated in triplicate. Cell number was calculated from a standard curve of cell density against absorbance at a wavelength of 490 nm. Percentage cell viability was calculated relative to the cell only control.

Biocompatibility of the $Ti_3C_2T_x$ Coated Lens–Cytotoxicity: Cytotoxicity was assessed using the CytoTox96 non-radioactive cytotoxicity assay measuring LDH release by lysed cells (Promega, USA). HLE cells were passaged by standard trypsinization, plated at a seed density of 5×10^4 cells per well in a 96 well plate and were incubated at 37 °C, 5% CO_2 for 24 h. Leachate media was prepared and introduced to the seeded cells as described in Section 2.6.1 and plates were incubated at 37 °C, 5% CO_2 for 24 h. 10 µL Lysis solution was added to half of the plate to establish maximum LDH release and plates were then incubated for 45 min, 50 µL of media from each well were transferred to a new plate and 50 µL of the substrate mix, prepared according to manufacturer's instructions, were then added to each well. The plate was incubated at room temperature in the dark for 30 min prior to addition of 50 µL of the stop solution to each well. The absorbance at a wavelength of 490 nm was recorded using an ELx800 Universal Microplate reader (Biotek, UK). The experiment was repeated in triplicate.

Biocompatibility of the $Ti_3C_2T_x$ Coated Lens–Immune Response: Cytokine production was quantified following incubation of coated lenses with monocyte THP-1 cells (ATCC TIB-202) using an enzyme-linked immunosorbent (ELISA) assay for interleukin 6 (IL-6), interleukin 8 (IL-8), and Tumor necrosis factor (TNF-α). The following ELISA assay kits were used: BD OptEIA Human IL-6 ELISA Kit II, BD OptEIA Human IL-8 ELISA Kit II and BD OptEIA Human TNF ELISA Kit II (BD Biosciences, USA). THP-1 cells were purchased from the ECACC and cultured in growth medium Roswell Park Memorial Institute (RPMI) with 10% FBS at 37 °C, 5% CO_2. The sterile, coated and uncoated lens samples were transferred into the wells of a 48 well plate. THP-1 cells were centrifuged and 300 µL of a 1×10^6 cells mL^{-1} cell suspension was added to each of the lens and control wells. 30 µL of lipopolysaccharide (LPS) (Sigma, UK) at a concentration 20 µg mL^{-1} was added to half of the plate at time zero as a positive control. The plate was incubated at 37 °C, 5% CO_2 for 24 h. Media from each well was removed and centrifuged with a Heraeus Pico 17 Microcentrifuge (Thermo Fisher Scientific, UK) at 800 g. The supernatant was analyzed by ELISA (BD Biosciences, UK) according to manufacturer's instructions using sample dilutions of 1 in 5, 1 in 5, and 1 in 600 for IL6, TNF-α, and IL8, respectively. Each experiment was repeated in triplicate.

Biocompatibility of the $Ti_3C_2T_x$ Coated Lens–Oxidative Stress: Sterilized, coated, and uncoated lenses in a 48 well plate were incubated with THP-1 cells to evaluate ROS production on exposure to $Ti_3C_2T_x$ coated lenses. Cells were stained with dichloro-dihydro-fluorescein diacetate (DCFH-DA) at a working concentration of 50 mM for 40 min followed by washing cycles with PBS until the cells were redispersed in FBS free RPMI. 300 µL of the cell suspension prepared at a seeding density of 3×10^5 cells mL^{-1} was added to each well. Hydrogen peroxide (H_2O_2) was added to half of the plate at a concentration of 0.8 mM at time zero as a positive control for induction of ROS. The plates were incubated at 37 °C, 5% CO_2 for 1 h. After incubation, 100 µL of the media was transferred into an opaque walled 96 well plate and fluorescence was measured at an excitation/emission wavelength of 485 nm/520 nm. Each experiment was repeated in triplicate.

A proof of Concept Accommodative Focus Lens Design: A test cell was fabricated when a LC layer was sandwiched between two $Ti_3C_2T_x$ spin-coated microscope slides. Before spin-coating the microscope slides (Superfrost plus microscope slides, VWR international, UK) were subject to oxygen plasma using a Henniker plasma etcher (Henniker plasma, UK) for 10 min at 100 W and 10 cm^3 min^{-1}. Next, 500 µL of a 5 mg mL^{-1} MXene solution was deposited on to the glass and a two-step spin coating method was used with an Ossila spin coater (Ossila, UK), 5000 rpm for 2 min followed by 6000 rpm for 1 min to ensure drying of the coating. MXene coated slides were placed in the oven at 80 °C for 24 h, to dry. A solution of 3% PVA (in water) was spin-coated onto the $Ti_3C_2T_x$ coated slide (1500 rpm for 1 min) and placed in the oven (80 °C) for 1 h. PVA coated $Ti_3C_2T_x$ slides were wiped with a microfiber cloth parallel to the long edge of the slides for alignment of the LC. A 50 µm film was used as a spacer and the glass slides were assembled (Figure S9, Supporting Information). Once constructed, the test cell was filled with LC (5CB (Sigma-Aldrich, UK)), by allowing capillary action to draw the 5CB into the void between the layers. Copper tape was placed on the $Ti_3C_2T_x$ coating and wires connected to a Keithley SMU 2450 Source meter (Tektronix, USA).

The refractive index of the test cell was measured both with and without applying an electric field, using a purpose-built in-line laser refractometer. The experimental setup (Figure S10, Supporting Information) was composed of a diode laser (Thorlabs CPS405, USA) emitting a beam at 405 nm, a 100 µm precision pinhole to clip the laser beam, translation and rotation stages to position the microscope slide assembly, and a CMOS camera (Basler ace acA1920-40gm, Germany) to record the beam's position shift. The position of the laser beam was recorded both with and without applying a 20 V electric field, allowing the beam shift (measured by sub-pixel affine image registration) to yield the change in refractive index using Snell's law.

The angle of the test cell holder relative to the laser beam was precisely measured by replacing the test cell with a sapphire optical flat and computing its angle from the induced laser beam shift. Once the angle of the test cell is known the only remaining unknown in the beam shift calculation is the refractive index of the LC layer in the test cell. Although the laser beam had a Gaussian profile, microscopic-scale refractive index gradients within the LC disrupted the radial energy distribution of the beam. The aberration was corrected by applying a frequency filter to the distorted beam profile images, so that the beam shift could be accurately measured.

Optical focus of the test cell was investigated when an electric field was applied, and the changes observed. An Olympus em10ii camera connected to a M.Zuiko 12-40 f2.8 pro lens was used to capture the data. Figure S11, Supporting Information, shows a schematic of the experimental setup, with the text being viewed through a lens, then through the test cell, by the camera. The object, lens, and test cell were all set at fixed distances in order to observe the expected change in optical power and therefore focal length. The electric field was applied to the test cell using a Keithley SMU 2450 Source meter (Tektronix, USA). A range of voltages were applied incrementally and held for 15 s before each image captured (Figure 4b). The investigation of the optical effects over time was performed on 10, 15, and 30 V, the voltage was applied for 30 s. The camera was set to record for 1 min to allow the initial switching time to be observed as well as the molecular relaxation time (Figure 4c).

The data were processed using a Laplacian differential function of the OpenCV 4.2.0 library written in Python (Figure S13, Supporting Information). All image frames were aligned prior to the processing. Examples are shown in Figure S14, Supporting Information, as controls to demonstrate the function of the operator with examples of high and

low variance where the images are in and out of focus respectively. An example of the image processing from the operator can be seen in Figure S12, Supporting Information.

Statistical Analysis: The statistical software package GraphPad Prism 7 was used for all statistical analyses. All biological data were analyzed using a Shapiro–Wilk normality test followed by a one-way ANOVA and a Tukey's multiple comparison test, $p < 0.05$. Optical power measurements were analyzed with the Shapiro–Wilk normality test followed by a paired *t*-test, $p < 0.05$. Errors are shown as standard deviation (SD) and standard error of the mean (SEM) where stated.

Supporting Information

Supporting Information is available from the Wiley Online Library or from the author.

Acknowledgements

This work was supported by a Medical Research Council Training Grant [MR/P015891/1]. The authors thank Mohamed Alhabeb and Tyler Mathis (Drexel) for providing MAX phase, XRD, and SEM characterization. XRD, XPS, and SEM were performed at Core Research Facilities (CRF) at Drexel University. The authors thank Nic Fusciardi for assistance with digital image processing.

Conflict of Interest

The authors declare no conflict of interest.

Keywords

accommodating intraocular lens, liquid crystals, MXene, nanomaterials, ophthalmic medical device, optoelectronic materials

Received: January 29, 2020
Revised: March 19, 2020
Published online:

[1] V. Gupta, M. Rajagopala, B. Ravishankar, *Indian J. Ophthalmol.* **2014**, *62*, 103.
[2] J. L. Alió, J. L. Alió del Barrio, A. Vega-Estrada, *Eye and Vision.* **2017**, *4*, 16.
[3] J. A. Venter, M. Pelouskova, B. M. Collins, S. C. Schallhorn, S. J. Hannan, *J. Cataract Refractive Surg.* **2013**, *39*, 1477.
[4] T. E. Lockhart, W. Shi, *Ergonomics* **2010**, *53*, 892.
[5] M. Walckling, R. Beck, O. Stachs, R. F. Guthoff, *Ophthalmology J.* **2018**, *3*, 29.
[6] J. L. Alio, A. Simonov, A. B. Plaza-Puche, A. Angelov, Y. Angelov, W. van Lawick, M. Rombach, *Am. J. Ophthalmol.* **2016**, *164*, 37.
[7] H. Siatiri, M. Mohammadpour, A. Gholami, E. Ashrafi, N. Siatiri, R. Mirshahi, *J. Current Ophthalmol.* **2017**, *29*, 274.
[8] H. E. Milton, P. B. Morgan, J. H. Clamp, H. F. Gleeson, *Opt. Express* **2014**, *22*, 8035.
[9] E. Lueder, in *Liquid Crystal Displays*, John Wiley & Sons, New York **2010**, pp. 57–82.
[10] J. Bailey, S. Kaur, P. B. Morgan, H. F. Gleeson, J. H. Clamp, J. C. Jones, *J. Phys. D: Appl. Phys.* **2017**, *50*, 485401.
[11] J. Bailey, P. B. Morgan, H. F. Gleeson, J. C. Jones, *Crystals* **2018**, *8*, 29.
[12] J. N. Coleman, P. J. King, U. Khan, M. Lotya, S. De, *ACS Nano* **2010**, *4*, 4238.
[13] X. Chen, F. Luo, M. Yuan, D. Xie, L. Shen, K. Zheng, Z. Wang, X. Li, L. Tao, *Adv. Funct. Mater.* **2019**, *29*, 1904706.
[14] K. Choi, H. G. Park, *ACS Nano* **2017**, *11*, 5223.
[15] C. Choi, M. K. Choi, S. Liu, M. S. Kim, O. K. Park, C. Im, J. Kim, X. Qin, G. J. Lee, K. W. Cho, M. Kim, E. Joh, J. Lee, D. Son, S.-H. Kwon, N. L. Jeon, Y. M. Song, N. Lu, D.-H. Kim, *Nat. Commun.* **2017**, *8*, 1664.
[16] T. Hwang, H.-Y. Kwon, J.-S. Oh, J.-P. Hong, S.-C. Hong, Y. Lee, H. Ryeol Choi, K. Jin Kim, M. Hossain Bhuiya, J.-D. Nam, *Appl. Phys. Lett.* **2013**, *103*, 023106.
[17] B. Anasori, M. R. Lukatskaya, Y. Gogotsi, *Nat. Rev. Mater.* **2017**, *2*, 16098.
[18] Z. Fu, N. Wang, D. Legut, C. Si, Q. Zhang, S. Du, T. C. Germann, J. S. Francisco, R. Zhang, *Chem. Rev.* **2019**, *119*, 11980.
[19] A. Lipatov, H. Lu, M. Alhabeb, B. Anasori, A. Gruverman, Y. Gogotsi, A. Sinitskii, *Sci. Adv.* **2018**, *4*, eaat0491.
[20] H. Kim, H. N. Alshareef, *ACS Mater. Lett.* **2020**, *2*, 55.
[21] B. Anasori, Y. Gogotsi, *2D Metal Carbides and Nitrides (MXenes)* (Eds: B. Anasori, Y. Gogotsi), Springer, Berlin **2019**.
[22] M. Alhabeb, K. Maleski, B. Anasori, P. Lelyukh, L. Clark, S. Sin, Y. Gogotsi, *Chem. Mater.* **2017**, *29*, 7633.
[23] M. Naguib, M. Kurtoglu, V. Presser, J. Lu, J.-J. Niu, M. Heon, L. Hultman, Y. Gogotsi, M. W. Barsoum, *Adv. Mater.* **2011**, *23*, 4248.
[24] K. Hantanasirisakul, M.-Q. Zhao, P. Urbankowski, J. Halim, B. Anasori, S. Kota, C. E. Ren, M. W. Barsoum, Y. Gogotsi, *Adv. Electron. Mater.* **2016**, *2*, 1600050.
[25] B. Anasori, Y. Xie, M. Beidaghi, J. Lu, B. C. Hosler, L. Hultman, P. R. C. Kent, Y. Gogotsi, M. W. Barsoum, *ACS Nano* **2015**, *9*, 9507.
[26] K. Hantanasirisakul, Y. Gogotsi, *Adv. Mater.* **2018**, *30*, 1804779.
[27] Y.-Y. Peng, B. Akuzum, N. Kurra, M.-Q. Zhao, M. Alhabeb, B. Anasori, E. C. Kumbur, H. N. Alshareef, M.-D. Ger, Y. Gogotsi, *Energy Environ. Sci.* **2016**, *9*, 2847.
[28] M. R. Lukatskaya, S. Kota, Z. Lin, M.-Q. Zhao, N. Shpigel, M. D. Levi, J. Halim, P.-L. Taberna, M. W. Barsoum, P. Simon, Y. Gogotsi, *Nat. Energy* **2017**, *2*, 17105.
[29] F. Shahzad, M. Alhabeb, C. B. Hatter, B. Anasori, S. Man Hong, C. M. Koo, Y. Gogotsi, *Science* **2016**, *353*, 1137.
[30] R. Bian, G. He, W. Zhi, S. Xiang, T. Wang, D. Cai, *J. Mater. Chem. C* **2019**, *7*, 474.
[31] K. Rasool, R. P. Pandey, P. A. Rasheed, S. Buczek, Y. Gogotsi, K. A. Mahmoud, *Mater. Today* **2019**, *30*, 80.
[32] J. Saththasivam, K. Wang, W. Yiming, Z. Liu, K. A. Mahmoud, *RSC Adv.* **2019**, *9*, 16296.
[33] X. Yu, X. Cai, H. Cui, S. W. Lee, X. F. Yu, B. Liu, *Nanoscale* **2017**, *9*, 17859.
[34] Q. Xue, H. Zhang, M. Zhu, Z. Pei, H. Li, Z. Wang, Y. Huang, Y. Huang, Q. Deng, J. Zhou, S. Du, Q. Huang, C. Zhi, *Adv. Mater.* **2017**, *29*, 1604847.
[35] L. Wu, X. Lu, Z. Wu, Y. Dong, X. Wang, S. Zheng, J. Chen, *Biosens. Bioelectron.* **2018**, *107*, 69.
[36] S. Kumar, Y. Lei, N. H. Alshareef, K. N. Salama, *Biosens. Bioelectron.* **2018**, *121*, 243.
[37] S. J. Kim, H.-J. Koh, C. E. Ren, O. Kwon, K. Maleski, S.-Y. Cho, B. Anasori, C.-K. Kim, Y.-K. Choi, J. Kim, Y. Gogotsi, H.-T. Jung, *ACS Nano* **2018**, *12*, 986.
[38] K. Rasool, K. A. Mahmoud, D. J. Johnson, M. Helal, G. R. Berdiyorov, Y. Gogotsi, *Sci. Rep.* **2017**, *7*, 1598.
[39] K. Rasool, M. Helal, A. Ali, C. E. Ren, Y. Gogotsi, K. A. Mahmoud, *ACS Nano* **2016**, *10*, 3674.
[40] Z. Liu, M. Zhao, H. Lin, C. Dai, C. Ren, S. Zhang, W. Peng, Y. Chen, *J. Mater. Chem. B* **2018**, *6*, 3541.

[41] X. Han, X. Jing, D. Yang, H. Lin, Z. Wang, H. Ran, P. Li, Y. Chen, *Theranostics* **2018**, *8*, 4491.
[42] G. Liu, J. Zou, Q. Tang, X. Yang, Y. Zhang, Q. Zhang, W. Huang, P. Chen, J. Shao, X. Dong, *ACS Appl. Mater. Interfaces* **2017**, *9*, 40077.
[43] A. M. Jastrzębska, A. Szuplewska, T. Wojciechowski, M. Chudy, W. Ziemkowska, L. Chlubny, A. Rozmysłowska, A. Olszyna, *J. Hazard. Mater.* **2017**, *339*, 1.
[44] P. Salles, D. Pinto, K. Hantanasirisakul, K. Maleski, C. E. Shuck, Y. Gogotsi, *Adv. Funct. Mater.* **2019**, *29*, 1809223.
[45] Y. Gogotsi, A. Sarycheva, A. Polemi, Y. Liu, B. Anasori, K. Dandekar, *Sci. Adv.* **2018**, *4*, eaau0920.
[46] N. Driscoll, A. G. Richardson, K. Maleski, B. Anasori, O. Adewole, P. Lelyukh, L. Escobedo, D. K. Cullen, T. H. Lucas, Y. Gogotsi, F. Vitale, *ACS Nano* **2018**, *12*, 10419.
[47] J. K. El-Demellawi, S. Lopatin, J. Yin, O. F. Mohammed, H. N. Alshareef, *ACS Nano* **2018**, *12*, 8485.
[48] S. De, J. N. Coleman, *ACS Nano* **2010**, *4*, 2713.
[49] G. D. Boreman, in *Modulation Transfer Function in Optical and Electro-optical Systems*, SPIE Press, Bellingham, WA **2001**, p. 120.
[50] T. Dutta, R. Sarkar, B. Pakhira, S. Ghosh, R. Sarkar, A. Barui, S. Sarkar, *RSC Adv.* **2015**, *5*, 80192.
[51] M. Schadt, *Annual Rev. Mater. Sci.* **1997**, *27*, 305.
[52] J. Li, *Refractive Indices Of Liquid Crystals And Their Applications In Display And Photonic Devices*, University of Central Florida, Florida **2005**.
[53] S. Y. Lee, Y. Kumar, J. M. Cho, S. W. Lee, S. W. Kim, *IEEE Transact. Circuits Systems Video Technol.* **2008**, *18*, 983.
[54] X. Wang, *IEEE Transactions on Pattern Analysis and Machine Intelligence* **2007**, *29*, 886.
[55] K. Maleski, C. E. Ren, M.-Q. Zhao, B. Anasori, Y. Gogotsi, *ACS Appl. Mater. Interfaces* **2018**, *10*, 24491.
[56] G. B. Hadjichristov, Y. G. Marinov, A. G. Petrov, L. Marino, N. Scaramuzza, *J. Phys.: Conf. Ser.* **2016**, *682*, 012015.

Appendix 7 – Competitions related to the PhD program

1. Second place NanoArtography 2019, 2D Liquid Crystalline World, an international science image competition.

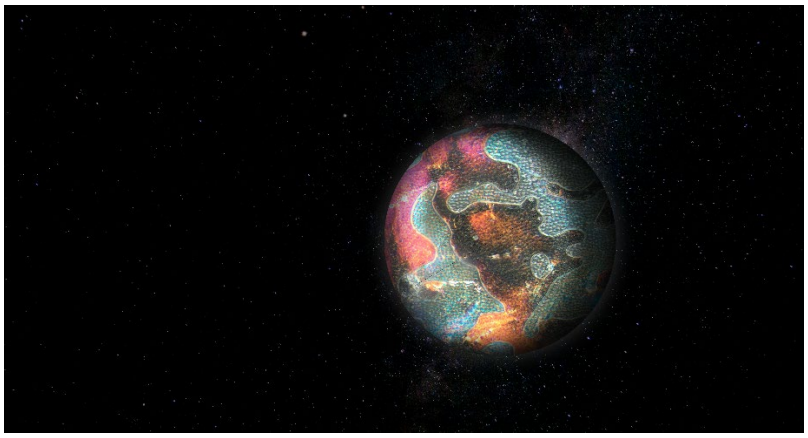

2. Bake your thesis winner 2019, Distorted Vision.